https://doi.org/10.15388/vu.thesis.751
https://orcid.org/0000-0003-0189-386X

VILNIUS UNIVERSITY
CENTER FOR PHYSICAL SCIENCES AND TECHNOLOGY

Mantas Gaidys

Laser Polishing and Colouring of Metals Using Ultrashort Pulses

DOCTORAL DISSERTATION

Technological Sciences,
Material Engineering (T 008)

VILNIUS 2025

The dissertation was prepared between 2020 and 2024 at Center for Physical Sciences and Technology. The research was supported by Research Council of Lithuania:
Grants – P-DAP-24-249, P-DAK-23-30;
Projects – 01.2.2-LMT-K-718-03-0050, S-MIP-22-89;

Academic Supervisor – Dr. Mindaugas Gedvilas (Center for Physical Sciences and Technology, Technological Sciences, Materials Engineering – T 008)

This doctoral dissertation will be defended in a public meeting of the Dissertation Defence Panel:

Chairman – Prof. Dr. Mangirdas Malinauskas (Vilnius University, Technological Sciences, Materials Engineering – T 008).
Members:
Prof. Dr. Zigmas Balevičius (Vilnius Gediminas Technical University, Technological Sciences, Materials Engineering – T 008),
Prof. Dr. Saulius Juodkazis (Swinburne University of Technology, Technological Sciences, Materials Engineering – T 008),
Prof. Dr. Domas Paipulas (Vilnius University, Technological Sciences, Materials Engineering – T 008),
Prof. Dr. Tomas Tamulevičius (Kaunas University of Technology, Technological Sciences, Materials Engineering – T 008).

The dissertation shall be defended at a public meeting of the Dissertation Defence Panel at 10 a.m. on 2nd of May 2025 in the hall of FTMC Institute of Physics.
Address: Savanoriu ave. 231, LT-02300 Vilnius, Lithuania
Tel. +370 5 266 1640; e-mail: office@ftmc.lt.

The text of this dissertation can be accessed at the library of Vilnius University, as well as on the website of Vilnius University: www.vu.lt/lt/naujienos/ ivykiu-kalendorius

https://doi.org/10.15388/vu.thesis.751
https://orcid.org/0000-0003-0189-386X

VILNIAUS UNIVERSITETAS
FIZINIŲ IR TECHNOLOGIJOS MOKLSŲ CENTRAS

Mantas Gaidys

Lazerinis metalų poliravimas bei spalvinimas naudojant ultratrumpuosius impulsus

DAKTARO DISERTACIJA

Technologijos mokslai,
Medžiagų inžinerija (T 008)

VILNIUS 2025

Disertacija rengta 2020–2024 metais Fizinių ir technologijos mokslų centre.
Mokslinius tyrimus rėmė Lietuvos mokslo taryba:
Stipendijos – P-DAP-24-249, P-DAK-23-30;
Projektai – 01.2.2-LMT-K-718-03-0050, S-MIP-22-89;

Mokslinis vadovas – dr. Mindaugas Gedvilas (Fizinių ir technologijos mokslų centras, technologijos mokslai, medžiagų inžinerija – T 008)

Gynimo taryba:
Pirmininkas – prof. dr. Mangirdas Malinauskas (Vilniaus universitetas, technologijos mokslai, medžiagų inžinerija – T 008).
Nariai:
prof. dr. Zigmas Balevičius (Vilniaus Gedimino technikos universitetas, technologijos mokslai, medžiagų inžinerija – T 008),
prof. dr. Saulius Juodkazis (Svinburno technologijų universitetas, technologijos mokslai, medžiagų inžinerija – T 008),
prof. dr. Domas Paipulas (Vilniaus universitetas, technologijos mokslai, medžiagų inžinerija – T 008),
prof. dr. Tomas Tamulevičius (Kauno technologijos universitetas, technologijos mokslai, medžiagų inžinerija – T 008).

Disertacija ginama viešame Gynimo tarybos posėdyje 2025 m. gegužės mėn. 2 d. 10 val. Fizinių ir technologijos mokslų centro Fizikos instituto salėje. Adresas: Savanorių pr. 231, LT-02300 Vilnius, Lietuva, tel. + 370 5 266 1640; el. paštas: office@ftmc.lt.

Disertaciją galima peržiūrėti VU bibliotekoje ir VU interneto svetainėje adresu:
https://www.vu.lt/naujienos/ivykiu-kalendorius.

LIST OF ABBREVIATIONS 8
INTRODUCTION 9
Aim of the thesis 10
Tasks of the thesis 10
Scientific novelty 11
Practical value 11
Statement for defence 12
Author Contribution 12
Publication List 13
Conference Presentation List 15
Literature overview 19
1.1 Pulsed laser matter interactions on metals 19
1.2 Laser ablation 20
1.3 Laser burst modes 22
1.4 Colour theory 23
1.5 Laser colouring on metals 24
1.5.1 Laser colouring due surface oxidation 24
1.5.2 Important parameters for oxide formation 26
1.5.3 Laser colouring due to surface oxidation applications. 29
1.5.4 Laser colouring due to LIPSS 30
1.5.5 Achieving LIPPS for laser colouring 30
1.5.6 Applications of laser colouring due to LIPSS 32
1.5.7 Laser colouring due to nanoparticles/nanostructures ... 34
1.5.8 Applications of laser colouring due to nanoparticles/nanostructures 34
1.6 Laser polishing 35
1.6.1 Surface roughness parameters and measurement 37
1.6.2 Laser polishing applications 39
Experimental setups and characterisations 41
Experiments 44

2 Laser colouring of metals 44
2.1 Laser colouring of stainless steel 44
2.1.1 Experimental setup 44
2.1.2 Laser colouring using MHz, GHz and biburst modes .. 46
2.1.3 Rapid laser colouring using GHz burst mode 50
2.1.4 Coloured surface hydrophobicity 61
2.2 Laser colouring of copper 62
2.2.1 Wettablity theory 62
2.2.2 Experimental setup 64
2.2.3 Contant angle and other measurements 65
2.2.4 Area fraction evaluation 65
2.2.5 Luminance and color distance evaluations 67
2.2.6 Copper colouring and wettability 68
2.3 Summary 71
3 Laser polishing of metals 73
3.1 Influence of nonlinear and saturable absorption 73
3.1.1 Influence of nonlinear and saturable absorption on laser lift-off threshold 74
3.2 Laser polishing on copper and stainless-steel 81
3.2.1 Experimental setup 81
3.2.2 Beam characteristics 82
3.2.3 Laser polishing on copper and stainless steel 83
3.3 Bi-stability in femtosecond laser polishing by MHz bursts 89
3.3.1 Experimental setup 89
3.3.2 Bi-stability 90
3.3.3 Shielding and redeposition 93
3.4 Summary 93
CONCLUSIONS 95
SANTRAUKA 96
PADĖKA 107

REFERENCE LIST 108
CURRICULUM VITAE 120
APIE AUTORIŲ 121
REPRINTED PUBLICATIONS 122

LIST OF ABBREVIATIONS

2.5D – two-and-a-half dimensional
3D – three-dimensional
CA – contact angle
CW – continuous wave
FTMC – Center for Physical Sciences and Technology in Lithuanian
GHz – gigahertz
HAZ – heat affected zone
HSFL – high spatial frequency laser induced periodic surface structures
HSL – hue, saturation, lightness
ID – identity document
IR – infrared
LED – light-emitting diode
LIPSS – laser induced periodic surface structures
LSFL – low spatial frequency laser induced periodic surface structures
LTS – Department of Laser Technology in Lithuanian
MHz – megahertz
RGB – red, green, blue
SEM – scanning electron microscope
SP – surface plasmons
SPP – surface plasmon polaritons
SWCA – static water contact angle
TTM – two-temperature model
UV – ultraviolet
VAD – ventricular assist device
WoS – Web of Science
XRD – X-ray diffraction

INTRODUCTION

Many products used in various industries are significantly influenced by texture and surface quality [1]. Laser micromachining is an appealing method because of the abundance of applications: from cutting [2–5] and drilling [6–8] of various materials to forming two and a half dimensional (2.5D) structures on different surfaces [9,10]. With continuing improvements to laser micromachining, further techniques such as laser colouring and polishing are becoming popular as well.

Humans attach a great deal of importance to colours. It aids with object and pattern recognition, as well as navigating the environment. In addition, particular colours may invoke emotions and create associations, which is widely used in marketing and branding. Laser surface colouring has quickly surpassed conventional marking techniques [11] since it is an adaptable, versatile and environmentally friendly technology with many different applications. While the utilization of laser colouring is growing rapidly, the colourization process itself has not been sufficiently studied. There are three main mechanisms of metal colouring using laser irradiation. First method is laser induced oxidation where a substrate material reacts with oxygen significantly more quickly when heated by laser irradiation. An oxide layer forms on the metal, which is of different colour to the original metal [12–14]. Another explanation for the colour change with an oxide layer is the thin film effect, when light reflects from the surface of the oxide and the surface of the metal, interference happens and if the optical path difference is equal to a certain wavelength or its product with an integer a corresponding colour is seen [11]. The second method is structural colours that are angle dependent and arise from laser induced periodic surface structures (LIPSS). LIPSS is the development of wavy structures on a range of materials and requires surface characteristics with a periodicity equal to or less than the wavelength of the laser irradiation [15]. LIPSS similar to one dimensional grating can produce colours due to diffraction. These colours are called structural colours and are heavily angle dependent [16–18]. The third method of laser colouring uses nanoparticles and nanostructures on metals to activate plasmonic colours. These colours are also structural. In contrast to the second mechanism, the colour does not change depending on the viewing angle since the surface structures that excite the surface colours are randomly distributed without regularity. The primary causes of this form of colours are surface plasmon resonance (SPR) effects brought on by nanostructures and nanoparticles on metals [19–21]. Laser colouring depends on many processing parameters, including: laser power, scanning speed, hatch, pulse repetition rate and others.

By optimizing the laser processing parameters, it is also possible to gain a wanted structural surface change as well, which may result in useful properties such as hydrophobicity.

Similarly, laser polishing is also a wanted and popular laser micromachining technique. Because sub-micrometer surface roughness is wanted in friction and wear resistance and aerodynamics, laser polishing is a very perspective polishing method. Laser polishing allows high precision, a vast range of possible materials, reaching delicate places, polishing complex forms [22,23], and also the ability to micromachine and polish samples using the same laser system.

However, optimal laser processing parameters such as pulse repetition rate, pulse energy, pulse overlap, and others have to be chosen correctly to achieve the best results, which is tedious and time-consuming. Lasers and systems designed for laser micro/nano-fabrication are improved daily. It is now possible to have systems that use megahertz (MHz) and gigahertz (GHz) repetitions rates with femtosecond laser pulses and high average optical power using burst and biburst (burst-in-the-burst) modes [24]. These modes allow a significant increase in ablation efficiency [25,26] as well as significantly improve the ablated surface roughness [15] if the laser processing parameters are optimized correctly. Laser bursts also provide faster processing due to burst energy division into pulse energies closer to optimal fluences, resulting in the exploitation of more average laser power [27]. Moreover, because of the short time between burst pulses, any residual heat from the previous pulse is reused [28].

This dissertation was dedicated to finding optimal sets of various laser processing parameters to achieve lowest surface roughness using laser polishing and highest number of colours and highest colouring rate using laser colouring on copper and stainless steel. The dissertation is split into two main parts: one for laser colouring and one for laser polishing. Laser colouring was performed on stainless steel with low fluence slow scanning speed colouring and rapid colouring using higher fluences, where for copper, grayscale colouring was performed. For laser polishing, optimization of number of pulses in bursts, burst mode bi-stability, as well as nonlinear and saturable absorption influence on laser lift-off threshold was performed.

Aim of the thesis

The aim of this thesis was to achieve the optimal number of pulses in MHz, GHz, and biburst modes, as well as to achieve the optimal fluence, to minimize surface roughness and maximize the number of colours and the colouring rate

of metals, therefore increasing the applicability of laser polishing and colouring in industrial uses.

Tasks of the thesis

1. To investigate the influence of the number of pulses within MHz, GHz and biburst modes and their effects on laser polishing and colouring.
2. To achieve the lowest possible surface roughness on different metals after ablation to simulate real life applications.
3. To achieve the highest number of colours on stainless steel with laser colouring more rapidly than has ever been done by optimising laser processing parameters.
4. To achieve functional surfaces that would increase the applicability of the coloured surfaces.

Scientific novelty

In this thesis laser polishing and colouring was performed on copper and stainless steel. Different burst regimes including MHz, GHz and biburst as well as different laser processing parameters were tested. Getting lowest surface roughness on stainless steel and copper would be very useful for industrial applications and it this dissertation, 0.1 µm surface roughness was achieved using optimal laser processing parameters. A wide array of colours has also been achieved on stainless steel. To the best of our knowledge, highest laser colouring rate has been achieved in our experiments. The achieved colours are long lasting and the coloured surfaces are hydrophobic, which increases their applicability greatly.

Practical value

Laser polishing and colouring are used in medical and automotive industries as an environmentally friendly, adaptable and long-lasting methods to polish and colour free-form parts or instruments as well as potential uses in watch making and colouring. Our in-depth experiments that resulted in wide range of colours, rapid colouring rates, hydrophobic coloured surfaces and sub-micrometer polished surfaces furthers the processes applicability in industrial use.

Statement for defence

1. Stainless steel colouring rate reaching 42.5 mm^2/s, while using GHz burst mode with 4250 mm/s scanning speed, was used to achieve various colours, including blue, yellow, orange, purple and dark green on stainless steel by femtosecond laser colouring technique due to surface oxidation.
2. All three burst modes: MHz, GHz and biburst, with femtosecond pulses can be used for laser colouring to achieve a wide spectrum of colours on stainless steel and these coloured surfaces are hydrophobic, which increases their applicability.
3. Dependence of the copper oxide film's transparency on laser irradiation intensity due to nonlinear and saturable absorption changes the film's lift-off threshold, which is the threshold laser energy required to detach a thin oxide film by vaporizing the underlying metal, assists laser polishing of the metal surface.
4. Using GHz burst mode with up to 15 pulses and biburst mode with 3 pulses in the MHz burst with up to 10 pulses in the GHz burst, it is possible to achieve <0.1 µm R_a surface roughness on copper and <0.5 µm R_a surface roughness on stainless steel, which shows the importance of optimal number of pulses within the burst.

Author Contribution

In publication [P1] the author wrote the manuscript, performed all the laser colouring and wettability experiments, the data analysis and was responsible for the representation of the results in the form of graphs, figures, tables and images.

In publication [P2] the author helped to conceive the original idea for the research alongside co-authors, performed some of the ablation experiments and analysed the data and discussed the results and commented on the manuscript.

In publication [P3] the author wrote the manuscript, performed the data analysis, as well as, SEM, optical and stylus profilers' imaging. The author was also responsible for the representation of the results in the form of graphs, figures, tables and images.

In publication [P4] the author performed the data analysis and manuscript corrections.

In preprint of the publication [PP1] author wrote the manuscript, performed all the laser colouring and wettability experiments, the data analysis and was

responsible for the representation of the results in the form of graphs, figures, tables and images.

In the preprint of the publication [PP2] author helped to conceive the original idea for the project, conducted the surface topography measurements and surface roughness measurements using a 3D optical profiler. As well as analysed the findings, discussed the results, and commented on the manuscript.

PUBLICATION LIST

The results of the thesis were presented in 4 scientific publications [P1-P4], one scientific publication still currently as preprints [PP1-PP2] and 3 conferences proceedings [P5-P7]. Five more scientific publication [P8-P12] and 2 conferences proceedings [P13-P14] were written but are not directly related to the thesis.

Scientific publications directly related to the thesis:

[P1] **M. Gaidys**, A. Selskis, P. Gečys, M. Gedvilas, "Stainless steel colouring using burst and biburst mode ultrafast laser irradiation", *Opt. Laser Technol.* **174**, 110561, (2024). DOI: 10.1016/j.optlastec.2024.110561

[P2] A. Žemaitis, **M. Gaidys**, P. Gečys, M. Gedvilas, "Bi-stability in femtosecond laser ablation by MHz bursts", *Sci. Rep.* **14**, 5614 (2024). DOI: 10.1038/s41598-024-54928-7

[P3] **M. Gaidys**, A. Žemaitis, P. Gečys, M. Gedvilas, "Efficient surface polishing using burst and biburst mode ultrafast laser irradiation", *RSC Adv.* **13**, 3586-3591 (2023). DOI: 10.1039/D2RA05208C

[P4] A. Žemaitis, **M. Gaidys**, P. Gečys, M. Gedvilas, "Influence of nonlinear and saturable absorption on laser lift-off threshold of an oxide/metal structure", *Opt. Lett.* **45**, 6166 (2020). DOI: 10.1364/OL.404760

[PP1] **M. Gaidys**, A. Selskis, P. Gečys, M. Gedvilas, "High-rate Stainless Steel Laser Colouring with GHz Femtosecond Bursts". *Opt. Laser Technol.* (2025). (submitted, major review).

[PP2] **M. Gaidys**, S. Maragkaki, A. Mimidis, A. Papadopoulos, A. Lemonis, E. Skoulas, A. Žemaitis, E. Stratakis, M. Gedvilas, Wettability and Color Change of Copper by Controlling Area Fraction of Laser Ablated Surface, *Opt. Laser Technol.* (2025). (submitted, under revision) DOI: 10.48550/arXiv.2411.17324

Scientific publications directly related to the thesis (conference proceedings):

[P5] **M Gaidys**, P Gečys, M Gedvilas, Laser Functionalization of Stainless Steel Surface Using MHz, GHz, and Biburst Modes Proceedings of the 7th International Conference on Optics, Photonics and Lasers (OPAL' 2024) 15-17 May 2024 Palma de Mallorca (Balearic Islands), Spain Edited by Sergey Y. Yurish, 142 (2024).

[P6] **M. Gaidys**, A. Žemaitis, P. Gečys, M. Gedvilas, High-throughput laser ablation and polishing of copper cylinders, Proc. CYSENI 1, 777-781 (2021).

[P7] A. Žemaitis, **M. Gaidys**, P. Gečys, M. Gedvilas, Saturable and Nonlinear Absorption Role in Laser Lift-off Threshold Fluence of the Oxide Layer from a Metal Substrate in z-scan Type Experiments, OPAL' 2021 Conf. Proc. 1, 114-120 (2021).

Scientific publications not directly related to the thesis:

[P8] A. Žemaitis, **M. Gaidys**, P. Gečys, M. Gedvilas "Femtosecond laser ablation by bibursts in MHz and GHz pulse repetition rate", *Opt. Express* **29**, 5 (2021). DOI: 10.1364/OE.417883

[P9] **M. Gaidys**, A. Žemaitis, P. Gečys, M. Gedvilas, "Efficient picosecond laser ablation of copper cylinders", *Appl. Surf. Sci.* **483**, 962-966 (2019). DOI: 10.1016/j.apsusc.2019.04.002

[P10] A. Žemaitis, J. Mikšys, **M. Gaidys**, P. Gečys, M. Gedvilas, "High-efficiency laser fabrication of drag reducing riblet surfaces on pre-heated Teflon", *Mater. Res. Express*, **6** 065309 (2019). DOI: 10.1088/2053-1591/ab0b12

[P11] A. Žemaitis, **M. Gaidys**, P. Gečys, G. Račiukaitis, M. Gedvilas, "Rapid high-quality 3D micro-machining by optimised efficient ultrashort laser ablation", *Opt. Lasers Eng.* **114**, 83-89 (2019). DOI: 10.1016/j.optlaseng.2018.11.001

[P12] A. Žemaitis, **M. Gaidys**, M. Brikas, P. Gečys, G. Račiukaitis, M. Gedvilas, "Advanced laser scanning for highly-efficient ablation and ultrafast surface structuring: experiment and model", *Sci. Rep.* **8**, 17376 (2018). DOI: 10.1038/s41598-018-35604-z

Scientific publications not directly related to the thesis (conference proceedings):

[P13] A. Žemaitis, **M. Gaidys**, J. Mikšys, P. Gečys, M. Gedvilas, Functional surface formation by efficient laser ablation using single-pulse and burst-modes, *Proc. SPIE* **11673**, 116730S (2021) DOI: 10.1117/12.2574840

[P14] A. Žemaitis, **M. Gaidys**, P. Gečys, M. Gedvilas, Laser processing by ultrafast bursts of pulses, OPAL' 2021 Conf. Proc. 2, 103-105 (2022).

CONFERENCE PRESENTATION LIST

The results of the thesis were also presented in 10 conferences [C1-C10]. [C1-C9] were presented by the thesis author as oral presentations and [C1-C3] were chosen for the best or outstanding oral presentation awards. 15 more conferences were co-authored [C10-C25] but were not directly related to the thesis. [C17-C20] were presented by the thesis author as poster presentations with [C20] being presented as oral presentation as well.

Conferences that are directly related to the thesis with the presenter underlined:

[C1] **M. Gaidys**, P. Gečys, M. Gedvilas, „Efficient laser surface colouring of stainless-steel using femtosecond GHz bursts, The 25th International Symposium On Laser Precision Microfabrication (LPM2024), San Sebastian, Spain, June 11-14, 2024. **Oral presentation, chosen as the best oral presentation in the conference.**

[C2] **M. Gaidys**, P. Gečys, M. Gedvilas, "Laser surface colouring on metals using femtosecond burst regimes", The 24th International Symposium on Laser Precision Microfabrication (LPM2023), Hirosaki, Japan, June 13 – 16, 2023. **Oral presentation, chosen among the 5 best oral presentations in the conference.**

[C3] **M. Gaidys**, A. Selskis, P. Gečys, M. Gedvilas, "Lazerinis plieno spalvinimas ultratrumpųjų impulsų voromis", 13th FTMC PhD students and young scientists Conference (FizTech13), Vilnius, Lithuania, October 18–19, 2023. **Oral presentation, chosen among the 7 best oral presentations in the conference.**

[C4] **M. Gaidys**, P. Gečys, M. Gedvilas, „Laser functionalization of stainless steel surface using MHz, GHz, and biburst modes", 7th International Conference on Optics, Photonics and Lasers (OPAL2024), Palma de Mallorca, Spain, May 15-17, 2024. **Oral presentation.**

[C5] **M. Gaidys**, A. Žemaitis, P. Gečys, M. Gedvilas, "Efficient femtosecond laser polishing of metals using MHz, GHz, and biburst regimes",

The 23rd International Symposium on Laser Precision Microfabrication (LPM2022), Dresden, Germany, 2022. **Oral presentation.**

[C6] **M. Gaidys**, A. Žemaitis, P. Gečys, M. Gedvilas, "Efficient laser drilling, milling and polishing on metals using ultrashort bursts and bibursts", The 2021 International High Power Laser Ablation Symposium (HPLA2021). **Oral presentation.**

[C7] **M. Gaidys**, A. Žemaitis, P. Gečys, M. Gedvilas, "Influence of laser pulse repetition rate on the ablation efficiency and surface quality of copper", The 22nd International Symposium on Laser Precision Microfabrication (LPM2021), Virtual, 2021. **Oral presentation.**

[C8] **M. Gaidys**, A. Žemaitis, P. Gečys, M. Gedvilas, "Našus lazerinis metalų poliravimas ultratrumpųjų impulsų voromis", 12th FTMC PhD students and young scientists Conference (FizTech12), Vilnius, Lithuania, 2022. **Oral presentation.**

[C9] **M. Gaidys**, A. Žemaitis, P. Gečys, M. Gedvilas, "High-throughput laser ablation and polishing of copper cylinders", The 17th International conference of young scientists on energy and natural sciences issues (Cyseni17), Virtual, 2021. **Oral presentation.**

[C10] A. Žemaitis, **M. Gaidys**, P. Gečys, M. Gedvilas, Saturable and nonlinear absorption role in laser lift-off threshold fluence of the oxide layer from a metal substrate in z-scan type experiments, 4th International Conference on Optics, Photonics and Lasers (OPAL' 2021), Corfu, Greece, 2021. **Oral presentation.**

Conferences that are not directly related to the thesis with the presenter underlined:

[C11] A. Žemaitis, **M. Gaidys**, P. Gečys, M. Gedvilas, "Laser processing by ultrafast bursts of pulses," 5th International Conference on Optics, Photonics and Lasers (OPAL' 2022), Tenerife, Spain, 2022, **Poster presentation**.

[C12] A. Žemaitis, **M. Gaidys**, P. Gečys, G. Račiukaitis, M. Gedvilas, "Ultrafast laser ablation by bi-bursts in MHz and GHz pulse repetition rate", Photonics West, Laser Applications in Microelectronic and Optoelectronic Manufacturing (LAMOM) XXVI, Virtual, 2021. **Oral presentation.**

[C13] A. Žemaitis, **M. Gaidys**, J. Mikšys, P. Gečys, M. Gedvilas, "Functional surface formation by efficient laser ablation using single-pulse and burst-modes," Photonics West, Laser Applications in Microelectronic and Optoelectronic Manufacturing (LAMOM) XXVI, Virtual, 2021. **Oral presentation.**

[C14] I. Žičkienė, R. Adomavičius, A. Krotkus, M. Gedvilas, **M. Gaidys**, G. Račiukaitis, "Terahertz radiation induced by surface ballistic photogalvanic effect in GaAs LIPSS structures", 17th International conference on Advanced properties and processes in optoelectronics materials and systems (Apropos 17), Vilnius, Lithuania, 2020. **Oral presentation.**

[C15] A. Žemaitis, **M. Gaidys**, P. Gečys, M. Gedvilas, Novel biburst ultrafast laser ablation: burst-in-burst regime, The 21th International Symposium on Laser Precision Microfabrication (LPM 2020), Dresden, Germany, 2020. **Oral presentation.**

[C16] A. Žemaitis, **M. Gaidys**, P. Gečys, M. Gedvilas, "Efficient laser milling technology for bio-inspired functional surface formation," 22nd International Conference – School Advanced Materials and Technologies 2020, Palanga, Lithuania, 2020. **Oral presentation.**

[C17] **M. Gaidys**, A. Žemaitis, P. Gečys, M. Gedvilas, "Lazerinės abliacijos efektyvumas apdirbant metalus ultratrumpųjų impulsų voromis: gręžimas ir frezavimas", 10th FTMC PhD students and young scientists Conference (FizTech10), Vilnius, Lithuania, 2020. **Poster presentation.**

[C18] **M. Gaidys**, A. Žemaitis, P. Gečys, G. Račiukaitis, M. Gedvilas, "Efficient picosecond laser ablation on cylindrical surfaces", 11th International Conference on Photo-Excited Processes and Applications (ICPEPA 11), Vilnius, Lithuania (2018). **Poster presentation.**

[C19] **M. Gaidys,** A. Žemaitis, P. Gečys, M. Gedvilas, "Study of efficient copper laser ablation", 61th International Conference for Students of Physics and Natural Sciences "Open Readings 2018", Vilnius, Lithuania (2018). **Poster presentation.**

[C20] **M. Gaidys**, A. Žemaitis, P. Gečys, G. Račiukaitis, M. Gedvilas, „Efficient laser ablation on flat and cylindrical surfaces", 6th International School on Lasers in Materials Science (SLIMS), S. Servolo Island, Venice, Italy, (2018). **Oral and poster presentations.**

[C21] M. Gedvilas, A. Žemaitis, **M. Gaidys**, P. Gečys, G. Račiukaitis, Efficient Laser Scanning Ablation Procedure for Ultrafast Surface Structuring, 11th International Conference on Photo-Excited Processes and Applications (ICPEPA 11), Vilnius, Lithuania (2018). **Oral presentation.**

[C22] A. Žemaitis, **M. Gaidys**, M. Gedvilas, Efficient ultrashort pulsed laser ablation for 3D engraving, 61th International Conference for Students of Physics and Natural Sciences „Open Readings 2018", Vilnius, Lithuania (2018). **Oral presentation.**

[C23] I. Beleckaitė, R. Adomavičius, A. Krotkus, M. Gedvilas, **M. Gaidys**, G. Račiukaitis, Terahertz emission enhancement by forming LIPS structures on the surface of GaAs, Advanced Properties and Processes in Optoelectronic

Materials and Systems (APROPOS 16) Vilnius, Lithuania, (2018). **Oral presentation.**

[C24] A. Abakevičienė, M. Lukauskas, D. Jucius, A. Lazauskas, V. Grigaliūnas, M. Gedvilas, **M. Gaidys**, G. Račiukaitis, *Structural Properties of Temperature-UV Affected Fluorinated Ethylene Propylene Film*, "Nanotechnology and Innovation in the Baltic Sea Region" (NIBS2017), Kaunas, Lithuania (2017). **Oral presentation.**

[C25] I. Beleckaitė, R. Adomavičius, A. Krotkus, M. Gedvilas, **M. Gaidys**, G. Račiukaitis, *Laser induced periodic surface structures on the GaAs surface investigated by THz emission measurements,* 19-th International Conference-School "Advanced Materials and Technologies" (AMT2017), Palanga, Lithuania (2017). **Oral presentation.**

LITERATURE OVERVIEW

1.1 Pulsed laser matter interactions on metals

Through the inverse Bremsstrahlung phenomena, laser energy is directly absorbed by metals' free electrons. The electrons are then thermalized through femtosecond timescale collisions with other electrons. Since ions are far heavier than electrons, the lattice structure cannot directly absorb the laser energy. Instead, it is heated by the collisions with the energetic electrons. Only a limited amount of energy is exchanged in each electron-lattice collision due to the high ion-electron mass difference. Consequently, the electron-phonon relaxation characteristic time τ_e is significantly longer than the electron-electron collision time τ_{ee}. Typical metals have τ_{ep} ranging from tens of ps to several hundred of fs. After a few multiples of τ_{ep}, the electron system and lattice finally achieve thermodynamic equilibrium [29]. The well-known one-dimensional two-temperature model provides a broad description of this process and takes into consideration the thermal diffusion, also known as Fourier's law, and the energy relaxation between electrons and phonons [30]:

$$C_e(T_e)\frac{\partial T_e}{\partial t} = \nabla(k_e \nabla T_e) - g(T_e - T_l) + S(z,t), \quad (1)$$

$$C_l\frac{\partial T_l}{\partial t} = g(T_e - T_l), \quad (2)$$

$$S(z,t) = I(t)(1-R)\alpha e^{-\alpha z}, \quad (3)$$

where C – heat capacity, k – thermal conductivity, T – temperature. The subscripts e means the electron system and the subscript l means the lattice system. z is the direction perpendicular to the target's surface and S – energy absorbed by the laser excitation. I(t) – is the laser intensity, R – surface reflectivity, α – optical absorption coefficient. Parameter g denotes the electron–lattice coupling.

The electrons and lattice have enough time to reach thermal equilibrium (i.e., $T_e = T_l = T$) after a single pulse stimulation in the ns or longer pulse regime. Thus, the normal heat diffusion equation can be obtained from the aforementioned equations:

$$C\frac{\partial T}{\partial t} - k\nabla^2 T = S(z,t) \tag{4}$$

Ultrafast laser pulses exhibit more intricate phenomena. When electron-phonon relaxation takes as long as the pulse or more, the electron energy cannot go to the lattice before the laser excitation. Comparing the two scenarios, the ultrashort laser pulses would have a higher maximum lattice temperature at the surface and a shorter thermal diffusion range after laser excitation [29].

1.2 Laser ablation

Laser ablation is a process that uses laser irradiation to remove a specific amount of material from the surface of a selected sample. For this process to take place, it is necessary for the absorbed laser irradiation of the material to heat the area where the absorption takes place to the evaporation temperature. As the laser irradiation reaches the surface of the material, some of the laser irradiation is reflected, some is scattered, some passes through (if the thickness of the sample is less than the depth of absorption) and some is absorbed [31]. The absorbed part penetrates deeply and is attenuated according to the Beer–Bouguer–Lambert law:

$$I(z) = (1 - R)I_0 \mathrm{e}^{-\alpha z} \tag{5}$$

where I_0 is the initial incident light intensity, R is the reflection coefficient of the material, α is the absorption coefficient and z is the depth.

The absorption coefficient β is equal to [1]:

$$\alpha = \frac{4\pi\kappa}{\lambda} \tag{6}$$

where κ is the extinction coefficient and λ is the wavelength of the laser irradiation.

Equation (6) shows that the absorption coefficient is independent of the initial laser intensity, but only linear optical phenomena are included in this formula. Laser irradiation is used to achieve very high intensities which produce absorption-enhancing nonlinear effects.

There are several mechanisms of material removal using pulsed laser irradiation, depending on the pulse duration and other temporal parameters of the material. These temporal parameters are: τ_e – electron cooling time, τ_i – grating heating time and τ_L – laser pulse duration. The electron cooling time is much shorter than the grating heating time, which for most materials is of the order of picoseconds [32,33]. There are three different ablation mechanisms depending on the pulse duration:

a) nanosecond and longer: $\tau_e < \tau_i < \tau_L$

b) picosecond: $\tau_e < \tau_L < \tau_i$

c) femtosecond: $\tau_L < \tau_e < \tau_i$

For nanosecond and longer pulse durations the absorbed laser energy melts the material and raises the melt temperature to the boiling point. This time interval is sufficient to allow the heat to diffuse deeper into the material. As the material begins to evaporate, the resulting plasma and vapour pressure removes some of the molten material from the ablation cavity, but some remains due to surface tension. When the pulse is over, the heat is dissipated deep into the material and a stagnant melt layer is formed [33]. Nanosecond laser pulses induce a more diverse ablation mechanism because they exert a long-time thermal effect after excitation. Machining materials with nanosecond and longer pulses produces a variety of secondary ablation effects including: heat-affected zone (HAZ), hardened melt layer, surface damage due to the shock wave, and a large amount of surface debris deposited after ablation. The vapourised material also forms a plasma from the beginning to the end of the pulse. This results in plasma shielding, where the plasma absorbs some of the radiation and the material is exposed to a lower fluences [34].

For picosecond and femtosecond pulses, the two primary processes for removing material from regions exposed to ultrafast laser radiation are spallation and phase explosion. Compressive stresses are produced by the quick energy deposition that occurs during the brief laser pulse irradiation. In the stress-confinement regime, when the laser-heating duration is less than the mechanical relaxation time, these tensions are particularly significant. The irradiated sample's free surface may interact with the laser-induced compressive stress, producing a tensile wave strong enough to produce subsurface cavities. The development and connectivity of these subsurface cavities results in spallation, which causes the top layer to separate and be ejected from the target [35]. The other mechanism occurs with high-fluence laser pulses, where the material removal is dominated by phase explosion.

The exterior layers of a target are quickly heated when exposed to high-power ultrafast laser pulses. The regular boiling process caused by the

heterogeneous nucleation of vapor bubbles is negligible in such a rapid heating process. As a result, the melted surface area in the laser-irradiated region is heated past the liquid phase's thermodynamic stability limit. The heated melted components quickly break down into a mixture of liquid droplets and vapor [36]. A dramatic shift in the ablation plume's composition from big liquid droplets to mixed vapor-phase atoms and clusters/droplets of varying sizes marks the change from spallation to phase explosion [37].

1.3 Laser burst modes

When micromachining materials with ultrashort laser pulses, negative side effects that reduce the ablation efficiency and the quality of the machining process occur, such as plasma shielding of the laser beam by the ablation products, such as ablated material particles and plasma, as well as thermal phenomena at the surface of the material. To overcome these problems, burst modes are used [38].

Burst modes have several advantages. Because of the short time between burst pulses, any residual heat from the previous pulse is reused [28]. Therefore, when the pulse repetition rate is increased, the HAZ is reduced, because the heat is removed together with ablation products. Moreover, laser bursts provide faster processing due to burst energy division into pulse energies closer to optimal fluences, resulting in the exploitation of more average laser power [27]. This also helps preventing plasma shielding effects [38]. If pulse repetition rate was increased without changing the pulse energy, plasma shielding would increase as well, because the plume of plasma and ablated material cloud absorbs, reflects and scatters laser irradiation [39].

However, for the MHz burst regimes, there were some drawbacks as well. While using the MHz burst mode for laser ablation it has been shown, that ablation efficiency drops almost in half when two pulses are used in the MHz burst. This happens due to the fact that the ablated material forms an ablated material cloud that does not have enough time to dissipate. It was simulated that particles can move as fast as 2 km/s [37] when ablated from the target‘s material, but the time interval after the first pulse was 15.5 ns, which corresponds to only 31 µm [25]. This leads to shielding of the second pulse [40]. On the other hand, the overall ablation efficiency increases by up to 20% when there are three pulses in the MHz burst because the ablated material cloud is heated and some of it is forced to redeposit to the target reducing the shielding effect and increasing the samples temperature [41].

For the GHz burst modes, the literature is divided whether or not there are benefits for laser ablation. An ablation cooling effect was proposed where

laser pulses ablate the target material before the residual heat deposited by previous pulses diffuses away from the processing region. Using the GHz burst mode this effect allows lower fluences to be used for laser ablation, and the ablation rate is increased almost by an order of magnitude. In order for the ablation cooling effect to be significant, the time between pulses has to be reduced to a point where the workpiece does not have time to cool significantly [38]. On the other hand it was shown that the ablation removal rate is decreased by up to 90% for metals including coper, brass and steel [26,42], which contradicts the previous research article.

1.4 Colour theory

Colours are integral in human perception, significantly affecting mood, decision-making, and interpretation. From nature to various man-made designs, colours help people to notice and differentiate objects and affect their emotions or even moods. Currently, colours server multiple purposes in such fields as safety, communication, aesthetics, culture, marketing and even health, where they impose particular reactions or associations. Different colour models are used and are highly helpful as they offer a methodical means of accurately and consistently representing colours on different platforms. One of the most popular colour models is RGB (Red, Green, Blue), which creates a large range of colours by adding the three main colours at different intensities. In the RGB model, every colour is commonly represented by a set of three values, each of which has a value between 0 and 255. For instance, white, which is the combination of all three primary colours at maximum intensity, is (255, 255, 255), whereas pure red is (255, 0, 0). This model is crucial in most day-to-day devices. sRGB (standard Red Green Blue) is a standardized colour space within the RGB model, created to ensure consistent colour representation across different devices. The model provides a baseline for colour accuracy, so when an image is viewed on different screens, the colours appear the same or very similar. Nevertheless, there are also other colour models that are quite useful and popular. The HSL colour model, meaning hue, saturation and lightness, is another way of representing colours, but it focuses more on human perception of colour. Unlike RGB, which deals with intensity of light, HSL organizes colours differently. First one being the hue, which is the type of colour, represented as an angle on a colour wheel, like red, blue, or green. Second one being the saturation, which is the intensity or vividness of the colour. Lastly, lightness which is the brightness or darkness of the colour. Hue is measured in degrees, where red is 0º (or 360º), green is 120º and blue is 240º. Saturation is measured in

percentages, where 0% is grayscale and 100% is fully vivid and lastly lightness which is also measured in percentages, where 0% is black and 100% is white. HSL is particularly useful in design and art because it allows creators to adjust colours in a way that feels more intuitive and aligned with how people perceive colour.

1.5 Laser colouring on metals

Various industries have utilized different colouring methods including anodizing [43,44], electroplating [45–47], powder or physical vapor deposition coating [48,49], patination [50], as well as heat, chemical and electrochemical colouring [51–53]. All these methods have various benefits and drawbacks; however, laser colouring has unique and sought-after advantages that resulted in its rise in popularity. Laser colouring offers high precision, permanence, non-contact nature, versatility with materials, environmental friendliness, and suitability for automation and rapid production. A wide range of metals have been coloured using laser irradiation such as, stainless-steel [54–60], titanium [61–65], copper [66–68], aluminium [18,69] and others [70–73].

Laser colouring is used in the medical field to mark surgical instruments, equipment or implants with serial numbers, barcodes and logos, for greater differentiation [74]. Because no coatings or chemicals are used, there is no added risk of harm to the patients. It is also used in the aerospace and automotive industries for marking various parts and components because of laser colourings higher permanence and precision which ensures traceability and compliance with stringent regulations. Moreover, laser colouring can be used as an anti-counterfeiting measure by incorporating hidden or embedded colour-changing elements into documents, banknotes [75] and in the jewellery and branding industries to colour different decorative designs, detailed patterns or logos [65,73].

1.5.1 Laser colouring due surface oxidation

Laser oxidation of metals is a rapid gaseous corrosion process occurring at high temperatures. The process of laser oxidation and the growth of the oxide layer can be divided into several steps. The first one being, heating of the metal surface using laser radiation. When the metal is exposed to laser irradiation in air or in an oxygen environment, the energy of the irradiation is transferred to electrons which are excited from a lower to a higher energy state. The excited electrons quickly return to the ground energy state by transferring energy to

the lattice, which causes an increase in the temperature of the sample in the affected area. After the high temperature causes a reaction between the oxygen in the air and the metal. The oxidation process starts with the physical adsorption of oxygen on the metal surface. This is followed by the dissociation of the oxygen-oxygen bonds and the formation of ionic bonds between oxygen free electrons and metal ions, which leads to the oxide germ forming on the surface of the sample. The oxide germ expands laterally to form a continuous thin film of a metal oxide at the site of the laser exposure. The diffusion of cations and anions at the metal-oxide interface results in perpendicular oxide growth [76]. Theoretically, the course and outcome of laser induced oxidation reactions can be predicted from thermodynamic data and kinetic coefficients. However, in reality, the laser heating process involves a number of complex factors which make the oxidation a non-isothermal process. The process is non-linear and takes place under non-equilibrium conditions. With short pulse duration laser pulses, the temperature change can be faster than chemical reactions. The reaction rate is high due to the local high temperatures. Therefore, the laser induced oxidation process is complex and the variation of oxidation rate with time are different from the isothermal processes. Thus, providing a universal physical/chemical mechanism is a very difficult task [77].

The colour changes due to oxidation of the metal when it is irradiated by the laser beam is two-fold. First of all, the colour can arise due to the thin film effect (Fig. 1). Thin film effect is seen when interference happens between reflected light from the oxide layer and the light reflected from the metal surface itself.

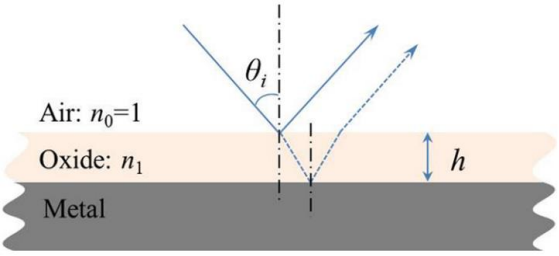

Fig. 1 Schematic diagram of the interference effect of the thin oxide film. n_0 – air refraction index, n_1 – oxide refraction index, h – oxide layer thickness, θ_i – light incidence angle. Reprinted with permission from ref. [11], © 2019 AIP Publishing.

If the optical path difference δ is equal to a certain wavelength λ or its product with an integer mλ, the specific colour will be seen as shown in Eq. (7).

$$\delta = \frac{2h}{\sqrt{n_1^2 - sin^2\theta_i}}, \quad (7)$$

The second mechanism is the colours of the oxides themselves. For example, analysis of the composition of laser-induced titanium oxide has shown that there is a correlation between the final surface colour and the laser-induced oxide films. The gold colour is the same as that of TiO, the violet colour is the same as that of Ti_2O_3, all of which is confirmed by X-ray diffraction (XRD) analysis. The white colour can be attributed to TiO_2 additives [63,78]. Lu et al. investigated the mechanism of laser colouration in stainless steels by quantitative analysis. The laser coloured surfaces were due to coloured oxides and spinel compounds, which acted as natural pigments with different colour characteristics [13].

These two mechanisms are supported and validated by experimental and theoretical studies. Studies on titanium and stainless steel show that both interference and the colour of the oxide films themselves determined the final surface colour. Which of these mechanisms dominates depends on the specific colour and the properties of a specific sample [11].

1.5.2 Important parameters for oxide formation

For practical use of laser colouring, the key is to precisely control the formation of oxide films to obtain the desired colours. Regardless of which mechanism dominates, the thickness and composition of the oxide film are the most important factors in determining the final surface colours. The thickness and composition are determined by a number of factors: the laser processing parameters, the state of the environment and the properties of the sample itself. Many studies have been carried out on how each of these factors affects oxide films and the resulting colours.

Li et al. have obtained results using a UV laser which show that oxide formation is influenced by laser power, beam defocus, beam scanning direction and speed, and number of scans [57]. Lavisse et al. demonstrated that fluence is also an important parameter [79]. When the fluence was varied from 4 to 60 J/cm^2, the colour of the surface changed from colourless and yellow at low fluences (<25 J/cm^2) to violet and blue at higher fluences.

Since the colours produced by the laser irradiation are due to the oxide film formed by the reaction between the sample and the oxygen around it, the influence of the environment on the resulting colours is very important. Zheng et al. performed laser colouring in different gases: O_2, N_2, Ar and He [80]. The

results showed that a high concentration of O_2 can help to accelerate the oxidation and reduce the number of laser pulses required. On the other hand, low O_2 concentration slows down the oxidation process, but allows a more precise control of the oxide layer growth and surface colours. Luo et al. found that the O_2 concentration has a significant influence on the surface morphology and chemical composition of the resulting oxide films and hence on the surface colours [80]. Laser micromachining was carried out in four different gases: air, oxygen (O_2), nitrogen (N_2) and argon (Ar) (Fig. 2). It can be seen that the coloured surfaces were obtained in air (Fig. 2a) and oxygen (Fig. 2b) environments. The colours obtained in the oxygen environment are richer than those obtained in air. Meanwhile, in the oxygen-free environments of nitrogen (Fig. 2c) and argon (Fig. 2d) only black and grey surfaces are obtained. The main reason for these results is that oxygen is needed for oxide layers to form and they do form only in air and O_2 environment, where oxygen is present [81].

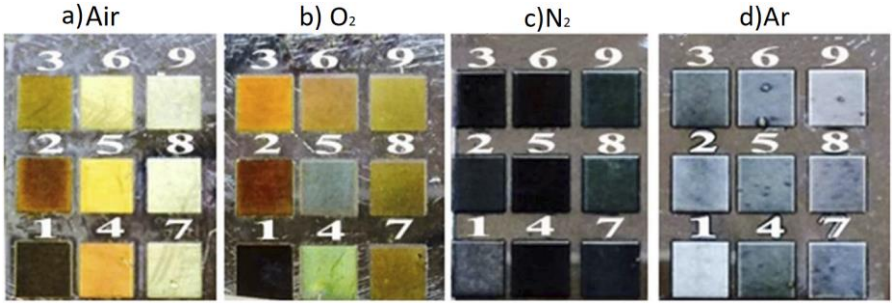

Fig. 2. Various colours achieved on stainless steel with a nanosecond laser in different environments: a) air; b) oxygen; c) nitrogen; d) argon. Numbers 1 – 9 correspond to 10 – 90 mm/s laser scanning speeds accordingly. Reprinted with permission from ref. [81], © 2015 Elsevier B.V

Colours of the laser-treated surfaces are also highly dependent on the composition and thickness of the sample. Different colours can be obtained on different types of stainless steel using the same laser processing parameters [76]. Since the laser colouring process is carried out by heating the sample with a laser, the thickness of the sample can have a significant influence on the resulting colours. A thick sample can provide higher thermal conductivity. Conversely, a thin sample can suffer significant thermal affects [82].

With a precise choice of laser parameters, it is possible to obtain a variety of individual colours or even a full colour palette [83]. (Fig. 3) shows the colour palette obtained on a 304-grade stainless steel surface using a nanosecond pulse duration fibre laser combined with raster scanning. Vivid colours were obtained with different scanning speeds and different distance

between scanned lines (hatch). Both the laser scanning speed and hatch increase the area scanning rate, which is important not only for personal but industrial use as well.

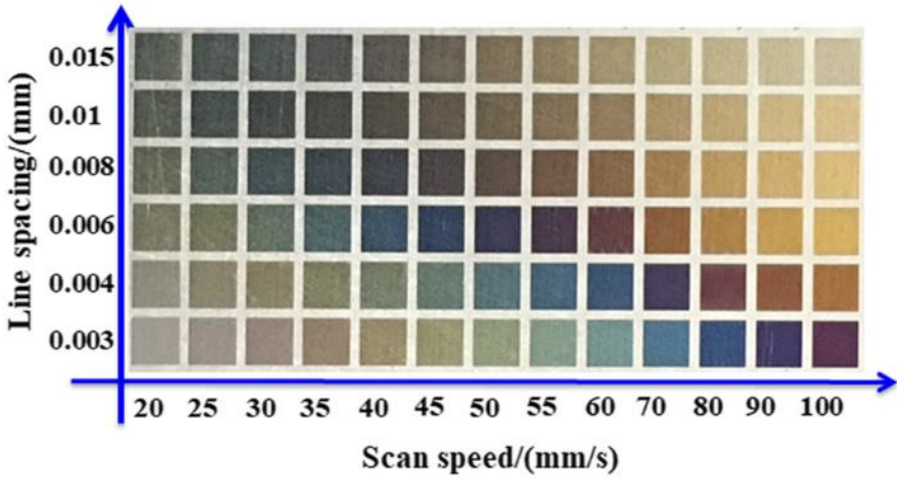

Fig. 3. Colour pallet on 304 stainless steel using different laser scanning speed and line spacing (hatch). Pulse repetition rate was 300 kHz, laser power was 4.5 W and pulse duration was 10 ns. Reprinted with permission from ref. [11], © 2019 AIP Publishing.

A CIE 1931 chromaticity diagram can be seen in (Fig. 4). It shows the colours that were obtain by D.P. Adams et al. with laser colouring on titanium. It can be seen that the resulting colours cover a wide range of *x* and *y* values and are bright but not saturated. It should also be noted that the colours obtained do not cover the entire field. The authors struggled to obtain red and green colours on the titanium surface by laser oxidation [61]. This could be explained by the thickness of the oxide film, which becomes too large for interference effect to occur inside the film [14].

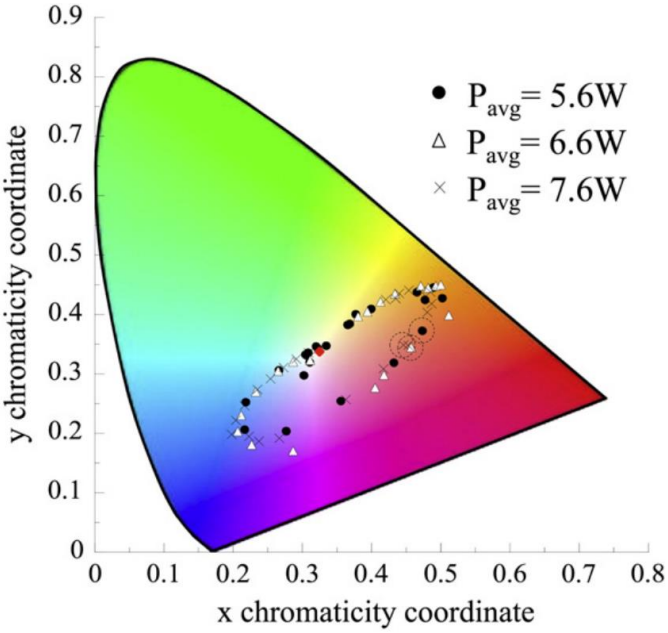

Fig. 4. CIE 1931 chromaticity diagram that shows different colours achieved with laser colouring using different average laser powers. Red diamond shows the unaffected titanium colour. Reprinted with permission from ref. [61], © Elsevier B.V.

1.5.3 Laser colouring due to surface oxidation applications

Laser colouring can be widely used in various industries to create colourful labels, logos and decorative artwork. (Fig. 5) shows specific examples of these applications. Laser colouring on stainless steel has been used to produce a bar code and different artworks [11].

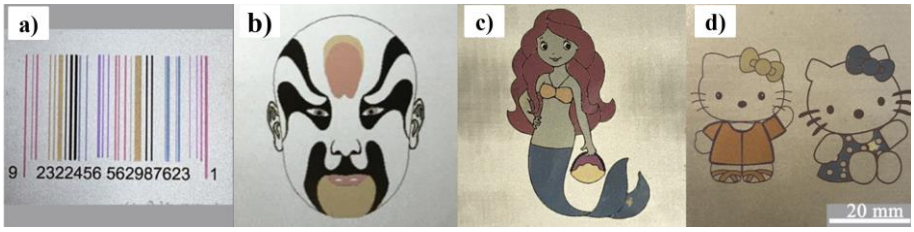

Fig. 5. Laser colouring examples on stainless steel: (a) Colour bar code (b) painted face; (c) mermaid; (d) cartoon characters. Reprinted with permission from ref. [11], © 2019 AIP Publishing.

Many laser colouring studies have been carried out on titanium and its alloys due to the extremely wide range of applications of this metal. Carey et

al. and O'Hana et al. both demonstrated that it is possible to change the colour of titanium jewellery and to add various ornaments and decorations on it as well [84,85].

1.5.4 Laser colouring due to LIPSS

Another way of obtaining colours on metals using laser colouring is structural colours [86], which are not due to oxidation, but due to diffraction, interference or scattering from micro/nanostructures. A surface micromachined by laser irradiation can produce LIPSS. Laser-induced periodic surface structures (LIPSS) are nano/microscale patterns that form on material surfaces when irradiated with ultrafast laser pulses. These periodic ripples result from the interaction between the laser and the material. Two main types of the LIPSS have been identified, low spatial frequency LIPSS (LSFL) and high spatial frequency LIPSS (HSFL) [87]. Both of these types can be formed either parallel or perpendicular to laser beam polarization [87] and can be conventionally divided to subfamilies depending on periodicity and depth-to-period aspect ratio [88]. These surface structures, which typically have a spacing in the order of the laser wavelength, are useful in tailoring surface properties like wettability, adhesion, optical reflectivity, and antimicrobial functions. Like a one-dimensional grating, LIPSS can produce structural colours due to the diffraction effect [11].

1.5.5 Achieving LIPPS for laser colouring

LIPSS can be compared to diffraction gratings. A diffraction grating has a periodic structure which, due to diffraction, splits the incident light into several wavelengths that are reflected off the grating at different angles (Fig. 6).

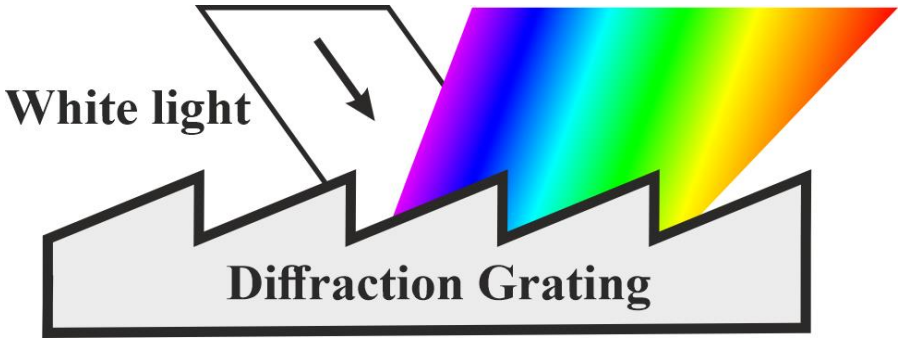

Fig. 6. White light splitting into different colours due to diffraction.

LIPSS structures provide a simple way to control the optical properties of metal surfaces and their colours. Colours have been obtained with LIPSS on various metals including titanium [89], aluminium [18], silver [71], stainless steel [75,90] and copper [66]. The fundamental difference from the colours obtained from laser colouring due to oxide films is that the colours generated by LIPSS strongly depend on the viewing angle. In (Fig. 7a) Zhong et al. [66] showed that using a 1064 nm picosecond laser, a copper sample can be micromachined to achieve LIPSS on the surface. The spatial periodicity of the LIPSS was 750 ± 31 nm, which is slightly lower than the used wavelength. The copper sample changes colour when the viewing angle is changed (Fig. 7b-c).

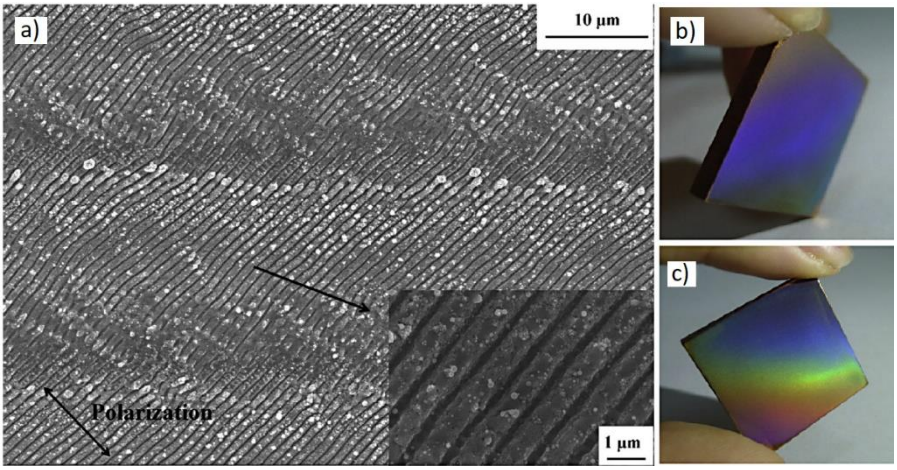

Fig. 7. a) SEM photograph of the copper surface when the average laser fluence was 0.43 J/cm^2 b-c) photographs of the 25 × 25 mm^2 copper sample at different viewing angles to achieve different colours. Reprinted with permission from ref. [66], © Elsevier B.V.

LIPSS are highly dependent on polarization. The periodic structures obtained on metals are perpendicular to the polarization of the laser beam. This correlation makes it easy to control the resulting surface colours by controlling the polarization of the laser beam [66,89]. LSFL are typically created by irradiating the material surface with nanosecond and picosecond lasers. When a surface has a random roughness, interference between the incident light and the surface scattered wave can occur which results in LSFL [91,92]. While using femtosecond lasers, the mechanism is a bit different. A surface plasmon polariton (SPP) is an electromagnetic excitation existing on the surface of a metal [93]. The interference between the incident light and the excited surface plasmon waves leads to a periodic spatial modulation of the surface energy distribution and results in the formation of periodic structures on the surface. The interference between the incident laser and the spatial harmonics of the excited SPPs results in a finer periodic modulation on the samples surface, leading to the formation of periodic nanostructures [11]. This is how HSFL are achieved, however, they require higher fluences and their period is of a fraction of the incident wavelength [94].

1.5.6 Applications of laser colouring due to LIPSS

Laser colouring due to LIPSS produces colours that are angle dependant. LIPSS direction can be control when controlling polarization. This allows for some interesting combinations as if LIPSS are micromachined

perpendicularly to one another, certain colours and figures will only be seen at a specific angle. This allows this laser colouring method to be used for decoration and anti-counterfeiting [75]. Lan et al. [75] have shown that angle dependant colours have a lot of advantages. (Fig. 8a) shows a laser micromachining scheme where a square area is scanned on the surface of a 301L stainless steel to produce LIPSS. The area of the micromachined square is divided into two parts, where the ripples are oriented perpendicular to one another. On the other hand (Fig. 8b) shows a slightly more complex micromachining scheme. The laser beam will micromachine an overlapping five and eight figures, but the laser beam scanning directions are perpendicular to one another. In both cases the micromachined LIPSS achieved on the samples' surface were perpendicular to the laser beam scanning direction. The machining parameters were: fluence 0.16 J/cm^2, beam scanning speed 4 mm/s, hatch 50 µm.

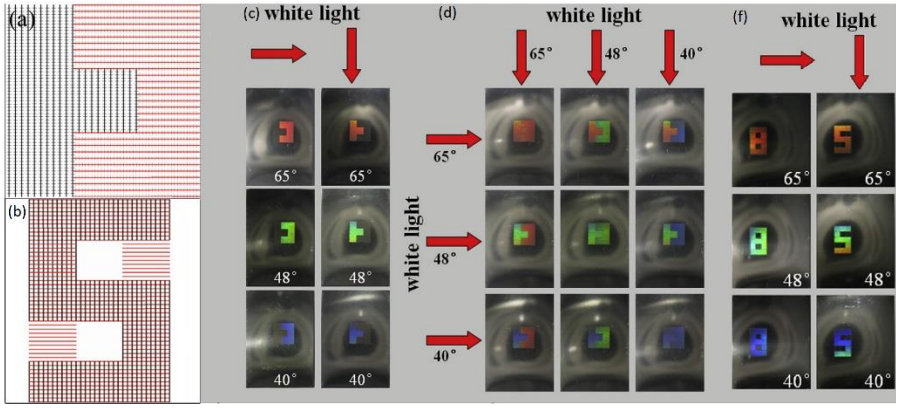

Fig. 8. (a) Principal laser micromachining scheme for machining a square by scanning the beam in two perpendicular directions. The polarisation is always parallel to the scanning direction; (b) Overlapping 5 and 8 symbols micromachined by scanning the beam in two perpendicular directions; (c) depending on the direction of illumination, either one or the other of the two parts of (a) is visible; (d) when illuminated from the two directions, the entire machined colour area is visible; (f) depending on the illumination direction, the different numbers, either 5 or 8 are visible. The red arrows indicate the direction of illumination. Reprinted with permission from ref. [75], © Elsevier B.V.

When the incident light coincides with the laser beam scanning direction or is perpendicular to the LIPSS on the target's surface, colours depending on the incident lights' angle are seen in the micromachined shape (Fig. 8c). Otherwise, no colours are seen, except for the stainless steel surface being

visibly micromachined by laser irradiation. By choosing to illuminate the sample with white light from two perpendicular directions at different angles of incidence, a combination of the desired patterns and colours can be seen (Fig. 8d). The same can be seen in (Fig. 8e) where the pattern for (Fig. 8b) was used. Depending on the direction and angle of the incident light we can see either a five or eight in different colours [75]. Angle-dependent colours can be applied to banknotes, passports, and ID cards to create highly secure and difficult-to-replicate holographic effects, similar to current holographic security features but with added customization and complexity.

1.5.7 Laser colouring due to nanoparticles/nanostructures

The structural colours due to surface ripples depend on the viewing angle. However, scanning of metal surfaces with picosecond and femtosecond lasers has shown that it is possible to change the colour of metals with the colour being independent of the viewing angle. This process is explained by a localised surface plasmon resonance effect due to metal nanostructures and nanoparticles on plasmonic metals such as gold, silver [73], and copper [20]. The dielectric permittivity ε of metals depends on the wavelength of the incident light. When the dielectric permittivity of the metal nanoparticles is approximately double and of the opposite sign to that of the ambient dielectric permittivity, the electromagnetic field is amplified at that wavelength. This resonance of the surface plasmons leads to an enhancement of the absorption for the resonant wavelength [19,95]. When the wavelength of the amplified absorption is in the visible range of light, the reflection properties of the surface and the visible colours change. The maximum absorption location depends on the size of the nanoparticles, the metal itself and the dielectric permittivity of the environment. By controlling these parameters, it is possible to control the surface colours of metals. Laser-induced nanostructures are usually randomly distributed over the surface of the sample. Examples of nanostructures are nanocavities, nanospikes, and nanoparticles.

1.5.8 Applications of laser colouring due to nanoparticles/nanostructures

Laser colouring of plasmonic metals such as silver and gold offers vibrant and durable micromachining of the selected surface. In jewellery and fashion accessories, it enables intricate and colourful designs while ensuring long-lasting wear resistance. Watchmakers use it to enhance dials and bezels with

aesthetic details and precise markings, while jewellers use this process to create vibrant ornaments on various necklaces, bracelets and earrings [11].

It has been shown (Fig. 9) that using picosecond laser irradiation in the non-burst and burst modes, it is possible to colour different metals including silver, gold, copper and aluminium. Vibrant blue, purple and yellow colours were achieved as well as intricate drawings were also shown [73].

Fig. 9. Laser colouring of independent of the viewing angle colours: (a) image of an eagle on a silver coin; (b) and (d) image of a butterfly on a silver coin before and after laser colouring, respectively; (c) microscope image showing the size of the protrusions to be up to 2 mm and the roughness of the surface to be between 1 and 2 µm; (e) a 5 kg silver coin with a diameter of 21 cm and a thickness of 2.5 cm with a coloured tiger and the Canadian inscription (coin (d) is shown next to the coin for comparison); (f) a zoomed-in photograph of the tiger to better show the contrast between black and white; (g) the colouring of an identical silver coin in other colours; (h) a zoomed-in photograph of the eyebrows and the nose; (i) the colouring of a gold coin in various colours. Reprinted with permission from ref. [73], © Springer Nature Limited.

1.6 Laser polishing

Surface texture and quality have a big impact on items' functionality and quality in various industries. Numerous industrial applications make use of microstructured surfaces [96]. A thin layer of a metal is melted as part of the laser polishing procedure in laser micromachining yielding a surface devoid

of fractures and other flaws. The goal of this technique is to level out the peaks and valleys on metals to a range that is lower. Laser polishing is mainly done at three levels. The first method is big area ablation polishing, which involves polishing large surfaces. The second being localized ablation where by controlling power density only rough surfaces are melted to reach a surface level and lastly, polishing by remelting. Surface tension causes material to be moved from the peaks to the valleys, smoothing surface roughness in the molten state [97]. This is because laser polishing, in contrast to other polishing techniques, depends on material conservation. Conventional laser polishing can be further separated into laser macro-polishing and laser micro-polishing based on the initial surface roughness to be polished and the consequent melting depth [96].

Continuous wave laser radiation is the primary tool used for macro polishing. The polishing process enables the top surface layer of the sample to be continuously remelted throughout a range of 10 to 80 mm. The material and the initial surface roughness must be taken into consideration when selecting the re-melting depth. Fiber-coupled lasers typically have laser powers between 100 and 300 W. Depending on the kind of material, the desired roughness rate, and the initial surface roughness, the processing time ranges from 10 to 200 s/cm^2 [98]. Heat conductivity, surface tension, viscosity, melting and evaporating temperatures, the starting surface roughness of the material to be polished, and the substance's homogeneity are some of the thermophysical characteristics that affect roughness [97].

Laser micro-polishing uses pulsed laser light with a usual pulse duration in the range of ns to μs if the goal is to reduce micro roughness and increase gloss level [96]. Pulsed laser radiation is typically used for micro-polishing on a previously ground and machined surface. The duration and intensity of the pulses are the most crucial factors in micro polishing [97]. For micro laser polishing the beam is moved along the target’s surface to melt the peaks into the valleys and, as a result, gain a more even surface. The molten material is already re-solidified when the subsequent laser pulse hits the surface and creates a new molten pool [97]. Shallow surface melting is the primary cause of this phenomena. The shallow surface melting zone is created by capillary pressure and liquid curvature caused by the shallow melting of micro asperities, which finally fill the metal surface's valleys with molten metal [99]. The laser beam's intensity must be chosen based on the pulse duration and the type of material that will be polished. As a result, one of the most important parameters for effective laser polishing is laser fluence, which is easily controllable using laser bursts. Even little changes in fluence can result in a wide range of surface quality finishes. Another major factor is the temperature

of the sample's surface. In the case of stainless-steel, studies have revealed that a surface temperature reaching 600 ºC before the next pulse has a detrimental influence on surface roughness [100]. However, the accumulated heat can be also used as an advantage when using various burst modes. Using burst modes with fluences lower than the ablation threshold fluence results in a thin melt layer that enhances surface quality, according to several studies [101–103].

1.6.1 Surface roughness parameters and measurement

There are quite a few parameters that are numerical values which express the unevenness of a surface. However, each parameter is slightly different and is used for different purposes. R_a is arithmetic average roughness, which is the average of how far each point on the surface deviates in height from the mean height. It's the most widely used parameter because it provides a simple overall roughness value and the average roughness is a good first-pass indicator of the overall height of the surface texture. It has proven useful for tracking manufacturing processes in industries from automotive to medical devices. R_a measures absolute deviations from the mean height, treating peaks and valleys equivalently. However, many very different surfaces: some uniform roughness, some with deep valleys or sharp peaks, may all have the exact same R_a value, which means R_a cannot distinguish the location of surface features across a profile. A surface with randomly scattered peaks will have the same R_a as a surface with those same peaks clustered at one end of the polished part [104]. Another parameter R_z is mean peak to valley height which is often defined as the average of the sum of the heights of the highest peak and the deepest valley across several sampling lengths. The average is usually done from 5 highest peaks and 5 deepest valleys. R_z is best for evaluating surfaces where the extreme values (peaks and valleys) are critical, such as in sealing surfaces or where contact stress concentrations might occur. It can be overly influenced by a single abnormal spike or valley, and if the surface is noisy, R_z may not represent the overall texture effectively [105]. Third parameter is R_q which is the root mean square roughness which is the square root of the mean of the squares of the profile deviations. Because of the squared values, R_q is more sensitive to peaks and valleys compared to R_a. This parameter is used in optical surfaces and precision bearings where small variations are important. Nevertheless, similarly to R_z is highly sensitive to outliers. In cases where isolated spikes or defects exist, it may overemphasize their effect, potentially misrepresenting the typical surface condition [104]. Fourth parameter is R_t, which is the total roughness height, which means the

vertical distance between the highest peak and the lowest valley within the evaluation length. This parameter is used for assessing the full range of surface irregularities when even one outlier would be important and it is less representative of the general surface roughness. There is also R_p and R_v parameters that correspond to maximum profile peak height and maximum profile valley depth, respectively. R_p is the height of the highest peak above the mean line, where R_v is the depth of the deepest valley below the mean line. They are best used for identifying isolated high peaks or deep valleys that might cause interference or initiate wear, critical in assessing potential surface damage, but offer no information on the distribution of the rest of the surface texture. Lastly, R_{sk} is skewness, which is a statistical measure that describes the asymmetry of the surface profile's height distribution. Where a positive R_{sk} indicates that there are more peaks than valleys and a negative R_{sk} indicates that there are more valleys than peaks. This parameter is used for predicting lubrication behaviour and wear characteristics, as the asymmetry can influence how surfaces interact under load, but does not provide direct information about the amplitude of the roughness [106].

Surface roughness refers to the fine, closely spaced irregularities on a surface, often resulting from the inherent characteristics of the material or the machining process used. However, there is another parameter called surface waviness that encompasses more widely spaced, macroscopic deviations on the surface that are more regular. It arises from systematic process-induced patterns, such as overlapping laser beam scanned lines or thermal gradients during laser polishing. Unlike surface roughness, waviness reflects larger, more regular deviations that can affect functional properties like friction and optical scatter [107].

Surface roughness measurements can be divided into two primary methods: contact and non-contact. The most common contact method is stylus profilometry which is broadly used in the industrial sector for measuring surface roughness. Contact type stylus profilometers are widely used in industrial fields, research, and development. The main reasons for the dominance of the roughness tester with a stylus are the accumulated measurement and analysis technique to date, self-reliance by measuring direct contact with the actual measurement surface, and compatibility with past accumulated measurement data [108]. Stylus profilometers, which utilize diamond-tipped styluses with typical tip radii of 2–5 μm, offer high vertical resolution that is sub nanometer and are widely used for 2D profile measurements. However, they risk damaging delicate surfaces and are limited by contact-induced wear and a relatively small measurement area. Moreover, atomic force microscopes that are used in contact mode provide atomic-scale

resolution over very small areas but are slow and less practical for larger samples [108].

Non-contact methods, such as optical interferometers and confocal microscopes, enable fast, damage-free, three-dimensional surface characterization with lateral resolutions down to approximately 0.1 µm and sub-nanometer vertical resolution, but these techniques can be sensitive to variations in surface reflectivity, require stringent environmental control, and often involve higher costs and more complex calibration procedures. When optical measurement instruments are used, unwanted distorted shape components are included in the resulting profile according to the beam shape, measurement principle, shape of the measured surface, and characteristics of light reflection and transmission. However, when contact type instruments are used, systematic error occurs between the real contact point and the point measured by the stylus tip radius [109]. Similarly, the profile distortion phenomenon that occurs with the stylus profilometer also depends on the shape and size of the stylus tip [108].

1.6.2 Laser polishing applications

Laser polishing is a versatile technique employed across various industries to enhance surface quality and performance of components. In the tool and automotive industries, laser polishing is applied to moulds to achieve superior surface finishes, resulting in higher-quality end products. Furthermore, laser polishing is used to improve the aesthetics and durability of various free form components, increasing overall wanted characteristics. Kumstel et al. showed that moulds and free form parts for automotive industries could be laser polished to achieve a wanted surface. The mould for glass forming was polished with continuous laser radiation. The mould insert out of grey cast iron (EN-GJS-400-15) was ballend-milled to a roughness of R_a 0.8 – 1.1 µm. Laser polishing reduced the roughness to R_a 0.3 – 0.4 µm (Fig. 10a). Several laser-polished glass forming moulds were tested in the glass forming production and the tests revealed an increased wear resistance in comparison to manually polished parts. The group also reported an increased in the parts hardness due to the remelting process principle during laser polishing [110]. The subsequent heating and cooling result in a heat treatment of the surface layer. The group also performed laser polishing on an implantable ventricular assist device (VAD) made of the titanium alloy Ti6Al4V, showing the applicability in medical field as well, because the surface roughness of the blood transporting component is crucial for the bio- and hemocompatibility of the whole implant (Fig. 10b).

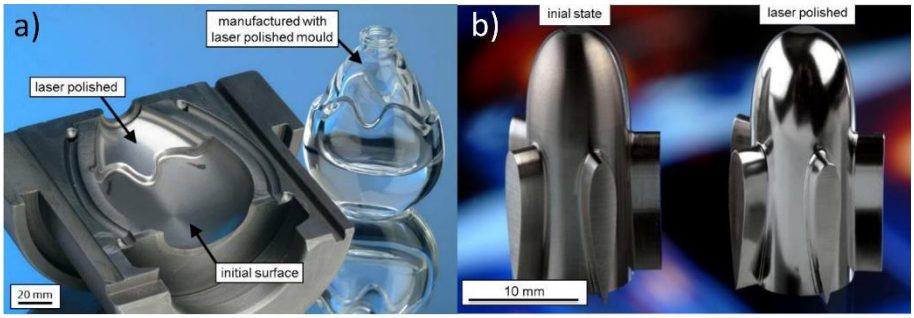

Fig. 10. Laser polishing applications. a) Partially laser-polished mould for glass forming; b) Ventricular assist device (VAD), left: initial, fine milled state, right: laser polished [110].

Manual polishing usually leaves grooves and scratches on the surface, which can be smeared up during subsequent polishing steps as well as some hidden surface defects could be induced. These defects reduce the biocompatibility of implants significantly. Manual polishing of the VADs takes about 3.5 hours and with laser polishing the time is reduced to 2 minutes. The surface roughness using pulsed laser irradiaton with pulse duration of 150 ns, the roughness of the VAD component, measured by tactile stylus, can be reduced from R_a – 0.3 μm to R_a – 0.08 μm [110]. On the same alloy continuous wave fibre laser was used to reduce surface roughness from 10.2 μm to 2.4 μm by another scientific group [111].

These applications show the adaptability of laser polishing in meeting the stringent surface quality requirements across diverse industrial needs.

EXPERIMENTAL SETUPS AND CHARACTERISATIONS

To perform the experiments, multiple different laser sources utilizing different pulse lengths and burst modes were used. A table of the different lasers and their parameters is listed (Table 1). A typical optical scheme consisted of a laser source, mirrors for beam guiding, a beam expander, galvanometric scanner, F-theta lens that can be controlled on a *Z* stage and *XY* stages that control the samples' position.

Table 1. Laser parameters used in experiments.

Laser source	Baltic, Ekspla	Atlantic, Ekspla	Pharos, Light Conversion	Carbide, Light Conversion
Wavelength	1064 nm	1064 nm	1030 nm	1030 nm
Pulse duration	10 ns	10 ps	210 fs	210 fs
Pulse rep. rate	100 kHz	100 kHz	100 kHz	100 kHz
F-theta lens	80 mm	80 mm	100 mm	100 mm
Beam positioning	Scangine 14, ScanLab	Scangine 14, ScanLab	Intelliscan 14, ScanLab	Intelliscan 14, ScanLab
Irradiation mode	Pulsed	Pulsed	MHz burst, GHz burst, Biburst	MHz burst, GHz burst, Biburst
Experiments	Wettability and colour change of copper	Laser colouring on copper, Influence of absorptions on lift-off threshold	Laser polishing, Bi-stability measurements	Laser colouring of stainless steel, Rapid laser colouring of stainless steel, Wettability
Publications	[PP2]	[P4, P7, PP2]	[P2, P3, P6]	[P1, PP1, P5]

The lasers were capable of different burst regimes: MHz, GHz and biburst. When the laser is working in the normal pulsed mode (Fig. 11a) at 100 kHz the time difference between pulses is equal to 10 µs. These pulses can be divided into smaller subpulses with either MHz or GHz intra-burst repetition rates and the MHz and GHz burst modes work quite similarly. In the MHz burst mode (Fig. 11b), the intra-burst repetition rate is equal to 64.68 MHz with a time difference between subpulses of 15.5 ns, while in the GHz burst mode (Fig. 11c), the intra-burst repetition rate is equal to 2.27 GHz with a time difference between subpulses of 440 ps. The number of pulses within the MHz and GHz bursts are notated by letters *N* and *P*, respectively. For the biburst

mode (Fig. 11d), when we divide the MHz burst pulses further into the GHz burst pulses, we get the aforementioned biburst mode. It is important to remember, that it does not matter into how many subpulses the pulse is divided into, the overall pulse energy stays the same.

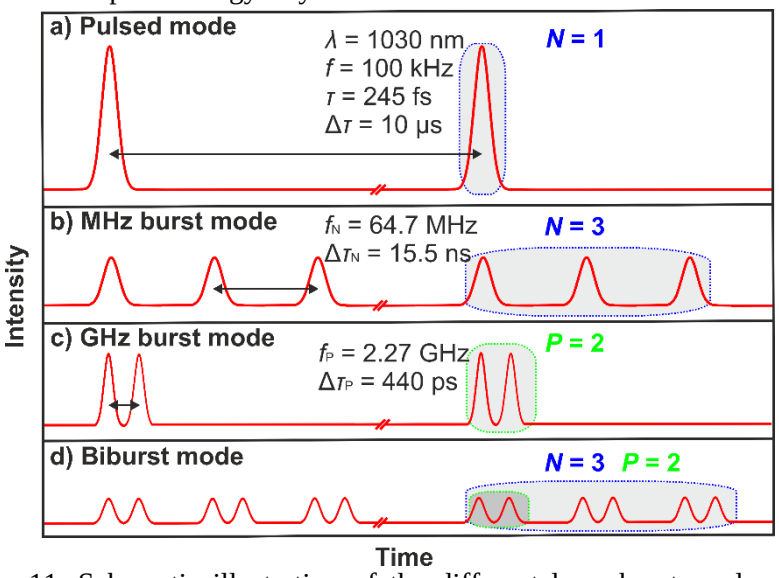

Fig. 11. Schematic illustration of the different laser burst modes. a) pulsed mode b) MHz burst mode; c) GHz burst mode; d) Biburst mode [PP1].

For the experiment two different kinds of stainless steel samples and one kind copper sample were used.

Stainless steel (304, Ekstremalė) plates with the size of 120 × 120 × 0.4 mm^3 were used for stainless steel colouring [P1, PP1, P5]. Stainless steel 304 has 18% chromium and 8% nickel and is the most commonly used grade of stainless steel with properties such as: excellent resistance to the corrosion and temperature, high tensile strength and durability, but is still easily formable. A scanning electron microscope (Helios NanoLab 650, FEI) was used to visualize the samples.

For the laser polishing, copper colouring, bi-stability measurements and influence of absorptions on lift-off threshold [P2, P3, P4, P6, P7, PP2] 5 mm × 50 mm × 50 mm copper (CW004A, Ekstremalė) samples were used with a surface roughness R_a of 0.1 µm. The copper purity was 99%. The ablated surface roughness R_a was measured using a stylus profiler (Dektak 150, Veeco). A scanning electron microscope (JSM-6490LV, JEOL) was used for the samples' visualization.

For laser polishing of stainless-steel [P2] (1.4301, Ekstremalė) 5 mm × 50 mm × 50 mm stainless-steel plates were used with a surface

roughness R_a of 0.5 µm. The ablated surface roughness R_a was measured using a stylus profiler (Dektak 150, Veeco). A scanning electron microscope (JSM-6490LV, JEOL) was used for the samples' visualization.

In order to change the laser fluence, the sample *z* position was changed. This is known as a *z*-scan experiment in scientific literature. The beam radius increased when the sample was moved in either the positive or negative *z*-direction. A well-known *D*-squared method was used to calculate the different beam radii values [112]. During this method, a sample is damaged using laser irradiation at different average laser powers, and the radius of the damage is measured using an optical microscope (BX51, Olympus). A graph of the squared radius of the irradiated damage dependence on fluence is drawn.

$$D^2 = 2w^2 \ln\left(\frac{F}{F_{\text{th}}}\right) \tag{8}$$

here D – diameter of the laser irradiation damage of the sample, w – beam radius at a given z position, F – fluence, F_{th} – ablation threshold.

Fitting Eq. (8) onto the graph allows us to find the ablation threshold as well as the beam radius at a given *z* position.

$$w(z) = w_0 \sqrt{\left(\frac{(z - z_0)\lambda M^2}{\pi w_0^2}\right)^2} \tag{9}$$

here w_0 – beam waist, z_0 – samples position at beams waist, z – samples current position, λ – laser wavelength, which was 1030 nm, M^2 – beam quality parameter.

Then when beam radius is calculated for all *z* positions using Eq. (9) we can get the beam waist value.

Surface wettability was also measured for [P1, P5, PP1, PP2] experiments. The static water contact angle (SWCA) was measured by depositing a 6 µL volume water drop on a specific laser coloured area using a micropipette (Transferpette, Brand GmbH). The sample was illuminated from one side by a high-parallelism diode backlight and an image of the drop was taken from the other side using a digital camera. The SWCA angle was deduced by using ImageJ software's [113] plugin LBADSA [114]. Each measurement was done 5 times and the standard deviation was calculated.

EXPERIMENTS

2 Laser colouring of metals

2.1 Laser colouring of stainless steel

While many metals and different colours have been achieved using laser colouring, the process has not yet been fully optimized. Copious amount of laser processing and material parameters have an effect on laser colouring, therefore increasing the time required to perfect the method. MHz, GHz and biburst burst modes were tested to achieve the highest number of colours and highest possible colouring rate. Laser processing parameters including hatch, repetition of scans and laser frequency were also tested to see whether they increase the colouring rate. Micromachined surface structure was analysed and the static water contact angles were measured to see if the surface became hydrophobic. [P1], [PP1], [PP2] and [P5] results will be presented here.

2.1.1 Experimental setup

The experiment was carried out using a solid-state laser (Carbide, Light Conversion) with listed laser parameters in (Table 1). The beam waist radius was 20.6 µm and the beam quality factor M^2 was 1.08. Two different laser colouring experiments were performed. First experiment was to find which burst mode and pulse number within the burst combination produced most colours. Results from the [P1] publication will be presented. The second experiment was performed to find the highest scanning speed and colouring rate possible to achieve colours. Results from [P5] and [PP1] publication will be presented. During the first experiment the galvanometric scanner horizontal lines were scanned by the laser beam on the stainless-steel plate with the controllable scanning speed of 100 mm/s and 333 mm/s. The distance between the lines or hatch h was constant and equal to 10 µm. The area of one scanned rectangle was equal to 6×6 mm^2 (Fig. 12). Horizontally in the x direction number of pulses in the MHz or GHz burst were changed from 2 to 9 with a step of 1. For the GHz burst mode 10, 15, 20 and 40 pulses within the burst were also tested. For the biburst mode, the GHz experiment was repeated while using different number of pulses within the MHz burst, changing from 2 to 8 with a step of 1. Vertically in the y direction laser output power was gradually decreased and equal to 5.6 W, 4.4 W, 3.5 W, 2.8 W, 2.5 W, 1.7 W, 1.4 W, 0.98 W, 0.73 W, and 0.26 W. This corresponded to pulse fluences of 7.6 J/cm^2, 6.0 J/cm^2, 4.8 J/cm^2, 3.8 J/cm^2, 3.4 J/cm^2, 2.3 J/cm^2, 1.9 J/cm^2,

1.3 J/cm^2, 1.0 J/cm^2 and 0.34 J/cm^2, respectively. Afterwards, the micromachined stainless-steel plate with different laser induced colours was put in a light box with all white walls (Lightroom, LR0001). Inside the box, the samples were illuminated by light-emitting diode (LED) lights, which were on the top part of the box and the samples themselves were photographed using a digital camera (Leopard Imaging, LI-IMX563-MIPI-AF) equipped with 7.05 mm lens and 12 MP CMOS image sensor (Sony, IMX563) that was on the roof of the white box to maintain constant conditions for the whole experiment.

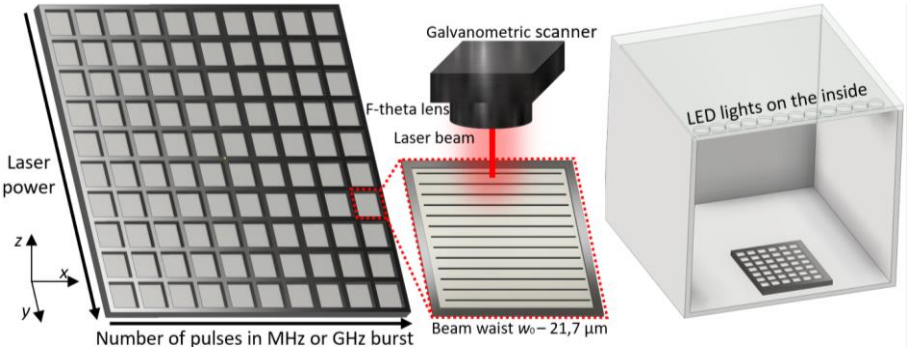

Fig. 12. Design of the laser colouring experiment. First using a galvanometric scanner coloured rectangle squares are micromachined using laser irradiation on the stainless-steel plates. Afterwards, the stainless-steel plates are photographed inside a white walled light box with LED lights [P1].

During the second experiment on the stainless-steel plates, using a galvanometric scanner 5 mm horizontal lines were scanned in a square shape with a 10 µm distance or hatch between the lines. The area of the square was set to 5 mm × 5 mm. An array of squares was achieved where laser scanning speed was increased vertically and average laser power was increased horizontally. The scanning speed was increased from 1000 mm/s to 4250 mm/s, while the average laser power was increased from 9.6 W to 40 W. The experiment was repeated at different burst modes with varying number of pulses within the burst. Other laser parameters were also tested. The same experiment was performed but instead of horizontally changing the laser power, other parameters, including hatch, pulse duration, laser frequency and repetition of scans were chosen.

2.1.2 Laser colouring using MHz, GHz and biburst modes

The CIE 1931 (Fig. 13) chromaticity diagram represents colour based on human visual perception and is used in many industries, such as printing, photography, television and also scientific literature [12,61,73,90,115–117]. The diagram represents all visible colours as seen by the human eye, mapped within a two-dimensional space defined by the x and y chromaticity coordinates. The horseshoe-shaped curve, known as the spectral locus, outlines the limits of human vision in the diagram. Every colour visible to the human eye falls within this curve, however not all colours can be replicated by technology. Therefore, various approximation models are used, and because no model can replicate all colours within the diagram, only the colours in the black triangle can be shown. The triangle is an overlay that shows the range of colours that can be produced by a specific set of three primary colours. In other words, the triangle's vertices mark the chromaticities of the red, green, and blue primaries, and every colour inside the triangle is one that can be achieved by additively mixing those primaries. Colours outside the triangle cannot be reproduced with the RGB system. The diagram includes a point representing white light, located at coordinates x – 0.333, y – 0.333. Colours closer to this point appear more desaturated, meaning they look closer to white or grey. As can be seen in the colour space in (Fig. 13) a wide range of colours was achieved in our experiment, from multiple shades of brown and yellow, to blue and green. Notably the hardest colour to achieve was red, with only purple colour being close to it.

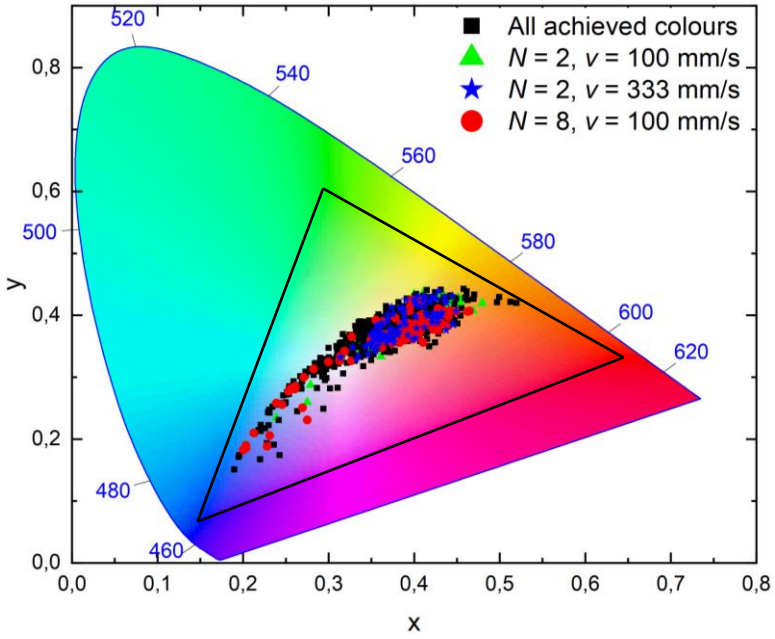

Fig. 13. CIE 1931 colour diagram containing all achieved colours. Black triangle shows all achievable colours due to the usage of XYZ colour model. Green squares – biburst mode with $N = 2$ pulses in the MHz burst and a scanning speed of 100 mm/s; blue stars – biburst mode with $N = 2$ pulses in the MHz burst and a scanning speed of 333 mm/s, red circles – biburst mode with $N = 8$ pulses in the MHz burst and a scanning speed of 100 mm/s [P1].

Three different burst regimes: MHz, GHz and biburst were used to achieve different colours on stainless steel.

MHz burst mode was not very effective in producing a broad spectrum of varied colours, as shown in (Fig. 14) Only different tones of brown were achieved. When using the GHz burst mode, the situation marginally improved and more colours, including many hues of green and one very dark purple, were produced. The bulk, however, continued to be brown, just like in the MHz burst mode.

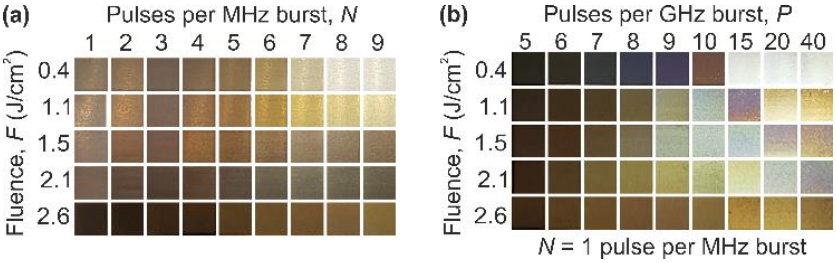

Fig. 14. Stainless steel colour achieved by laser colouring dependence on fluence *F* in the (a) MHz and (b) GHz burst modes [P1].

The majority of colours are achieved when using the biburst mode. In picture (Fig. 15a) we see the GHz mode with brown and green colours. However, starting with the biburst mode in (Fig. 15b) the first blue colour is visible. Increasing the number of pulses in the MHz burst yields greater number of shades of blue with (Fig. 15f-h) showing that half of the grid is either blue or purple. Achieving these colours is a difficult and time-consuming task because of the parameters involved. We can see that the optimal window for achieving colours is between 1.1 J/cm^2 and 2.1 J/cm^2 which is quite narrow. Furthermore, while the fluence for the entire burst ranges from 1.1 J/cm^2 to 2.1 J/cm^2, the intra-burst fluence for a single pulse is only about 0.01 J/cm^2 to 0.02 J/cm^2 for purple colours and 0.02 J/cm^2 to 0.04 J/cm^2 for blue colours, making the use of various burst modes a very practical and precise way to attain such low fluences.

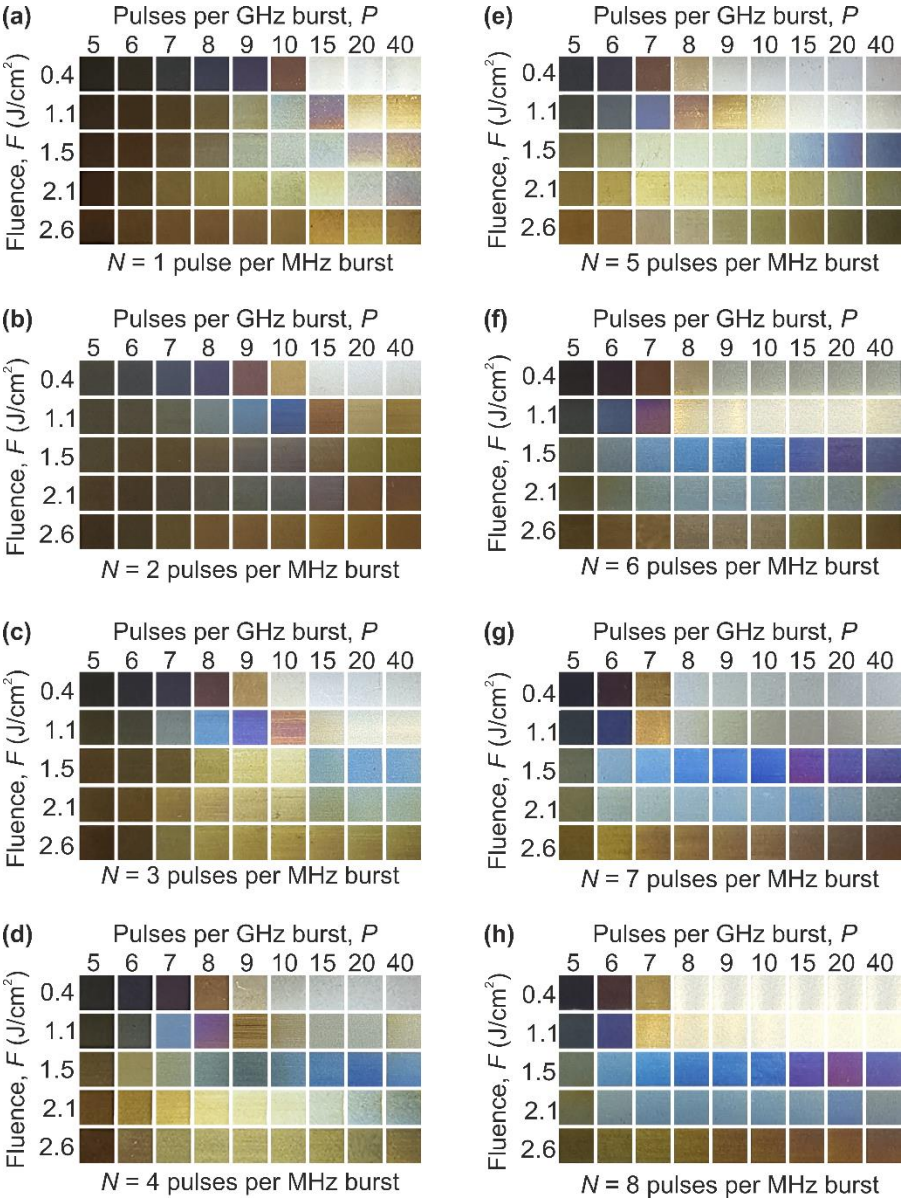

Fig. 15. Stainless steel colour achieved by laser colouring dependence on fluence F and number of pulses per GHz burst P, at different number of pulser per MHz burst N: (a) N = 1; (b) N = 2; (c) N = 3; (d) N = 4; (e) N = 5; (f) N = 6; (g) N = 7; (h) N = 8 [P1].

Scanning speed is also a very important processing parameter for laser colouring. Comparing two arrays in the biburst mode with 2 pulses in the MHz burst (Fig. 16) we can see that increasing the scanning speed threefold yielded only shades of brown. While using a scanning speed of 100 mm/s resulted in

a few blue and purple colours. Further optimising the set of parameters by increasing the number of pulses in the MHz burst to 8 yielded a high range of colours, with more than half of the array being blue or purple. We can see these results in (Fig. 13) as well, where the second set of parameters resulted in a small range of colours, while the third set spanned throughout the whole possible triangle.

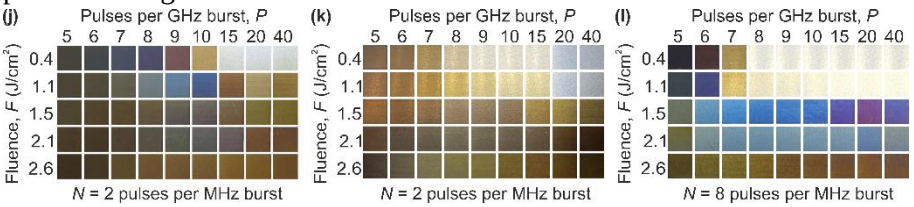

Fig. 16. Stainless steel colour achieved by laser colouring dependence on fluence F and number of pulses per GHz burst P, at different number of pulses in the MHz burst and scanning speed: (a) N = 2, v = 100 mm/s; (b) N = 2, v = 333 mm/s; (c) N = 8, v = 100 mm/s [P1].

Although we achieved numerous colours, the colouring rate with a scanning speed of 100 mm/s is low and is equal to only 1 mm^2/s, as it depends on the scanning speed and the distance between the scanned lines, so a second experiment was carried out to find the highest scanning speed to achieve the highest colouring rate.

2.1.3 Rapid laser colouring using GHz burst mode

It is important to not only achieve a wide range of colours, but to do it as rapidly as possible. To define the speed of colouring a certain area we use the colouring rate, denoted as dS/dt, which is defined as the total coloured area divided by the processing time. For a square area with side length l, the coloured area is equal to l^2. The processing time t can be calculated by considering the number of lines N needed to cover the whole area, each of length l, and the scanning speed v. The number of lines is determined by dividing the side length by the hatch h, so $N = l/h$. Therefore, the processing time becomes $t = Nl/v = l^2/vh$. Substituting this back into the colouring rate equation yields $dS/dt = l^2/t = vh$. This demonstrates that the colouring rate simplifies to the product of the scanning speed and the hatch distance. Thus, despite the complexity of various processing parameters, the colouring rate provides a straightforward metric for comparison by focusing on these two key variables. With a scanning speed of 100 mm/s and a hatch of 10 µm the colouring rate in the biburst mode was only 1 mm^2/s. Our second experiment

was conducted to achieve the highest possible colouring rate while also increasing the number of colours.

Different laser processing parameters result in different colours. Our experiment was carried out with P = 2, 4, 7, 10, 15 and 25 pulses within the GHz burst and beam scanning speeds from 1000 mm/s to 4250 mm/s. As can be seen from (Fig. 17) we get similar results with P = 2, 4, 7, 10 pulses within the GHz burst. Increasing the number of bursts further to P = 15 (Fig. 18) results in colours that are far less vibrant but still quite similar to the ones in (Fig. 17). However, increasing the number of pulses within the burst further to P = 25 drastically reduces the number of different colours achieved (Fig. 18) as only brown and dark green or dark purple colours can be seen.

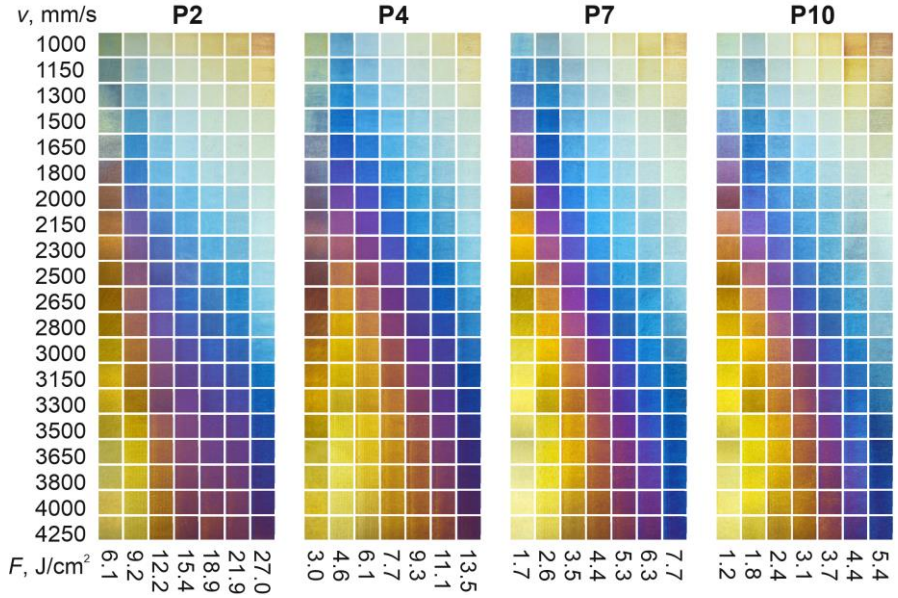

Fig. 17. Different colours achieved with laser colouring. The laser beam scanning speed was increased from 1000 mm/s to 4250 mm/s and average pulse fluence was increased from 12.1 J/cm^2 to 54.1 J/cm^2. The experiment was repeated at P2, P4, P7 and P10 pulses within the GHz burst with individual intra-burst pulse fluence listed [PP1].

When the accumulated pulse fluence is at F – 12.11 J/cm^2, for P – 2, 4, 7, 10, 15 pulses within the GHz burst a pattern of the colours going from light green, to blue, to purple, to orange and lastly yellow was seen when the laser beam scanning speed was increased from 1000 mm/s to 4250 mm/s. Increasing the accumulated pulse fluence resulted in the existing pattern being kept, however, the colour transitions were more gradient with more transitional colours appearing. When F – 24.31 J/cm^2 and higher accumulated

pulse fluences were achieved, the colour pattern changed slightly. The starting colours were light brown, going to light green and turning into light blue that changed to purple, orange and lastly yellow. This allowed to achieve certain colours at a much higher scanning speed. Increasing the laser beam scanning speed further than 4250 mm/s resulted in unstable and not uniform colours that were somewhere between yellow, purple, blue.

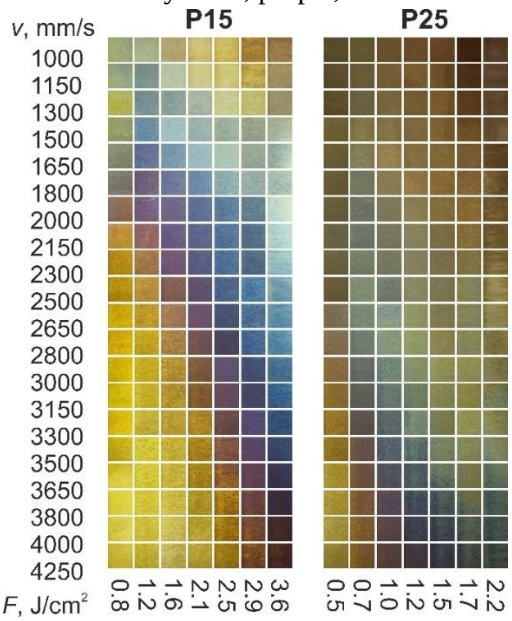

Fig. 18. Different colours achieved with laser colouring. The laser beam scanning speed was increased from 1000 mm/s to 4250 mm/s and average pulse fluence was increased from 12.1 J/cm^2 to 54.1 J/cm^2. The experiment was repeated at *P*15 and *P*25 pulses within the GHz burst with individual intra-burst pulse fluence listed [PP1].

As it can be seen in (Fig. 19) we have also increased the number of colours filling almost the entire triangle area. Many different blue, purple, orange and yellow colours have been achieved, as well as, a few green and red colours. The later are the fewest and most difficult to obtain in our experiments.

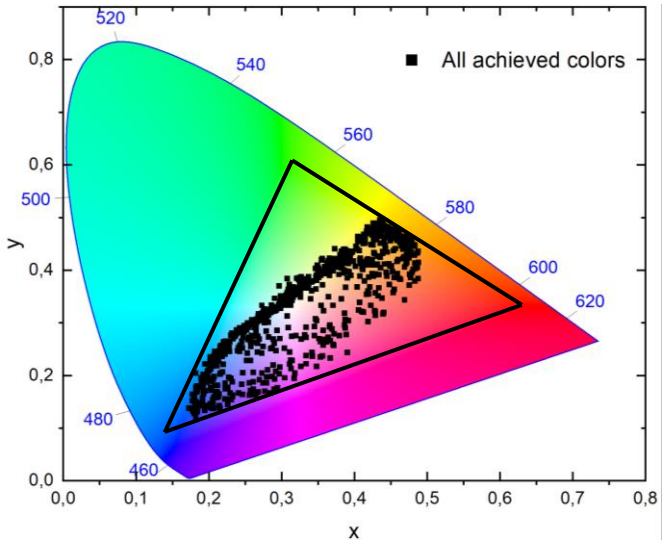

Fig. 19. 1931 chromaticity diagram. Black dots – achieved colours in the experiments. Black triangle – colours that are possible achieve in the model [PP1].

Besides the commonly used RBG colour model there are other popular models such as HSL (Hue, Saturation, Lightness). The CIE diagram (Fig. 19) reveals that only a limited number of vibrant green and red colours are achieved. Vibrant colours correspond to high saturation levels, typically values of 80 or greater. However, the observed saturation of some of our colours is quite low, ranging from 20 to 30, while the lightness is relatively high, between 60 and 85, at different fluences when using 7 or 10 pulses within the GHz burst (Fig. 20, a and b) for the green colours. Increasing the number of pulses within the GHz burst to 15 and 25 (Fig. 20, c and d) causes the green colour saturation to drop further into the 5 to 20 range, and the lightness decreases to between 40 and 70. Similar trends are observed for the red colours, with saturation and lightness values never exceeding 60.

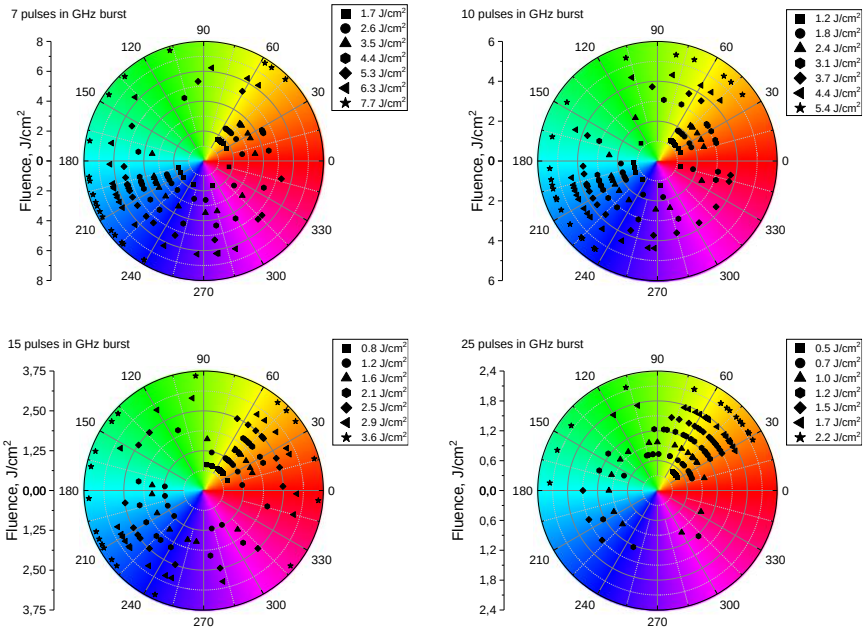

Fig. 20. Hue dependence on fluence polar diagrams with P = 7, 10, 15 and 25 pulses within the GHz burst [PP1].

Additional burst modes were tested to determine whether more colours and higher colouring rates could be achieved (Fig. 21a). In the MHz burst mode, regardless of the scanning speed, only brown colours were produced. Notably, similar brown hues could be obtained at scanning speeds exceeding 4250 mm/s. In contrast, in our previous work [56] we primarily achieved various colours using the biburst mode at a much lower scanning speed of 100 mm/s. By increasing the scanning speed to the 1000 – 4250 mm/s range and utilizing $N2P7$ and $N2P10$ biburst modes, it was possible to produce different colours, although these were less vibrant than those in the GHz burst modes. Moreover, increasing the number of pulses in the MHz burst mode to four or more still resulted only in brown colours. This shows, that the GHz burst mode is far superior in achieving vibrant colours and only when increasing the number of N by a minimal amount can any colours be visible at all in the biburst mode. Multiple scans were also tested (Fig. 21b), however no significant changes in colours can be seen. The small visible change can be explained by the fluence change due to the fact that some of the material is ablated with every scan. The last test was performed to see whether more colours or higher scanning rates could be achieved when different burst modes were used on top of one another (Fig. 21c). Since MHz burst yielded no colours at all, it was not tested. In (Fig. 21c) we can see that vibrant colours

can be achieved with *P*10 ten pulses in the GHz burst and if we use *N*5*P*10 biburst mode with 5 pulses in the MHz burst mode and 10 pulses in the GHz burst mode, we will achieve only brown colours. Mixing these two parameter sets yielded some interesting results. If the GHz burst mode is used first, with biburst mode going after, no new colours are seen. Contrary, if the biburst mode is used first with the GHz mode going afterwards, some colours are achieved. The new colours are not as vibrant as in the GHz burst mode but are more vibrant than the ones in the biburst mode even with optimal parameters. While it might be possible to achieve some new duller colours compared to the GHz burst mode, the scanning rate would be significantly lower using this method since multiple scans are needed and using speeds higher than 3000 mm/s yielded different shades of brown only. Therefore, due to these findings, mixing of the burst modes was not studied further.

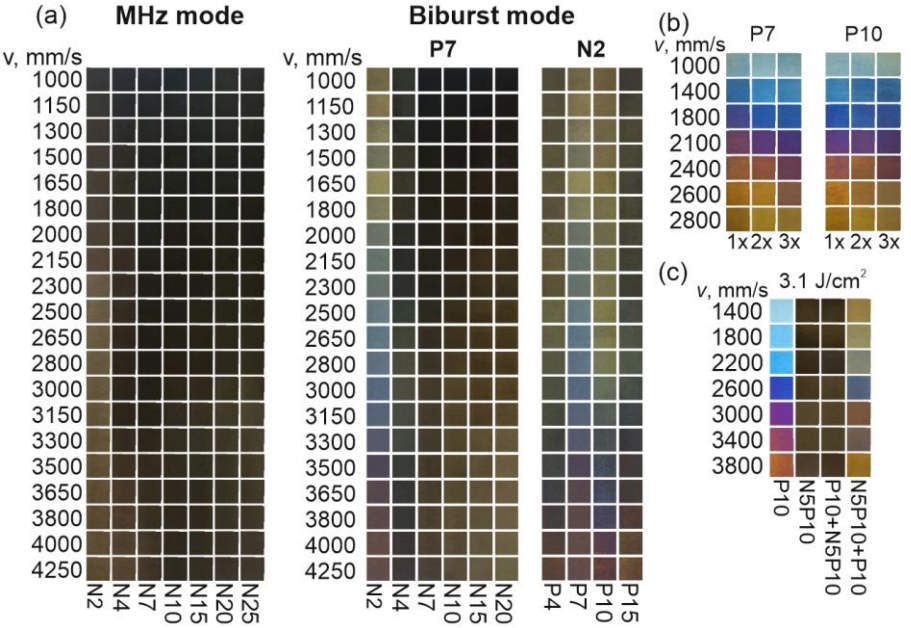

Fig. 21. MHz and Biburst mode colouring tests. The laser beam scanning speed was increased from 1000 mm/s to 4250 mm/s and average pulse fluence was constant at 30.8 J/cm^2. N = 2, 4, 7, 10, 15, 20 and 25 pulses within the MHz burst were tested for the MHz burst mode. For the biburst mode *N*2*P*7, *N*4*P*7, *N*7*P*7, *N*10*P*7, *N*15*P*7, *N*20*P*7, *N*2*P*4, *N*2*P*7, *N*2*P*10 and *N*2*P*15 sets were tested [PP1].

Based on the equation dS/dt = vh, there are two primary methods to improve the colouring rate: increasing the laser beam scanning speed or the distance between the lines. If identical colours can be achieved with a larger hatch spacing, fewer scanned lines are necessary to colour a given area,

potentially improving the colouring rate. As can be seen in (Fig. 22), multiple colours can still be produced even as the hatch spacing increases. However, the colouring rate does not necessarily improve because, to achieve the same colours with a doubled hatch spacing, the scanning speed must be reduced proportionally. Another possibility to increase the colouring rate could be increasing the laser's repetition rate. This could allow for higher scanning speeds to be used if pulse overlap is one of the critical parameters for laser colouring. Pulse overlap would remain the same if both the repetition rate and scanning speed would be increased proportionally. Nevertheless, the results shown in (Fig. 22) indicate that increasing the repetition rate produces the same colours at the same speed and those colours are significantly less stable as well. This could be explained by the intra-burst repetition rate having the most significant impact on heat accumulation on the target surface.

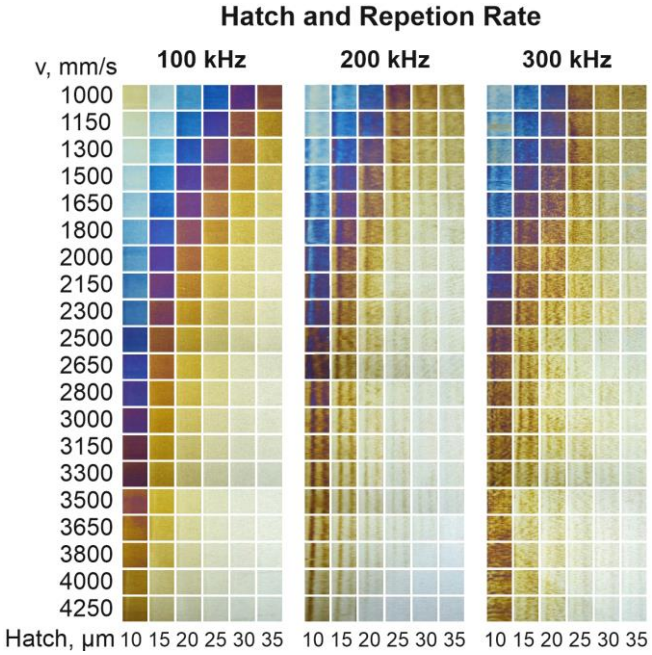

Fig. 22. Colour change from laser colouring when changing hatch, pulse repetition rate and beam scanning speed. P = 7 pulses within the GHz burst mode were used with a constant pulse fluence of 30.8 J/cm^2 [PP1].

Due to the fact that our laser colouring method utilizes hatching, it is possible to fill any custom form or figure with lines with a pre-set spacing. In (Fig. 23) we can see various shapes and colours that can be achieved using laser irradiation. Specifically, (Fig. 23a) displays two half circles with two wavy lines in the middle, all in different colours such as blue, light blue,

purple, and orange. In contrast, (Fig. 23 b, c, d) present the same floral circle pattern with a circle in the middle but in different colour schemes: (Fig. 23 b) is entirely blue, while in (Fig. 23 c and d) each leaf and the central circle have different colours ranging from shades of blue to purple and orange. Lastly, (Fig. 23e) shows the logo of the Center for Physical Sciences and Technology (FTMC). These examples demonstrate that even complex shapes are not problematic for this method. However, a significant drawback is the process's extreme sensitivity to minor changes in fluence. Although the laser's irradiation is highly stable, particularly because we can use high powers and divide those pulses into ones with lower individual fluence, we still face challenges in maintaining the sample precisely at the focal position. The primary issue arises from heat accumulation, which increases the sample's temperature and causes slight deformations of the sample surface, thereby altering the focal point. Even though, the deformations can be very small and hard to see with the naked eye, the colour difference is easily noticeable.

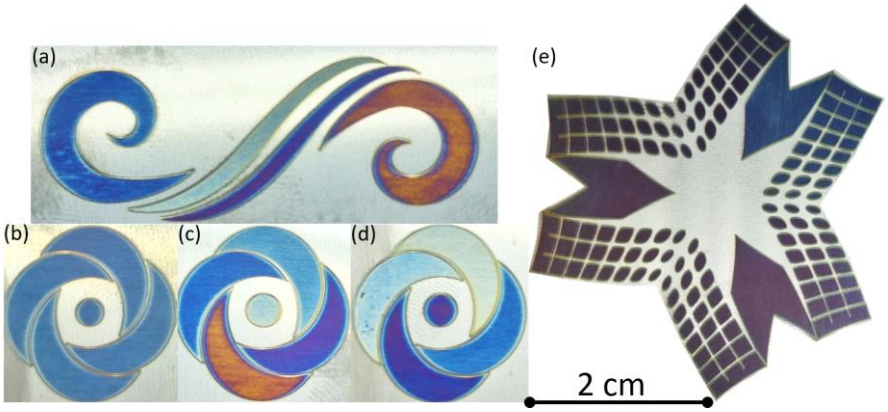

Fig. 23. Laser coloured figures on a stainless-steel sample. a) two half circles with two wavy lines: blue colour's scanning speed 2500 mm/s, grey blue – 1150 mm/s, purple – 3000 mm/s, orange – 4250 mm/s; b) floral pattern: dark blue – 2650 mm/s; c) floral pattern: blue – 2500 mm/s, light blue – 2300 mm/s, purple – 3000 mm/s, orange – 4250 mm/s, grey blue (middle circle) – 1150 mm/s; d) floral pattern: light blue – 1500 mm/s, turquoise – 1000 mm/s, blue – 2300 mm/s, purple – 3000 mm/s. Laser processing parameters: 7 pulses in the GHz burst, pulse fluence 30.8 J/cm^2, intra-burst pulse fluence 4.4 J/cm^2. e) logo of FTMC; dark blue – 3500 mm/s, purple – 4000 mm/s. 7 pulses in the GHz burst, pulse fluence 43.8 J/cm^2, intra-burst pulse fluence 6.3 J/cm^2 [PP1].

From the three ways that a metal surface could be coloured using laser micromachining, two of them can be easily dismissed. Plasmonic metals are

materials that support localised surface plasmon resonances which result in colours that arise from nanostructures and nanoparticles on the metals surface. This effect is the result of the confinement of a surface plasmon in a nanoparticle of size comparable to or smaller than the wavelength of light used to excite the plasmon. However, this happens in noble metals such as gold and silver, with other metals such as copper and aluminium also showing some of these properties. While stainless steel nanoparticles can exhibit localized surface plasmon resonance (LSPR), the resonances are typically broad and weak due to significant damping from high optical losses. The heterogeneous composition of stainless steel introduces multiple scattering centers and impurities, further hindering the efficiency of plasmonic oscillations. Given the weak plasmonic properties of stainless steel, LSPR contributes negligibly to surface coloration. Structural colours arising from LIPSS is also not the reason our stainless-steel samples are coloured. Checking our sample under scanning electron microscope, we did not find any LIPSS on the target's surface, only various different nanoparticles and nanostructures that are ununiformly scattered (Fig. 24d-g). Furthermore, structural colours change from green, to red and blue depending on the viewing angle, whereas our colours do get significantly darker depending on the viewing angle, but do not change colour. Lastly there is the surface oxidation. Because the laser is a significant heat source and various burst modes also assist in heat accumulation [65] it could fasten the oxidation process which results in different colours on the stainless-steel surface. The thin film effect would also explain two observable phenomena. The first one is our small amount of green and red colours achieved (Fig. 19). It could be explained by the fact that the oxide layer was too thick for the light to reflect from the sample and interference could not be seen. Also, because the colour is dependent on the optical path difference which in itself depends on the incident angle of the light, it explains why the colour becomes significantly darker when the angle is changed (Fig. 24a-c).

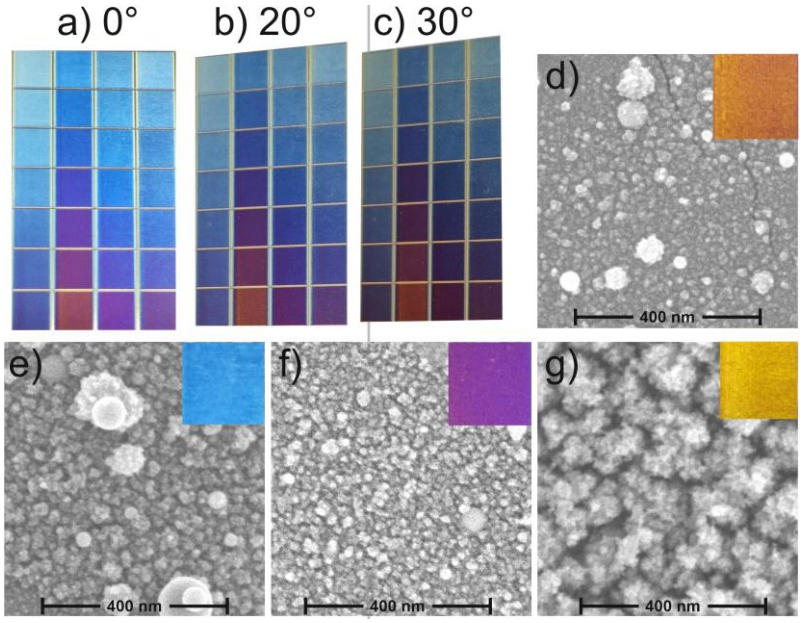

Fig. 24. Laser colouring tilt experiment: a) 0º tilt; b) 20º tilt; c) 30º tilt. d-g) scanning electron microscope images of different colours. Laser processing parameters: 7 pulses within the GHz burst, 18 J/cm^2 pulse fluence [PP1].

In this experiment, a variety of colours were achieved on stainless steel using scanning speeds between 1000 mm/s and 4250 mm/s, with colouring rates ranging from 10 mm²/s to 42.5 mm²/s. If optimal fluence and pulse numbers within GHz bursts are selected, colours such as yellow, orange, blue, purple, and dark green can be achieved at the maximum colouring rate of 42.5 mm²/s. To the best of our knowledge, no other study has reported colouring rates of stainless-steel exceeding 15 mm²/s (Table 2). This is also, to the best of our knowledge, the highest colouring rate achieved through oxidation mechanisms and is only comparable to plasmonic colours obtained from nanoparticles and nanostructures on plasmonic metals.

Table 2. Comparison of laser colouring rates and other parameters in scientific literature. *marks the first experiment and ** marks the second one.

Mechanism	Material	Parameters			
		λ, nm	v, mm/s	h, µm	dS/dt, mm^2/s
Oxidation[54]	Stainless–steel	532	100 – 600	5 – 15	0.5 – 9
Oxidation[55]	Stainless–steel	1062	50 – 225	10 – 20	0.5 – 4.5
Oxidation*	Stainless–steel	1030	100	10	1
Oxidation[57]	Stainless–steel	355	400 – 500	30	12 – 15
Oxidation[58]	Stainless–steel	532	70 – 600	4 – 10	2.8 – 6
Oxidation[59]	Stainless–steel	1064	2500	10	25
Oxidation[60]	Stainless–steel	1064	50 – 750	10	0.5 – 7.5
Oxidation[118]	Stainless–steel	1061	2.5 – 190	20	0.05 – 3.8
Oxidation[64]	Titanium	1064	25 – 150	200	5 – 30
Oxidation[61]	Titanium	1064	90 – 600	10	0.9 – 6
Oxidation[62]	Titanium alloy	1030	20 – 100	5	0.1 – 0.5
Oxidation[68]	Copper	1030	100	1 – 20	0.1 – 2
Oxidation**	Stainless–steel	1030	1000 – 4250	10	10 – 42.5
LIPSS[75]	Stainless–steel	800	1 – 4	50	0.05 – 0.2
LIPSS[91]	Stainless–steel	515	300 – 2000	1 – 3	0.3 – 6
LIPSS[119]	Copper	800	0.1 – 3	100	0.01 – 0.3
LIPSS[18]	Aluminium	800	0.1 – 16	50	0.005 – 0.8
LIPSS[120]	Silicon	800	1	30	0.03
Nanoparticles[73]	Gold and Silver	1064	11 – 3000	1 – 13.5	0.011 – 40.5
Nanoparticles[20]	Copper	1064	50 – 5000	10 – 20	0.5 – 100

Comparing colouring rates across the literature is challenging, mainly because distance between scanned lines (hatch) is often not listed if the parameter remains constant. However, based on the beam scanning speed alone, our method is at minimum three times faster than reported in comparable studies (Table 3).

Table 3 Comparison of laser beam scanning speeds and other parameters in scientific literature. *marks second experiment.

Mechanism	Material	Parameters	
		λ, nm	v, mm/s
Oxidation[81]	Stainless–steel	1064	10 – 90
Oxidation[13]	Stainless–steel	1064	100 – 1300
Oxidation[76]	Stainless–steel	1064	10 – 500
Oxidation[83]	Stainless–steel	1060	1 – 250
Oxidation[14]	Stainless–steel/Ti	1060	1 – 250
Oxidation*	Stainless–steel	1030	1000 – 4250
LIPSS[90]	Stainless–steel	1030	20 – 33.3
LIPSS[121]	Stainless–steel	240 – 2600	13
LIPSS[122]	Stainless–steel	800	10 – 130

2.1.4 Coloured surface hydrophobicity

Changing the colour of a metal is a wanted task, but it could be improved with additional surface functionalities. Changing a metals colour and also making it hydrophobic would be very beneficial because it would make the colours even more long lasting since it would help the metal withstand the environment significantly better. For a surface to be consider hydrophobic it needs to have SWCA of at least 90º and to be considered superhydrophobic, a SWCA of higher than 150º. The SWCA was measured for uncoloured stainless steel and also for the first 18 colours for the 7 pulses within the GHz burst with 3.5 J/cm^2 intra-burst pulse fluence regime. Each measurement was done 5 times and the standard deviation was calculated. Uncoloured stainless steel was not hydrophobic and had a contact angle of 50.4 ± 4.4º. In (Fig. 25) it can be seen that all achieved coloured surfaces are hydrophobic because their SWCA is higher than 90º independent of the hue of the colour. Due to our usage of femtosecond pulses, the sample had nanostructures and nanoparticles (Fig. 24d-g) on the surface after laser irradiation, which lead to their increase to hydrophobicity [123,124]. The time frame between the laser colouring and wettability tests was greater than 6 months making not only the colours but also the hydrophobicity long lasting. The samples were kept in ambient air conditions indoors without any noticeable change.

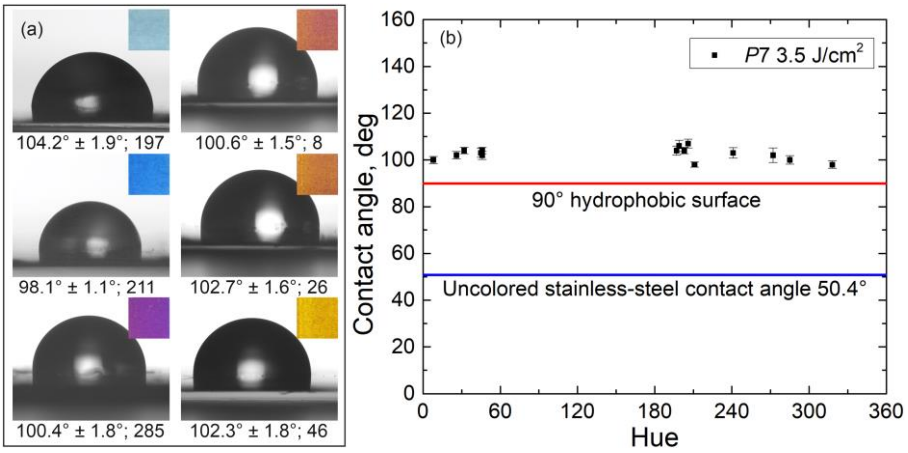

Fig. 25. Wettability experiments on laser coloured stainless steel with 7 pulses within the GHz burst with 3.5 J/cm^2 intra-burst pulse fluence. (a) water droplets on the surface of laser coloured stainless-steel, first number under the picture is the contact angle with standard deviation, second number is the hue of the colour; (b) contact angle dependence hue. Blue line is the contact angle on uncoloured stainless-steel – 50.4 ± 4.4º [PP1].

2.2 Laser colouring of copper

A novel, single-step, chemical-free fabrication method for producing super-wetting and highly hydrophobic copper surfaces using ns and ps lasers was demonstrated. For the first time, simultaneous control of the wettability and color of copper is achieved by systematically varying the area fraction of the laser-ablated surface, offering a versatile approach for surface modification. The study adopted the Cassie, Cassie-Baxter, and Wenzel models to explain that as the ablated area fraction increases, the contact angle decreases, enhancing hydrophilicity. Furthermore, significant visual and optical changes such as variations in color distance, gray value, and gray luminance correlate linearly with the ablated area fraction, showcasing the transformative impact of laser parameters. [PP2] results will be discussed here.

2.2.1 Wettablity theory

The characterization of the wetting properties of a surface is defined on the static contact angle measured by a sessile droplet technique [125]. For water droplets, a surface having a contact angle smaller than 90° is hydrophilic, while one larger than 90° is hydrophobic. The Wenzel, Cassie, and Cassie-

Baxter models are widely used in the research of wetting behaviour and surface interactions, particularly in the context of hydrophobicity and super-hydrophobicity.

This Wenzel model assumes that the liquid completely penetrates the rough surface. The apparent contact angle is a function of the intrinsic contact angle and the surface roughness [126]:

$$\cos\theta^* = r_1 \cos\theta_1 \tag{10}$$

where θ^* – is the measured contact angle on the rough surface, r_1 is the ratio of actual surface area to projected surface area, and θ_1 is the intrinsic contact angle on a smooth surface. Wenzel state has a larger surface wettability because the liquid on the surface enters the grooves, increasing the contact area.

The Cassie model addresses surfaces with regions of different wettability coexist caused by surface chemical heterogeneity [127,128]:

$$\cos\theta^* = f_1 \cos\theta_1 + f_2 \cos\theta_2 \tag{11}$$

where f_1 and f_2 are the fractions of the surface with different wettability angles θ_1 and θ_2, respectively. The fractional areas of two different surface components fulfill the requirement for the sum of the fractions must be equal as $f_1 + f_2 = 1$, this constraint ensures that no overlapping or missing regions exist.

For the Cassie-Baxter model when the composite contact surface is composed of air and solid since the contact angle of liquid and air is 180°, Eq. (11) can be simplified to [129,130]:

$$\cos\theta^* = f_1(1 + \cos\theta_1) - 1 \tag{12}$$

where θ^* is the measured contact angle on a composite surface, f_1 is the fraction of the solid-liquid interface area, while the rest fraction $(1 - f_1)$ is air, θ_1 is the intrinsic contact angle. This model assumes that the liquid rests on top of surface roughness features, with air pockets trapped underneath. This creates a composite surface of solid and air, which can drastically increase hydrophobicity. In scientific literature, the terms Cassie-Baxter and Cassie are commonly used. Cassie-Baxter is used to refer to uneven surfaces incompletely wetted by a liquid when vapor remains under the drop. Cassie is

used only for even or rough surfaces of a solid state that is completely wetted by the liquid.

Lastly, the Wenzel and Cassie-Baxter model describes the wetting angle on rough and heterogeneous surfaces [130,131]:

$$\cos\theta^* = r_1 f_1 \cos\theta_1 + f_2 \cos\theta_2 \qquad (13)$$

which considers surface roughness, where the Wenzel part of Eq. (10) with roughness factor r_1 amplifies the wetting properties (hydrophilic or hydrophobic) and Cassie-Baxter's part of Eq. (11) accounts for surface heterogeneity, using a fractional areas f_1 and f_2 of different surface components to adjust the contact angle.

2.2.2 Experimental setup

The principal experimental scheme of laser processing using an irradiation source with optional pulse durations and a galvanometer scanner is depicted in (Fig. 26).

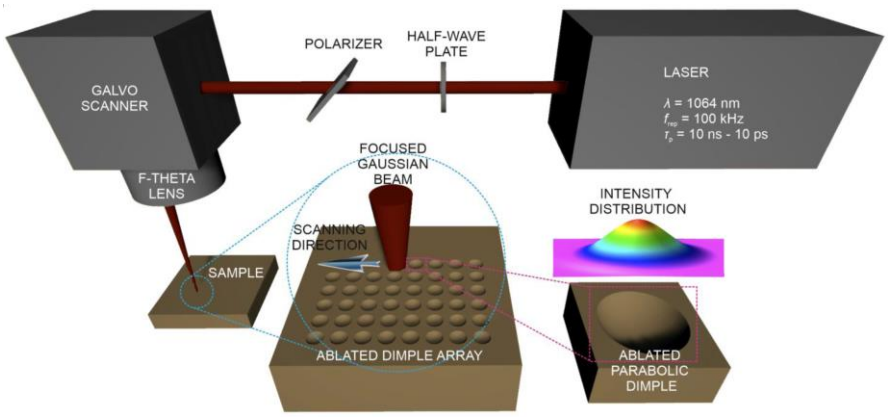

Fig. 26. Principal scheme of laser structuring experimental setup [PP2].

Laser structuring experiments were conducted using two laser irradiation sources (Baltic HP, Ekspla, and Atlantic HE, Ekspla) with laser parameters listed in (Table 1). Both lasers provided light pulses with pulse energy from E_p = 1 μJ up to E_p = 60 μJ. Translation of the laser spot on the target material at a controllable speed up to v_{scan} = 1.0 m/s provided the controllable distances between the transverse irradiation spots and distances between bidirectional scanned lines. The array of rectangular areas with transverse spatial dimensions of 11.5 × 12 mm^2 was laser textured in 29.9 s processing time including all scanner delays. The texturing rate of ~ 5 mm^2/s excluding delays

of the scanner was achieved for the area of the whole scanner field of 60×60 mm^2. The path of the scanned beam on the copper sample followed a snake-like trajectory consisting of parallel lines of overlapped laser pulses. The beam was scanned along the horizontal axis at a speed of $v_{scan} = 1.0$ m/s. The distance between consecutive laser pulses was $\Delta x = v_{scan} / f_{rep} = 10$ µm. A slower translation of the beam, at a speed of 10 mm/s, was applied along the vertical axis. The distance between scanned lines in the vertical direction (hatch) was $\Delta y = 5$ µm. The polarization of the beams was oriented along the vertical axis. The laser power was changed during the test from 0.1 W to 0.9 W (step 0.1 W, 9 tests) and from 1.0 W to 6.0 W (step 1.0 W, 6 tests) which provided controllable laser fluence on the sample. The 15 rectangular squares were marked using each laser at different laser powers which provided different laser fluence on the samples. The 15 different values of laser fluences were used, from 0.16 J/cm^2 to 1.44 J/cm^2 (step 0.16 J/cm^2, 9 tests) and from 1.6 J/cm^2 to 9.6 J/cm^2 (step 1.6 J/cm^2, 6 tests). Laser untreated copper is declared in graphs at the laser output power of 0.0 W and corresponding laser fluence of 0.0 J/cm2.

2.2.3 Contant angle and other measurements

The contact angle measurements methology is listed in Experimental setups and characterisations section. While, for the optical microscope imaging, digital images of both laser-processed and untreated copper surfaces were captured using an optical microscope (Nikon Eclipse LV100).

2.2.4 Area fraction evaluation

The digital image processing procedure used for area fraction calculations of laser-damaged Cu is presented in (Fig. 27).

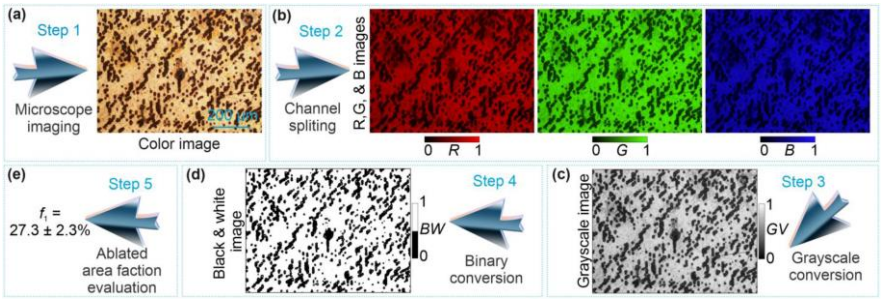

Fig. 27. Digital image processing procedure designed for area fraction calculations: (a) step 1 – microscope imaging of laser-treated copper surface; (b) step 2 – colour image split to red (R), green (G), and blue (B) channels; (c) step 3 – colour-to-grayscale conversion by Eq. (14); (d) step 4 – grayscale image conversion to a black-and-white binary image using Eq. 15; (e) step 5 – calculation of the area fraction of AF = 27.3 ± 2.3 % by Eq. 17 [PP2].

In step 1 (Fig. 27 (a)) microscope color image of laser treated copper surface was taken. In step 2 (Fig. 27 (b)), the color image was split into red (R), green (G), and blue (B) channels. In step 3 (Fig. 27 (c)) the image was transformed to the grayscale mode by calculating the grayscale value GV using the formula [132]:

$$GV = \max(R, G, B) \tag{14}$$

where R, G, and B are the red, green, and blue components, respectively. The five color-to-grayscale conversion methods have been tested in our work: intensity, luminance, luma, luster, and value 7. The value method has been chosen because of the highest achieved contrast between grayscale images of the laser-treated and untreated Cu. In step 4 (Fig. 27 (d)), the grayscale pictures were converted to black-and-white binary mode by using a certain threshold value GV_{th} using formula [133]:

$$BW = \begin{cases} 1, & \text{if } GV \geq GV_{\text{th}} \\ 0, & \text{if } GV < GV_{\text{th}} \end{cases} \tag{15}$$

Where he threshold was selected as a mean of average values of untreated Cu (0.0 W) and laser-treated copper at maximum available laser power (6.0 W) [133]:

$$GV_{\text{th}} = \frac{GV_{\text{untreated}} + GV_{\text{max fluence}}}{2} \tag{16}$$

The threshold value calculated by Eq. 16 was $GV_{th} = 0.48 \pm 0.02$.

In step 5 (Fig. 27 (e)), the area fraction f_1 of the laser-treated copper Cu in percent was calculated by averaging the equation of binary image intensity 100:

$$f_1 = \frac{1}{n}\sum_{i=1}^{n} BW_i \times 100\% \tag{17}$$

where n is the total number of picture pixels, i is the pixel index, BW_i is the binary black-and-white intensity of each pixel in the picture. The computational error in the area fraction f_1 evaluation was taken as the standard deviation of measurements from five sections of the microscope images.

2.2.5 Luminance and color distance evaluations

The luminance GL of grayscale was computed from RGB optical microscope images by using a formula based on the NTSC standard [133,134]:

$$GL = 0.3R + 0.59G + 0.11B \tag{18}$$

where R, G, and B are red, green, and blue components of the sample images after laser treatment

The color distance CD was calculated between digital optical microscope images of the copper surface before and after laser treatment was calculated by using equation [135]:

$$CD^2 = (R_u - R_f)^2 + (G_u - G_f)^2 + (B_u - B_f)^2 \tag{19}$$

where R_u, G_u, B_u, R_f, G_f, and B_f are red, green, and blue components of the sample images before (untreated) and after laser treatment (at a certain value of laser fluence). The averaging procedure is performed by using equation 20:

$$\langle GV \rangle = \frac{1}{n}\sum_{i=1}^{n} GV_i \tag{20}$$

where the average is denoted by angle brackets, n is the total number of picture pixels, i is the pixel index, GV_i is the grayscale value of each pixel in the picture. The standard deviation as a computational error in the grayscale value $\langle GV \rangle$ evaluation was taken from five sections of the microscope images. The average color difference ⟨CD⟩ and the standard deviation of it were calculated from the data achieved from five sections of images as well.

2.2.6 Copper colouring and wettability

The experimental results of the wettability and color change of copper depending on the laser fluence are depicted in (Fig. 28):

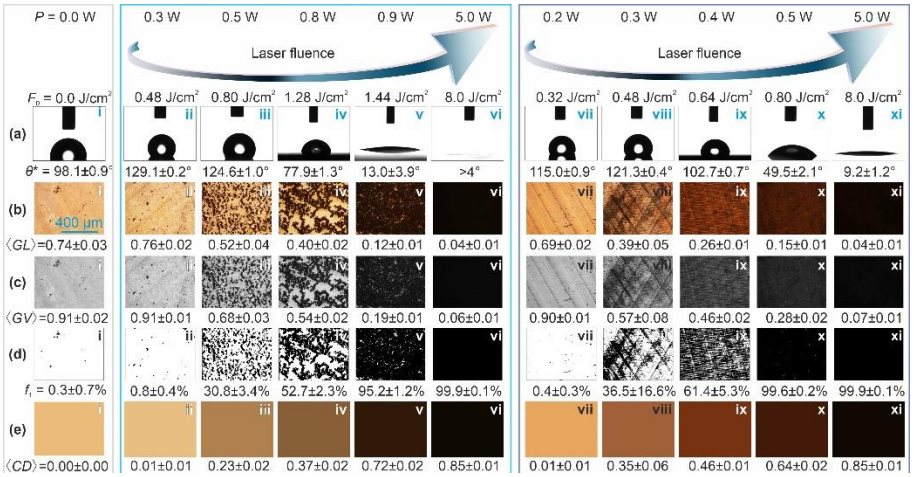

Fig. 28. (a) Water droplet images on copper surface treated by laser at different laser fluences. (b) RGB colour digital optical microscope images of the Cu surface. (c) Colour optical microscope images converted to grayscale mode. (d) Grayscale images were converted to black-and-white binary images with the threshold value of $GV_{th} = 0.48 \pm 0.02$. (e) The reconstructed average colour of colour images of copper. The scale bar provided in (b)(i) is valid for all images in (b-d) rows [PP2].

Water droplet images on copper surfaces treated by laser at different laser fluences are provided in (Fig. 28 (a)). The measured contact angle θ^* values are given below each image. The contact angle decreased with increasing laser fluence for both nanosecond and picosecond laser irradiation regimes. The contact angle also decreases to zero degrees, the Wenzel model can not be directly applied for the interpretation of the experimental results.The microscope RGB colour images are provided in (Fig. 28 (b)). The average grayscale luminance $\langle GL \rangle$ calculated by Eq. (18) is given below each image.

The size of each RGB microscope image is 0.87×0.65 mm^2. The RGB colour image conversion to the grayscale mode is provided in (Fig. 28 (c)). The average grayscale value $\langle GV \rangle$ calculated by Eq. (20) is given below each image. The grayscale image conversion and black-and-white images are provided in (Fig. 28(d)). The area fraction is calculated from black-and-white images by using Eq. (17) given below each image. The area fraction of the laser-ablated surface increases with increasing peak laser fluence for both nanosecond and picosecond laser irradiation regimes. The reconstructed colour of microscope RGB images of the surface of copper is provided in (Fig. 28(e)). The average colour distance $\langle CD \rangle$ calculated by Eq. (14) is provided below each image. The grayscale luminance $\langle GL \rangle$, grayscale value $\langle GV \rangle$ and colour distance $\langle GV \rangle$ of each image increased linearly with increasing peak laser fluence for both nanosecond and picosecond laser irradiation regimes.

The plots depicting how different surface characteristics (contact angle, color distance, gray value, and gray luminance) vary with the ablated area fraction for two different laser pulse durations: τ_p = 10 ns and τ_p = 10 ps is depicted in (Fig. 29)

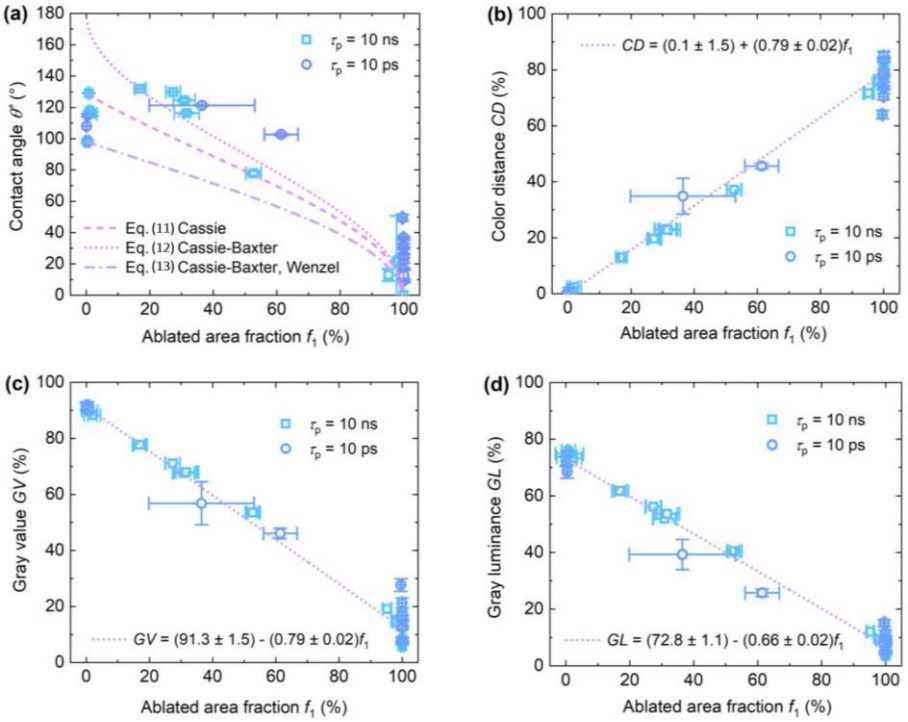

Fig. 29. Water static contact angle θ^* (a), colour distance CD (b), depend on the area fraction f_1 of laser-ablated copper. The open squares and open circles correspond to laser processing using irradiation at different pulse durations of τ_p = 10 ns and τ_p = 10 ps, respectively. The dot, dash, and dot-dash lines in (a) are fits of the experimental data point by Eq. (11), Eq. (12), and Eq. (13), respectively. The horizontal error bars indicate the standard deviation in the area fraction measurements taken from five sections of the microscope images. Vertical error bars in (a) correspond to the difference in contact angle measured on the left and right sides of the droplet. Vertical error bars in (b) indicate the standard deviation in the colour distance evaluation from five sections of the microscope images [PP2].

The contact angle decreases as the ablated area fraction increases, meaning the surface becomes more hydrophilic (Fig. 29 (a)). For Cassie model Eq. (11) the contact angles of $\theta_1 = 0°$ which correspond well to the experimental value minimal contacted angle of <4° of laser structured copper at high fluence (8 J/cm²) (Fig. 28 (a)(vi)), and $\theta_2 = 129°$ correspond well to the experimental value maximal measures angle of laser structured copper at low fluence (0.48 J/cm²) (Fig. 28 (a)(ii)).

For Cassie-Baxter model Eq. (12) the contact angles of $\theta_1 = 0.0°$ which correspond well to the experimental value minimal contacted angle of <4° of

laser structured copper at high fluence (8 J/cm²) For the combined Cassie-Baxter and Wenzel model Eq. (13) the contact angles of $\theta_1 = 4°$ which correspond well to the experimental value minimal contacted angle of <4° of laser structured copper at high fluence (8 J/cm²) (Fig. 28 (a)(vi)), and $\theta_2 = 98°$ correspond well to the experimental value maximal measures angle of laser unstructured copper (0.0 J/cm²) (Fig. 28 (a)(i)).

There is good agreement between experimental data and theoretical fits, especially for the $\tau_p = 10$ ps pulses (Fig. 29 (a)). The colour change increases linearly with the ablated area fraction. A linear fit is provided: $CD = (0.1\pm1.5) + (0.79\pm0.02)f_1$ (Fig. 29 (a)). The $\tau_p = 10$ ps pulses appear to cause a more rapid color change compared to $\tau_p = 10$ ns pulses at low ablation fractions. (Fig. 29 (b)). The gray value decreases as the ablated area fraction increases, suggesting that the surface becomes darker as more material is ablated. The linear fit equation is: $GV = (91.3\pm1.5) - (0.79\pm0.02)f_1$ Similar trends are observed for both $\tau_p = 10$ ns and $\tau_p = 10$ ps, though there may be subtle differences in behaviour at low ablation fractions (Fig. 29 (c)). Gray luminance decreases as the ablation fraction increases, consistent with the gray value trends. The linear fit is $GL = (72.8\pm1.1) - (0.66\pm0.02)f_1$. Both $\tau_p = 10$ ns and $\tau_p = 10$ ps pulses show similar trends, with a gradual reduction in luminance as ablation increases (Fig. 29 (d)).

2.3 Summary

Laser colouring on stainless steel was investigated by optimising different burst modes and scanning speeds. Other laser processing parameters were also tested including: pulse repetition rates, number of scans, hatch and combinations of the burst modes.

It was shown that laser colouring on stainless steel can achieve numerous colours including blue, purple, dark green, brown, yellow and others if the parameters are chosen correctly. Out of the three used burst regimes, MHz yielded only brown colours, while majority of colours have been achieved using the GHz and biburst mode. The GHz burst mode colours had greater variety and were more vibrant. Increasing other parameters such as pulse repetition rates, number of scans or hatch does not increase the highest possible colouring rate.

While using biburst or combination of burst modes, it be might be possible to achieve some new duller colours compared to the GHz burst mode, However, since neither the colouring rate nor vividness of the colours did not exceed the GHz burst mode results, mixing of the burst modes was not studied further.

Optimizing the number of pulses withing the GHz burst with the scanning speed allows for the highest colouring rate and the greatest interval of colours to be achieved simultaneously. To the best of our knowledge, fastest stainless-steel colouring rate of 42.5 mm^2/s has been achieved with optimal parameters. The colouring method is due to the oxide formation on the targets surface, because stainless-steel is not a plasmonic metal and no LIPSS were seen under the scanning electron microscope. Because the laser colouring method is based on hatching, various intricate designs including the logo for the Center of Physical Sciences and Technology (FTMC) was coloured. The coloured surfaces were also hydrophobic for all achieved colours which increases the applicability greatly. The colours remained unchanged for a period of time greater than 9 months and the wettability was tested 6 months after the colouring, making both effects long lasting.

A novel single-step and chemical-free fabrication method for the creation of super-wetting and highly hydrophobic copper surfaces using nanosecond and picosecond lasers was shown. The wettability and colour of copper were controlled by controlling the area fraction of the laser-ablated surface. Our adopted Cassie, Cassie-Baxter, and Wenzel models indicate that as the ablated area fraction increases, the contact angle decreases, indicating that the surface becomes more hydrophilic. Both colour distance, gray value, and gray luminance change linearly with the ablated area fraction of the copper surface, indicating significant visual and optical changes due to surface modification. The pulse duration (ps or ns) plays a role in the degree of these changes, with shorter pulse durations (10 ps) typically having a stronger effect.

3 Laser polishing of metals

Laser polishing using pulsed laser irradiation is a widely used technique to reduce the roughness of the target's surface. While performing laser polishing on metals, laser processing parameters were optimised to achieve efficient laser ablation, as well as, laser lift-off threshold of an oxide/metal structure was included into the ablation model. Furthermore, bi-stability effect on laser ablation was also measured for laser polishing. Results from [P2], [P3], [P4], [P6] and [P7] will be presented here.

3.1 Influence of nonlinear and saturable absorption

While performing laser polishing experiments we have noticed that the copper had an oxide layer on top of the metal that affects laser micromachining and decided to further investigate the mechanism to see whether it has a significant impact on the laser polishing.

Metals are covered with oxide layers with thicknesses ranging from tens of nanometers to tens of micrometers [7], which usually are semi-opaque semiconductors and transparent insulators depending on the bandgap. Though, incoming laser irradiation first interacts with the metal oxides and only afterward with the metals themselves. However, the metal oxides are hard to ablate because they possess high laser ablation thresholds [8], which are by the order of magnitude higher than the metal ablation thresholds [9], and the laser ablation is initiated on an oxide/metal interface during the lift-off process [10]. The lift-off process is where laser irradiation reaches the metal surface going through the thin oxide film, it then heats and vaporises the metal sample and causes rapid thermal expansion and stress accumulation at the interface between the thin oxide film and the metal sample. This leads to buckle delamination and the thin film oxide detaches. This thin films lift-off threshold is lower than the ablation threshold of the oxide itself. Nonlinear and saturable absorption [11] are commonly observed when metal oxide films are exposed to intense light with intensities ranging from MW/cm^2 to TW/cm^2. Therefore, those oxide layers covering the metal affect the fraction of the incoming laser irradiation dose that reaches the target substrate depending on the intensity applied. The laser lift-off threshold of the metal covered by an oxide is influenced by the nonlinear processes in the oxide layer and has to be taken into account. Thus, the laser lift-off threshold of an oxide/metal depends on the laser intensity applied and can be called the effective lift-off threshold fluence.

Therefore, novel experimental and theoretical research on the effective laser lift-off threshold change with varying peak intensities in *z*-scan experiments has been created. Results from publications [P2] and [P7] will be discussed here. The nonlinear and saturable absorption in the oxide layer on the metal substrate are the two most influencing factors for the effective laser lift-off threshold dependence on the different peak intensities in *z*-scan experiments. The existing analytical normalized transmission equation of the semi-transparent thin layer in open aperture *z*-scan was incorporated into the effective laser lift-off threshold dependence on the sample position in the newly presented model. The *z*-scan-type laser ablation experiment was conducted, and lift-off thresholds were measured at different sample positions, which caused different beam peak intensities on the processed oxidized copper target material. The numerical calculations using the new proposed model equation coincided well with the experimental results of effective laser lift-off threshold dependence on the *z*-scan position.

3.1.1 Influence of nonlinear and saturable absorption on laser lift-off threshold

The laser-irradiated area consisted of two distinct areas, laser ablation of pristine copper and lift-off of the oxide layer (Fig. 30a). The thickness of the oxide layer measured from the height profile was $L = 1.0 \pm 0.1$ µm (Fig. 30b).

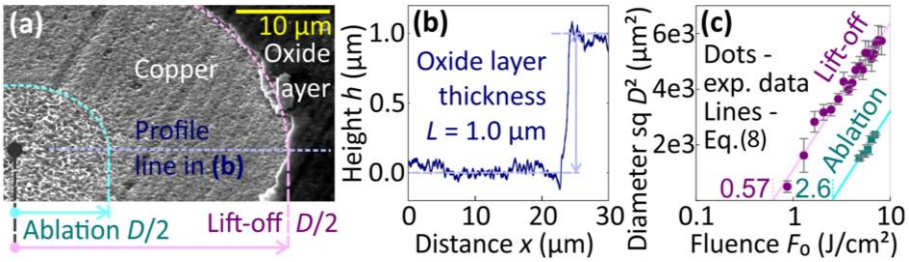

Fig. 30 (a) SEM micrograph, (b) profile, and (c) diameter squared D^2 versus peak laser fluence F_0 of ablated copper and removed oxide layer from copper substrate by lift-off technique. The oxide layer thickness $L = 1.0 \pm 0.1$ µm was evaluated from the height profile. The oxide lift-off threshold fluence 0.57 ± 0.03 J/cm^2 and copper ablation threshold 2.6 ± 0.3 J/cm^2 were retrieved from line fits of experimental data points by Eq. (8) in (c) [P4].

The fluence threshold was measured by D^2 method described in Experimental setups and characterizations section. The line extrapolation of $D^2(E_p)$ to the $D^2 = 0$ µm^2 in Eq. (8) gives the threshold pulse energy E_{pth}, the function slope is related to the beam radius *w*, and the ablation threshold then

can be evaluated by $F_{th} = 2E_{pth}/(\pi w^2)$. The optical microscope (Eclipse LV100, Nikon) was used for the measurements of the ablated diameters of pristine copper and diameters of the removed oxide layer of Cu_2O/Cu samples (Fig. 30c). Threshold values of F_{th} = 0.57 ± 0.03 J/cm^2 and 2.6 ± 0.3 J/cm^2 were retrieved from line fits by Eq. (8) for oxide lift-off and copper ablation, respectively (Fig. 30c). The literature value of the lift-off threshold for copper oxide removal from the copper sample is F_{th} = 0.62 J/cm^2 (τ = 12 ps, λ = 1064 nm, f_p = 100 kHz, w = 17 µm, N = 1) [136]. The literature value of ablation threshold of copper by (τ = 0 ps, λ = 1064 nm, f_p = 50 kHz, w = 41.8 µm, N = 1) laser is F_{th} = 2.0 J/cm^2 [23]. The literature threshold fluence values coincided well with our current work.

The light attenuation propagating through a linearly and nonlinearly absorbing material can be described as [137]:

$$\frac{\mathrm{d}I}{\mathrm{d}z} = -\alpha I - \beta I^2 \tag{21}$$

where $I = I(z)$ is the peak intensity within the sample material, depending on the propagation distance z in the sample; α is the linear absorption coefficient; and β is the nonlinear absorption coefficient. The normalized transmission through the sample can be extracted from the solution of Eq. (21) and expressed as [138]:

$$T = \frac{e^{-\alpha L}}{\beta I L_{\mathrm{eff}} + 1} \tag{22}$$

where I is the incident intensity, L is the physical sample thickness, and L_{eff} is the effective thickness of the sample [138]:

$$L_{\mathrm{eff}} = \frac{(1 - e^{-\alpha L})}{\alpha} \tag{23}$$

Because of the linear absorption saturation behaviour, the linear absorption coefficient $\alpha = \alpha(I)$ depends on the peak intensity I, and for homogenous saturation can be expressed as [139]:

$$\alpha(I) = \frac{\alpha_0}{\left(1 + \left(\frac{I}{I_s}\right)^2\right)} \tag{24}$$

where α_0 is the low-intensity absorption coefficient and I_s is the saturation intensity. The Gaussian beam intensity in the *z*-scan- type experiment can be expressed as:

$$I = \frac{I_0}{1 + \left(\frac{z}{z_R}\right)^2} \tag{25}$$

where $I_0 = 2E_p/(\pi w_0^2 \tau)$ is the peak pulse intensity in the center of the Gaussian beam at a focus position, w_0 is the focused beam radius at $1/e^2$ level, τ is the pulse duration, $z_R = \pi w_0^2/(\lambda M^2)$ is the Rayleigh length, λ is the wavelength of irradiation, and M^2 is the quality parameter of the Gaussian beam.

The direct bandgap for Cu_2O is 2.1 eV [140], which is larger than the photon energy 1.17 eV at the wavelength of 1064 nm. The linear absorption coefficient of Cu_2O is $\alpha = 5.2 \times 103$ cm^{-1} [141]. Therefore, the transmission of a linearly absorbing oxide layer at low peak intensities in the GW/cm^2 range evaluated by Eq. (22) is $T_0 = \exp(-\alpha_0 L) \approx 60\%$, and the layer can be assumed as semi-opaque. The saturation intensity of the linear absorption coefficient for Cu_2O is $I_s \sim 0.1$ TW/cm^2 [142]; thus, the semi-opaque oxide layer suddenly becomes fully transparent, when peak intensities exceed the saturation intensity. However, by further increasing intensity, the nonlinear absorption becomes dominant, and the oxide layer changes to opaque again. The nonlinear absorption coefficients of Cu_2O are $\beta = 4.3 \times 10^{-9}$ cm/W [141]. Thus, a focused picosecond laser beam with high peak intensities up to 3 TW/cm^2 obtained in our experimental conditions induces nonlinear absorption in the transparent oxide layer on top of the copper target. The nonlinearly absorbing oxide layer transmits only a part of the incoming laser beam to the metal substrate and has to be taken into account when predicting effective ablation characteristics of an oxide/metal structure. Equations (22) – (25) have been numerically solved and normalized T/T_0 transmission of the Cu_2O layer was calculated (Fig. 31a).

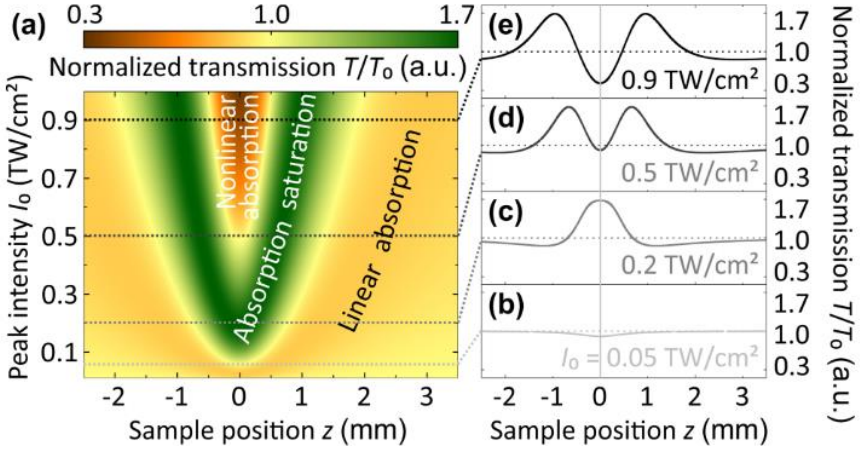

Fig. 31. a) Calculated normalized transmission T/T_0 (colour scale) versus sample position z (bottom axis) and peak pulse intensities I_0 (left axis) for Cu_2O layer. The three different absorption regions are indicated: yellow, linear absorption; green, linear absorption saturation; brown, nonlinear absorption. Profiles of normalized transmission T/T_0 (right axis) dependence on the sample position z (bottom axis) at different peak intensities I_0: (b) 0.05 TW/cm^2; (c) 0.2 TW/cm^2; (d) 0.5 TW/cm^2; (e) 0.9 TW/cm^2 [P4].

At low peak pulse intensities of $I_0 \approx 0.05$ TW/cm^2 that are smaller than the saturation intensity $I_s \sim 0.1$ TW/cm^2, just linear absorption is observed with no saturation and very small nonlinear absorption in the focal position $z \ll \pm z_R$; thus, almost constant normalized transmission $T/T_0 \approx 1$ in all sample z positions is observed (Fig. 31b). With the peak intensity values of ~ 0.2 TW/cm^2 exceeding the saturation intensity, the oxide layer becomes nearly fully transparent $T/T_0 \approx 1.7$ with a sample position close to the focal point $z \ll \pm z_R$ (Fig. 31 c). When peak intensity reaches the value of $\sim$ 0.5 TW/cm^2, the nonlinear absorption equals the linear intensity saturation; thus, the normalized transmission in the oxide layer reaches a value close to $T/T_0 \approx 1$ in the focal region $z \approx 0$ mm (Fig. 31 d). However, the nonlinear absorption is very sensitive to the peak intensity and occurs only in fine focus $z \ll \pm z_R$. Out of the focus in $z \approx \pm 1$ mm, the Cu_2O layer is still transparent with a transmission value of $T/T_0 \approx 1.7$ (Fig. 31d). When peak pulse intensity reaches a high value of ~ 0.9 TW/cm^2, the nonlinear absorption exceeds the absorption saturation, and normalized transmission drops to the value of $T/T_0 \approx 0.4$ in the focal point. Therefore, the Cu_2O layer becomes opaque in the focal range of the beam. However, the defocused beam in the Rayleigh range

$z \approx \pm z_R$ is still transparent because of the saturation of linear absorption with normalized transparency of $T/T_0 \approx 1.7$ (Fig. 31e).

The *z*-scan-type laser lift-off threshold evaluation experiments with controlled laser peak pulse intensities have been conducted in this work. The peak pulse intensities I_0 were ranging from 20 GW/cm^2 to 3.0 TW/cm^2. The Rayleigh length of the focused beam was of $z_R \approx 0.83$ mm. The squared lift-off diameters of an oxide layer from copper at different positions *z* are depicted in (Fig. 32a and b).

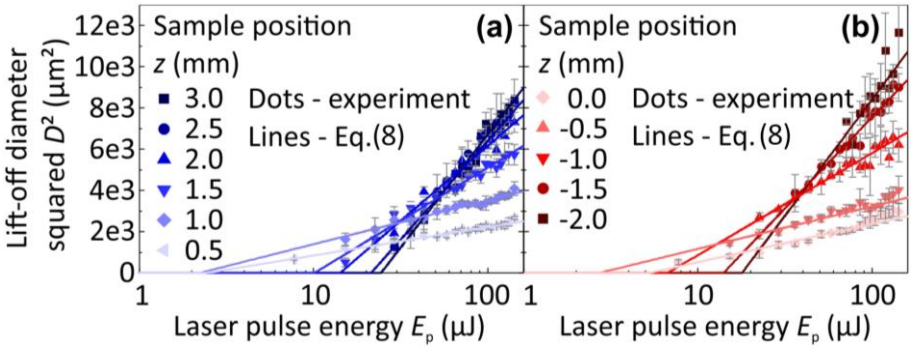

Fig. 32. Lift-off diameter squared D^2 of oxide layer removed from copper dependence on the laser pulse energy E_p at various sample position *z* values ranging from (a) 0.5 mm to 3.0 mm, step 0.5 mm and from (b) 0.0 mm to − 2.0 mm, step − 0.5 mm. Solid dots represent the experimental data points, error bars are the statistical deviation from average crater diameter from 10 dimples ablated using the same pulse energy, and solid lines are fits by Eq. (8)[P4].

Pulse energies of 20 different values have been used at each of the 11 fixed z-scan positions with a fixed laser spot radius on the sample. Every test has been repeated 10 times to get the statistical deviation errors bars. Experimental data points of ablated crater diameters were fitted using Eq. (8), and laser spot radiuses at different sample positions *z* were retrieved as fitting parameters and its errors. The laser spot radius values on the sample ranged from $w_0 = 17.2 \pm 0.3$ μm in the focal region to $w = 48.6 \pm 1.2$ μm out of focus. The fit of experimental data points by Eq. (8) (Fig. 32a and b) also provided information about the effective lift-off threshold fluence of the oxide/copper structure at various positions *z* of the sample (Fig. 33a).

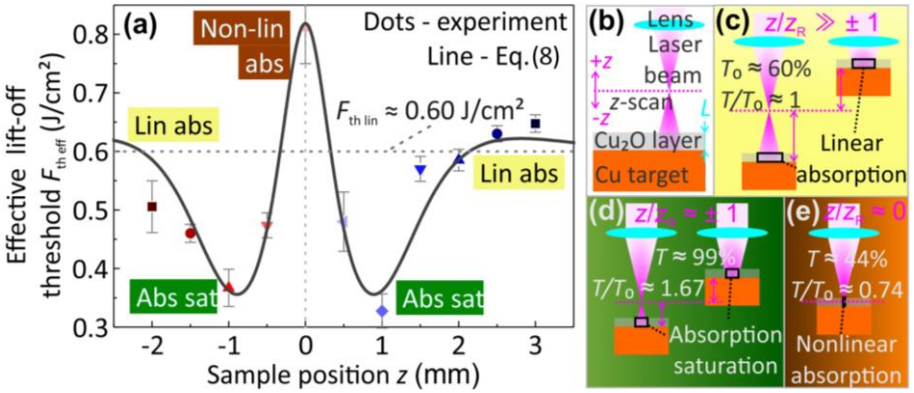

Fig. 33. (a) Effective lift-off threshold $F_{th.eff}$ of oxide/copper dependence on sample *z* position. Solid dots and error bars represent the effective lift-off threshold values retrieved from the fitting parameters by Eq. (8) (Fig. 27a and b), and the solid gray line is the fit of experimental data points by Eq. (26). (b) Principal visual scheme of the proposed model with semi-transparent Cu_2O layer on top of the Cu sample. The different Cu_2O layer transmission cases are indicated depending on peak pulse intensities: (c) out of focus with sample positions $z/z_R \gg \pm 1$, low intensities of the defocused beam, and linear absorption with transmission value $T_0 \approx 60\%$; (d) sample position $z/z_R \approx \pm 1$ in the saturable absorption intensity region with transmission value $T \approx 99\%$; (e) sample position $z/z_R \approx 0$ in the focus of the beam and high peak intensities, and nonlinear absorption exceeds absorption saturation in the oxide layer and transmission drop to $T \approx 44\%$ [P4].

It was found that the effective lift-off threshold is highest near the beam waist $z = 0$ mm, then we saw a sharp drop of effective lift-off threshold to a minimum value at $z = \pm 1$ mm, and afterward it increased again (Fig. 33a). A similar drop of the laser-ablated volume per pulse in *z*-scan ablation at the sample position of $z/z_R \approx 0$ has been observed by Chen et al. [143]; however, the drop of ablation rate was not attributed to the increase of threshold fluence in their research. Thus, in this work, we have proposed a new model for the effective lift-off threshold fluence, which considers the attenuation of the incoming laser irradiation by the oxide layer on the metal substrate.

In our proposed ablation model, the laser irradiation is attenuated by the semi-transparent oxide layer, and only a fraction of the incoming laser beam reaches the copper target. The principal visual scheme of our threshold model of a semi- transparent Cu_2O layer with the thickness of $L = 1.0$ μm on the Cu substrate is depicted in (Fig. 33b). The Gaussian picosecond laser beam is focused by the objective lens, and the peak pulse intensity is varied on the target material by controlling the *z*-scan position of the sample. The three

different absorbing scenarios depending on the peak pulse intensities applied are linear absorption, a saturation of linear absorption, and non linear absorption depicted in (Fig. 33 c, d and e), respectively. By having the sample out of the focal position, moderate values of effective lift-off threshold of $F_{\text{th.lin}} \approx 0.60$ J/cm^2 are observed (Fig. 33a). This is explained by our proposed model that when a highly defocused beam $z/z_R \gg \pm 1$ with low peak intensities is applied on the sample, only linear absorption is observed in the attenuating Cu_2O layer (Fig. 33c) thus, just a fraction $T_0 \approx 60\%$ of the incoming laser beam interacts with the copper in the oxide/metal interface, and moderate energy densities are needed to ablate the copper target material. However, when laser intensities reach the saturable absorption, the oxide layer suddenly becomes transparent, and almost all incoming laser irradiation reaches the pristine copper. Thus, the drop of effective lift-off threshold to ~ 0.36 J/cm^2 is observed (Fig. 33a). It is graphically depicted in our proposed model with moderate intensities above the saturation intensity at sample position $z/z_R \approx \pm 1$ and moderate peak intensities with the normalized transmission of the oxide layer of $T/T_0 \approx 1.67$ (Fig. 33d). Thus, the major part of the incoming laser irradiation $T \approx 99\%$ is transmitted through the oxide layer. When peak pulse intensities in the focal range reach the TW/cm^2 values, the nonlinear absorption becomes dominant and exceeds the absorption saturation; consequently, only a fraction of the incoming laser beam reaches the copper, and the effective lift-off threshold increases to the value of 0.81 J/cm^2 (Fig. 33a). It is explained with our model that at the focal position $z/z_R \approx 0$, the beam is focused, and the highest peak intensities are achieved; therefore, the non-linear absorption is reached, and the oxide layer becomes opaque $T/T_0 \approx 0.74$ (Fig. 33e). Only a small fraction $T \approx 44\%$ of the incoming laser beam goes through the Cu_2O layer and reaches the Cu substrate.

Therefore, taking into account linear absorption, absorption saturation, and nonlinear absorption in the model, it can be assumed that the effective lift-off threshold of oxide/metal is the product of the ablation threshold in linear absorption regime $F_{\text{th.lin}}$ at low peak intensities and the inverse normalized transitivity T_0/T of cuprous oxide layer defined by Eq. (22). The effective lift-off threshold can be expressed as follows:

$$F_{\text{th.eff}} = F_{\text{th.lin}} \left(\frac{T_0}{T} \right) \tag{26}$$

The effective lift-off threshold $F_{\text{th.eff}} = F_{\text{th.eff}}(z)$ defined by Eq. (26) depends on the sample position z in the z-scan-type laser ablation experiments. The

model fit is in good coincidence with the experiment (Fig. 33a). The new model predicts the fall of the effective ablation threshold to minimum values of $F_{\text{th.eff}} \sim 0.36$ J/cm^2 near the sample position of $z \approx \pm 1$ mm. Also, the model predicts a steep rise of ablation threshold value up to $F_{\text{th.eff}} \sim 0.81$ J/cm^2 in the focus of the beam. The moderate values of effective ablation threshold $F_{\text{th.eff}}$ close to $F_{\text{th.lin}} \approx 0.60$ J/cm^2 out of the focus are also predicted.

3.2 Laser polishing on copper and stainless-steel

3.2.1 Experimental setup

A state-of-the-art solid-state laser (Pharos, Light Conversion) with laser parameters listed in (Table 1) was used in the experiment. The beam radii values were needed in various sample *z* positions during the experiment and were measured using a well-known *D*-squared method. The beam radius in the focal plane was equal to 21 μm. The rectangular-shaped cavities with a top dimension of 2 mm × 1 mm were ablated in the copper and stainless-steel samples (Fig. 34). The distance between scanning lines was kept constant at 10 μm, and the scanning speed was set to 333 mm/s. The sample position was changed in the *z*-direction in order to get different fluence values. Each rectangle was scanned numerous times in order to achieve a depth that could be easily measured using a stylus profiler (Dektak 150+, Veeco). Using the stylus profiler, 2 mm length rectangular shaped cavities surface roughness's R_a were measured using Eq. (27), without any ISO standards being kept:

$$R_a = \frac{1}{L}\int_0^L |Z(x)|dx \tag{27}$$

where L – profile length, $Z(x)$ – deviations from the mean line along the entire sampling length.

During the MHz and GHz burst experiments, the number of pulses in bursts was changed from $N = 2$ to $N = 9$ and from $P = 2$ to $P = 25$, respectively. During the biburst experiment, every N and P combination was tested.

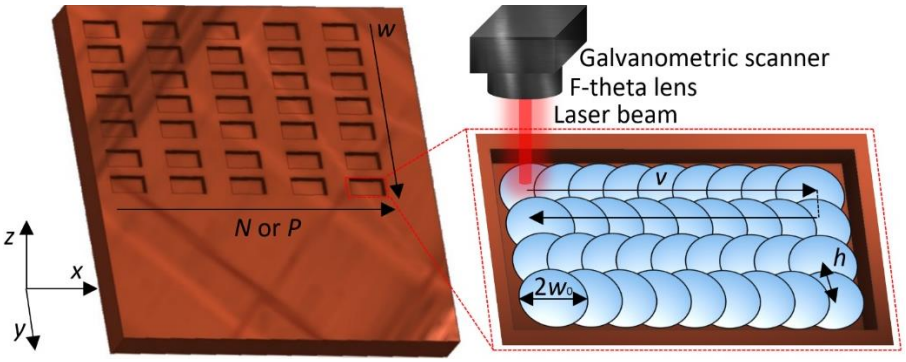

Fig. 34. Design of laser milling and polishing experiment. Rectangle cavities were ablated in a copper and a stainless-steel sample. Beam size was changed in columns by changing the sample's *z* position. *N* or *P* were changed in matrix lines. *v* is the scanning speed and was kept constant at 333 mm/s, *h* is the hatch and was 10 µm, w_0 is the beam radius and was changed from 21 µm to 95 µm. The dashed line represents galvanometric scanners' mirrors' jump [P3].

3.2.2 Beam characteristics

D-squared method described in Experimental setups and characterisations section was repeated for all *z* values, which were 0.2, 0.4, 1.0, 1.4, 1.9, 2.4, 2.7, 3.1, 3.8, 4.9 mm in both directions. Measured beam radii values are shown in (Fig. 35).

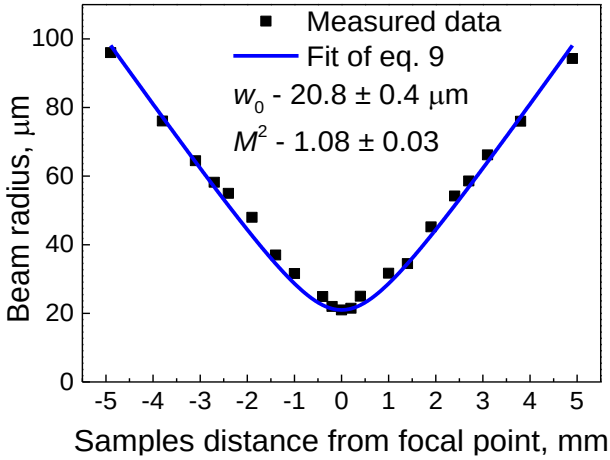

Fig. 35 Laser beam radii at different samples *z* positions. Black squares – experimental data, blue line – equation (9) fit. The received parameters were beam waist w_0 – 20.8 ± 0.4 µm, beam quality parameter M^2 – 1.08 ± 0.03 [P3].

3.2.3 Laser polishing on copper and stainless steel

While using MHz burst mode with fluences lower than 0.5 J/cm^2 the surface roughness was quite high, reaching around 1 µm in copper (Fig. 36a). We can see also scanning electron microscope pictures (SEM) in (Fig. 36). The rectangle cavity marked with a blue dot, two pulses in the MHz burst were used and the depth is equal to 36 µm with a roughness of 1.07 µm. From 0.5 to 1 J/cm^2 fluence, the surface roughness improved greatly to an interval from 0.2 µm to 0.5 µm. The lowest roughness is seen with 4 or more pulses in the MHz burst. There are a few effects at play here. First of all, there is the incubation effect, which is the ablation threshold decrease with increasing number of pulses in the same spot [144]. Secondly and most importantly, is the heat accumulation. Subsequent pulses reach the target material before the heat affected zone has cooled off so less energy is needed to remove the material [145]. We can see in (Fig. 36) a SEM image with a much more even surface with a low roughness of 0.23 µm and an ablated depth of 18.1 µm. For fluences higher than 1 J/cm^2 the roughness increased again to an interval of 0.5 – 0.7 µm. With higher fluences particle shielding also has a stronger negative effect scattering and absorbing the incoming laser irradiation. We can see in (Fig. 36) a SEM image marked with a black dot of a milled rectangle with a surface roughness of 0.53 µm. It has been shown [25] that the highest ablation efficiency was reached when a MHz burst had 3 pulses. The aforementioned regime resulted in relatively good quality of surface roughness compared to other results. However, it could be improved by adding a polishing step using $N = 6$ regime to decrease the surface roughness even further.

We see similar tendencies with stainless steel (Fig. 36b), but because stainless steel has a higher specific heat capacity 0.500 J/(g·K) to copper's 0.385 J/(g·K) it takes more pulses and higher fluences to reach the optimal heat accumulation. For fluences lower than 0.8 J/cm^2 the surface quality is quite poor. Visible graining can be seen in (Fig. 36) SEM image with a red dot. The ablated depth is equal to 41.7 µm and the surface roughness is 5.4 µm. For higher fluences than 0.8 J/cm^2 and with 5 and more pulses in the MHz burst we have seen the optimal window for highest surface quality on stainless steel. In (Fig. 36) a SEM image with a green dot showed a surface roughness of only 0.67 µm while using 7 pulses in the MHz burst. However, a similar finish quality can be achieved with less pulses in the burst but higher fluence as we can see in (Fig. 36) SEM image with a black dot, where using a fluence of 4.4 J/cm^2 and 2 pulses in the MHz burst, 0.63 µm surface roughness was achieved. Stainless steel had an overall higher surface roughness but that

was due to the fact that the starting roughness was higher as well and equal to 0.5 μm compared to 0.1 μm of copper.

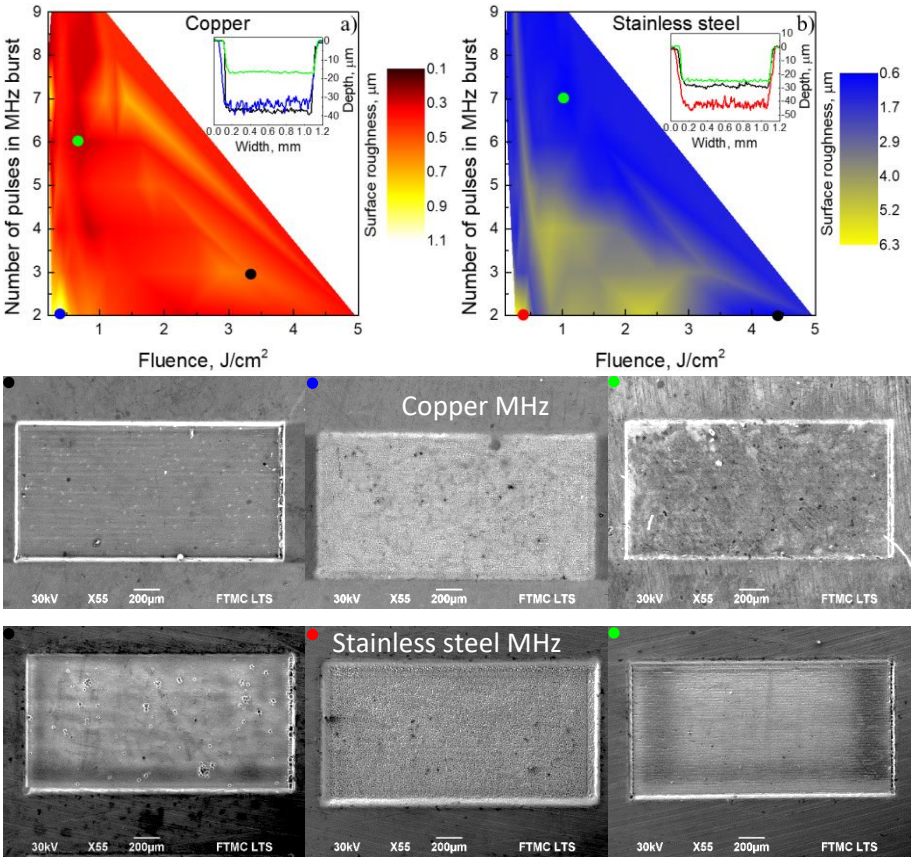

Fig. 36. Surface roughness dependence on fluence and number of pulses in the a) GHz burst and b) biburst modes. a) Black dot and solid line 2 pulses in the GHz burst, 1.1 J/cm^2 fluence, 0.10 μm surface roughness; green dot and solid line 3 pulses in the GHz burst, 0.5 J/cm^2 fluence, 0.10 μm surface roughness; blue dot and solid line 5 pulses in the GHz burst, 0.16 J/cm^2 fluence, 0.72 μm surface roughness. b) N – number of pulses in MHz burst, P – number of pulses in the GHz burst. Black dot and solid line N = 3, P = 2 pulses in the biburst, 0.6 J/cm^2 fluence, 0.20 μm surface roughness; blue dot and solid line N = 3, P = 5 pulses in the biburst, 0.07 J/cm^2 fluence, 0.74 μm surface roughness; green dot and solid line N = 3, P = 3 pulses in the biburst, 0.4 J/cm^2 fluence, 0.08 μm surface roughness. For all color dots, scanning electron microscope pictures are shown.

Using the GHz laser polishing regime, for copper the surface roughness was in the 0.1 – 0.35 um interval for the vast majority of fluence and number of pulses within the burst combinations. SEM images of 0.1 μm roughness is

shown for two and three pulses in the GHz burst in (Fig. 37) marked with black and blue dots, respectively, with different fluences the first one being 0.5 J/cm^2 and the other 1.1 J/cm^2. Even taking the worst results for the GHz burst polishing regime, the roughness was only 0.53 μm as is shown in the (Fig. 37) SEM image marked with a blue dot. This was the worst combination of parameters being 5 pulses at 0.22 J/cm^2 fluence when the sample is 3.8 mm out of focal plane. GHz burst mode uses heat accumulation to its fullest effect because of the incredibly small time window between subsequent pulses. However, we should keep in mind that it has been shown that the ablation efficiency drops by about 90% [42] in the GHz burst mode so it should only be used as a polishing step. As we can see from (Fig. 37a) the polishing process is very parameter independent.

In the biburst mode polishing, the surface roughness again becomes more parameter dependent. The vast majority of parameter combinations will lead to a surface roughness of lower than 0.5 μm. However, using 10 and less pulses in the GHz burst and fluences for each individual sub-pulse lower than 0.6 J/cm^2 will result in roughness lower than 0.2 μm. SEM images are shown in (Fig. 37b). High quality polishing was shown in SEM images with black and green dots, corresponding to N = 3, P = 2, 0.10 μm roughness and N = 3, P = 3, 0.08 μm roughness, respectively. Again, the low surface quality is only seen in the very out of focus 3.1 mm and more, milled cavities, and low fluences such as in (Fig. 37b) SEM image with blue dot. Overall, bibursts result similar surface roughness at optimal parameters but slightly higher roughness for sub-optimal ones. These tendencies do not change depending on the number of pulses in the MHz burst.

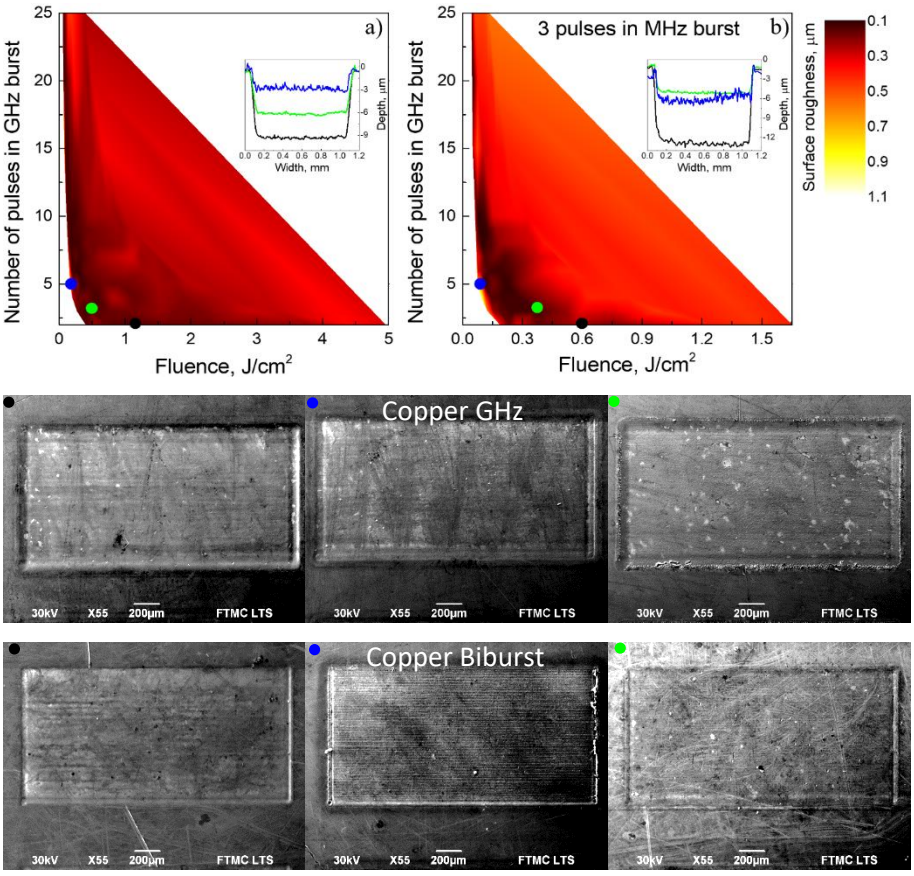

Fig. 37. Surface roughness dependence on fluence and number of pulses in the a) GHz burst and b) biburst modes. a) Black dot and solid line 2 pulses in the GHz burst, 1.1 J/cm^2 fluence, 0.10 µm surface roughness; green dot and solid line 3 pulses in the GHz burst, 0.5 J/cm^2 fluence, 0.10 µm surface roughness; blue dot and solid line 5 pulses in the GHz burst, 0.16 J/cm^2 fluence, 0.72 µm surface roughness. b) N – number of pulses in MHz burst, P – number of pulses in the GHz burst. Black dot and solid line N = 3, P = 2 pulses in the biburst, 0.6 J/cm^2 fluence, 0.20 µm surface roughness; blue dot and solid line N = 3, P = 5 pulses in the biburst, 0.07 J/cm^2 fluence, 0.74 µm surface roughness; green dot and solid line N = 3, P = 3 pulses in the biburst, 0.4 J/cm^2 fluence, 0.08 µm surface roughness. For all colour dots, scanning electron microscope pictures are shown [P3].

As with copper, the GHz burst results in the highest quality on stainless steel with vastly different parameters We can see in (Fig. 38a) SEM images with red and black dots with surface roughness of 0.66 µm and 0.55 µm was reached with 2 pulses in the GHz burst, 1.1 J/cm^2 fluence, and 3 pulses in the

GHz burst, 0.5 J/cm^2 fluence, respectively. As with copper, the only poor-quality results are received when the sample is 3.8 mm or more out of focus when the fluence is 0.1 J/cm^2. An example is shown with a SEM image with green dot, with a corresponding surface roughness of 1.4 μm.

For the biburst mode surface roughness (Fig. 38b) was similar to the GHz burst mode at optimal parameters with the roughness of 0.57 μm at $N = 3$, $P = 2$ in SEM image with black dot and 0.45 μm at $N = 3$, $P = 2$ SEM image with a red dot, respectively. A high surface roughness is shown as well with the SEM image with a green dot, corresponding to a surface roughness of 1.89 μm at $N = 3$, $P = 15$.

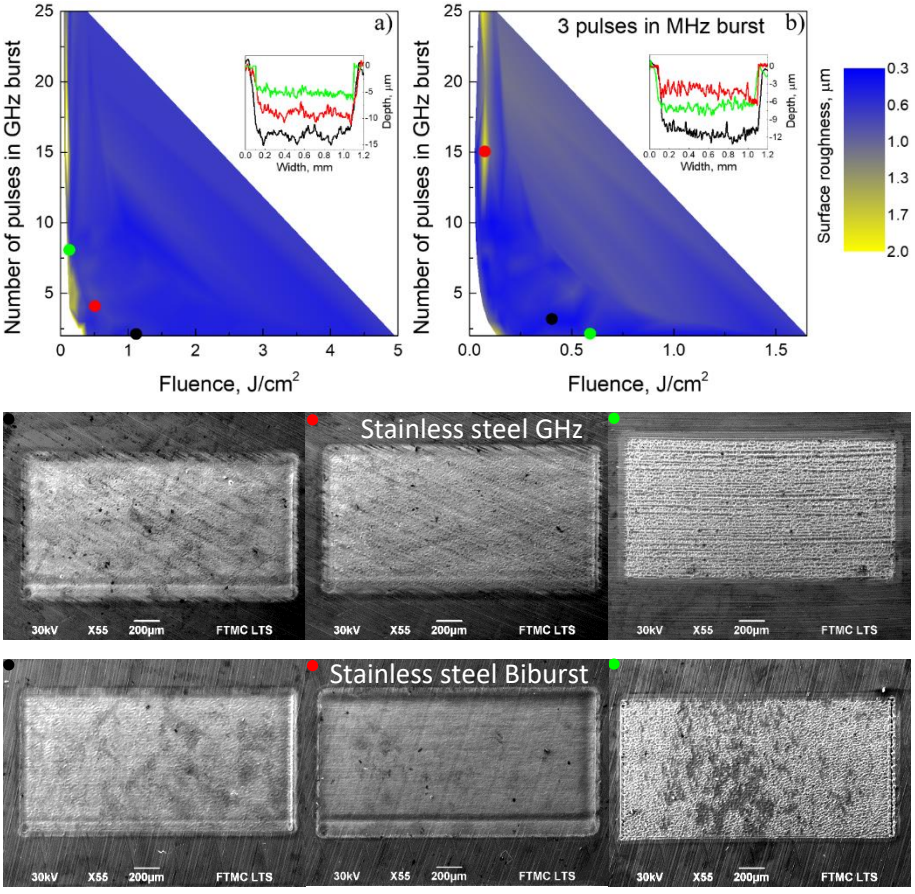

Fig. 38. Surface roughness dependence on fluence and number of pulses in the a) GHz burst and b) biburst modes. a) Black dot and solid line 2 pulses in the GHz burst, 1.1 J/cm^2 fluence, 0.66 μm surface roughness; red dot and solid line 3 pulses in the GHz burst, 0.5 J/cm^2 fluence, 0.55 μm surface roughness; green dot and solid line 8 pulses in the GHz burst, 0.1 J/cm^2 fluence, 1.4 μm surface roughness. b) N – number of pulses in MHz burst, P – number of pulses in the GHz burst. Green dot and solid line $N = 3$, $P = 2$ pulses in the biburst, 0.6 J/cm^2 fluence, 0.57 μm surface roughness; black dot and solid line $N = 3$, $P = 3$ pulses in the biburst, 0.4 J/cm^2 fluence, 0.45 μm surface roughness; red dot and solid line $N = 3$, $P = 15$ pulses in the biburst, 0.05 J/cm^2 fluence, 1.89 μm surface roughness. For all colour dots, scanning electron microscope pictures are shown [P3].

3.3 Bi-stability in femtosecond laser polishing by MHz bursts

It has been shown that ablation efficiency in the burst modes has bi-stability, which means that the ablation efficiency depends whether there are equal or even number of pulses within the burst. The same thing to an extent, can be seen with laser polishing as well. Also, in majority of the reports, the shielding or/and re-deposition are indicated as the main reasons resulting in bistable dependence of ablation efficiency on the pulse number in the burst. The redeposition hypothesis by second sub-pulse for copper has investigated and verified by atomistic simulations [146]. The re-deposition has been experimentally studied by shadowgraph technique; however, no clear experimental evidence of re-deposited material was found [41]. The shielding effect has been identified as the dominating effect resulting drop in ablation efficiency for the second sub-pulse in time-resolved experiments for copper [147]. It has been shown experimentally that incoming irradiation is attenuated by ejected particles, vapor, and plasma of the previous pulse, thus reduced ablation efficiency is observed for even pulses [148–150]. For odd pulses, higher efficiency is observed, because the previous even pulse produces fewer ablation products and more incoming laser radiation reaches the sample [151]. This leads to bi-stable ablation and polishing efficiency.

3.3.1 Experimental setup

A solid-state femtosecond burst laser (Pharos, Light Conversion) with laser parameters listed in (Table 1) was used for the experiment. The number of pulses per bust number was controlled from $N = 1$ (single pulse regime) to $N = 9$. Rectangular-shaped cavities have been ablated by laser into copper plate samples with transverse dimensions of $2\ \text{mm} \times 1\ \text{mm}$. The laser processing experiments were conducted at room temperature in air. Several layers ranging from 3 to 21 were ablated to increase the cavity depth up to 100 μm for the higher accuracy of depth profile measurement. The Rayleigh length of the Gaussian beam was 1.2 mm and was more than 10 times larger than the cavity depth. The saturation behavior of ablation depth per layer was never reached and the laser-milled cavity depth had a linear dependence on the number of ablated layers. The lateral distance between bi-directional beam scanning lines of $\Delta y = 10$ μm and scanning speed of $v_x = 0.33$ m/s, were kept constant during experiments.

3.3.2 Bi-stability

The surface roughness R_a of laser ablated cavity bottom dependence on laser fluence was investigated experimentally with the burst fluences ranging from 0.52 to 9.9 J/cm^2 and 9 different numbers N of pulses in the burst (1, 2, 3, 4, 5, 6, 7, 8, and 9). The experiment showed bi-stability in surface roughness R_a depending on the laser processing parameters (Fig. 39). The surface roughness R_a dependence on the burst fluence and the number of pulses in the burst are depicted in (Fig. 39a). The burst fluence was increased from 0.52 to 9.9 J/cm^2 and the number of pulses in the burst was increased from 1 to 9. The surface roughness R_a in most of the cases was slightly smaller for even numbers (N = 2, 4, 6, and 8) than for odd numbers (N = 1, 3, 5, 7, and 9) of pulses in a burst if compared to the same burst fluence at large values (2.3 J/cm^2 − 9.9 J/cm^2) (Fig. 39a). However, for small values of burst fluence (0.52 J/cm^2 − 1.7 J/ cm^2) opposite behaviour could be observed with a surface roughness R_a smaller for odd than for even numbers of pulses in the burst (except for N = 1) (Fig. 39a). This bi-stability effect of surface roughness R_a depending on the burst fluence can be seen when the profiles of the colour plot depicted in (Fig. 39a) are extracted at constant odd and even numbers of pulses in the burst (Fig. 39b-e). For example, for N = 8 the surface roughness R_a was slightly higher than N = 9 for several fluence values, and slightly lower for the rest of the fluence values with a relative difference in roughness only of 2% (Fig. 39b). For N = 6 surface roughness R_a was slightly lower than N = 7 up for all fluence values ranging from 1.7 up to 4.6 J/cm^2. The average relative surface roughness R_a difference increased to 39% (Fig. 39c). This ablation regime can be called the bi-stable regime (Fig. 39c). Moreover, for N = 4 and N = 5 bistable surface roughness R_a from 1.7 J/cm^2 to 9.9 J/cm^2 is observed (Fig. 39d). The average relative surface roughness R_a difference was 18% (Fig. 39d). A slightly different bi-stability was observed for N = 2 and N = 3 pulses (Fig. 39e). For low fluence values ranging from 0.52 to 2.3 J/cm^2 surface roughness, R_a was higher for an even number of pulses in burst with the average relative surface roughness R_a difference of 26% (Fig. 39e). For high fluence values ranging from 3.3 to 9.9 J/cm^2 surface roughness, R_a was higher for an odd number of pulses in burst with the average relative surface roughness R_a difference of 31% (Fig. 39e). The bi-stability effect of surface roughness R_a depending on the number of pulses in the burst can be seen when the profiles of the colour plot depicted in (Fig. 39a) are extracted at constant burst fluence (Fig. 39f-i). For example, for F_{burst} = 1.7 J/cm^2 the surface roughness R_a sudden jumps are seen for every next number of pulses in a burst from N = 1 to N = 6 (Fig. 39f). The gradual decrease of the surface roughness

R_a with an increasing number of pulses in a burst from $N = 1$ to $N = 9$ for larger values of burst fluence of $F_{burst} = 2.3$ J/cm^2 with small sudden jumps are observed (Fig. 39g). The decrease of the surface roughness R_a with an increasing number of pulses and larger values of burst fluence of $F_{burst} = 4.6$ J/cm^2 with large sudden jumps are observed (Fig. 39h). For the largest burst fluence of $F_{burst} = 9.9$ J/cm^2 the bi-stable regime with sudden jumps of drastic decrease of surface roughness R_a at even numbers ($N = 2$, 4, 6, and 8) of pulses is observed (Fig. 39i). This bi-stability regime of surface roughness R_a depending on the burst fluence can be seen when the surface roughness of N pulse burst depending on ($N + 1$) pulse burst is extracted from colour plot (Fig. 39a) and depicted in (Fig. 39j–m). The bi-stable regimes occur because for surface roughness R_a every even number ($N = 2$, 4, 6, and 8) several possible values of surface roughness R_a exist corresponding $N + 1$ odd numbers (3, 5, 7, and 9) every even number. The experimental results provided in (Fig. 39) showed stable and bi-stable surface roughness R_a regions depending on the burst fluence and the burst length. The laser polishing regime with the lowest overall value of surface roughness R_a of 0.23 µm was found at the burst fluence of $F_{burst} = 4.6$ J/cm^2 and the number of pulses in a burst of $N = 6$.

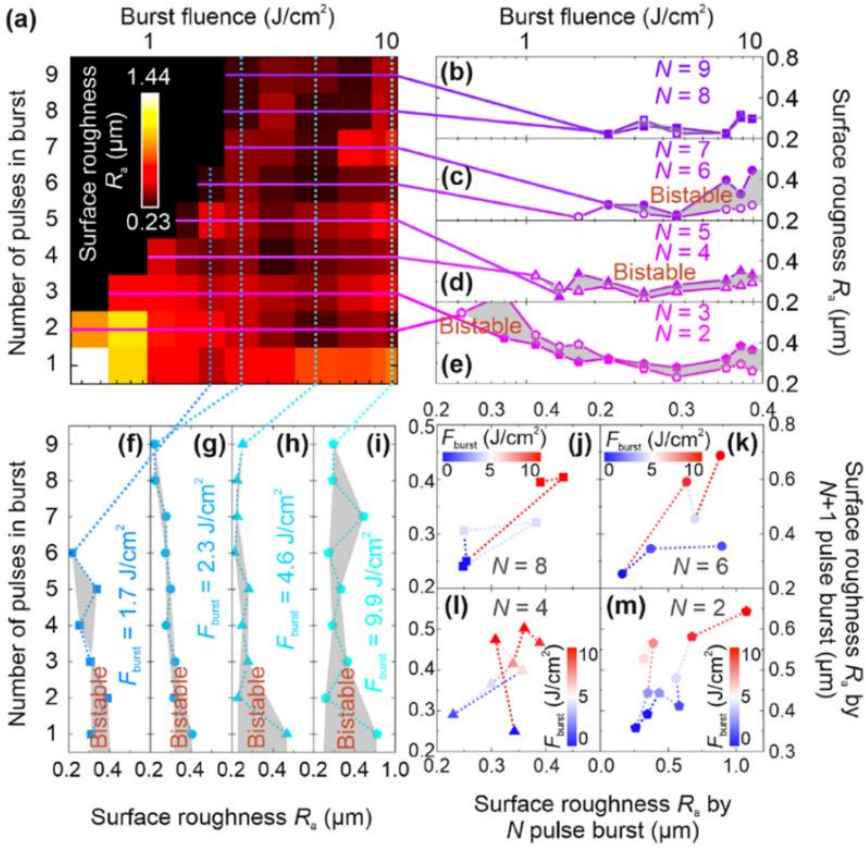

Fig. 39 Experimental results of bi-stable behaviour of surface roughness R_a of laser ablated cavity bottom. (a) Surface roughness R_a of laser ablated cavity bottom of copper (colour scale) dependence on the burst fluence (top axis) and the number of pulses in femtosecond burst (left axis), the squares indicated by black colour are not measured points because of pulse laser fluence below the ablation threshold. The surface roughness R_a (right axis) dependence on burst fluence (top axis) at different numbers of pulses in burst: (b) N = 8, 9; (c) N = 6, 7; (d) N = 4, 5; (e) N = 2, 3. Profiles of surface roughness R_a (bottom axis) dependence on the number of pulses in the burst (left axis) at different burst fluences: (f) 1.7 J/cm^2; (g) 2.3 J/cm^2; (h) 4.6 J/cm^2; (i) 9.9 J/cm^2. The surface roughness R_a created by (N + 1) pulse burst (right axis) dependence on surface roughness R_a created by N pulse burst (bottom axis) at different burst fluences (colour scale): (j) N = 8; (k) N = 6; (l) N = 4; (m) N = 2. Pulse duration τ_{FWHM} = 210 fs, laser wavelength λ = 1030 nm, burst repetition rate f_{burst} = 100 kHz, and the temporal distance between pulses in burst t_{pulse} = 15.5 ns (intra-burst pulse repetition rate f_{pulse} = 64.7 MHz) [P2].

3.3.3 Shielding and redeposition

The bi-stable behaviour of ablation efficiency initiated by bursts of ultrafast pulses has been reported in numerous of scientific papers for copper [25,26,41,148,151], brass [152] and aluminium [152]. The shielding or/and re-deposition has been identified main reasons of bi-stable behaviour of ablation efficiency depending in the pulse number in burst in most of the research works. Shielding together with the redeposition effect are wildly attributed to bistable ablation efficiency in the field, however, the mostly it is only hypothesis with no direct observation of the phenomenon. The shielding and re-deposition of copper target has been experimentally studied by shadowgraph technique with similar experimental conditions (wavelength 1030 nm, pulse duration 400 fs, repetition rate 400 kHz, delay between pulses 12.2 ns, fluence 0.69 J/cm^2, spot diameter 44 μm) [41]. The shielding effect by ablation cloud has been directly visualized via the shadowgraph technique, however, no clear experimental evidence of re-deposited material was seen [41]. Generally, for the re-deposition, the negative ablation depth for the second sub-pulse in burst is supposed to be measured, resulting the efficiency decrease for two sub-pulse burst below 50%, if compared with a single pulse ablation efficiency of 100%. Since some material ejected by the first pulse is reposited by the second, and the total volume ablated by both pulses is less than that ablated by a single first pulse is divided by double pulse energy of two sub-pulses.

3.4 Summary

The attenuation of the incoming laser beam by a copper oxide layer on a copper target was included in the ablation model and the new model had a good agreement with the experimental data.

Using 210 fs laser pulses in the burst and biburst regimes, copper and stainless-steel samples were ablated to receive the highest surface quality. It was shown that both MHz and GHz bursts are useful in reducing surface roughness, with MHz burst having the advantage of higher ablation efficiency, while GHz bursts were very parameter independent for the surface quality. The GHz bursts make use of the heat accumulation better because of the shorter time between pulses. R_a surface roughness of 0.23 μm, 0.1 μm and 0.08 μm were achieved for copper in the MHz, GHz and biburst modes, respectively. As well as, a large number of parameters yielded < 0.15 μm R_a for the GHz burst mode. The same tendencies were seen for stainless-steel. The lowest surface roughness for the MHz burst was 0.63 μm, 0.55 μm for

the GHz burst, and 0.45 µm for the biburst mode. Using the MHz burst mode the ablation efficiency is the highest while using 3 pulses in the bursts at the optimal fluence, but the surface roughness is lowest with 6 pulses within the burst. GHz and biburst modes have a much lower ablation efficiency, but a significantly higher polishing quality that could be used a finishing step to achieve the wanted surface roughness.

As with efficient laser ablation bi-stability in surface roughness R_a depending on the laser processing parameters can be seen due to the shielding and re-deposition effects.

CONCLUSIONS

1. It was shown that all burst modes: MHz, GHz and biburst mode can produce colours on stainless steel, with MHz burst having only brown colour and GHz having the largest spectrum of vivid colours due to oxidation process.
2. Highest colouring rate in scientific literature due to oxidation was achieved using the GHz burst mode equalling 42.5 mm^2/s.
3. Due to the laser colouring process depending on hatching, it was shown that any kind of shape can be coloured even with multiple colours at once.
4. Different laser processing parameters, including: hatch, pulse repetition rate, number of scans and burst mode mixing were tested but did not yield significant amount of new colours and did not increased the colouring rate.
5. Due to usage of femtosecond pulses, the coloured stainless steel sample had nanoformations on the surface, which made the coloured surface have a SWCA of greater than 90 degrees making them hydrophobic, which increases their applicability.
6. Grayscale colouring and wettability control was shown for copper samples.
7. Lift-off threshold changes due to copper oxide transparency that depends on the laser irradiation intensity because of the nonlinear and saturable absorptionn.
8. Surface roughness of 0.23 µm, 0.1 µm and 0.08 µm were achieved for copper in the MHz, GHz and biburst modes and lowest surface roughness of 0.63 µm, 0.55 µm, and 0.45 µm for the stainless steel. With stainless steel having a higher surface roughness due to the highest starting roughness.
9. GHz burst mode yielded the lowest average surface roughness R_a, especially for copper which was < 0.15 µm due to a better usage of heat accumulation.
10. It was shown that with efficient laser ablation bi-stability in surface roughness R_a depending on the laser processing parameters can be seen due to the shielding and re-deposition effects.

SANTRAUKA

Įvadas

Daugeliui įvairiose pramonės šakose naudojamų gaminių didelę įtaką daro paviršiaus kokybė ir šiurkštumas. Lazerinis mikroapdirbimas yra patrauklus metodas dėl gausybės taikymo sričių: nuo įvairių medžiagų pjovimo ir gręžimo iki dviejų su puse dimensijų (2,5D) struktūrų formavimo ant įvairių paviršių. Nuolat tobulinant lazerinio mikroapdirbimo technologiją, populiarėja ir kiti metodai, pavyzdžiui, lazerinis spalvinimas ar lazerinis poliravimas.

Lazerinis paviršiaus spalvinimas greitai pranoko įprastinius ženklinimo būdus, nes tai yra lengvai pritaikoma, universali ir aplinkai nekenksminga technologija, turinti daugybę įvairių pritaikymo sričių. Nors lazerinio spalvinimo panaudojimas sparčiai auga, pats spalvinimo procesas nėra pakankamai ištirtas. Egzistuoja trys pagrindiniai metalo spalvinimo lazeriu fizikiniai mechanizmai. Pirmasis – tai lazerio sukelta oksidacija, kai įkaitinta lazeriu medžiaga žymiai greičiau reaguoja su deguonimi. Ant metalo susidaro oksido sluoksnis, kurio spalva skiriasi nuo pradinio metalo spalvos. Kitas spalvos pasikeitimo susidarius oksido sluoksniui paaiškinimas yra plonos plėvelės efektas. Kai šviesa atsispindi nuo oksido ir metalo paviršiaus, įvyksta interferencija, ir jei optinio kelio skirtumas yra lygus tam tikram bangos ilgiui arba jo sandaugai su sveikuoju skaičiumi, matoma atitinkama spalva. Antrasis metodas nuo kampo priklausančios struktūrinės spalvos, atsirandančios dėl lazerio sukeltų periodinių paviršiaus struktūrų (LIPSS). LIPSS, veikia panašiai kaip ir vienmatė gardelė ir dėl difrakcijos matomos spalvos. Šios spalvos vadinamos struktūrinėmis spalvomis ir priklauso nuo žiūrėjimo kampo. Paskutinis lazerinio spalvinimo metodas yra plazmoninės spalvos. Šios spalvos taip pat struktūrinės. Skirtingai nuo antrojo mechanizmo, spalva nesikeičia priklausomai nuo žiūrėjimo kampo, nes paviršiaus spalvas sužadinančios paviršiaus struktūros pasiskirsčiusios atsitiktinai, be dėsningumų. Spalvos matomos dėl paviršiaus plazmonų rezonanso (SPR) efekto, kurį sukelia nanostruktūros ir nanodalelės ant metalų paviršiaus. Lazerinis spalvinimas priklauso nuo daugelio apdirbimo parametrų: lazerio galios, pluošto skenavimo greičio, atstumo tarp skenuojamų linijų, impulsų pasikartojimo dažnio ir kitų. Optimizuojant lazerio parametrus, taip pat galima gauti ir norimą struktūrinį paviršiaus pokytį, kuris gali lemti naudingas savybes, pavyzdžiui, hidrofobiškumą.

Lazerinis poliravimas taip pat yra pageidaujamas ir populiarus lazerinio mikroapdirbimo metodas. Kadangi submikrometrinio paviršiaus šiurkštumas pageidaujamas trinties, atsparumo dilimui ir aerodinamikos srityse, lazerinis

poliravimas yra labai perspektyvus poliravimo metodas. Lazerinis poliravimas leidžia pasiekti didelį tikslumą, gerą apdailos kokybę, platų galimų medžiagų pasirinkimą bei lengvą sudėtingų formų poliravimą. Taip pat ta pačia lazerine sistema galima apdirbti ir poliruoti bandinius. Tačiau norint pasiekti geriausius rezultatus, reikia tinkamai parinkti optimalius lazerinio apdirbimo parametrus, tokius kaip impulsų pasikartojimo dažnis, impulsų energija, impulsų persiklojimas ir kitus, o tai yra varginantis ir daug laiko reikalaujantis darbas. Lazeriai ir sistemos, skirtos lazerinei mikro ir nano gamybai, kasdien tobulinamos. Dabar galimos sistemas, kuriose naudojami MHz ir GHz impulsų pasikartojimo dažniai su femtosekundiniais lazerio impulsais ir didele vidutine optine galia, naudojant impulsų vorų ir bivorų (vorų-vorose) režimus. Šie režimai leidžia gerokai padidinti abliacijos efektyvumą, taip pat gerokai pagerinti abliuojamo paviršiaus šiurkštumą, jei tinkamai optimizuojami lazerinio apdorojimo parametrai. Lazerio impulsų voros taip pat užtikrina greitesnį apdirbimą dėl impulso energijos padalijimo į mažesnes energijas, artimesnes optimaliam energijos įtekiui, todėl išnaudojama didesnė vidutinė lazerio galia. Be to, dėl trumpo laiko tarp voros impulsų pakartotinai panaudojama bet kokia išlikusi ankstesnio impulso šiluma.

Ši disertacija buvo skirta rasti optimalius lazerinio apdirbimo parametrų rinkinius, kad būtų pasiektas mažiausias paviršiaus šiurkštumas naudojant lazerinį poliravimą ir didžiausias spalvų skaičius bei didžiausia spalvinimo sparta naudojant vario ir nerūdijančiojo plieno lazerinį spalvinimą. Disertacija suskirstyta į dvi pagrindines dalis: viena skirta lazeriniam spalvinimui, kita – lazeriniam poliravimui. Nerūdijantis plienas buvo spalvinamas lazeriu naudojant mažo energijos įteko ir mažo pluošto skenavimo greičio spalvinimą ir spartų spalvinimą naudojant didesnius energijos įtekius, o varis buvo spalvinimas naudojant pilkąją skalę. Poliruojant lazeriu buvo optimizuojamas impulsų skaičius vorose, vorų bistabilumas, taip pat netiesinės ir sotumo absorbcijos įtaka atsiskyrimo slenksčiui.

Darbo tikslas

Disertacijos darbo tikslas – pasiekti optimalų impulsų skaičių MHz, GHz ir bivoros režimuose, taip pat rasti optimalų energijos įtekį, kad būtų minimalus įmanomas paviršiaus šiurkštumas ir maksimaliai padidintas spalvų skaičius bei metalų spalvinimo sparta, taip padidinant lazerinio poliravimo ir spalvinimo pritaikomumą pramonėje.

Darbo užvadiniai

1. Ištirti impulsų skaičiaus MHz, GHz ir bivoros režimuose poveikį lazeriniam poliravimui ir spalvinimui.
2. Pasiekti kuo mažesnį metalų paviršiaus šiurkštumą po abliacijos imituojant realų taikymą.
3. Optimizuojant apdirbimo parametrus, pasiekti didžiausią spalvų skaičių ant nerūdijančiojo plieno spalvinant lazeriu greičiau nei kitos mokslinės grupės.
4. Gauti lazeriu apdirbtus paviršius, turinčius naudingas savybes, kurios padidintų spalvotų paviršių pritaikomumą.

Mokslinis naujumas

Šiame darbe buvo atliekamas vario ir nerūdijančiojo plieno poliravimas bei spalvinimas. Buvo išbandyti skirtingi impulsų voros režimai: MHz, GHz ir bivoros, taip pat skirtingi lazerio apdirbimo parametrai. Mažiausias nerūdijančiojo plieno ir vario paviršiaus šiurkštumas būtų labai naudingas pramoniniam naudojimui. Šioje disertacijoje naudojant optimalius parametrus buvo pasiektas 0,1 μm paviršiaus šiurkštumas ant vario paviršiaus. Lazeriniu spalvinimu ant nerūdijančiajam plieno buvo gauta daug ryškių spalvų. Mūsų turimomis žiniomis, mūsų eksperimentų metu buvo pasiektas didžiausias lazerinio spalvinimo greitis. Pasiektos spalvos yra hidrofobinės, o tai labai padidina jų pritaikomumą.

Praktinis pritaikomumas

Lazerinis poliravimas ir spalvinimas naudojamas medicinos ir automobilių pramonėje kaip aplinkai nekenksmingas, lengvai pritaikomas ir ilgaamžis laisvos formos dalių ar instrumentų poliravimo ir spalvinimo būdas, kuris taip pat gali būti naudojamas laikrodžių gamyboje ir spalvinime. Mūsų išsamūs eksperimentai, kuriuos atlikus pavyko išgauti platų spalvų spektrą, didelę spalvinimo spartą, hidrofobinius spalvotus paviršius ir submikrometrinius poliruotus paviršius, dar labiau padidina procesų pritaikomumą pramonėje.

Ginamieji teiginiai

1. Ant nerūdijančio plieno, naudojant femtosekundinius impulsus GHz impulsų voroje, dėl paviršiaus oksidacijos buvo pasiekta 42,5 mm^2/s spalvinimo sparta esant 4250 mm/s pluošto skenavimo greičiui, kuri leido išgauti skirtingas spalvas: mėlyną, geltoną, oranžinę, violetinę ir tamsiai žalią.

2. Visi trys impulsų voros režimai – MHz, GHz ir bivoros, naudojant femtosekundinius impulsus gali būti naudojami lazeriniam spalvinimui, siekiant išgauti plačią spalvų gamą ant nerūdijančio plieno, o susiformavę spalvoti paviršiai yra hidrofobiški, dėl ko didėja jų pritaikomumas.
3. Dėl netiesinės ir įsisotinimo sugerties vario oksido plėvelės pralaidumo priklausomybė nuo lazerinės spinduliuotės intensyvumo keičia plėvelės atsiskyrimo slenkstį, t. y. slenkstinę lazerio energiją, reikalingą plonai oksido plėvelei pašalinti išgarinant pagrindinį metalą, o tai prisideda prie efektyvesnio metalo paviršiaus lazerinio poliravimo.
4. Naudojant GHz impulsų voros režimą su iki 15 impulsų ir bivoros režimą, kuriame MHz impulsų voroje yra 3 impulsai, o GHz impulsų voroje – iki 10 impulsų, galima pasiekti mažesnį nei 0,1 µm R_a paviršiaus šiurkštumą ant vario ir mažesnį nei 0,5 µm R_a paviršiaus šiurkštumą ant nerūdijančio plieno, kas pabrėžia optimalaus impulsų skaičiaus voroje svarbą.

Autorius indelis

Publikacijoje [P1] autorius parašė rankraštį, atliko visus lazerinio spalvinimo ir drėkinimo matavimo eksperimentus, duomenų analizę ir buvo atsakingas už rezultatų pateikimą grafikų, paveikslų, lentelių ir nuotraukų pavidalu.

Publikacijoje [P2] autorius kartu su bendraautoriais padėjo sugalvoti pirminę tyrimo idėją, atliko kai kuriuos abliacijos eksperimentus, analizavo duomenis, aptarė rezultatus ir pateikė pastabas dėl rankraščio.

Publikacijoje [P3] autorius parašė rankraštį, atliko duomenų analizę, taip pat padarė SEM, optinio ir adatinio profiliavimo prietaisų nuotraukas. Autorius taip pat buvo atsakingas už rezultatų atvaizdavimą grafikų, paveikslų ir lentelių pavidalu.

Publikacijoje [P4] autorius atliko z-skenavimo eksperimentus, analizavo duomenis ir taisė rankraštį.

Publikacijoje [PP1] autorius parašė rankraštį, atliko visus lazerinio spalvinimo ir drėkinimo matavimo eksperimentus, duomenų analizę ir buvo atsakingas už rezultatų pateikimą grafikų, paveikslų, lentelių ir nuotraukų pavidalu.

Publikacijoje [PP2] autorius padėjo sugalvoti pradinę projekto idėją, atliko paviršiaus topografijos ir paviršiaus šiurkštumo matavimus naudodamas 3D

optinį profilometrą. Taip pat analizavo gautus rezultatus, juos aptarė ir pateikė pastabas dėl rankraščio.

Publikacijų ir konferencijų sąrašas.

Disertacijos rezultatai pateikti 4 mokslinėse publikacijose [P1-P4], dvejose mokslinėje publikacijoje, kuri šiuo metu vis dar spausdinamos [PP1-PP2], ir 3 konferencijų tezėse [P5-P7]. Dar penkios mokslinės publikacijos [P8-P12] ir 2 konferencijų tezės [P13-P14] buvo parašytos, tačiau nėra susijusios su disertacija.

Disertacijos rezultatai taip pat buvo pristatyti 10 konferencijų [C1-10]. Disertacijos autorius pristatė [C1-C9] žodinius pranešimus, o [C1-C3] buvo išrinkti tarp geriausių konferencijos pranešimų. Dar 15-oje konferencijų pranešimus skaitė bendraautoriai [C10-C25], tačiau šie pranešimai nebuvo susiję su disertacija. [C17-C20] disertacijos autorius pristatė kaip stendinius pranešimus, o [C20] buvo pristatyta ir kaip žodinis pranešimas.

Eksperimentų rezultatai ir diskusija

Šis skyrelis yra paremtas keturiais moksliniais straipsniais ir trimis konferencijų tezėmis leidžiamuose periodiniuose mokslo leidiniuose turinčiuose cituojamumo rodiklį bei vienu moksliniu straipsniu, kuris šiuo metu yra priduotas į leidyklą. Eksperimentinių rezultatų ir diskusijos skyrius skirstomas į dvi pagrindines dalis: lazerinio spalvinimo ir lazerinio poliravimo.

Lazeriniam spalvinimui ištirti buvo atlikti du eksperimentai. Pirmojo eksperimento metu buvo norima išsiaiškinti, kuris voros režimas ir su kiek impulsų voroje leistų gauti didžiausią spalvų kiekį. Norint sumažinti kintamųjų skaičių, pluošto skenavimo greitis bei atstumas tarp skenuojamų linijų buvo pastovus ir atitinkamai lygus 100 mm/s ir 10 μm. Ant nerūdijančio plieno buvo skenuojamos linijos, kol buvo gautas 6×6 mm^2 nuspalvintas kvadratas. Buvo spalvinimas kvadratų masyvas, kur vertikaliai buvo keičiamas energijos įtekis nuo 0,34 J/cm^2 iki 7,6 J/cm^2, o horizontaliai impulsų skaičius vorose. Gauti rezultatai parodė, kad MHz impulsų voroje yra gaunamos vien tik rudos spalvos, GHz voroje labai mažas spalvų intervalas, o impulsų bivoroje gaunamos rudos, pilkos, geltonos, oranžinės, mėlynos, žalsvos ir violetinės spalvos. Naudojant tuos pačius parametrus bivoros režime, tačiau padidinus greitį iki 333 mm/s spalvų intervalas vėl sumažėjo. Nors pirmo eksperimento metu buvo gautas nemažas spalvų skaičius, tačiau skenavimo greitis nebuvo didelis, dėl to buvo atliktas antras eksperimentas. Antro eksperimento metu norint išlaikyti didesnes impulsų energijos vertes

buvo pasirinkta GHz impulsų vora ir energijos įtekis buvo keičiamas nuo 12,1 J/cm^2 iki 54,1 J/cm^2. Vertikaliai šiuo atveju buvo keičiamas skenavimo greitis nuo 1000 mm/s iki 4250 mm/s. Gauti rezultatai parodė, kad optimizavus impulsų skaičių GHz voroje, skenavimo greitį bei impulsų energijos įtek įmanoma gauti labai ryškias ir šviesas spalvas: geltoną, oranžinę, žydrą, mėlyną, violetinę, rausvą ir žalsvą. Taip pat, dėl didelio bandymų skaičiaus, spalvos gradientiškai pereina iš vienos į kitą. Padidinus impulsų skaičių GHz voroje iki 25, gaunamos tamsesnės spalvos. Efektyvus lazerinis spalvinimas buvo vertinamas pagal spalvinimo spartą, kurios didžiausia vertė siekė 42,5 mm^2/s, o tai mūsų žiniomis yra sparčiausias lazerinis spalvinimas mokslinėje literatūroje ant nerūdijančio plieno. Buvo atlikti ir kiti tyrimai norint padidinti lazerinio spalvinimo spartą, bet išlaikant didelį spalvų kiekį. Iš pradžių buvo tikrinami MHz ir bivoros režimai su didesniais pluošto skenavimo greičiais. Kaip ir pirmojo eksperimento metu, MHz impulsų vora leido gauti tik rudus atspalvius, tačiau bivoros atveju, buvo gautos tokios pačios bet žymiai tamsesnės spalvos, kaip ir GHz impulsų voroje. Didinant MHz impulsų skaičių bivoroje rezultatai tik prastėjo, o tai parodo, kad GHz impulsų vora yra geriausia lazeriniam spalvinimui. Taip pat buvo išbandyta keli skenavimai vienas ant kito, tačiau reikšmingų spalvų pokyčių nepastebėta. Nedidelį matomą pokytį galima paaiškinti energijos įtekio pokyčiu dėl to, kad maža dalis medžiagos abliuojama kiekvieno skenavimo metu. Paskutinis tyrimas buvo atliktas siekiant išsiaiškinti, ar galima pasiekti daugiau spalvų arba didesnę spalvinimo spartą, kai vienas ant kito naudojami skirtingi impulsų voros režimai. Kadangi naudojant MHz vorų režimą buvo gautos tik rudos spalvos, jis nebuvo išbandytas. Jei pirmiausia naudojamas GHz impulsų voros režimas, o po to bivoros režimas, gaunamos pilkos spalvos. Priešingai, jei pirmiausia naudojamas bivoros režimas, o po to – GHz vorų režimas, yra gaunamos tam tikros spalvos. Naujos spalvos nėra tokios ryškios kaip GHz impulsų voros režime, tačiau yra ryškesnės už tas, kurios gaunamos tiesiog bivoros režimu, net ir esant optimaliems parametrams. Nors, lyginant su GHz voros režimu, būtų galima pasiekti kai kurias naujas blankesnes spalvas, taikant šį metodą spalvinimo sparta būtų gerokai mažesnė, nes reikia daugkartinio skenavimo. Todėl dėl šių išvadų impulsų vorų režimų maišymas toliau nebuvo tiriamas. Buvo parodyta, kad lazerinio spalvinimo sparta priklauso nuo skenavimo greičio ir atstumo tarp skenuojamų linijų dS/dt = vh. Taigi, yra du pagrindiniai spalvinimo spartos didinimo būdai: padidinti lazerio spindulio skenavimo greitį arba atstumą tarp skenavimo linijų. Atlikti tyrimai parodė, kad net ir didėjant atstumui tarp skenavimo linijų, vis tiek galima gauti tam tikras spalvas. Tačiau spalvinimo sparta nebūtinai padidėja, nes norint gauti tas pačias spalvas, kai atstumas tarp

skenavimo linijų padvigubėja, reikia proporcingai sumažinti pluošto skenavimo greitį. Kita galimybė padidinti spalvinimo greitį galėtų būti lazerio pasikartojimo dažnio didinimas. Tai leistų naudoti didesnį skenavimo greitį, jei impulsų persidengimas yra vienas iš svarbiausių lazerinio spalvinimo parametrų. Impulsų persidengimas išliktų toks pat, jei proporcingai padidėtų ir impulsų pasikartojimo dažnis, ir impulsus skenavimo greitis. Vis dėlto gauti rezultatai rodo, kad, didinant pasikartojimo dažnį, esant tam pačiam skenavimo greičiui gaunamos tos pačios spalvos, be to, šios spalvos yra gerokai mažiau stabilios. Tai būtų galima paaiškinti tuo, kad vidinis impulsų voros pasikartojimo dažnis turi didžiausią įtaką šilumos kaupimuisi ant bandinio paviršiaus. Kadangi lazerinio spalvinimui naudojamas linijų skenavimas (angl. *hatching*), linijomis galima užpildyti bet kokią pasirinktinę formą ar figūrą. Pritaikant gautus parametrus buvo nuspalvintos įvairios figūros: du pusapskritimiai su dviem banguojančiomis linijomis viduryje, stilizuota gėlė bei Fizinių ir technologijos mokslų centro (FTMC) logotipas. Šie pavyzdžiai rodo, kad lazerinio spalvinimo metodui net ir sudėtingos formos nekelia problemų. Tačiau didelis trūkumas yra itin didelis proceso jautrumas nedideliems energijos įtekio pokyčiams. Nors lazerinė spinduliuotė yra itin stabili, ypač dėl to, kad galime naudoti dideles galias ir tuos impulsus padalinti į mažesnio atskiro energijos įtekio impulsus, vis tiek susiduriame su iššūkiais, kaip išlaikyti bandinį tiksliai židinio padėtyje. Pagrindinė problema kyla dėl šilumos kaupimosi, dėl kurio padidėja bandinio temperatūra ir atsiranda nedidelės bandinio paviršiaus deformacijos. Nors deformacijos gali būti labai mažos ir plika akimi sunkiai pastebimos, spalvų skirtumas yra lengvai pastebimas. Iš trijų būdų, kaip galima nuspalvinti metalo paviršių naudojant lazerinį spalvinimą, du iš jų galima lengvai atmesti. Kadangi nerūdijantis plienas nėra plazmoninis metalas, jame nėra matomos spalvos gaunamos dėl paviršiaus plazmonų rezonanso. Struktūrinės spalvos, atsirandančios dėl LIPSS, taip pat nėra mūsų nerūdijančio plieno bandinių spalvos priežastis. Patikrinę savo bandinį po skenuojančiu elektroniniu mikroskopu, bandinio paviršiuje nebuvo matomi LIPSS. Buvo matomos tik įvairios skirtingos nanodaleles ir nanostruktūros, kurios yra nevienodai išsidėsčiusios. Be to, struktūrinės spalvos, priklausomai nuo žiūrėjimo kampo, keičiasi nuo žalios, raudonos ir mėlynos, o mūsų gautos spalvos, priklausomai nuo žiūrėjimo kampo, tampa tik tamsesnės, tačiau spalvos nekeičia. Galiausiai yra paviršiaus oksidacija. Kadangi lazeris yra šilumos šaltinis, o įvairūs impulso vorų režimai taip pat padeda akumuliuoti šilumą apdirbimo vietoje, tai gali pagreitinti oksidacijos procesą, dėl kurio nerūdijančiojo plieno paviršiuje atsiranda skirtingos spalvos. Plonos plėvelės efektas taip pat paaiškintų, kodėl spalvos tampa gerokai tamsesnės. Kadangi spalva priklauso

nuo optinio kelio skirtumo, kuris pats savaime priklauso nuo šviesos kritimo kampo, tai paaiškina, kodėl keičiant kampą spalva tampa gerokai tamsesnė. Metalo spalvos keitimas yra norima užduotis, tačiau ją būtų galima pagerinti gaunant papildomas paviršiaus funkcijas. Metalų spalvos pakeitimas ir hidrofobizavimas būtų labai naudingas, nes spalvos taptų dar ilgaamžiškesnės, nes padėtų metalui žymiai geriau atlaikyti aplinkos poveikį. Buvo matuojamas statinis vandens drėkinimo kampas (SWCA), kiekvienas matavimas buvo atliekamas 5 kartus ir apskaičiuojamas standartinis nuokrypis. Kad paviršius būtų laikomas hidrofobiniu, jo SWCA turi būti ne mažesnis kaip 90º, o kad būtų laikomas superhidrofobiniu, SWCA turi būti didesnis kaip 150º. Nespalvotas nerūdijantis plienas nebuvo hidrofobiškas, jo drėkinimo kampas buvo 50,4 ± 4,4º. Buvo parodyta, kad visos pasiektos spalvos yra hidrofobiškos, nes jų SWCA nepriklausomai nuo spalvos atspalvio yra didesnis nei 90º. Laikotarpis tarp lazerinio spalvinimo ir drėkinimo bandymų buvo ilgesnis nei 6 mėnesiai, todėl ne tik spalvos, bet ir hidrofobiškumas yra ilgalaikis. Mėginiai buvo laikomi įprastomis oro sąlygomis patalpose ir jų būklė pastebimai nepakito.

Lazeriniam poliravimui ištirti buvo atlikti trys skirtingi eksperimentai. Atliekant lazerinio poliravimo eksperimentus buvo pastebėta, kad ant vario metalo viršaus yra oksido sluoksnis, kuris turi įtakos lazeriniam mikroapdirbimui, ir ši sąveika buvo ištirta, kad būtų įvertina įtaka lazeriniam poliravimui. Metalai yra padengti oksidų sluoksniais, kurių storis svyruoja nuo dešimčių nanometrų iki dešimčių mikrometrų ir kurie, priklausomai nuo draustinės juostos pločio, paprastai yra pusiau skaidrūs puslaidininkiai arba skaidrūs izoliatoriai. Bandinį pasiekusi lazerinė spinduliuotė pirmiausia sąveikauja su metalų oksidais, o tik po to su pačiais metalais. Vario (Cu) bandinys su vario oksido (Cu_2O) sluoksniu buvo abliuotas naudojant pikosekundinę lazerio spinduliuotę skirtingose padėtyse lyginant su pluošto sąsmaukos padėtimi. Energijos įtekio slenkstis buvo matuojamas pagal abliuoto kraterio skersmens priklausomybę nuo impulso energijos. Tiesiškai absorbuojančio oksido sluoksnio pralaidumas esant mažam smailiniam intensyvumui yra GW/cm^2 eilės ir buvo apskaičiuotas pagal $T_0 = \exp(-\alpha_0 L)$ formulę. $T_0 = 60\%$, o tai reiškia, kad sluoksnis yra pusiau neskaidrus. Cu_2O tiesinės sugerties koeficiento soties intensyvumas yra $I_s \sim 0{,}1$ TW/cm^2 ; todėl pusiau neskaidrus oksido sluoksnis staiga tampa visiškai skaidrus, kai smailinis intensyvumas viršija soties intensyvumą. Tačiau toliau didinant intensyvumą, dominuojančia tampa netiesinė sugertis, ir oksido sluoksnis vėl tampa neskaidrus. Netiesiškai sugeriantis oksido sluoksnis praleidžia tik dalį įeinančios lazerinės spinduliuotės į metalo paviršių, todėl į jį reikia atsižvelgti prognozuojant efektyvias oksido ir metalo struktūros abliacijos

charakteristikas. Esant mažam maksimaliam impulsų intensyvumui $I_0 \approx 0{,}05$ TW/cm^2, kuris yra mažesnis už soties intensyvumą $I_s \sim 0{,}1$ TW/cm^2, stebima tik tiesinė sugertis be soties ir labai maža netiesinė sugertis židinio padėtyje; todėl visose bandinio z padėtyse stebimas beveik pastovus normalizuotas pralaidumas $T/T_0 \approx 1$. Kai didžiausios intensyvumo vertės $\sim$ 0,2 TW/cm^2 viršija soties intensyvumą, oksido sluoksnis tampa beveik visiškai skaidrus $T/T_0 \approx 1{,}7$, kai bandinys yra arti židinio padėties. Kai didžiausias intensyvumas pasiekia $\sim$ 0,5 TW/cm^2 vertę, netiesinė sugertis prilygsta tiesiniam intensyvumo įsotinimui, todėl normalizuotas oksido sluoksnio pralaidumas židinio srityje pasiekia vertę, artimą $T/T_0 \approx 1$. Tiek sugerties įsisotinimas, tiek netiesinė sugertis turi įtaką efektyviam abliacijos oksido pašalinimo nuo metalo slenkstiniam energijos įtekiui, kuris naujame abliacijos modelyje gali būti išreikštas kaip $F_{\text{th.eff}} = F_{\text{th.lin}} \left(\frac{T_0}{T}\right)$. Šis modelis gerai sutampa su gautais eksperimentiniais rezultatais.

Antrojo eksperimento metu vario ir nerūdijančiojo plieno bandiniai buvo apdirbami naudojant 210 fs trukmės lazerinės spinduliuotės impulsus su 7,3 W vidutine optine galia. Ant vario ir nerūdijančiojo plieno bandinių buvo abliuojamos stačiakampio formos ertmės, kurių viršutinis matmuo buvo 2 mm × 1 mm. Atstumas tarp skenavimo linijų buvo pastovus – 10 μm, o skenavimo greitis – 333 mm/s. Bandinio padėtis buvo keičiama z kryptimi, kad būtų gautos skirtingos energijos įtekio vertės. Kiekvienas stačiakampis buvo nuskenuotas daug kartų, kad būtų pasiektas gylis, kurį būtų galima lengvai išmatuoti naudojant adatinį profilometrą. Atliekant eksperimentus su MHz ir GHz impulsų voromis, impulsų skaičius vorose buvo keičiamas atitinkamai nuo $N = 2$ iki $N = 9$ ir nuo $P = 2$ iki $P = 25$. Atliekant bivoros eksperimentą buvo išbandyti visi N ir P deriniai. Naudojant MHz impulsų voros režimą su mažais energijos įtekiais ir nedideliu impulsų skaičiumi MHz voros metu, abiejose medžiagose buvo pastebėtas didelis paviršiaus šiurkštumas. Padidinus impulsų skaičių iki 4 ir daugiau, dėl mažesnio energijos įtekio sumažėjo paviršiaus šiurkštumas dėl inkubacijos efekto, t. y. abliacijos slenksčio mažėjimo didėjant impulsų skaičiui toje pačioje vietoje, taip pat dėl šilumos akumuliacijos. Vėlesni impulsai pasiekia apdirbimo vietą medžiagoje anksčiau, nei atvėsta termiškai paveikta zona, todėl medžiagai pašalinti reikia mažiau energijos. Esant didesniems energijos įtekiais dalelių ekranavimas taip pat turėjo didesnį neigiamą poveikį išsklaidant ir sugeriant įeinančią lazerio spinduliuotę, todėl padidėjo paviršiaus šiurkštumas. Mažiausias vario paviršiaus šiurkštumas buvo 0,23 μm, o nerūdijančio plieno – 0,63 μm. Geriausi rezultatai buvo pasiekti naudojant GHz impulsų vorą, nes, esant plačiam energijos įtekių ir impulsų skaičiaus intervalo, vario paviršiaus

šiurkštumas buvo labai mažas < 0,15 µm. Šis voros režimas dėl trumpo pasikartojimo dažnio efektyviau išnaudoja šilumos akumuliacija. Mažiausias vario paviršiaus šiurkštumas buvo 0,1 µm, o nerūdijančiojo plieno – 0,55 µm. Panašūs rezultatai buvo gauti ir naudojant bivoros režimą, kai mažiausias paviršiaus šiurkštumas buvo 0,08 µm variui ir 0,45 µm nerūdijančiajam plienui.

Trečiasis eksperimentas buvo atliktas todėl, kad iš ankstesnių eksperimentų matėme, jog efektyvi abliacija turi bistabilumą, o nelyginio skaičiaus impulsai yra daug efektyvesni, ypač 3 impulsai MHz voroje. Norėta patikrinti, ar taip pat yra ir poliravimo lazeriu atveju. Eksperimentiškai buvo ištirta lazeriu abliuoto ertmės dugno paviršiaus šiurkštumo R_a priklausomybė nuo energijos įtekio, kai impulsų vorų energijos įtekis buvo keistas nuo 0,52 iki 9,9 J/cm^2, o impulsų skaičius MHz voroje nuo 1 iki 9. Eksperimentas parodė, kad paviršiaus šiurkštumas R_a priklausomai nuo lazerinio apdirbimo parametrų yra bistabilus. Daugeliu atvejų paviršiaus šiurkštumas R_a buvo šiek tiek mažesnis esant lyginiam nei nelyginiam impulsų skaičiui voroje, jei lyginsime su tuo pačiu voros energijos įtekiu esant didelėms vertėms (2,3 J/cm^2 – 9,9 J/cm^2). Tačiau esant mažoms energijos įtekio vertėms (0,52 J/cm^2 – 1,7 J/cm^2) galima pastebėti priešingą efektą, kai paviršiaus šiurkštumas R_a yra mažesnis esant nelyginiam nei lyginiam impulsų skaičiui voroje. Pavyzdžiui, $N = 8$ atveju paviršiaus šiurkštumas R_a buvo šiek tiek didesnis nei $N = 9$ ties keliomis energijos įtekio vertėmis, o likusioms energijos įtekio vertėms yra šiek tiek mažesnės, santykinis šiurkštumo skirtumas buvo tik 2 %. $N = 6$ atveju paviršiaus šiurkštumas R_a buvo šiek tiek mažesnis nei $N = 7$, kai energijos įtekio vertės svyravo nuo 1,7 iki 4,6 J/cm^2. Vidutinis santykinis paviršiaus šiurkštumo R_a skirtumas padidėjo iki 39%. Šį abliacijos režimą galima vadinti bistabiliu režimu. Be to, esant $N = 4$ ir $N = 5$ stebimas bistabilus paviršiaus šiurkštumas R_a nuo 1,7 J/cm^2 iki 9,9 J/cm^2. Vidutinis santykinio paviršiaus šiurkštumo skirtumas buvo 18%. Daugumoje mokslinių darbų pagrindinėmis abliacijos efektyvumo bistabilumo priežastimis, priklausomai nuo impulsų skaičiaus voroje, buvo įvardytos dalelių ekranavimas arba pakartotinis nusodinimas. Šie procesai ypač matomi esant antram impulsui impulsų voroje, nes pirmo impulso išabliuotų medžiagų debesis nespėja pasitraukti iš apdirbimo vietos ir ekranuoja antrą impulsą.

Pagrindiniai rezultatai ir išvados

1. Buvo įrodyta, kad visi impulsų voros režimai: MHz, GHz ir bivoros režimas gali būti naudojami gauti spalvas ant nerūdijančio plieno. MHz impulsų voros režimas pasižymi tik ruda spalva, o GHz - dideliu ryškių spalvų intervalu.

2. Buvo pasiekta didžiausia mokslinėje literatūroje nurodoma lazerinio spalvinimo sparta 42,5 mm^2/s ant nerūdijančio plieno, kai spalvos gaunamas dėl oksidacijos efekto.

3. Kadangi lazerinis spalvinimas paremtas linijų skenavimu (angl. *hatching*), buvo parodyta, kad galima skirtingomis spalvomis nuspalvinti bet kokios sudėtingos formos figūrą.

4. Buvo išbandyti įvairūs lazerinio apdirbimo parametrai, įskaitant: atstumą tarp linijų, impulsų pasikartojimo dažnį, skenavimų skaičių ir impulsų vorų maišymą, tačiau nebuvo gautas reikšmingas naujų spalvų kiekis ar padidinta spalvinimo sparta.

5. Kadangi buvo naudojami femtosekundiniai impulsai, ant spalvotas nerūdijančio plieno paviršius buvo matomi nanodariniai, dėl kurių lazerio apdirbtų spalvotų metalų paviršių drėkinimo kampas buvo virš 90 laipsnių, kas parodo jų hidrofobiškumo savybes ir padidina jų pritaikomumą.

6 Buv parodyta vario bandinių pilkosios skalės (angl. *grayscale*) spalvinimas ir drėkinimo kampo kontrolė.

7. Buvo pademonstruota, kad ant vario esantis vario oksido sluoksnis slopina varį pasiekiančią lazerinę spinduliuotę, o tai turi įtakos oksido/metalo struktūros lazerinio atsiskyrimo slenksčiui, priklausomai nuo fokusavimo padėties ir su ja susijusiu lazerio smailiniu intensyvumu impulse.

8. Naudojant MHz, GHz ir bivoros režimus buvo atitinkamai pasiektas 0,23 µm, 0,1 µm ir 0,08 µm vario paviršiaus šiurkštumas, o nerūdijančiojo plieno mažiausias paviršiaus šiurkštumas atitinkamai buvo 0,63 µm, 0,55 µm ir 0,45 µm. Nerūdijančiojo plieno paviršiaus šiurkštumas buvo didesnis dėl didžiausio pradinio bandinio šiurkštumo.

9. GHz impulsų voros režimu gautas mažiausias vidutinis paviršiaus šiurkštumas R_a, ypač vario, kuris buvo < 0,15 µm daugelio impulsų verčių, dėl geresnio šilumos akumuliacijos panaudojimo.

10. Buvo parodyta, kad esant efektyviai lazerinei abliacijai, dėl dalelių ekranavimo ir pakartotinio nusodinimo efektų galima pastebėti paviršiaus šiurkštumo R_a bistabilumą priklausomai nuo impulsų skaičiaus voroje.

PADĖKA

Norėčiau padėkoti FTMC Lazerinių technologijų skyriaus (LTS) vadovui dr. Gediminui Račiukaičiui, kad prieš 8 metus atrašė į bakalauro elektroninį laišką ir priėmė į savo skyrių. Taip pat ačiū Lazerinio mikroapdirbimo technologijų laboratorijos vadovui dr. Pauliui Gečiui už pagalbą, kai jos prireikdavo.

Didžiausia padėka doktorantūros vadovui dr. Mindaugui Gedvilui, kad sutiko priimti mane kaip studentą jau nuo trečio bakalauro kurso ir nuo pirmų dienų mokė savarankiško ir kokybiško mokslinio darbo. Be jo tikrai nebūčiau pasiekęs tokių rezultatų.

Ačiū kolegoms – Juozui, Justui, Klemensui, Rodrigui, Laimiui, Miglei, Kerniui, Vitai, Andriui, Evaldui, Edgarui, Simonui, Karoliui – esantiems LTS ir už LTS sienų už smagiai praleistą laiką, juoką ir begalinius klausimus, kada bus parašyta disertacija.

Taip pat ačiū visai šeimai, draugams ir ypatingai mamai, už nuolatinį ir begalinį palaikymą bei skundų išklausymą.

REFERENCE LIST

[1] S. Mishra and V. Yadava, Laser Beam MicroMachining (LBMM) – A review, Opt. Lasers Eng. **73**(6), 89–122 (2015).

[2] M. Radovanovic and M. Madic, Experimental investigations of CO2 laser cut quality: a review, Rev. Tehnol. Neconv. **15**(4), 35 (2011).

[3] D. Lee, R. Patwa, H. Herfurth, and J. Mazumder, Computational and experimental studies of laser cutting of the current collectors for lithium-ion batteries, J. Power Sources **210**, 327–338 (2012).

[4] A. Riveiro, F. Quintero, F. Lusquiños, R. Comesaña, and J. Pou, Effects of processing parameters on laser cutting of aluminium–copper alloys using off-axial supersonic nozzles, Appl. Surf. Sci. **257**(12), 5393–5397 (2011).

[5] D. Lee, R. Patwa, H. Herfurth, and J. Mazumder, High speed remote laser cutting of electrodes for lithium-ion batteries: Anode, J. Power Sources **240**, 368–380 (2013).

[6] A. Weck, T. H. R. H. R. Crawford, D. S. S. Wilkinson, H. K. K. Haugen, and J. S. S. Preston, Laser drilling of high aspect ratio holes in copper with femtosecond, picosecond and nanosecond pulses, Appl. Phys. A Mater. Sci. Process. **90**(3), 537–543 (2008).

[7] G. Zhou, W. Li, Q. Xiang, W. He, S. Wang, Y. Chen, Y. Hong, W. Yang, M. Lai, S. Chen, and H. Xu, Copper induced direct CO2 laser drilling blind hole with the aid of brown oxidation for PCB CCL, Appl. Surf. Sci. **479**(2), 512–518 (2019).

[8] X. Jia, Y. Zhang, Y. Chen, H. Wang, G. Zhu, and X. Zhu, Combined pulsed laser drilling of metal by continuous wave laser and nanosecond pulse train, Int. J. Adv. Manuf. Technol. **104**(1–4), 1269–1274 (2019).

[9] A. Žemaitis, M. Gaidys, P. Gečys, G. Račiukaitis, and M. Gedvilas, Rapid high-quality 3D micro-machining by optimised efficient ultrashort laser ablation, Opt. Lasers Eng. **114**(4), 83–89 (2019).

[10] M. Gaidys, A. Žemaitis, P. Gečys, and M. Gedvilas, Efficient picosecond laser ablation of copper cylinders, Appl. Surf. Sci. **483**(3), 962–966 (2019).

[11] H. Liu, W. Lin, and M. Hong, Surface coloring by laser irradiation of solid substrates, APL Photonics **4**(5), 051101 (2019).

[12] D. P. Adams, V. C. Hodges, D. A. Hirschfeld, M. A. Rodriguez, J. P. McDonald, and P. G. Kotula, Nanosecond pulsed laser irradiation of stainless steel 304L: Oxide growth and effects on underlying metal, Surf. Coatings Technol. **222**(l), 1–8 (2013).

[13] Y. Lu, X. Shi, Z. Huang, T. Li, M. Zhang, J. Czajkowski, T. Fabritius, M. Huttula, and W. Cao, Nanosecond laser coloration on stainless steel surface, Sci. Rep. **7**(1), 7092 (2017).

[14] V. Veiko, G. Odintsova, E. Ageev, Y. Karlagina, A. Loginov, A. Skuratova, and E. Gorbunova, Controlled oxide films formation by nanosecond laser pulses for color marking, Opt. Express **22**(20), 24342

(2014).
[15] P. Shukla, D. G. Waugh, J. Lawrence, and R. Vilar, "Laser surface structuring of ceramics, metals and polymers for biomedical applications," in *Laser Surface Modification of Biomaterials* (Elsevier, 2016), pp. 281–299.
[16] Y. C. Guan, W. Zhou, Z. L. Li, H. Y. Zheng, G. C. Lim, and M. H. Hong, Femtosecond laser-induced ripple structures on magnesium, Appl. Phys. A **115**(1), 13–18 (2014).
[17] S. Sakabe, M. Hashida, S. Tokita, S. Namba, and K. Okamuro, Mechanism for self-formation of periodic grating structures on a metal surface by a femtosecond laser pulse, Phys. Rev. B **79**(3), 033409 (2009).
[18] G. Li, J. Li, L. Yang, X. Li, Y. Hu, J. Chu, and W. Huang, Evolution of aluminum surface irradiated by femtosecond laser pulses with different pulse overlaps, Appl. Surf. Sci. **276**, 203–209 (2013).
[19] J. Z. Zhang and C. Noguez, Plasmonic Optical Properties and Applications of Metal Nanostructures, Plasmonics **3**(4), 127–150 (2008).
[20] P. Fan, M. Zhong, L. Li, P. Schmitz, C. Lin, J. Long, and H. Zhang, Angle-independent colorization of copper surfaces by simultaneous generation of picosecond-laser-induced nanostructures and redeposited nanoparticles, J. Appl. Phys. **115**(12), 124302 (2014).
[21] A. Y. Vorobyev and C. Guo, Direct femtosecond laser surface nano/microstructuring and its applications, Laser Photon. Rev. **7**(3), 385–407 (2013).
[22] K. C. Phillips, H. H. Gandhi, E. Mazur, and S. K. Sundaram, Ultrafast laser processing of materials: a review, Adv. Opt. Photonics **7**(4), 684 (2015).
[23] A. Žemaitis, M. Gaidys, M. Brikas, P. Gečys, G. Račiukaitis, and M. Gedvilas, Advanced laser scanning for highly-efficient ablation and ultrafast surface structuring: experiment and model, Sci. Rep. **8**(1), 17376 (2018).
[24] P. Elahi, H. Kalaycioğlu, Ö. Akçaalan, Ç. Şenel, and F. Ömer Ilday, Burst-mode thulium all-fiber laser delivering femtosecond pulses at a 1 GHz intra-burst repetition rate, Opt. Lett. **42**(19), 3808 (2017).
[25] A. Žemaitis, P. Gečys, M. Barkauskas, G. Račiukaitis, and M. Gedvilas, Highly-efficient laser ablation of copper by bursts of ultrashort tuneable (fs-ps) pulses, Sci. Rep. **9**(1), 12280 (2019).
[26] A. Žemaitis, M. Gaidys, P. Gečys, M. Barkauskas, and M. Gedvilas, Femtosecond laser ablation by bibursts in the MHz and GHz pulse repetition rates, Opt. Express **29**(5), 7641 (2021).
[27] B. Jaeggi, S. Remund, R. Streubel, B. Goekce, S. Barcikowski, and B. Neuenschwander, Laser Micromachining of Metals with Ultra-Short Pulses: Factors Limiting the Scale-Up Process, J. Laser Micro/Nanoengineering **12**(3), 267–273 (2017).

[28] X. Wolters, G. Bonamis, K. Mishchick, E. Audouard, C. Hönninger, and E. Mottay, High power GHz femtosecond laser for ablation efficiency increase, Procedia Manuf. **36**(3), 200–207 (2019).
[29] M. Zhong and J. Long, "Laser Surface Structuring of Metals and Functionalization," in *Handbook of Laser Micro- and Nano-Engineering* (Springer International Publishing, 2020), pp. 1–38.
[30] S. I. Anisimov, B. L. Kapeliovich, and T. L. Perel'man, "Electron emission from metal surfaces exposed to ultrashort laser pulses," in *Sov. Phys.* (1974), **39**(2), pp. 375–377.
[31] M. Stafe, A. Marcu, and N. N. Puscas, *Pulsed Laser Ablation of Solids* (2014).
[32] B. Jaeggi, B. Neuenschwander, J. Zuercher, T. Meier, M. Zimmermann, and G. Hennig, High precision and high surface structuring by synchronizing mechanical axes with an ultrashort pulsed laser system in MOPA arrangement, Proc. ICALEO **41**(0), 1046–1053 (2012).
[33] D. T. Pham, S. S. Dimov, P. V Petkov, and S. P. Petkov, Laser milling, Proc. Inst. Mech. Eng. Part B J. Eng. Manuf. **216**(5), 657–667 (2002).
[34] W. Kautek and J. Krueger, "Femtosecond pulse laser ablation of metallic, semiconducting, ceramic, and biological materials," in *Laser Materials Processing: Industrial and Microelectronics Applications*, E. Beyer, M. Cantello, A. V. La Rocca, L. D. Laude, F. O. Olsen, and G. Sepold, eds. (1994), **2207**, p. 600.
[35] G. Paltauf and P. E. Dyer, Photomechanical Processes and Effects in Ablation, Chem. Rev. **103**(2), 487–518 (2003).
[36] R. Kelly and A. Miotello, Comments on explosive mechanisms of laser sputtering, Appl. Surf. Sci. **96**–**98**, 205–215 (1996).
[37] C. Wu and L. V. Zhigilei, Microscopic mechanisms of laser spallation and ablation of metal targets from large-scale molecular dynamics simulations, Appl. Phys. A **114**(1), 11–32 (2014).
[38] C. Kerse, H. Kalaycıoğlu, P. Elahi, B. Çetin, D. K. Kesim, Ö. Akçaalan, S. Yavaş, M. D. Aşık, B. Öktem, H. Hoogland, R. Holzwarth, and F. Ö. Ilday, Ablation-cooled material removal with ultrafast bursts of pulses, Nature **537**(7618), 84–88 (2016).
[39] A. Ancona, F. Röser, K. Rademaker, J. Limpert, S. Nolte, and A. Tünnermann, High speed laser drilling of metals using a high repetition rate, high average power ultrafast fiber CPA system., Opt. Express **16**(12), 8958–68 (2008).
[40] T. Kramer, Increasing the Specific Removal Rate for Ultra Short Pulsed Laser-Micromachining by Using Pulse Bursts, J. Laser Micro/Nanoengineering **12**(2), 107–114 (2017).
[41] D. J. Förster, S. Faas, S. Gröninger, F. Bauer, A. Michalowski, R. Weber, and T. Graf, Shielding effects and re-deposition of material during processing of metals with bursts of ultra-short laser pulses, Appl. Surf. Sci. **440**, 926–931 (2018).

[42] S. M. Remund, M. Gafner, M. V. Chaja, A. Urniezius, S. Butkus, and B. Neuenschwander, Milling applications with GHz burst: Investigations concerning the removal rate and machining quality, Procedia CIRP **94**, 850–855 (2020).
[43] G. Napoli, A. Di Schino, M. Paura, and T. Vela, Colouring titanium alloys by anodic oxidation, Metalurgija **57**(1–2), 111–113 (2018).
[44] C. J. Donahue and J. A. Exline, Anodizing and Coloring Aluminum Alloys, J. Chem. Educ. **91**(5), 711–715 (2014).
[45] V. Zalyhina, V. Cheprasova, V. Belyaeva, and V. Romanovski, Pigments from spent Zn, Ni, Cu, and Cd electrolytes from electroplating industry, Environ. Sci. Pollut. Res. **28**(25), 32660–32668 (2021).
[46] W. Giurlani, F. Gambinossi, E. Salvietti, M. Passaponti, and M. Innocenti, Color Measurements in Electroplating Industry: Implications for Product Quality Control, ECS Trans. **80**(10), 757–766 (2017).
[47] W. Giurlani, G. Zangari, F. Gambinossi, M. Passaponti, E. Salvietti, F. Di Benedetto, S. Caporali, and M. Innocenti, Electroplating for Decorative Applications: Recent Trends in Research and Development, Coatings **8**(8), 260 (2018).
[48] F. J. Maile, G. Pfaff, and P. Reynders, Effect pigments—past, present and future, Prog. Org. Coatings **54**(3), 150–163 (2005).
[49] S. C. Cha and A. Erdemir, *Coating Technology for Vehicle Applications* (Springer International Publishing, 2015).
[50] B. Gilmour and A. Giumlia-Mair, What Did Iron Really Look Like? Patination and Coloring Treatments on Iron and Steel, Mater. Manuf. Process. **24**(9), 999–1006 (2009).
[51] T. Letsou, M. ElKabbash, S. Iram, M. Hinczewski, and G. Strangi, Heat-induced perfect light absorption in thin-film metasurfaces for structural coloring, Opt. Mater. Express **9**(3), 1386 (2019).
[52] G. T. Alliott, R. L. Higginson, and G. D. Wilcox, Producing a thin coloured film on stainless steels – a review. Part 1: electrochemical processes, Trans. IMF **100**(3), 128–137 (2022).
[53] S. John, A. Perumal, and B. A. Shenoi, Chemical colouring of aluminium, Surf. Technol. **22**(1), 15–20 (1984).
[54] X. Ma, X. Nie, J. Zhao, P. Shrotriya, Y. Zhang, Y. Cui, and J. Wang, Effect of nanosecond pulsed laser parameters on the color making of 304 stainless steel, Opt. Laser Technol. **126**(2), 106104 (2020).
[55] A. J. Antończak, D. Kocoń, M. Nowak, P. Kozioł, and K. M. Abramski, Laser-induced colour marking—Sensitivity scaling for a stainless steel, Appl. Surf. Sci. **264**, 229–236 (2013).
[56] M. Gaidys, A. Selskis, P. Gečys, and M. Gedvilas, Stainless steel colouring using burst and biburst mode ultrafast laser irradiation, Opt. Laser Technol. **174**(9), 110561 (2024).
[57] Z. L. Li, H. Y. Zheng, K. M. Teh, Y. C. Liu, G. C. Lim, H. L. Seng,

and N. L. Yakovlev, Analysis of oxide formation induced by UV laser coloration of stainless steel, Appl. Surf. Sci. **256**(5), 1582–1588 (2009).
[58] X. Ma, X. Nie, J. Zhao, Y. Han, P. Shrotriya, Y. Wang, and J. Guo, Coloring stability analysis of nanosecond pulsed laser induced surface coloring on stainless steel, Opt. Laser Technol. **123**(10), 105936 (2020).
[59] Y. F. Xiang, R. L. Mei, F. Azad, L. Z. Zhao, S. C. Su, G. G. Lu, and S. P. Wang, Investigation by nanosecond fiber laser for hybrid color marking and its potential application, Opt. Laser Technol. **147**(1), 107553 (2022).
[60] H. Roozbahani, M. Alizadeh, H. Handroos, and A. Salminen, Color Laser Marking: Repeatability, Stability and Resistance against Mechanical, Chemical and Environmental Effects, IEEE Access **8**, 214196–214208 (2020).
[61] D. P. Adams, R. D. Murphy, D. J. Saiz, D. A. Hirschfeld, M. A. Rodriguez, P. G. Kotula, and B. H. Jared, Nanosecond pulsed laser irradiation of titanium: Oxide growth and effects on underlying metal, Surf. Coatings Technol. **248**(7), 38–45 (2014).
[62] X. Sun, W. Wang, X. Mei, A. Pan, Y. Chen, and J. Cui, High capacity color code prepared on titanium alloy using femtosecond laser, Opt. Laser Technol. **145**, 107521 (2022).
[63] A. Pérez del Pino, P. Serra, and J. . Morenza, Oxidation of titanium through Nd:YAG laser irradiation, Appl. Surf. Sci. **197**–**198**, 887–890 (2002).
[64] A. Pérez del Pino, P. Serra, and J. . Morenza, Coloring of titanium by pulsed laser processing in air, Thin Solid Films **415**(1–2), 201–205 (2002).
[65] V. Veiko, G. Odintsova, E. Vlasova, Y. Andreeva, A. Krivonosov, E. Ageev, and E. Gorbunova, Laser coloration of titanium films: New development for jewelry and decoration, Opt. Laser Technol. **93**(93), 9–13 (2017).
[66] J. Long, P. Fan, M. Zhong, H. Zhang, Y. Xie, and C. Lin, Superhydrophobic and colorful copper surfaces fabricated by picosecond laser induced periodic nanostructures, Appl. Surf. Sci. **311**, 461–467 (2014).
[67] Z. Ou, M. Huang, and F. Zhao, Colorizing pure copper surface by ultrafast laser-induced near-subwavelength ripples, Opt. Express **22**(14), 17254 (2014).
[68] G. Killaire, J. Walia, S. Rashid, P. Berini, and A. Weck, Structural and oxide-based colours on laser textured copper, Appl. Surf. Sci. **583**(11), 152440 (2022).
[69] A. Y. Vorobyev and C. Guo, Colorizing metals with femtosecond laser pulses, Appl. Phys. Lett. **92**(4), 041914 (2008).
[70] Y. F. Lu and H. Qiu, Laser coloration and bleaching of amorphous

WO3 thin film, J. Appl. Phys. **88**(2), 1082–1087 (2000).
[71] A. Y. Vorobyev and C. Guo, Spectral and polarization responses of femtosecond laser-induced periodic surface structures on metals, J. Appl. Phys. **103**(4), 16–19 (2008).
[72] A. V. Dostovalov, T. J. Y. Derrien, S. A. Lizunov, F. Přeučil, K. A. Okotrub, T. Mocek, V. P. Korolkov, S. A. Babin, and N. M. Bulgakova, LIPSS on thin metallic films: New insights from multiplicity of laser-excited electromagnetic modes and efficiency of metal oxidation, Appl. Surf. Sci. **491**(3), 650–658 (2019).
[73] J.-M. Guay, A. Calà Lesina, G. Côté, M. Charron, D. Poitras, L. Ramunno, P. Berini, and A. Weck, Laser-induced plasmonic colours on metals, Nat. Commun. **8**(1), 16095 (2017).
[74] N. G. Henriksen, K. Poulios, M. A. J. Somers, and T. L. Christiansen, Impact of Laser Marking on Microstructure and Fatigue Life of Medical Grade Titanium, SSRN Electron. J. **873**(2), 145020 (2023).
[75] J. Yao, C. Zhang, H. Liu, Q. Dai, L. Wu, S. Lan, A. V. Gopal, V. A. Trofimov, and T. M. Lysak, Selective appearance of several laser-induced periodic surface structure patterns on a metal surface using structural colors produced by femtosecond laser pulses, Appl. Surf. Sci. **258**(19), 7625–7632 (2012).
[76] E. H. Amara, F. Haïd, and A. Noukaz, Experimental investigations on fiber laser color marking of steels, Appl. Surf. Sci. **351**(2), 1–12 (2015).
[77] L. Nánai, R. Vajtai, and T. F. George, Laser-induced oxidation of metals: state of the art, Thin Solid Films **298**(1–2), 160–164 (1997).
[78] C. Langlade, A. B. Vannes, J. M. Krafft, and J. R. Martin, Surface modification and tribological behaviour of titanium and titanium alloys after YAG-laser treatments, Surf. Coatings Technol. **100**–**101**(1–3), 383–387 (1998).
[79] L. Lavisse, J. M. Jouvard, L. Imhoff, O. Heintz, J. Korntheuer, C. Langlade, S. Bourgeois, and M. C. M. de Lucas, Pulsed laser growth and characterization of thin films on titanium substrates, Appl. Surf. Sci. **253**(19), 8226–8230 (2007).
[80] H. Y. Zheng, G. C. Lim, X. C. Wang, J. L. Tan, and J. Hilfiker, Process study for laser-induced surface coloration, J. Laser Appl. **14**(4), 215–220 (2002).
[81] F. Luo, W. Ong, Y. Guan, F. Li, S. Sun, G. C. Lim, and M. Hong, Study of micro/nanostructures formed by a nanosecond laser in gaseous environments for stainless steel surface coloring, Appl. Surf. Sci. **328**(5), 405–409 (2015).
[82] K. Tse and J. Robertson, Work function control at metal high-dielectric-constant gate oxide interfaces, Microelectron. Eng. **85**(1), 9–14 (2008).
[83] V. Veiko, G. Odintsova, E. Gorbunova, E. Ageev, A. Shimko, Y. Karlagina, and Y. Andreeva, Development of complete color palette

based on spectrophotometric measurements of steel oxidation results for enhancement of color laser marking technology, Mater. Des. **89**(11), 684–688 (2016).

[84] A. M. Carey, W. M. Steen, and D. Watkins, "Laser-surface ornamentation," in *International Congress on Applications of Lasers & Electro-Optics* (Laser Institute of America, 1998), **1998**(1), pp. D170–D179.

[85] S. O'Hana, A. J. Pinkerton, K. Shoba, A. W. Gale, and L. Li, Laser surface colouring of titanium for contemporary jewellery, Surf. Eng. **24**(2), 147–153 (2008).

[86] A. R. Parker, 515 million years of structural colour, J. Opt. A Pure Appl. Opt. **2**(6), R15–R28 (2000).

[87] J. Bonse, J. Krüger, S. Höhm, and A. Rosenfeld, Femtosecond laser-induced aperiodic surface structures, J. Laser Appl. **24**(4), 042006 (2012).

[88] J. Bonse, S. Hohm, S. V. Kirner, A. Rosenfeld, and J. Kruger, Laser-Induced Periodic Surface Structures-A Scientific Evergreen, IEEE J. Sel. Top. Quantum Electron. **23**(3), 109–123 (2017).

[89] A. A. Ionin, S. I. Kudryashov, S. V. Makarov, L. V. Seleznev, D. V. Sinitsyn, E. V. Golosov, O. A. Golosova, Y. R. Kolobov, and A. E. Ligachev, Femtosecond laser color marking of metal and semiconductor surfaces, Appl. Phys. A **107**(2), 301–305 (2012).

[90] S. Zhang, Y. Wang, H. Wang, L. Zhong, X. Zhu, G. Zhu, J. Qiu, and X. Zeng, Laser Writing of Multilayer Structural Colors for Full-Color Marking on Steel, Adv. Photonics Res. **5**(1), 1–9 (2024).

[91] T. Karkantonis, A. Gaddam, X. Tao, T. L. See, and S. Dimov, The influence of processing environment on laser-induced periodic surface structures generated with green nanosecond laser, Surfaces and Interfaces **31**(6), 102096 (2022).

[92] W. Liu, J. Hu, L. Jiang, J. Huang, J. Lu, J. Yin, Z. Qiu, H. Liu, C. Li, S. Wang, and S. Wang, Formation of laser-induced periodic surface nanometric concentric ring structures on silicon surfaces through single-spot irradiation with orthogonally polarized femtosecond laser double-pulse sequences, Nanophotonics **10**(4), 1273–1283 (2021).

[93] A. V. Zayats, I. I. Smolyaninov, and A. A. Maradudin, Nano-optics of surface plasmon polaritons, Phys. Rep. **408**(3–4), 131–314 (2005).

[94] X. Shi and X. Xu, Laser fluence dependence of ripple formation on fused silica by femtosecond laser irradiation, Appl. Phys. A **125**(4), 256 (2019).

[95] J. Tong, F. Suo, J. Ma, L. Y. M. Tobing, L. Qian, and D. Hua Zhang, Surface plasmon enhanced infrared photodetection, Opto-Electronic Adv. **2**(1), 18002601–18002610 (2019).

[96] A. Sassmannshausen, A. Brenner, and J. Finger, Ultrashort pulse laser polishing by continuous surface melting, J. Mater. Process. Technol. **293**(1), 117058 (2021).

[97] A. Krishnan and F. Fang, Review on mechanism and process of surface polishing using lasers, Front. Mech. Eng. **14**(3), 299–319 (2019).
[98] J. Pong-Ryol, J. Tae-Sok, K. Nam-Chol, F. Xing, and J. Kum-Hyok, Laser micro-polishing for metallic surface using UV nano-second pulse laser and CW laser, Int. J. Adv. Manuf. Technol. **85**(9–12), 2367–2375 (2016).
[99] S. Mohajerani, J. D. Miller, O. R. Tutunea-Fatan, and E. V. Bordatchev, Thermo-Physical Modelling of Track Width During Laser Polishing of H13 Tool Steel, Procedia Manuf. **10**, 708–719 (2017).
[100] F. Bauer, A. Michalowski, T. Kiedrowski, and S. Nolte, Heat accumulation in ultra-short pulsed scanning laser ablation of metals, Opt. Express **23**(2), 1035 (2015).
[101] P. Lickschat, A. Demba, and S. Weissmantel, Ablation of steel using picosecond laser pulses in burst mode, Appl. Phys. A **123**(2), 137 (2017).
[102] A. Michalowski, F. Nyenhuis, and G. Kunz, Smooth Surfaces by Pulsed Laser Processing with Bursts, PhotonicsViews **17**(3), 42–45 (2020).
[103] T. Herrmann, F. Harth, B. Henrich, J. L'huillier, and M. Hajri, How to Improve Efficiency in USP Laser Micromachining, Laser Tech. J. **13**(1), 16–19 (2016).
[104] W. dos Santos Motta Neto, J. E. S. Leal, L. J. Arantes, and R. V. Arencibia, The effect of stylus tip radius on Ra, Rq, Rp, Rv, and Rt parameters in turned and milled samples, Int. J. Adv. Manuf. Technol. **99**(5–8), 1979–1992 (2018).
[105] J. Dobes, J. E. S. Leal, J. Profeta, M. M. de Sousa, F. P. L. Neto, A. Piratelli-Filho, and R. V. Arencibia, Effect of mechanical vibration on Ra, Rq, Rz, and Rt roughness parameters, Int. J. Adv. Manuf. Technol. **92**(1–4), 393–406 (2017).
[106] R. B and R. B, Review of Surface Roughness Prediction in Machining Process by Using various Parameters, Int. J. Recent TRENDS Eng. Res. **06**(01), 7–12 (2020).
[107] L. Chen, B. Richter, X. Zhang, K. B. Bertsch, D. J. Thoma, and F. E. Pfefferkorn, Effect of laser polishing on the microstructure and mechanical properties of stainless steel 316L fabricated by laser powder bed fusion, Mater. Sci. Eng. A **802**(June 2020), 140579 (2021).
[108] D.-H. Lee and N.-G. Cho, Assessment of surface profile data acquired by a stylus profilometer, Meas. Sci. Technol. **23**(10), 105601 (2012).
[109] J. Park, K. Kwon, and N. Cho, Development of a coordinate measuring machine (CMM) touch probe using a multi-axis force sensor, Meas. Sci. Technol. **17**(9), 2380–2386 (2006).
[110] R. Ostholt, E. Willenborg, and K. Wissenbach, "Laser polishing of metallic freeform surfaces," in *International Congress on Applications of Lasers & Electro-Optics* (Laser Institute of America, 2010), **103**(March), pp. 597–603.

[111] S. Marimuthu, A. Triantaphyllou, M. Antar, D. Wimpenny, H. Morton, and M. Beard, Laser polishing of selective laser melted components, Int. J. Mach. Tools Manuf. **95**, 97–104 (2015).
[112] H. Sun, Thin lens equation for a real laser beam with weak lens aperture truncation, Opt. Eng. **37**(11), 2906 (1998).
[113] C. A. Schneider, W. S. Rasband, and K. W. Eliceiri, NIH Image to ImageJ: 25 years of image analysis, Nat. Methods **9**(7), 671–675 (2012).
[114] A. F. Stalder, T. Melchior, M. Müller, D. Sage, T. Blu, and M. Unser, Low-bond axisymmetric drop shape analysis for surface tension and contact angle measurements of sessile drops, Colloids Surfaces A Physicochem. Eng. Asp. **364**(1–3), 72–81 (2010).
[115] J.-M. Guay, G. Killaire, P. G. Gordon, S. T. Barry, P. Berini, and A. Weck, Passivation of Plasmonic Colors on Bulk Silver by Atomic Layer Deposition of Aluminum Oxide, Langmuir **34**(17), 4998–5010 (2018).
[116] J. Geng, L. Xu, W. Yan, L. Shi, and M. Qiu, High-speed laser writing of structural colors for full-color inkless printing, Nat. Commun. **14**(1), 565 (2023).
[117] S. N. Chowdhury, P. Nyga, Z. A. Kudyshev, E. Garcia Bravo, A. S. Lagutchev, A. V. Kildishev, V. M. Shalaev, and A. Boltasseva, Lithography-Free Plasmonic Color Printing with Femtosecond Laser on Semicontinuous Silver Films, ACS Photonics **8**(2), 521–530 (2021).
[118] A. Schkutow and T. Frick, Laser color marking of stainless steel – Investigation of the fluence-dependent and thermal mechanisms in generating laser induced surface modifications, Procedia CIRP **124**(9), 661–664 (2024).
[119] A. Y. Vorobyev and C. Guo, Multifunctional surfaces produced by femtosecond laser pulses, J. Appl. Phys. **117**(3), 1033–1040 (2015).
[120] C.-Y. Zhang, J.-W. Yao, H.-Y. Liu, Q.-F. Dai, L.-J. Wu, S. Lan, V. A. Trofimov, and T. M. Lysak, Colorizing silicon surface with regular nanohole arrays induced by femtosecond laser pulses, Opt. Lett. **37**(6), 1106 (2012).
[121] G. Li, J. Li, Y. Hu, C. Zhang, X. Li, J. Chu, and W. Huang, Femtosecond laser color marking stainless steel surface with different wavelengths, Appl. Phys. A **118**(4), 1189–1196 (2015).
[122] B. Dusser, Z. Sagan, H. Soder, N. Faure, J. P. Colombier, M. Jourlin, and E. Audouard, Controlled nanostructrures formation by ultra fast laser pulses for color marking, Opt. Express **18**(3), 2913 (2010).
[123] R. Fürbacher, G. Liedl, and A. Otto, Fast transition from hydrophilic to superhydrophobic, icephobic properties of stainless steel samples after femtosecond laser processing and exposure to hydrocarbons, Procedia CIRP **111**(September 2022), 643–647 (2022).
[124] E. Liu, H. J. Lee, and X. Lu, Superhydrophobic Surfaces Enabled by

Femtosecond Fiber Laser-Written Nanostructures, Appl. Sci. **10**(8), 2678 (2020).
[125] W. C. Bigelow, D. L. Pickett, and W. A. Zisman, Oleophobic monolayers, J. Colloid Sci. **1**(6), 513–538 (1946).
[126] R. N. Wenzel, Resistance of solid surfaces to wetting by water, Ind. Eng. Chem. **28**(8), 988–994 (1936).
[127] S. Baxter and A. B. D. Cassie, The water repellency of fabrics and a new water repellency test, J. Text. Inst. Trans. **36**(4), T67–T90 (1945).
[128] A. B. D. CASSIE and S. BAXTER, Large Contact Angles of Plant and Animal Surfaces, Nature **155**(3923), 21–22 (1945).
[129] C. Li, J. Zhang, J. Han, and B. Yao, A numerical solution to the effects of surface roughness on water–coal contact angle, Sci. Rep. **11**(1), 459 (2021).
[130] A. J. B. Milne and A. Amirfazli, The Cassie equation: How it is meant to be used, Adv. Colloid Interface Sci. **170**(1–2), 48–55 (2012).
[131] M. H. Shim, J. Kim, and C. H. Park, The effects of surface energy and roughness on the hydrophobicity of woven fabrics, Text. Res. J. **84**(12), 1268–1278 (2014).
[132] C. Kanan and G. W. Cottrell, Color-to-Grayscale: Does the Method Matter in Image Recognition?, PLoS One **7**(1), e29740 (2012).
[133] M. Gedvilas, K. Ratautas, A. Jagminienė, I. Stankevičienė, N. Li Pira, S. Sinopoli, E. Kacar, E. Norkus, and G. Račiukaitis, Percolation effect of a Cu layer on a MWCNT/PP nanocomposite substrate after laser direct structuring and autocatalytic plating, RSC Adv. **8**(53), 30305–30309 (2018).
[134] M. Gedvilas, Grayscale Marking of Anodized Aluminium Plate by Using Picosecond Laser and Galvanometer Scanner, J. Laser Micro/Nanoengineering **9**(3), 267–270 (2014).
[135] M. Gedvilas, K. Ratautas, E. Kacar, I. Stankevičienė, A. Jagminienė, E. Norkus, N. Li Pira, and G. Račiukaitis, Colour-Difference Measurement Method for Evaluation of Quality of Electrolessly Deposited Copper on Polymer after Laser-Induced Selective Activation, Sci. Rep. **6**(1), 22963 (2016).
[136] H. Zhu, H. Zhang, X. Ni, Z. Shen, and J. Lu, Picosecond laser lift-off method for fracture and debonding of copper oxide layer grown on copper substrate, J. Laser Appl. **31**(4), (2019).
[137] G. Walters, B. R. Sutherland, S. Hoogland, D. Shi, R. Comin, D. P. Sellan, O. M. Bakr, and E. H. Sargent, Two-Photon Absorption in Organometallic Bromide Perovskites, ACS Nano **9**(9), 9340–9346 (2015).
[138] W. Liu, J. Xing, J. Zhao, X. Wen, K. Wang, P. Lu, and Q. Xiong, Giant Two-Photon Absorption and Its Saturation in 2D Organic–Inorganic Perovskite, Adv. Opt. Mater. **5**(7), 1–6 (2017).
[139] N. Dong, Y. Li, S. Zhang, N. McEvoy, R. Gatensby, G. S. Duesberg, and J. Wang, Saturation of Two-Photon Absorption in Layered

Transition Metal Dichalcogenides: Experiment and Theory, ACS Photonics **5**(4), 1558–1565 (2018).
[140] R. Marschall, Semiconductor Composites: Strategies for Enhancing Charge Carrier Separation to Improve Photocatalytic Activity, Adv. Funct. Mater. **24**(17), 2421–2440 (2014).
[141] G. Yang, A. Chen, M. Fu, H. Long, and P. Lu, Excimer laser deposited CuO and Cu2O films with third-order optical nonlinearities by femtosecond z-scan measurement, Appl. Phys. A **104**(1), 171–175 (2011).
[142] N. A. Saad, M. H. Dar, E. Ramya, S. R. G. Naraharisetty, and D. Narayana Rao, Saturable and reverse saturable absorption of a Cu2O–Ag nanoheterostructure, J. Mater. Sci. **54**(1), 188–199 (2019).
[143] T.-H. Chen, R. Fardel, and C. B. Arnold, Ultrafast z-scanning for high-efficiency laser micro-machining, Light Sci. Appl. **7**(4), 17181–17181 (2018).
[144] J. Byskov-Nielsen, J.-M. Savolainen, M. S. Christensen, and P. Balling, Ultra-short pulse laser ablation of metals: threshold fluence, incubation coefficient and ablation rates, Appl. Phys. A **101**(1), 97–101 (2010).
[145] B. Neuenschwander, T. Kramer, B. Lauer, and B. Jaeggi, "Burst mode with ps- and fs-pulses: Influence on the removal rate, surface quality, and heat accumulation," in S. Roth, Y. Nakata, B. Neuenschwander, and X. Xu, eds. (2015), p. 93500U.
[146] A. Amouye Foumani, D. J. Förster, H. Ghorbanfekr, R. Weber, T. Graf, and A. R. Niknam, Atomistic simulation of ultra-short pulsed laser ablation of metals with single and double pulses: An investigation of the re-deposition phenomenon, Appl. Surf. Sci. **537**(8), 147775 (2021).
[147] M. Spellauge, J. Winter, S. Rapp, C. McDonnell, F. Sotier, M. Schmidt, and H. P. Huber, Influence of stress confinement, particle shielding and re-deposition on the ultrashort pulse laser ablation of metals revealed by ultrafast time-resolved experiments, Appl. Surf. Sci. **545**(10), 148930 (2021).
[148] J. Mur and R. Petkovšek, Near-THz bursts of pulses – Governing surface ablation mechanisms for laser material processing, Appl. Surf. Sci. **478**(12), 355–360 (2019).
[149] D. Metzner, P. Lickschat, and S. Weißmantel, Influence of heat accumulation during laser micromachining of CoCrMo alloy with ultrashort pulses in burst mode, Appl. Phys. A **126**(2), 84 (2020).
[150] H. Le, T. Karkantonis, V. Nasrollahi, P. Penchev, and S. Dimov, MHz burst mode processing as a tool for achieving removal rates scalability in ultrashort laser micro-machining, Appl. Phys. A **128**(8), 711 (2022).
[151] B. Bornschlegel and J. Finger, In-Situ Analysis of Ultrashort Pulsed Laser Ablation with Pulse Bursts, J. Laser Micro/Nanoengineering **14**(1), 88–94 (2019).

[152] D. J. Förster, B. Jäggi, A. Michalowski, and B. Neuenschwander, Review on Experimental and Theoretical Investigations of Ultra-Short Pulsed Laser Ablation of Metals with Burst Pulses, Materials (Basel). **14**(12), 3331 (2021).

CURRICULUM VITAE

Mantas Gaidys was born in 1995 in Vilnius, Lithuania.

Education:

2020 – 2025	Center for Physical Sciences and Technology (FTMC) *Ph.D. studies*
2018 – 2020	Vilnius University Laser technology *Master's degree*
2014 – 2018	Vilnius University Physics *Bachelor's degree*

Work experience:

2020 – present	Center for Physical Sciences and Technology (FTMC) *Junior Researcher*
2018 – 2020	Center for Physical Sciences and Technology (FTMC) *Engineer*
2017 – 2018	Center for Physical Sciences and Technology (FTMC) *Technician*

APIE AUTORIŲ

Mantas Gaidys gimė 1995 m. Vilniuje, Lietuvoje.

Išsilavinimas:

2020 – 2025	Fizinių ir technologijos mokslų centras (FTMC) *Doktorantūros studijos*
2018 – 2020	Vilniaus universitetas Lazerinės technologijos *Magistro studijos*
2014 – 2018	Vilniaus universitetas Bendroji fizika *Bakalauro studijos*

Profesinė veikla:

2020 – dabar	Fizinių ir technologijos mokslų centras (FTMC) *Jaunesnysis mokslo darbuotojas*
2018 – 2020	Fizinių ir technologijos mokslų centras (FTMC) *Inžinierius*
2017 – 2018	Fizinių ir technologijos mokslų centras (FTMC) *Technikas*

REPRINTED PUBLICATIONS

P1

STAINLESS STEEL COLOURING USING BURST AND BIBURST MODE ULTRAFAST LASER IRRADIATION

M. Gaidys, A. Selskis, P. Gečys, M. Gedvilas

Opt. Laser Technol. **174**, 110561, (2024).
DOI: 10.1016/j.optlastec.2024.110561

Optics & Laser Technology 174 (2024) 110561

Contents lists available at ScienceDirect

Optics and Laser Technology

journal homepage: www.elsevier.com/locate/optlastec

Stainless steel colouring using burst and biburst mode ultrafast laser irradiation

Mantas Gaidys [a,*], Algirdas Selskis [b], Paulius Gečys [a], Mindaugas Gedvilas [a]

[a] Department of Laser Technologies (LTS), Center for Physical Sciences and Technology (FTMC), Savanorių Ave. 231 LT-02300, Vilnius, Lithuania
[b] Department of Characterisation of Materials Structure, Center for Physical Sciences and Technology (FTMC), Saulėtekio Ave. 3 LT-10257, Vilnius, Lithuania

ARTICLE INFO

Keywords:
Laser colouring
Femtosecond
Burst
Biburst
Stainless steel
Wettability
Hydrophobic

ABSTRACT

Laser surface colouring is an adaptable, versatile and environmentally friendly technology with many different applications. Using a femtosecond pulse laser in different burst regimes laser colouring on stainless steel was achieved. The mircomachined colours' dependence on fluence and different number of pulses within burst regimes were tested. The achieved colours were shown and their origin was explained. Because laser coloring is a very flexible method we have shown different colored images with intricate details. The achieved surface structures that resulted in colors mimicked those found in nature and were also hydrophobic which greatly increases their applicability.

1. Introduction

Humans attach a great deal of importance to colours. It aids with object and pattern recognition, as well as navigating the environment. In addition, particular colours may invoke emotions and create associations, which is widely used in marketing and branding. Chemical surface colouring of metals has been really popular in the past, including anodization [1], electroplating [2,3], patination [4] and physical vapor deposition [5], but recently has been gradually abandoned due to issues with environmental damage [6]. Laser surface colouring has quickly surpassed conventional marking techniques [7] since it is an adaptable, versatile and environmentally friendly technology with many different applications. For instance, it is used in the medical sector to colour medical equipment and devices with decorative patterns, identification labels, or colour-coded markers [8]. During surgical procedures, laser colouring can also aid in making medical instruments more visible and distinct. Laser colouring poses no additional danger of infection to patients because it does not employ any chemical paints or coatings. Branding and packaging are another topic. Logos, serial numbers, barcodes, and decorative features can all be added to package materials using laser colouring [9]. Moreover, it can be used to insert concealed or implanted colour-changing features into papers or banknotes as an anti-counterfeiting measure [10]. Lastly, the jewellery industry also uses laser colouring to impart vivid colours and elaborate designs to metals and other materials. It makes it possible to customize items precisely and in great detail, which improves the visual appeal of jewellery and fashion accessories [11]. In the automotive industry, laser colouring is also utilized to produce aesthetically pleasing finishes on various parts. Recently, fs laser pulses were used to color Sb_2S_3 laminate with sub-diffraction resolution [12].

While the utilization of laser colouring is growing rapidly, the colourization process itself has not been sufficiently studied. There are three main methods of metal colouring using laser irradiation. First one is laser induced oxidation where a substrate material reacts with oxygen significantly more quickly when heated by laser irradiation. An oxide layer forms on the metal, which is of different colour to the original metal [6,13,14]. This has been demonstrated on various metals, such as titanium [14], stainless-steel [15], copper [16] and others [17,18]. Another explanation for the colour change with an oxide layer is the thin film effect, when light reflects from the surface of the oxide and the surface of the metal, interference happens and if the optical path difference is equal to a certain wavelength or its product with an integer a corresponding colour is seen [7]. The second method is structural colours that are angle dependent and arise from laser induced periodic surface structures (LIPSS). LIPSS is the development of wavy structures on a range of materials and requires surface characteristics with a periodicity equal to or less than the wavelength of the laser irradiation [19]. LIPSS similar to one dimensional grating can produce colours due to diffraction. These colours are called structural colours and are heavily angle dependent [20,21]. The final method of laser colouring uses

* Corresponding author.
E-mail address: mantas.gaidys@ftmc.lt (M. Gaidys).

https://doi.org/10.1016/j.optlastec.2024.110561
Received 21 September 2023; Received in revised form 18 December 2023; Accepted 8 January 2024
Available online 13 January 2024

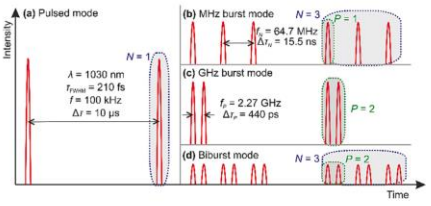

Fig. 1. Schematic illustration of the different laser regimes. a) standard pulsed mode with a repetition rate f – 100 kHz, time between pulses $\Delta\tau$ – 10 μs; b) MHz burst mode, where a pulse is divided into N – 3, MHz subpulses (blue dotted line), with a repetition rate f_N – 64.68 MHz, time between pulses $\Delta\tau_N$ – 15.46 ns; c) GHz burst mode, where a pulse is divided into P – 2 GHz subpulses (green dotted line), with a repetition rate f_P – 2.27 GHz, time between pulses $\Delta\tau_P$ – 440 ps; d) biburst mode where a pulsed mode pulse is divided into N – 3, MHz subpulses (blue dotted line in part b) and those subpulses are further divided into P – 2, GHz pulses each (green dotted line).

nanoparticles and nanostructures on metals to activate plasmonic colours. These colours are also structural. In contrast to the second mechanism, the colour does not change depending on the viewing angle since the surface structures that excite the surface colours are randomly distributed without regularity. The primary causes of this form of colours are surface plasmon resonance (SPR) effects brought on by nanostructures and nanoparticles on metals [22–24]. Laser colouring depends on many processing parameters, including: laser power, scanning speed, hatch, pulse repetition rate and others. By optimizing the laser parameters, it is also possible to gain a wanted structural surface change as well, which may result in useful properties such as hydrophobicity.

In this work, laser surface processing using different burst modes were used to achieve various colours on stainless steel. Influence on the colour of the number of pulses within bursts and laser power were investigated. Micromachined surface structure was analyzed and the static water contact angles were measured to see if the surface became hydrophobic.

2. Materials and methods

2.1. Experimental setup

A state-of-the-art solid-state laser (Carbide, Light Conversion) with a 1030 nm central wavelength laser irradiation and a pulse duration of 210 fs was used. Beam radius at the focal point was equal to 21.7 μm and the beam quality factor M^2 was 1.08. The repetition rate was constant and equal to 100 kHz. The laser allowed for MHz, GHz burst and biburst regimes, which were all used to perform the experiments. When the laser works in the standard pulsed mode, the repetition rate was 100 kHz with a time difference of 10 μs between pulses (Fig. 1a). If we divide each of those pulses into smaller subpulses with an intra–burst repetition rate of 64.68 MHz we have the MHz burst mode, where N is the number of MHz subpulses within the burst (Fig. 1b). Likewise, if we divide the pulses into sub–pulses with an intra–burst repetition rate of 2.27 GHz we have the GHz burst mode, where P is the number of GHz subpulses within the burst (Fig. 1c). On the other hand, the biburst mode works a bit differently. If we take the MHz burst and we further divide the MHz subpulses into GHz subpulses, we will have the aforementioned biburst mode (Fig. 1d). It is crucial to note, that even though the pulse is divided into many subpulses the overall pulse energy remains the same whether there is one pulse in the pulsed mode, three pulses in the MHz burst mode, two pulses in the GHz burst mode or six pulses in the biburst mode.

2.2. Experiment

The beam was positioned using a galvanometric scanner (Intelliscan 14, ScanLab) and focused using a 100 mm F–theta lens. Using the galvanometric scanner horizontal lines were scanned by the laser beam on the stainless-steel plate with the controllable scanning speed of 100 mm/s and 333 mm/s. The distance between the lines or hatch h was constant and equal to 10 μm. The area of one scanned rectangle was equal to 6 × 6 mm^2 (Fig. 2). Horizontally in the x direction number of pulses in the MHz or GHz burst were changed from 2 to 9 with a step of 1. For the GHz burst mode 10, 15, 20 and 40 pulses within the burst were also tested. For the biburst mode, the GHz experiment was repeated while using different number of pulses within the MHz burst, changing from 2 to 8 with a step of 1. Vertically in the y direction laser output power was gradually decreased and equal to 5.6 W, 4.4 W, 3.5 W, 2.8 W, 2.5 W, 1.7 W, 1.4 W, 0.98 W, 0.73 W, and 0.26 W. This corresponded to pulse fluences of 7.6 J/cm^2, 6.0 J/cm^2, 4.8 J/cm^2, 3.8 J/cm^2, 3.4 J/cm^2, 2.3 J/cm^2, 1.9 J/cm^2, 1.3 J/cm^2, 1.0 J/cm^2 and 0.34 J/cm^2 respectively. Afterwards, the micromachined stainless-steel plate with different laser induced colours was put in a box with all white walls (LightBox). Inside the box, the samples were illuminated by LED lights, which were on the top part of the box and the samples themselves were photographed using a digital camera (Sony, IMX563).

2.3. Sample characteristics

For the experiment, 120 mm × 120 mm × 0.4 mm stainless steel (304, Ekstremalė) plates were used. Stainless steel 304 has 18 % chromium and 8 % nickel and is the most commonly used grade of stainless steel with properties such as: excellent resistance to the corrosion and temperature, high tensile strength and durability, but is still easily formable. A scanning electron microscope (Helios NanoLab 650, FEI)

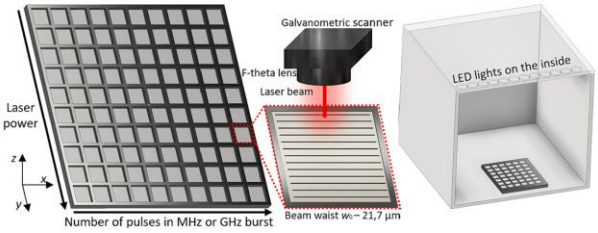

Fig. 2. Design of the laser colouring experiment. First using a galvanometric scanner coloured rectangle squares are micromachined using laser irradiation on the stainless-steel plates. Afterwards, the stainless-steel plates are photographed inside a white walled box with LED lights.

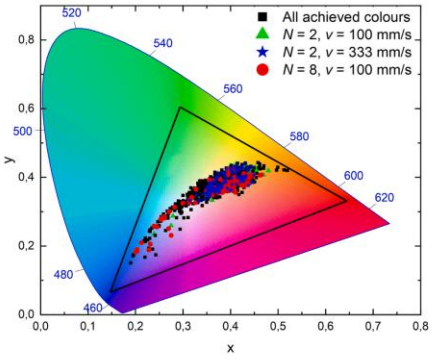

Fig. 3. CIE 1931 colour diagram containing all achieved colours. Black triangle shows all achievable colours due to the usage of XYZ colour model. Green squares – biburst mode with $N = 2$ pulses in the MHz burst and a scanning speed of 100 mm/s; blue stars – biburst mode with $N = 2$ pulses in the MHz burst and a scanning speed of 333 mm/s, red circles – biburst mode with $N = 8$ pulses in the MHz burst and a scanning speed of 100 mm/s.

was used to visualize the samples.

3. Results and discussion

CIE 1931 XYZ colour space is used for the laser induced surface colour characterization in numerous scientific works [11,25,26]. The XYZ colour model was utilized in our experiments. Fig. 3 shows a CIE 1931 chromaticity diagram. An average XYZ value of the produced colour was measured when the samples' pictures were taken. In order to represent all of the produced colours in the CIE 1931 diagram, x and y coordinates were calculated using XYZ variables.

As we can see in the colour space in Fig. 3 we achieved a wide range of colours, from multiple shades of brown and yellow, to blue and green. Notably the hardest colour to achieve was red, with only purple colour being close to it.

Three different burst regimes: MHz, GHz and biburst were used to achieve different colours on stainless steel.

MHz burst mode was not very effective in producing a broad spectrum of varied colours, as shown in Fig. 4. Only different tones of brown were achieved. When using the GHz burst mode, the situation marginally improved and more colours, including many hues of green and one very dark purple, were produced. The bulk, however, continued to be brown, just like in the MHz burst mode.

The majority of colours are achieved when using the biburst mode. In picture (Fig. 5a) we see the GHz mode with brown and green colours. However, starting with the biburst mode in (Fig. 5b) the first blue colour is visible. Increasing the number of pulses in the MHz burst yields greater number of shades of blue with (Fig. 5f–h) showing that half of the grid is either blue or purple. Achieving these colours is a difficult and time-consuming task because of the parameters involved. We can see that the optimal window for achieving colours is between 1.1 J/cm^2 and 2.1 J/cm^2 which is quite narrow. Furthermore, while the fluence for the entire burst ranges from 1.1 J/cm^2 to 2.1 J/cm^2, the intra-burst fluence for a single pulse is only about 0.01 J/cm^2 to 0.02 J/cm^2 for purple colours and 0.02 J/cm^2 to 0.04 J/cm^2 for blue colours, making the use of various burst modes a very practical and precise way to attain such low fluences.

Scanning speed is also a very important processing parameter for laser colouring. Comparing two arrays in the biburst mode with 2 pulses in the MHz burst (Fig. 6) we can see that increasing the scanning speed threefold yielded only shades of brown. While using a scanning speed of 100 mm/s resulted in a few blue and purple colours. Further optimising the set of parameters by increasing the number of pulses in the MHz burst to 8 yielded a high range of colours, with more than half of the array being blue or purple. We can see these results in (Fig. 3) as well, where the second set of parameters resulted in a small range of colours, while the third set spanned throughout the whole possible triangle.

Using the achieved parameters for different colours, Center for Physical Sciences and Technology logo (Fig. 7 a-c) and Lithuanian initials (Fig. 7 d) have been coloured. Because the colours are achieved by scanning straight lines, using beam controlling software, it is easy to draw any wanted shape.

Several experiments were done to deduce the cause of the surface colours induced by laser irradiation. Laser-induced periodic surface structures, often known as LIPSS, are one method by which a surface changes colour after laser colouring. Due of the diffraction effect, the LIPSSs can produce structural colours just like a one-dimensional grating, which are angle dependent. After conducting a tilt experiment (Fig. 8), it was shown that the manufactured colours are not angle dependent.

The remaining reasons are surface oxide causing a thin film effect and surface plasmon resonance arising from metallic nanostructures and nanoparticles. There will always be heat while working on a metal sample with laser irradiation to fasten the oxidation process, however nanosecond laser pulses are far more useful in this area than femtosecond ones. We got the fewest bright red colours, and this notion of thin film effect would explain it quite well, because the oxide would have to be the thickest, and light might not get through it so interference does not happen. On the other hand, if the colour was just related to the thickness of the oxide, the scanning electron microscope images should show a very similar structure. But they are quite different. In picture (Fig. 9a) and (Fig. 9b) an even surface with a few nanoparticles of varying sizes can be seen, but in pictures (Fig. 9c) and (Fig. 9d) we see small nanograining. And in pictures (Fig. 9g) and (Fig. 9h) spiky nano formations can be seen. Therefore, a combination of the thin film effect and surface plasmon resonance effect are responsible for the colours seen on stainless-steel during laser colouring.

Laser coloring has been shown on many different metals including

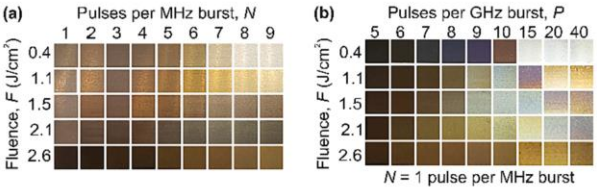

Fig. 4. Stainless steel colour achieved by laser colouring dependence on fluence F in the (a) MHz and (b) GHz burst modes.

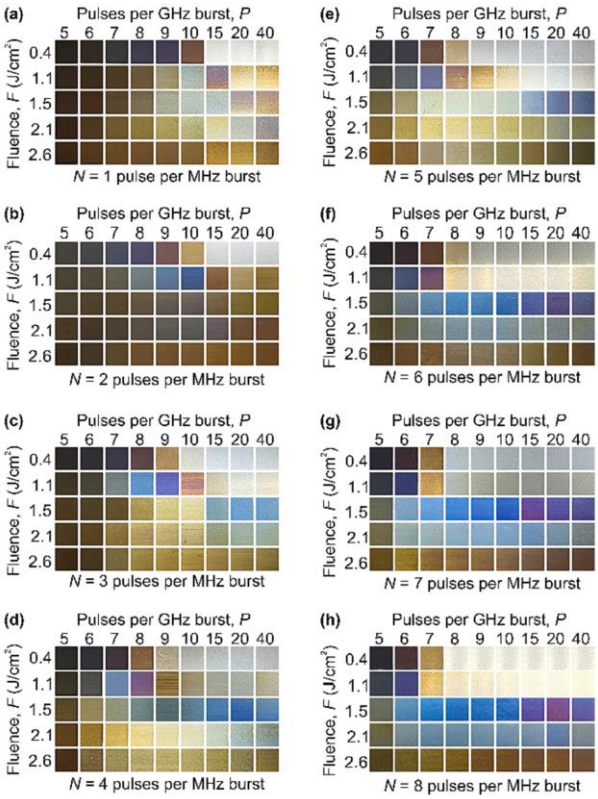

Fig. 5. Stainless steel colour achieved by laser colouring dependence on fluence F and number of pulses per GHz burst P, at different number of pulser per MHz burst N: (a) $N = 1$; (b) $N = 2$; (c) $N = 3$; (d) $N = 4$; (e) $N = 5$; (f) $N = 6$; (g) $N = 7$; (h) $N = 8$.

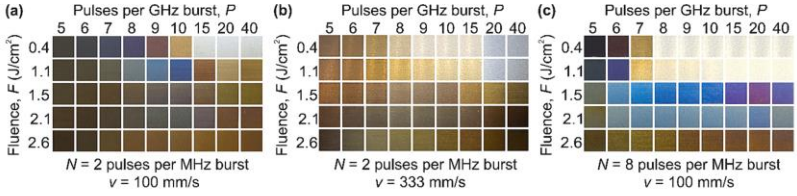

Fig. 6. Stainless steel colour achieved by laser colouring dependence on fluence F and number of pulses per GHz burst P, at different number of pulser per MHz burst and scanning speed: (a) $N = 2$, $v = 100$ mm/s; (b) $N = 2$, $v = 333$ mm/s; (c) $N = 8$ $v = 100$ mm/s.

stainless steel [10,13,14,26–33], silver [11,35], aluminium [21,36], titanium [37,38] and others. For stainless steel specifically, laser coloring has been shown using ns pulses with oxidation being the cause for the colors, or using fs pulses with the cause being LIPSS (Table 1). It was shown in (Fig. 8) that our colors are not angle dependent, which is the main characteristic for structural LIPSS colors, as well as, scanning electron microscope images in (Fig. 9) show that there are no visible LIPSS. Therefore, fs laser coloring due to oxidation and nanostructures

Fig. 7. Laser coloured Center for Physical Sciences and Technology logo and name in English in different colours a) blue 40 × 17 mm^2 *N7P*10, fluence 1.5 J/cm^2, b) purple 40 × 17 mm^2 *N7P*15fluence 1.5 J/cm^2, c) orange 30 × 13 mm^2 *N7P7*, fluence 1.1 J/cm^2 d) FTMC letters in blue colour 3 × 15 mm^2 *N7P*10, fluence 1.5 J/cm^2.

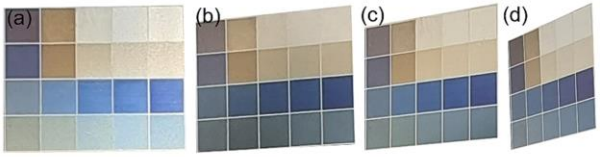

Fig. 8. Array of colours by laser colouring on stainless steel. (a) Stainless steel sample at rest position at 0°; (b) stainless steel sample tilted by 10°; (c) stainless steel sample tilted by 25°; (d) stainless steel sample tilted by 60°.

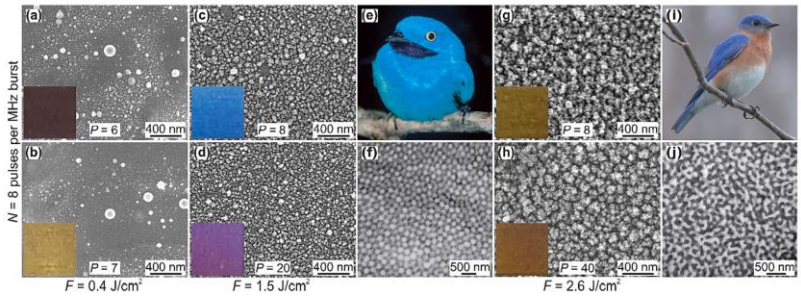

Fig. 9. Scanning electron microscope images of laser colouring on stainless steel using biburst regime with 8 pulses in the MHz burst with different number of pulses in the GHz burst: (a) P – 6, dark brown colour; (b) P – 7, sand colour; (c) P – 8, blue colour (d) P – 20, purple colour (g) P – 8, light brown colour (h) P – 40, brown colour. (e) Male Eastern Bluebird (Sialia sialis, Turdidae); (f) nanostructure from feather; (i) Male Plum-throated Cotinga (Cotinga maynana, Cotingidae); (j) nanostructure from feather. Pictures (e), (f), (i) and (j) reproduced with permission from ref. [40], ® 2009 Royal Society of Chemistry.

Table 1
Stainless steel laser coloring in literature compared to our work which is marked with *.

Type	Mechanism	Laser parameters			
		λ, nm	*τ*	*f*, kHz	*v*, mm/s
304	Oxidation [27]	1064	10–170 ns	225	350
	Oxidation [28]	1062	100 ns	20–100	50–225
	Oxidation [14]	1060	100 ns	20–99	1–250
	Oxidation [29]	532	20 ns	20	100–600
	Oxidation [30]	355	25 ns	40	400–500
316	Oxidation [15]	1064	100 ns	20–100	10–500
303	Oxidation [31]	248	20 ns	255	–
304	LIPSS [32]	800	100 fs	10	0.017–0.4
301L	LIPSS [10]	800	90 fs	1	1–4
316L	LIPSS [33]	800	150 fs	5	10–130
316L	LIPSS [34]	240–2600	104 fs	1	13
304	Oxidation/ Nanostructures*	1030	210 fs	100	100

on stainless steel has been shown for the first time. Burst regimes have the inherent advantage due to the short time between burst pulses, it is possible to reuse the residual heat of the previous pulses [39]. This allows us to achieve scanning speed of 100 mm/s that is difficult to achieve while using fs pulses.

Since our previous works with efficient laser ablation, we are always trying to mimic functional surfaces found in nature. We can see here our achieved colours structurally are similar to the birds' feathers of the similar colour (Fig. 9 c-f and g-j). Another and much more advantageous functionality is hydrophobicity. Having laser induced colours on metals that are hydrophobic would be very beneficial. Because real world applicability would increase dramatically if the colours could withstand the different elements outside. The contact angle of a water droplet on pristine stainless steel without processing by laser irradiation was 50.7 ± 0.9 degrees and a surface can be considered hydrophilic if the contact angle is significantly lower than 90 degrees. For a surface to be considered hydrophobic, it needs to have a contact angle of higher than 90 degrees and to be considered super hydrophobic a contact angle larger than 150 degrees is needed. The static water contact angle (SWCA) was measured by depositing a 6 μL volume water drop on a specific laser coloured area using a micropipette (Transferpette, Brand GmbH). The sample was illuminated from one side by a high-parallelism

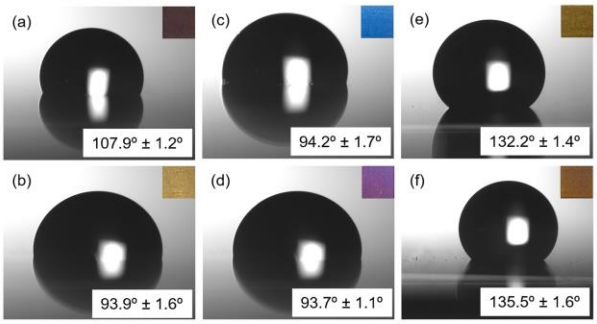

Fig. 10. Water droplets on the coloured stainless steel surface. (a) dark brown colour with SWCA of 107.9 ± 1.2 degrees; (b) sand colour with SWCA of 93.9 ± 1.6 degrees; (a) blue colour with SWCA of 94.2 ± 1.7 degrees; (d) purple colour with SWCA of 93.7 ± 1.1 degrees; (e) light brown colour with SWCA of 132.2 ± 1.4 degrees; (f) brown colour with SWCA of 135.5 ± 1.6 degrees.

diode backlight and an image of the drop was taken from the other side using a digital camera. The SWCA angle was deduced by using ImageJ software's [41] plugin LBADSA [42]. The SWCA for each colour was measured five times and a standard deviation of SWCA was calculated. As we can see (Fig. 10) for the structure of the few nanoparticles of varying sizes the contact angles were 107.9 ± 1.2 degrees and 93.9 ± 1.6 degrees, respectively, which does fulfil the criteria for a hydrophobic surface. For the nanograining structure, the criteria were also met with blue colour having a SWCA of 94.2 ± 1.7 degrees and purple having SWCA of 93.7 ± 1.1 degrees, respectively. For the spiky nano formations, the contact angle is close to the superhydrophobic criteria being equal to 132.2 ± 1.4 degrees and 135.5 ± 1.6 degrees. The time frame between colours being made and wettability testing is one year. The samples were kept in a standard air environment without any additional protection which proves that the hydrophobicity effect is long lasting.

4. Conclusions

In this work colouring of stainless-steel was investigated using different burst regimes. It was shown that laser colouring on stainless steel can achieve numerous colours including blue, purple, dark green, brown and others if the parameters are chosen correctly. Out of the three used burst regimes, MHz and GHz regimes did not yield a large variety of colours, while majority of colours have been achieved using the biburst mode. Increasing the beam scanning speed reduces the variance of colours achieved. It was shown that the colours are caused by the thin film effect and surface plasmon resonance effect arising from nanoparticles and nanostructures. The achieved surface structures that resulted in colours not only mimicked those found in nature, but also were hydrophobic increasing their applicability in industrial use. All colours had a static water contact angle greater than 90 degrees and some were higher than 130 degrees almost reaching super hydrophobicity.

CRediT authorship contribution statement

Mantas Gaidys: Conceptualization, Formal analysis, Investigation, Methodology, Writing – original draft, Writing – review & editing. **Algirdas Selskis:** Formal analysis, Resources. **Paulius Gečys:** Funding acquisition, Resources, Supervision, Validation. **Mindaugas Gedvilas:** Conceptualization, Funding acquisition, Project administration, Supervision, Validation, Visualization.

Declaration of competing interest

The authors declare that they have no known competing financial interests or personal relationships that could have appeared to influence the work reported in this paper.

Data availability

Data will be made available on request.

Acknowledgements

This project has received funding from the Research Council of Lithuania (LMTLT), agreement no. S-MIP-22-89.

Figures 8 pictures (e), (f), (i) and (j) reproduced with permission from ref. [1], ® 2009 Royal Society of Chemistry.

[1] E.R. Dufresne, H. Noh, V. Saranathan, S.G.J. Mochrie, H. Cao, R. O. Prum, Self-assembly of amorphous biophotonic nanostructures by phase separation, Soft Matter. 5 (2009) 1792. https://doi.org/10.1039/b902775k.

References

[1] C.J. Donahue, J.A. Exline, Anodizing and coloring aluminum alloys, J. Chem. Educ. 91 (2014) 711–715, https://doi.org/10.1021/ed3005598.
[2] W. Giurlani, F. Gambinossi, E. Salvietti, M. Passaponti, M. Innocenti, Color measurements in electroplating industry: Implications for product quality control, ECS Trans. 80 (2017) 757–766, https://doi.org/10.1149/08010.0757ecst.
[3] W. Giurlani, G. Zangari, F. Gambinossi, M. Passaponti, E. Salvietti, F. Di Benedetto, S. Caporali, M. Innocenti, Electroplating for decorative applications: Recent trends in research and development, Coatings 8 (2018) 1–25, https://doi.org/10.3390/coatings8080260.
[4] A. Giumlia-Mair, Plating and surface treatments on ancient metalwork, Adv. Archaeomater. 1 (2020) 1–26, https://doi.org/10.1016/j.aia.2020.10.001.
[5] M. Fenker, N. Jackson, M. Spolding, P. Nicole, K. Schönhut, G. Gregory, P. E. Hovsepian, W.-D. Münz, Corrosion performance of PVD-coated and anodised materials for the decorative market, Surf. Coat. Technol. 188–189 (2004) 466–472, https://doi.org/10.1016/j.surfcoat.2004.08.054.
[6] Y. Lu, X. Shi, Z. Huang, T. Li, M. Zhang, J. Czajkowski, T. Fabritius, M. Huttula, W. Cao, Nanosecond laser coloration on stainless steel surface, Sci. Rep. 7 (2017) 7092, https://doi.org/10.1038/s41598-017-07373-8.
[7] H. Liu, W. Lin, M. Hong, Surface coloring by laser irradiation of solid substrates, APL Photonics 4 (5) (2019) 051101.
[8] N.G. Henriksen, K. Poulios, M.A.J. Somers, T.L. Christiansen, Impact of laser marking on microstructure and fatigue life of medical grade titanium, SSRN Electron. J. 873 (2023) 145020, https://doi.org/10.2139/ssrn.4361273.
[9] J. Li, C. Lu, A. Wang, Y. Wu, Z. Ma, X. Fang, L. Tao, Experimental investigation and mathematical modeling of laser marking two-dimensional barcodes on surfaces of aluminum alloy, J. Manuf. Process. 21 (2016) 141–152, https://doi.org/10.1016/j.jmapro.2015.12.007.

[10] J. Yao, C. Zhang, H. Liu, Q. Dai, L. Wu, S. Lan, A.V. Gopal, V.A. Trofimov, T. M. Lysak, Selective appearance of several laser-induced periodic surface structure patterns on a metal surface using structural colors produced by femtosecond laser pulses, Appl. Surf. Sci. 258 (2012) 7625–7632, https://doi.org/10.1016/j.apsusc.2012.04.105.
[11] J.-M. Guay, A. Calà Lesina, G. Côté, M. Charron, D. Poitras, L. Ramunno, P. Berini, A. Weck, Laser-induced plasmonic colours on metals, Nat. Commun. 8 (2017) 16095, https://doi.org/10.1038/ncomms16095.
[12] K. Liu, Z. Lin, B. Han, M. Hong, T. Cao, Non-volatile dynamically switchable color display via chalcogenide stepwise cavity resonators, Opto-Electron Adv. 7 (2024) 1–12, https://doi.org/10.29026/oea.2024.230033.
[13] D.P. Adams, V.C. Hodges, D.A. Hirschfeld, M.A. Rodriguez, J.P. McDonald, P. G. Kotula, Nanosecond pulsed laser irradiation of stainless steel 304L: Oxide growth and effects on underlying metal, Surf. Coat. Technol. 222 (2013) 1–8, https://doi.org/10.1016/j.surfcoat.2012.12.044.
[14] V. Veiko, G. Odintsova, E. Ageev, Y. Karlagina, A. Loginov, A. Skuratova, E. Gorbunova, Controlled oxide films formation by nanosecond laser pulses for color marking, Opt. Express 22 (2014) 24342, https://doi.org/10.1364/OE.22.024342.
[15] E.H. Amara, F. Haïd, A. Noukaz, Experimental investigations on fiber laser color marking of steels, Appl. Surf. Sci. 351 (2015) 1–12, https://doi.org/10.1016/j.apsusc.2015.05.095.
[16] G. Killaire, J. Walia, S. Rashid, P. Berini, A. Weck, Structural and oxide-based colours on laser textured copper, Appl. Surf. Sci. 583 (2022) 152440, https://doi.org/10.1016/j.apsusc.2022.152440.
[17] Y.F. Lu, H. Qiu, Laser coloration and bleaching of amorphous WO3 thin film, J. Appl. Phys. 88 (2000) 1082–1087. https://doi.org/10.1063/1.373780.
[18] S. O'Hana, A.J. Pinkerton, K. Shoba, A.W. Gale, L. Li, Laser surface colouring of titanium for contemporary jewellery, Surf. Eng. 24 (2008) 147–153, https://doi.org/10.1179/174329408X315607.
[19] P. Shukla, D.G. Waugh, J. Lawrence, R. Vilar, Laser surface structuring of ceramics, metals and polymers for biomedical applications, in: Laser Surf. Modif. Biomater., Elsevier, 2016: pp. 281–299. https://doi.org/10.1016/B978-0-08-100883-6.00010-1.
[20] S. Sakabe, M. Hashida, S. Tokita, S. Namba, K. Okamuro, Mechanism for self-formation of periodic grating structures on a metal surface by a femtosecond laser pulse, Phys. Rev. B 79 (2009) 033409, https://doi.org/10.1103/PhysRevB.79.033409.
[21] G. Li, J. Li, L. Yang, X. Li, Y. Hu, J. Chu, W. Huang, Evolution of aluminum surface irradiated by femtosecond laser pulses with different pulse overlaps, Appl. Surf. Sci. 276 (2013) 203–209, https://doi.org/10.1016/j.apsusc.2013.03.067.
[22] J.Z. Zhang, C. Noguez, Plasmonic optical properties and applications of metal nanostructures, Plasmonics 3 (2008) 127–150, https://doi.org/10.1007/s11468-008-9066-y.
[23] P. Fan, M. Zhong, L. Li, P. Schmitz, C. Lin, J. Long, H. Zhang, Angle-independent colorization of copper surfaces by simultaneous generation of picosecond-laser-induced nanostructures and redeposited nanoparticles, J. Appl. Phys. 115 (2014) 124302. https://doi.org/10.1063/1.4869456.
[24] A.Y. Vorobyev, C. Guo, Direct femtosecond laser surface nano/microstructuring and its applications, Laser Photon. Rev. 7 (2013) 385–407, https://doi.org/10.1002/lpor.201200017.
[25] S.N. Chowdhury, P. Nyga, Z.A. Kudyshev, E. Garcia Bravo, A.S. Lagutchev, A. V. Kildishev, V.M. Shalaev, A. Boltasseva, Lithography-free plasmonic color printing with femtosecond laser on semicontinuous silver films, ACS Photonics 8 (2021) 521–530, https://doi.org/10.1021/acsphotonics.0c01506.
[26] J. Geng, L. Xu, W. Yan, L. Shi, M. Qiu, High-speed laser writing of structural colors for full-color inkless printing, Nat. Commun. 14 (2023) 565, https://doi.org/10.1038/s41467-023-36275-9.
[27] R. Linggamm, M.M. Quazi, M. Ishak, M.H. Aiman, A.Q. Zafiuddin, A. Qaban, Formation of colours on SS304L stainless steel induced by laser colouring, IOP Conf. Ser. Mater. Sci. Eng. 1078 (1) (2021) 012015.
[28] A.J. Antończak, D. Kocoń, M. Nowak, P. Kozioł, K.M. Abramski, Laser-induced colour marking—Sensitivity scaling for a stainless steel, Appl. Surf. Sci. 264 (2013) 229–236, https://doi.org/10.1016/j.apsusc.2012.09.178.
[29] X. Ma, X. Nie, J. Zhao, P. Shrotriya, Y. Zhang, Y. Cui, J. Wang, Effect of nanosecond pulsed laser parameters on the color making of 304 stainless steel, Opt. Laser Technol. 126 (2020) 106104, https://doi.org/10.1016/j.optlastec.2020.106104.
[30] Z.L. Li, H.Y. Zheng, K.M. Teh, Y.C. Liu, G.C. Lim, H.L. Seng, N.L. Yakovlev, Analysis of oxide formation induced by UV laser coloration of stainless steel, Appl. Surf. Sci. 256 (2009) 1582–1588, https://doi.org/10.1016/j.apsusc.2009.09.025.
[31] H.Y. Zheng, G.C. Lim, X.C. Wang, J.L. Tan, J. Hilfiker, Process study for laser-induced surface coloration, J. Laser Appl. 14 (2002) 215–220. https://doi.org/10.2351/1.1514222.
[32] Y. Tamamura, G. Miyaji, Structural coloration of a stainless steel surface with homogeneous nanograting formed by femtosecond laser ablation, Opt. Mater. Express 9 (2019) 2902, https://doi.org/10.1364/OME.9.002902.
[33] B. Dusser, Z. Sagan, H. Soder, N. Faure, J.P. Colombier, M. Jourlin, E. Audouard, Controlled nanostructrures formation by ultra fast laser pulses for color marking, Opt. Express 18 (2010) 2913, https://doi.org/10.1364/OE.18.002913.
[34] G. Li, J. Li, Y. Hu, C. Zhang, X. Li, J. Chu, W. Huang, Femtosecond laser color marking stainless steel surface with different wavelengths, Appl. Phys. A 118 (2015) 1189–1196, https://doi.org/10.1007/s00339-014-8868-3.
[35] A.Y. Vorobyev, C. Guo, Spectral and polarization responses of femtosecond laser-induced periodic surface structures on metals, J. Appl. Phys. 103 (2008) 16–19. https://doi.org/10.1063/1.2842403.
[36] A.Y. Vorobyev, C. Guo, Colorizing metals with femtosecond laser pulses, Appl. Phys. Lett. 92 (2008) 041914. https://doi.org/10.1063/1.2834902.
[37] A. Pérez del Pino, P. Serra, J. Morenza, Coloring of titanium by pulsed laser processing in air, Thin Solid Films 415 (2002) 201–205, https://doi.org/10.1016/S0040-6090(02)00632-6.
[38] A.A. Ionin, S.I. Kudryashov, S.V. Makarov, L.V. Seleznev, D.V. Sinitsyn, E. V. Golosov, O.A. Golosova, Y.R. Kolobov, A.E. Ligachev, Femtosecond laser color marking of metal and semiconductor surfaces, Appl. Phys. A 107 (2012) 301–305, https://doi.org/10.1007/s00339-012-6849-y.
[39] X. Wolters, G. Bonamis, K. Mishchick, E. Audouard, C. Hönninger, E. Mottay, High power GHz femtosecond laser for ablation efficiency increase, Procedia Manuf. 36 (2019) 200–207, https://doi.org/10.1016/j.promfg.2019.08.026.
[40] E.R. Dufresne, H. Noh, V. Saranathan, S.G.J. Mochrie, H. Cao, R.O. Prum, Self-assembly of amorphous biophotonic nanostructures by phase separation, Soft Matter 5 (2009) 1792, https://doi.org/10.1039/b902775k.
[41] C.A. Schneider, W.S. Rasband, K.W. Eliceiri, NIH Image to ImageJ: 25 years of image analysis, Nat. Methods 9 (2012) 671–675, https://doi.org/10.1038/nmeth.2089.
[42] A.F. Stalder, T. Melchior, M. Müller, D. Sage, T. Blu, M. Unser, Low-bond axisymmetric drop shape analysis for surface tension and contact angle measurements of sessile drops, Colloids Surf. A Physicochem. Eng. Asp. 364 (2010) 72–81, https://doi.org/10.1016/j.colsurfa.2010.04.040.

P2

BI-STABILITY IN FEMTOSECOND LASER ABLATION BY MHZ BURSTS

A. Žemaitis, **M. Gaidys**, P. Gečys, M. Gedvilas
Sci. Rep. **14**, 5614 (2024)
DOI: 10.1038/s41598-024-54928-7

scientific reports

Check for updates

OPEN

Bi-stability in femtosecond laser ablation by MHz bursts

Andrius Žemaitis, Mantas Gaidys, Paulius Gečys & Mindaugas Gedvilas✉

In this work, a bi-stable behavior of laser ablation efficiency and quality was controlled by fluence and burst length. The plasma shielding of incoming laser radiation caused sudden jumps with a significant decrease in ablation efficiency for every even number of pulses in the burst. The attenuation of incoming laser radiation by plasma created by the previous pulse was incorporated into the toy model of burst ablation efficiency. The mathematical recurrence relation has been derived for the first time, binding ablation efficiency for the next pulse with the efficiency of the previous pulse, which predicts bi-stability, as well as sudden jumps occurring in ablation efficiency depending on the number of pulses in burst with the response to changes of the control parameter of peak laser fluence in the pulse. The modeling results using new recurrence relation showed stable and bi-stable ablation efficiency depending on burst fluence and the number of pulses, which agreed well with experimental data. The extremely efficient laser ablation has been achieved by optimizing the shielding effect using three pulses in the burst.

Ultra-short laser pulses have been applied for precision micro/nano- fabrication for metals, semiconductors, insulators, and biological materials for science[1], technology[2], industry[3], and medicine[4]. The foundation of the ablation cooling effect by GHz bursts of femtosecond pulses has made a huge impact on the real industrial application of laser machining because of the enhancement of the ablation rate and minimization of thermal damage by an order of magnitude[5]. The burst mode irradiation is used in a wide range of pulse repetition rates from MHz[6–9], to GHz[7–12], and even THz[13–15]. However, a big difference in ablation efficiency has been reported depending on the parity of integer pulse number (odd or even) in the burst[6,7,11,13,16,17]. In majority of the reports, the shielding or/and re-deposition are indicated as the main reasons resulting in bistable dependence of ablation efficiency on the pulse number in the burst. The redeposition hypothesis by second sub-pulse for copper has investigated and verified by atomistic simulations in[18]. The re-deposition has been experimentally studied by shadowgraph technique; however, no clear experimental evidence of re-deposited material was found[17]. The shielding effect has been identified as the dominating effect resulting drop in ablation efficiency for the second sub-pulse in time-resolved experiments for copper[19]. It has been shown experimentally that incoming irradiation is attenuated by ejected particles, vapor, and plasma of the previous pulse, thus reduced ablation efficiency is observed for even pulses[13,20,21]. For odd pulses, higher efficiency is observed, because the previous even pulse produces fewer ablation products and more incoming laser radiation reaches the sample[6]. This leads to bi-stable ablation efficiency, however, there is no paper in scientific literature dedicated to the analytical/numerical modeling of the shielding effect influence on the ablation efficiency and stability/bi-stability analysis. Moreover, in the vast majority of experimental research works the bi-stable behavior of ablation efficiency depending on burst length was investigated for the single burst fluence[6,7,11,13,16,17], and there is no scientific paper dedicated to efficient bi-stability effect investigation dependence on bust fluence and length, simultaneously.

In this study, we present new experimental and theoretical results on the bi-stability control of ablation efficiency for MHz bursts of femtosecond laser pulses. The experiments were conducted to measure laser ablation efficiency using a femtosecond laser working in MHz burst mode. The experimental results showed stable and bi-stable ablation efficiency regions depending on the burst fluence and the number of pulses in a burst. The shielding effect by the cloud of ablation products (particles, vapor, and plasma) was included in the toy model of laser ablation efficiency of parabolic dimple for the first time. The analytical expression mathematically called recurrence relation has been found, which combines ablation efficiency for the next pulse with the efficiency of the previous pulse. Nonlinear recurrence relation predicts stable and bi-stabile ablation, as well as sudden jumps in ablation efficiency depending on burst fluence and the parity of an integer number of pulses in the burst. The equations of the toy model were numerically solved, and computational results showed bifurcation in ablation efficiency, which coincided well with experimental data. To the best of our knowledge, we have exceeded the highest laser milling efficiency for copper recorded in the scientific literature[11].

Department of Laser Technologies (LTS), Center for Physical Sciences and Technology (FTMC), Savanorių Ave. 231, 02300 Vilnius, Lithuania. ✉email: mgedvilas@ftmc.lt

Experiment

Laser milling setup

A solid-state femtosecond burst laser (Pharos, Light Conversion) with a pulse duration of $\tau_{FWHM} \sim 210$ fs, a central wavelength of $\lambda \sim 1030$ nm, the burst repetition rate of $f_{burst} \sim 100$ kHz, and an average laser power output of $P \sim 7.3$ W was used in experiments. The number of pulses per bust number was controlled from $N \sim 1$ (single pulse regime) to $N = 9$. The intra-burst pulse repetition rate was $f_{pulse} = 64.7$ MHz, which determined the temporal distance between pulses of $t_{pulse} = 15.5$ ns.

A galvanometer scanner (Intelliscan 14, Scanlab) equipped with an f-theta lens with a focal distance of 100 mm was used for beam focusing and positioning on the sample surface (Fig. 1a).

Rectangular-shaped cavities have been ablated by laser into copper with transverse dimensions of 2 mm × 1 mm. The laser processing experiments were conducted at room temperature in air. Several layers ranging from 3 to 21 were ablated to increase the cavity depth up to 100 µm for the higher accuracy of depth profile measurement. The Rayleigh length of the Gaussian beam was 1.2 mm and was more than 10 times larger than the cavity depth. The saturation behavior of ablation depth per layer was never reached and the laser-milled cavity depth had a linear dependence on the number of ablated layers. The lateral distance between bi-directional beam scanning lines of $\Delta y = 10$ µm and scanning speed of $v_s = 0.33$ m/s, were kept constant during experiments.

Fluence optimization

There are two competing techniques devoted to maximum laser ablation efficiency via laser fluence optimization: laser fluence variation by adjusting the average laser power at constant spot size and fluence control by varying the laser spot size keeping the highest available laser power[22,23]. Both techniques have advantages and disadvantages. For instance, the variation of laser fluence by changing the focus position on the target is not the

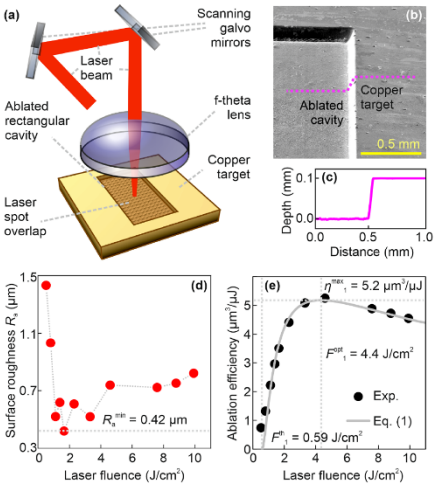

Figure 1. Laser ablation efficiency experiment using femtosecond single pulses. (**a**) Principal experimental setup: the position of the incoming laser beam on the copper target surface is controlled by two galvanometer-based scanning motors with mounted optical mirrors, the beam is focused using the telecentric f-theta lens, and a rectangular cavity is ablated in copper by bi-directional laser beam scanning which produces overlapped laser spots on the ablated cavity bottom. (**b**) SEM image of the rectangular-shaped cavity in copper ablated by using femtosecond pulses, cavity dimensions of 2.0 × 1.0 × 0.1 mm³, the image was taken at a tilt angle of 60°. (**c**) Profile of laser ablated cavity, average depth 100 ± 5 µm of the rectangular cavity. (**d**) Surface roughness R_a of laser ablated cavity bottom and (**e**) ablation efficiency of copper dependence on laser fluence by conventional single pulse irradiation mode. The number of pulses in the burst $N = 1$ (single pulse regime), pulse duration $\tau_{FWHM} = 210$ fs, laser wavelength $\lambda = 1030$ nm, pulse repetition rate $f_{pulse} = f_{burst} = 100$ kHz, dots—experimental data points, line–fit by Eq. (1), fit parameters $F^{th}_1 = 0.59 \pm 0.02$ J/cm², $\delta = 113 \pm 5$ nm.

best option to compare the results of burst ablation efficiency at different fluences. At small beam waist diameters obtained on target by strong focusing, the plasma expansion is more 3D than 1D, especially at long time scale as in multiple pulse regime. Thereby, the bi-stable behavior and the roughness of the ablated structure could be different in case the fluence would be varied by changing the pulse energy rather than the laser spot diameter on target. Therefore, in this work it would make sense to change pulse energy at the fixed spot radius, keeping similar beam focusing conditions during tests. However, the pulse variation procedure is usually performed with a high-power ultrafast laser with output powers up to 50 W[22–24], to reach all required fluence values with certain fixed pulse diameters. In this work, we have used a state-of-the-art burst laser with limited output power capabilities of 7.3 W, thus we had limited freedom in selecting the optimization test. Therefore, we used spot diameter optimization instead of pulse energy optimization to achieve optimal fluence for maximal ablation efficiency, which is common optimization at those power levels[25]. In our current ablation efficiency and surface roughness optimization experiments, we always used the maximal available laser power of 7.3 W. Even though, reaching optimal fluence for maximum ablation efficiency was challenging for a larger number of sub-pulses since burst energy is divided by several sub-pulses which drastically decreases peak pulse fluence.

The laser fluence on the sample surface was changed by controlling the z position of the sample in respect of the focused laser beam. The z position was varied from 0.0 mm (focus position) to 5.3 mm. The spot radius on the sample was characterized by a technique described in[25,26] and it ranged from 21 to 95 µm. The relative error on average for measured beam radiuses was less than 2.7%. The details of spot radius measurement are given in the Methods section.

Roughness characterization

Solid copper (CW004A, Ekstremalė) target with dimensions of 50 mm × 50 mm × 5 mm, purity of 99.9%, and roughness of the polished surface of $R_q < 0.1$ µm was used in laser milling experiments. For the characterization of surface morphology, the scanning electron microscope (SEM) (JSM-6490LV, JEOL) was employed (Fig. 1b). The depth of laser-milled cavities was measured by using a surface profilometer (Dektak 150, Veeco) (Fig. 1c). In the first part of the research, the surface roughness R_q of the laser-milled cavity and ablation efficiency dependence on laser fluence was investigated for the conventional single-pulse irradiation regime, with $N = 1$ pulse in the burst. From the measured profiles of the laser-ablated cavity bottom, the surface roughness was determined. The surface roughness can be characterized by different roughness parameters such as R_{sa}, R_q, R_v, R_p, R_z, R_{ds}, R_{ku}, R_{ms}, and R_a, however, the arithmetic average of the roughness profile R_a is by far the most common and mostly used in the scientific literature defining the surface of laser-milled areas[16,23,27–31]. Even though R_q is mostly used often for historical reasons rather than any particular advantage, as early roughness gauges could only measure surface roughness R_a. The experimentally measured surface roughness R_q dependence on laser fluence for $N = 1$ pulse in the burst is depicted in (Fig. 1d). The surface roughness R_q rapidly decreased from 1.43 to 0.42 µm with the increase of laser fluence from 0.52 to 1.66 J/cm^2, and then the surface roughness R_q value slowly increased from 0.42 to 0.82 µm with the increase of laser fluence from 1.66 to 9.9 J/cm^2 (Fig. 1d). The relative error on average for measured surface roughness R_q and fluence evaluation was less than 2.5% and 3.9%, respectively. The details of surface roughness and fluence evaluation are given in the Methods section.

Efficiency characterization

From the depth of the laser-ablated cavity measured from the profiles, the ablation efficiency was extracted. The ablation efficiency dependence on laser fluence for $N = 1$ pulse in the burst is depicted in (Fig. 1e). The experimentally measured ablation efficiency increased rapidly from 0.74 to 5.3 µm^3/µJ with the increase of laser fluence from 0.52 to 4.6 J/cm^2, and then the ablation efficiency value slowly decreased from 5.3 to 4.6 µm^3/µJ with the increase of laser fluence from 4.6 to 9.9 J/cm^2 (Fig. 1e). The relative error on average for measured ablation efficiencies was less than 3.0%. The details of ablation efficiency evaluation are given in the Methods section. The ablation efficiency η_n^{Pulse} which is equal to ablated volume per pulse V_n divided by the pulse energy E_{pulse} in the burst can be expressed by[32–34]:

$$\eta_n^{\text{pulse}} = \frac{\delta}{2F_{\text{pulse}}} \ln^2\left(\frac{F_n}{F_n^{\text{th}}}\right), \tag{1}$$

where δ is an effective penetration depth, F_{pulse} is the peak laser fluence in the center of the incoming pulse of Gaussian beam $F_{\text{pulse}} = 2E_{\text{pulse}}/(\pi w^2)$, w is Gaussian beam radius at $1/e^2$ level, n is the integer number indexing the pulse position in the burst. The F_n is the peak laser fluence that reaches the material. For the first pulse ($n = 1$) fluence at the material surface is equal to the fluence of the incoming beam as $F_{n=1} = F_{\text{pulse}}$ because there is no cloud above the material and all incoming fluence reaches the sample, however, for the next pulses ($n > 1$), the peak laser fluence which reaches the material is smaller then incoming fluence as $F_{n>1} < F_{\text{pulse}}$, because the incoming pulse is shielded by ablation cloud created by the previous ($n-1$) pulse. The theoretical optimal fluence for maximal ablation efficiency can be evaluated from the first derivative of Eq. (1) as $F^{\text{opt}}{}_1 = e^2 F^{\text{th}}{}_1 \approx 7.39 F^{\text{th}}{}_1$[32–34]. Also, knowing the optimal fluence the theoretical maximal laser ablation efficiency can be evaluated from Eq. (1) as $\eta^{\text{max}}{}_1 = 2\delta/(e^2 F^{\text{th}}{}_1) \approx 0.271\ \delta/F^{\text{th}}{}_1$. The experimental data were fitted by using Eq. (1) and the fit parameters $F^{\text{th}}{}_1 = 0.59 \pm 0.02$ J/cm^2, $\delta = 113 \pm 5$ nm were retrieved. The experiment had a good agreement with the ablation efficiency model equation (Fig. 1e) for a single pulse ablation regime ($N = 1$ pulse in the burst). Knowing single pulse ablation threshold, theoretical optimal laser fluence $F^{\text{opt}}{}_1 = e^2 F^{\text{th}}{}_1 = 4.4 \pm 0.2$ J/cm^2 for the most efficient ablation $\eta^{\text{max}}{}_1 = 5.2 \pm 0.2$ µm^3/µJ can be found from Eq. (1), which coincides well with experimentally observed optimal laser fluence $F^{\text{opt}}{}_1 = 4.6$ J/cm^2 for the most efficient ablation $\eta^{\text{max}}{}_1 = 5.3$ µm^3/µJ.

Results and discussion

Surface roughness

The surface roughness R_a of laser ablated cavity bottom dependence on laser fluence was investigated experimentally with the burst fluences ranging from 0.52 to 9.9 J/cm^2 and 9 different numbers N of pulses in the burst (1, 2, 3, 4, 5, 6, 7, 8, and 9). The experiment showed bi-stability in surface roughness R_a depending on the laser processing parameters (Fig. 2).

The surface roughness R_a dependence on the burst fluence and the number of pulses in the burst are depicted in Fig. 2a. The burst fluence was increased from 0.52 to 9.9 J/cm^2 and the number of pulses in the burst was increased from 1 to 9. The surface roughness R_a in most of the cases was slightly smaller for even numbers ($N = 2$, 4, 6, and 8) than for odd numbers ($N - 1$, 3, 5, 7, and 9) of pulses in a burst if compared to the same burst fluence at large values (2.3 J/cm^2 – 9.9 J/cm^2) (Fig. 2a). However, for small values of burst fluence (0.52 J/cm^2 – 1.7 J/cm^2) opposite behavior could be observed with a surface roughness R_a smaller for odd than for even numbers of pulses in the burst (except for $N - 1$) (Fig. 2a).

This bi-stability effect of surface roughness R_a depending on the burst fluence can be seen when the profiles of the color plot depicted in Fig. 2a are extracted at constant odd and even numbers of pulses in the burst (Fig. 2b–e). For example, for $N = 8$ the surface roughness R_a was slightly higher than $N = 9$ for several fluence values, and slightly lower for the rest of the fluence values with a relative difference in roughness only of 2% (Fig. 2b). For $N = 6$ surface roughness R_a was slightly lower than $N = 7$ up for all fluence values ranging from 1.7 up to 4.6 J/cm^2 (Fig. 3c). The average relative surface roughness R_a difference increased to 39% (Fig. 2c). This ablation regime can be called the bi-stable regime (Fig. 2c). Moreover, for $N - 4$ and $N - 5$ bistable surface roughness R_a from 1.7 J/cm^2 to 9.9 J/cm^2 is observed (Fig. 2d). The average relative surface roughness R_a difference was 18% (Fig. 2d). A slightly different bi-stability was observed for $N - 2$ and $N - 3$ pulses (Fig. 2e). For low fluence values ranging from 0.52 to 2.3 J/cm^2 surface roughness, R_a was higher for an even number of pulses in burst with the average relative surface roughness R_a difference of 26% (Fig. 2e). For high fluence values ranging from

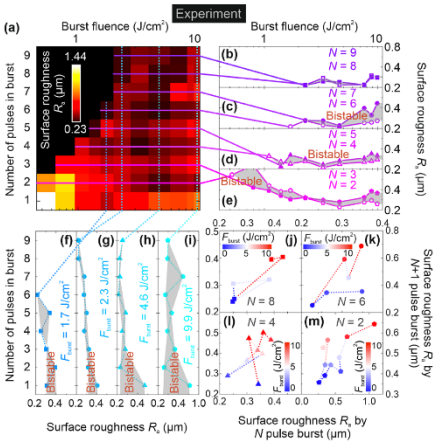

Figure 2. Experimental results of bi-stable behavior of surface roughness R_a of laser ablated cavity bottom. (**a**) Surface roughness R_a of laser ablated cavity bottom of copper (color scale) dependence on the burst fluence (top axis) and the number of pulses in femtosecond burst (left axis), the squares indicated by black color is not measured points because of pulse laser fluence below the ablation threshold. The surface roughness R_a (right axis) dependence on burst fluence (top axis) at different numbers of pulses in burst: (**b**) $N - 8$, 9; (**c**) $N - 6$, 7; (**d**) $N - 4$, 5; (**e**) $N - 2$, 3. Profiles of surface roughness R_a (bottom axis) dependence on the number of pulses in the burst (left axis) at different burst fluences: (**f**) 1.7 J/cm^2; (**g**) 2.3 J/cm^2; (**h**) 4.6 J/cm^2; (**i**) 9.9 J/cm^2. The surface roughness R_a created by ($N + 1$) pulse burst (right axis) dependence on surface roughness R_a created by N pulse burst (bottom axis) at different burst fluences (color scale): (**j**) $N - 8$; (**k**) $N - 6$; (**l**) $N - 4$; (**m**) $N - 2$. Pulse duration $\tau_{FWHM} - 210$ fs, laser wavelength $\lambda - 1030$ nm, burst repetition rate $f_{burst} - 100$ kHz, and the temporal distance between pulses in burst $t_{pulse} - 15.5$ ns (intra-burst pulse repetition rate $f_{pulse} - 64.7$ MHz).

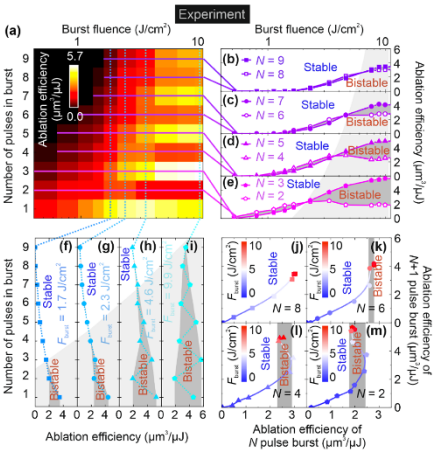

Figure 3. Experimental results of stable and bistable behavior of laser ablation efficiency. (**a**) Laser ablation efficiency of copper (color scale) dependence on the burst fluence (top axis) and the number of pulses in femtosecond burst (left axis), the squares indicated by black color is not measured points because of pulse laser fluence below the ablation threshold. Ablation efficiency (right axis) dependence on burst fluence (top axis) at different numbers of pulses in burst: (**b**) $N = 8, 9$; (**c**) $N = 6, 7$; (**d**) $N = 4, 5$; (**e**) $N = 2, 3$. Profiles of ablation efficiency (bottom axis) dependence on the number of pulses in the burst (left axis) at different burst fluences: (**f**) 1.7 J/cm^2; (**g**) 2.3 J/cm^2; (**h**) 4.6 J/cm^2; (**i**) 9.9 J/cm^2. Ablation efficiency of $(N+1)$ pulse in a burst (right axis) dependence on ablation efficiency of N pulse in a burst (bottom axis) at different burst fluences (color scale): (**j**) $N = 8$; (**k**) $N = 6$; (**l**) $N = 4$; (**m**) $N = 2$. Stable- and bi-stable laser efficiency regions are indicated by white and grey colors in (**b**–**m**). Pulse duration $\tau_{FWHM} = 210$ fs, laser wavelength $\lambda = 1030$ nm, burst repetition rate $f_{burst} = 100$ kHz, and the temporal distance between pulses in burst $t_{pulse} = 15.5$ ns (intra-burst pulse repetition rate $f_{pulse} = 64.7$ MHz).

3.3 to 9.9 J/cm^2 surface roughness, R_a was higher for an odd number of pulses in burst with the average relative surface roughness R_a difference of 31% (Fig. 2c).

The bi-stability effect of surface roughness R_a depending on the number of pulses in the burst can be seen when the profiles of the color plot depicted in Fig. 2a are extracted at constant burst fluence (Fig. 2f–i). For example, for $F_{burst} = 1.7$ J/cm^2 the surface roughness R_a sudden jumps are seen for every next number of pulses in a burst from $N = 1$ to $N = 6$ (Fig. 2f). The gradual decrease of the surface roughness R_a with an increasing number of pulses in a burst from $N - 1$ to $N - 9$ for larger values of burst fluence of $F_{burst} - 2.3$ J/cm^2 with small sudden jumps are observed (Fig. 2g). The decrease of the surface roughness R_a with an increasing number of pulses and larger values of burst fluence of $F_{burst} - 4.6$ J/cm^2 with large sudden jumps are observed (Fig. 2h). For the largest burst fluence of $F_{burst} - 9.9$ J/cm^2 the bi-stable regime with sudden jumps of drastic decrease of surface roughness R_a at even numbers ($N = 2$, 4, 6, and 8) of pulses is observed (Fig. 2i). This bi-stability regime of surface roughness R_a depending on the burst fluence can be seen when the surface roughness of N pulse burst depending on $(N+1)$ pulse burst is extracted from color plot Fig. 2a and depicted in (Fig. 2j–m). The bi-stable regimes occur because for surface roughness R_a every even number ($N = 2$, 4, 6, and 8) several possible values of surface roughness R_a exist corresponding $N+1$ odd numbers (3, 5, 7, and 9) every even number. The experimental results provided in Fig. 2 showed stable and bi-stable surface roughness R_a regions depending on the burst fluence and the burst length. The laser polishing regime with the lowest overall value of surface roughness R_a of 0.23 μm was found at the burst fluence of $F_{burst} - 4.6$ J/cm^2 and the number of pulses in a burst of $N - 6$.

Ablation efficiency

The ablation efficiencies dependence on laser fluence was investigated experimentally with the burst fluences ranging from 0.52 to 9.9 J/cm^2 and 9 different numbers N of pulses in the burst (1, 2, 3, 4, 5, 6, 7, 8, and 9). The experiment showed stable and bi-stable ablation efficiency depending on the laser processing parameters (Fig. 3).

The laser ablation efficiency dependence on the burst fluence and the number of pulses in the burst are depicted in Fig. 3a. The burst fluence was increased from 0.52 to 9.9 J/cm^2 and the number of pulses in the burst was increased from 1 to 9. The laser ablation efficiency was always smaller for even numbers (N = 2, 4, 6, and 8) than for odd numbers (N = 1, 3, 5, 7, and 9) of pulses in a burst if compared to the same burst fluence at large values (7–9.9 J/cm^2) (Fig. 3a). However, for small values of burst fluence (0.52–2.3 J/cm^2) opposite behavior could be observed with ablation efficiencies smaller for odd than for even numbers of pulses in the burst (except for N = 1) (Fig. 3a).

This stability and bi-stability effect of ablation efficiency depending on the burst fluence can be seen when the profiles of the color plot depicted in Fig. 3a are extracted at constant odd and even numbers of pulses in the burst (Fig. 3b–e). For example, for N = 8 the ablation efficiency was slightly higher than N = 9 up to fluencies of 7 J/cm^2, and then a switch to the opposite with a relative difference in efficiency only of 13% (Fig. 3b). The ablation regime can be characterized as stable up to a bust fluence of 7 J/cm^2 and small bifurcation starting when fluence exceeds 7 J/cm^2 (Fig. 3b). For N = 6 and N = 7 similar behavior was observed, however, more pronounced bifurcation was observed when burst fluence increased up to 4.6 J/cm^2 (Fig. 3c). When increasing fluence to 9.9 J/cm^2 the relative ablation efficiency difference increased up to 37% (Fig. 3c). This ablation regime can be called the bi-stable regime (Fig. 3c). Moreover, for N = 4 and N = 5 similar stable ablation efficiency up to 4.0 J/cm^2 is observed (Fig. 3d). However, an even more pronounced bifurcation burst fluence of 4.6 J/cm^2 was seen with the relative ablation efficiency difference increasing up to 64% (Fig. 3d). Further increase of bi-stability was observed for N = 2 and N = 3 pulses after exceeding 2.3 J/cm^2 the burst fluence with the relative ablation efficiency difference growing up to 101% (Fig. 3e).

The stability and bi-stability effect of ablation efficiency depending on the number of pulses in the burst can be seen when the profiles of the color plot depicted in Fig. 3a are extracted at constant burst fluence (Fig. 3f–i). For example, for F_{burst} = 1.7 J/cm^2 the ablation efficiency gradually decreases for an increasing number of pulses in a burst from N = 1 to N = 9 without any sudden jumps (Fig. 3f). A similar gradual decrease of the ablation efficiency with an increasing number of pulses in a burst from N = 1 to N = 9 for a larger value of burst fluence of F_{burst} = 2.3 J/cm^2 also without any sudden jumps are observed (Fig. 3g). The only exceptions and sudden jumps with a single decrease in ablation efficiency are observed for even numbers N = 2 (Fig. 3f,g). However, when moving to a larger burst fluence of F_{burst} = 4.6 J/cm^2 the bi-stable regime with two sudden jumps of drastic decrease of ablation efficiency at even numbers (N = 2 and 4) of pulses is observed (Fig. 3h). For the largest burst fluence of F_{burst} = 9.9 J/cm^2 the bi-stable regime with four sudden jumps of drastic decrease of ablation efficiency at even numbers (N = 2, 4, 6, and 8) of pulses is observed (Fig. 3i). The largest overall value of ablation efficiency of 5.66 μm^3/μJ is observed at the burst fluence of F_{burst} = 9.9 J/cm^2 and the number of pulses in a burst of N = 3. It exceeded by 1% the highest laser milling efficiency for copper reached in our previous work[11]. This stability and bi-stability regimes of ablation efficiency depending on the burst fluence can be seen when the ablation efficiencies of N pulse burst depending on (N + 1) pulse burst is extracted from color plot Fig. 3a and depicted in (Fig. 3j–m). The completely stable regime is observed for a large pulse value N = 8, with a line-type curve for all burst fluences ranging from 0.52 to 9.9 J/cm^2 (Fig. 3j). The straight-line curve means that for one value of ablation efficiency at a burst-pulse number of N = 8 there is only one possible value of ablation efficiency for burst pulse number of (N + 1) = 9. Therefore, the regime is completely stable, and there are no sudden jumps in ablation efficiency observed. A similar stable regime is observed for the smaller pulse value of N = 6 with a line-type curve for burst fluences ranging from 0.52 to 4.6 J/cm^2 (Fig. 3k). For fluences from burst fluences ranging from 4.6 to 9.9 J/cm^2 the line goes upwards, therefore, the beginning of bi-stability is observed (Fig. 3k). The bi-stable regime occurs when the number pulse value decreases to N = 4, with a parabola-type curve for burst fluences ranging from 4.6 to 9.9 J/cm^2 (Fig. 3l). The parabola-like curve is always bi-stable because for one single value of ablation efficiency at a burst-pulse number of N = 4 there are two possible values of ablation efficiency for a burst-pulse number of (N + 1) = 5. The complete bi-stability in ablation efficiency is seen in the number of pulse values decreasing to N = 2, with a parabola-type curve for burst fluences ranging from 2.3 to 9.9 J/cm^2 (Fig. 3m). The experimental results provided in Fig. 3 showed stable and bi-stable ablation efficiency regions depending on the burst fluence and the burst length. Further in this work, we will provide graphical assumptions and basic principles of the shielding effect by the cloud of ablation products (particles, vapor, and plasma) in the laser ablation efficiency of parabolic dimple, which later will be included in our analytical and numerical modeling.

Shielding versus re-deposition

The bi-stable behavior of ablation efficiency initiated by bursts of ultrafast pulses has been reported in numerous of scientific papers for copper[6,11,13,16,17], brass[35] and aluminum[35]. The shielding or/and re-deposition has been identified main reasons of bi-stable behavior of ablation efficiency depending in the pulse number in burst in most of the research works (Table 1).

Shielding together with the redeposition effect are wildly attributed to bistable ablation efficiency in the field, however, the mostly it is only hypothesis with no direct observation of the phenomenon. The shielding and re-deposition of copper target has been experimentally studied by shadowgraph technique with similar experimental conditions (wavelength 1030 nm, pulse duration 400 fs, repetition rate 400 kHz, delay between pulses 12.2 ns, fluence 0.69 J/cm^2, spot diameter 44 μm)[17]. The shielding effect by ablation cloud has been directly visualized via the shadowgraph technique, however, no clear experimental evidence of re-deposited material was seen[17]. Generally, for the re-deposition, the negative ablation depth for the second sub-pulse in burst is supposed to be measured, resulting the efficiency decrease for two sub-pulse burst below 50%, if compared with a single pulse ablation efficiency of 100%. Since some material ejected by the first pulse is reposited by the second, and the total volume ablated by both pulses is less than that ablated by a single first pulse is divided by double pulse energy of two sub-pulses. Even though, we see such efficiency drop down to 38% in our experiment: at single

Material	Irradiation mode	Pulse duration	Wavelength (nm)	Distance between pulses	Indicated bistability reason	References
Cu	Burst	2 ps	1030	25 ns	Shielding or re-deposition	6
Cu	Burst, bi-burst	210 fs	1030	15.5 ns, 205 ps	Shielding or re-deposition	11
Cu, Kevar	Burst	1.5 ps	1064	2.3 ps	–	13
Cu	Burst	10 ps–210 fs	1030	15.5 ns	Shielding and redeposition	16
Cu	Burst	400 fs	1030	12.2 ns	Shielding and redeposition	17
Al	Burst	350 fs	1035	17 ns	Shielding or re-deposition	35
Brass	Burst	350 fs	1035	25 ns	Shielding or re-deposition	35

Table 1. Scientific literature review of bistability in ablation efficiency depending on pulse number in burst with indicated reason of bistable behavior.

pulse ablation with peak pulse fluence of 4.6 J/cm^2 for most efficient ablation of 5.3 μm^3/μJ to efficiency drop of 2.0 μm^3/μJ for double pulse ablation with peak pulse fluence of 4.4 J/cm^2. We believe that this can be assumed as experimental evidence of re-deposition in our experimental conditions. However, for the simplicity of our toy model we neglected re-deposition and concentrated to the shielding by ablation cloud.

Toy model

The two-dimensional (2D) and three-dimensional (3D) graphical representation of the new toy model for laser ablation of parabolic dimples including the shielding effect of every next pulse by the cloud of ablation products created by every previous pulse is presented in Fig. 4.

Principal 3D scheme of the target material irradiated by a laser burst with the specified target material, the parabolical shape dimple ablated by the 1st pulse of the burst, the ablation debris cylindrical cloud resulting from the 1st pulse above the ablated crater, indicated by pink transparent color, the burst with the remaining five (2nd, 3rd, 4th, 5th, and 6th) pulses indicated by purple ellipsoids, the direction of propagation of the laser burst indicated by a pink arrow, and indicated *xyz* Cartesian coordinate system is depicted Fig. 4a. 2D cross-sections on a 3D image of the target material with a parabolic dimple ablated by the first pulse in the burst, the ablation debris cloud resulting from the first pulse, and the second pulse in the burst, are represented in Fig. 4b. A principal behavior of the ablated volume per pulse on pulse sequence number in burst for stable and bi-stable ablation scenarios is provided in Fig. 4c,d, respectively. The 2nd pulse is partially shielded by the debris cloud created by 1st pulse, so its intensity decreases exponentially according to the Beer-Lambert-Bouguer absorption law, depending on cloud thickness and the concentration of particles, vapor, and plasma in the cloud. The ablated volume of the 2nd pulse is always smaller than the ablated volume of the first pulse because of shielding. At low burst fluence, the ablation is stable and the ablation volume per pulse is similar in size for all pulse numbers except ($n = 1$) (Fig. 4c), but at high burst fluence the ablation is bi-stable and at even number of pulses the ablation volume per pulse is larger than for the odd pulse number (Fig. 4d). The graphical representation of a cross-section of the 2D geometry with the parabolic cavity ablated by the second pulse, and the cloud of ablation products (particles, vapors, and plasma) above the cavity is indicated by the cyan rectangle for a stable ablation process at low burst fluence provided in Fig. 4e, and for bi-stable ablation process at high burst fluence in Fig. 4f. At low fluence the medium size ablated volume is removed from the material by the first pulse which creates a thin cloud at low concentration, therefore, a weak shielding effect is observed. It results in a minor change in laser fluence at the target material for the second pulse, and it causes almost the same ablated volume per pulse. The process continues for every next pulse in burst and stable ablation with constant ablated volume per pulse Fig. 4e. At high fluence the large size ablated volume is removed from the material by the first pulse which creates a thick cloud at high concentration, therefore, a strong shielding effect is observed. It results in a major change in laser fluence at the target material for the second pulse, and it causes a big decrease in ablated volume per pulse for the second pulse. The process continues for every next pulse in burst and bi-stable ablation with jumping ablated volume per pulse observed Fig. 4f. The graphical representation of the sequence of the ablation process for the burst with the length of $N = 6$ pulses for the stable ablation with volume per pulse constant for every pulse is given in Fig. 4g and for the bi-stable ablation with jumping volume per pulse is given in Fig. 4h. The dashed lines indicate the volume ablated with each of the pulses during the burst irradiation. The amount of ablation products is directly related to the volume ablated by the first pulse, thus, the volume ablated by the second pulse depends on the volume ablated by the first pulse. A similar relationship can be extended for every next pulse (third, fourth, fifth, sixth, etc.). Furthermore, the generalized rule for the $(n+1)$th pulse ablation efficiency and its dependence on the ablation efficiency of the previous nth pulse, because partial shielding by the cloud created by nth pulse, can be created. Further in the work, we will provide detailed analytical and numerical modeling of the shielding effect by ablation products (particles, vapor, and plasma) which was included in toy model of the laser ablation efficiency of parabolic dimple for the first time.

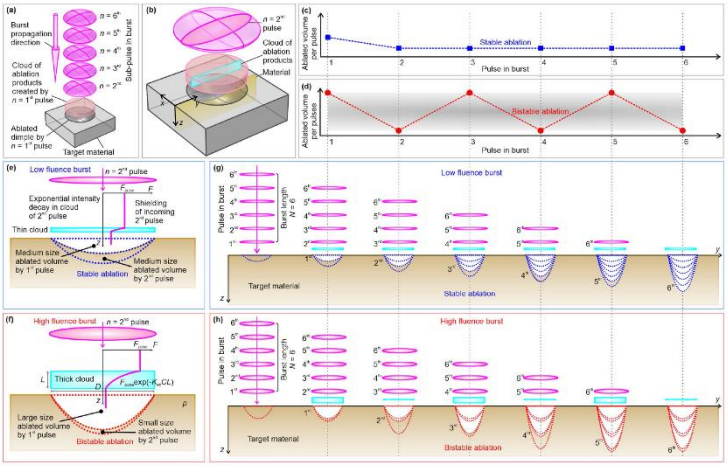

Figure 4. Graphical representation of toy model of the laser ablation with shielding effect and stable or bi-stable ablation. (**a**) 3D representation of target material irradiated with laser burst with the indicated target material, parabolic dimple ablated by 1st pulse in the burst, the cloud of ablation debris created by the first pulse in position above the dimple with cylindrical shape indicated by pink transparent color, the burst with five remaining (2nd, 3rd, 4th, 5th, and 6th) pulses indicated by magenta ellipsoids, and the burst propagation direction indicated by the pink arrow. (**b**) 2D cross-section on the 3D representation of target material with parabolic dimple ablated by the first pulse in the burst, cloud of ablation debris created by the first pulse, and the second pulse in a burst. Schematic representation of ablated volume per pulse dependence on the pulse in burst: (**c**) stabile ablation (blue color—low burst fluence), (**d**) bi-stable ablation (red color—high burst fluence). The second pulse in the burst is partially shielded by the debris cloud, therefore, with exponential intensity drop defined by the Beer-Lambert-Bouguer absorption law. The volume ablated by the second pulse is always smaller than the volume ablated by the first pulse in the burst. For the low burst fluence ablation is stable with a similar ablated volume per pulse (**c**), however, for high burst fluence ablation is bistable with a large ablated volume per pulse for an even number, and small for the odd number of pulses per burst (**d**). 2D cross-section of geometry with indicated parabolic dimple ablated by the second pulse and the cloud of ablation products (particles, vapor, and plasma) above the dimple is indicated by cyan rectangle: (**e**) stabile ablation (low burst fluence), (**f**) bistable ablation (high burst fluence). The sequence of ablation using burst with the burst length of $N-6$ pulses: (**g**) stabile ablation, (**h**) bi-stable ablation. Dashed lines where blue (stable ablation) and red (bi-stable ablation) lines indicate the volume ablated by each of the pulses in a burst in (**e**–**h**).

In our ablation model, the partial shielding of the incoming pulse by the cloud of ablation products created by the previous pulse in the burst is taken into account. The dimple with the shape of a paraboloid of revolution is created by ablation with the first pulse in the burst. The cloud of ablation debris is created above the dimple ablated by the first pulse. The second pulse in the burst is partially shielded by the debris cloud, as a consequence, the pulse with the smaller intensity reaches the target material, therefore, the volume ablated by the second pulse is affected by the volume ablated by the first pulse. If the large volume is ablated by the first pulse, then a big cloud of ablation debris is created, and shielding of the next pulse greatly influences the amount of radiation that reaches the sample. Therefore, the ablated volume of the second pulse is very low. It also creates a very small amount of ablation debris. Thus, the third pulse is not shielded by the cloud and the volume ablated by the third pulse is large again. And the bistable ablation rate with a large ablated volume for the odd numbers of pulses (first, third, fifth, etc.) and a small ablated volume of even numbers of pulses (second, fourth, sixth, etc.) continues. In general, the ablation efficiency of $(n+1)$th pulse is influenced by the ablation efficiency of the nth pulse, because the intensity of $(n+1)$th is partially shielded by the cloud created by nth pulse, and the part of absorption is proportional to the ablation efficiency of the nth pulse. The ablated volume V_n per pulse in the burst can be expressed by[32–34]:

$$V_n = \frac{\pi w^2 \delta}{4} \ln\left(\frac{F_n}{F_n^{\text{th}}}\right)^2, \tag{2}$$

where n is the integer number indicating the position of the pulse in the burst, w is the Gaussian beam radius on the surface of the sample, δ is effective penetration depth, F_n is peak laser fluence in the center of the beam of n pulse, F^{th}_n is the ablation threshold, which depends on the number $(n-1)$ of previous pulses which has already affected the material. The surface of the target material is modified after each successive pulse. For example, after the first pulse, it is expected that for the second pulse, the target surface is no longer flat, and is expected to have a parabolically shaped surface, with certain roughness. However, mathematically there is no equation describing ablated volume by Gaussian beam depending on fluence on the parabolically shaped surface with a certain roughness, thus we use approximation with the same formula (2) for the multi-pulse regime, neglecting surface modifications by previous pulses. A similar approach has been used in pioneering research works related to fluence optimization for max efficiency, where the volume of all succeeding pulses in a multi-pulse regime has been calculated by the same equations, nevertheless, the model had good coincidence experiment[32–34].

In our proposed ablation model, we assume, that, the incoming laser fluence of the nth pulse is attenuated by a cloud of particles, vapor, and plasma created from ablation products of $(n-1)$ pulse in a burst. We further show the derivations of the mathematical expression of the ablation efficiency recurrence relation. The mass m_N of ablation products created by nth pulse can be expressed:

$$m_n = \rho V_n = C_n L_n \frac{\pi D_n^2}{4}, \tag{3}$$

where ρ is the abated material density, V_n is the volume ablated by nth pulse described by Eq. (2), C_n is the total concentration of shielding cloud (particles, vapor, and plasma), L_n is the averaged cloud thickness, and D_n cloud diameter (see Fig. 4f). It is assumed in our model, that that cloud diameter is approximately equal to the ablated dimple diameter by nth pulse:

$$D_n^2 = 2w^2 \ln\left(\frac{F_n}{F_n^{\text{th}}}\right). \tag{4}$$

It is also considered, that the cloud of ablation products expands fast in longitudinal beam propagation z-direction. The lateral expansion of plume at 15 ns time scale might be significant, however, the recent research work shows the plasma expansion induced by femtosecond laser with a wavelength of 800 nm pulse duration of 50 fs is in the longitudinal direction rather than in the transverse one up to 100 ns[35]. The semi-spherical shock wave is usually recorded with expansion in both longitudinal and transverse directions, however, plasma plume expansion is mostly exposed in the longitudinal direction. The mechanisms of ultrafast GHz burst fs laser ablation of copper have been recently investigated by time-resolved scattering imaging, emission imaging, and emission spectroscopy in[37]. Similar conditions to our experimental setup have been used utilizing pulses with 500 fs duration at 1030 nm and GHz fs bursts (50 and 200 pulses at 1.28 GHz repetition rate) with focused beam diameter of 16 µm. After single-pulse irradiation, Cu plasmas were observed for approximately 30 ns. Also, Cu nanoparticle ejections with speeds ranging from 100 m/s to 350 m/s have been recorded, depending on particle type. At such speeds, the copper particles travel from 1.6 to 5.4 µm distances during sub-pulse delay of 15.5 ns, and from 12.4 to 43.4 µm, during 9 sub-pulse burst duration of 124 ns, which are comparable to spot radiuses ranging from 21 to 95 µm used in our experiments. Thus, it can be considered that the transverse expansion of the plasma plume can be neglected with some tolerance, as cloud expansion is much slower in transverse x- and y-directions since ejected particles have the velocity vectors mostly in the z-direction[38–40]. Therefore, for the short time interval, the shielding cloud concentration multiplied by the average cloud thickness will be constant and equal to ablated mass divided by dimple area as $C_n L_n = 4\, m_n/(\pi D_n^2) = \text{const.}$, because the diameter squared of ablated area, and ablated mass remains constant. It is assumed in our ablation model that, the incoming laser radiation is attenuated by the shielding effect which results in a decrease of incident fluence which reaches the material and results in a decrease in laser ablation efficiency. Thus, the attenuated fluence that reaches the surface of target materials after passing through a cloud of ablation products can be expressed by Beer-Lambert-Bouguer absorption law[41,42]:

$$F_{n+1} = F_{\text{pulse}} \exp\left(-K_{\text{eff}} C_n L_n\right), \tag{5}$$

where K_{eff}—effective shielding coefficient which takes into account attenuation by particles, vapor, and plasma generated by the previous pulse. By analytically solving Eqs. (1), (2), (3), (4) and (5) we get the final equation of the ablation efficiency of $(n+1)$th pulse, which is influenced by ablation efficiency by the previous nth pulse:

$$\eta^{\text{pulse}}_{n+1} = \frac{\delta}{2F_{\text{pulse}}}\left(\ln\left(\frac{F_{\text{pulse}}}{F^{\text{th}}_{n+1}}\right) - K_{\text{eff}}\rho\sqrt{\frac{\delta F_{\text{pulse}} \eta^{\text{pulse}}_n}{2}}\right)^2. \tag{6}$$

The detailed derivation of Eq. (6) is provided in the Methods section. This type of equation is known as recurrence relation because the efficiency $\eta^{\text{pulse}}{}_{n+1}$ of $(n+1)$th pulse is a function of efficiency $\eta^{\text{pulse}}{}_n$ of nth pulse as $\eta^{\text{pulse}}{}_{n+1} = f(\eta^{\text{pulse}}{}_n)$, mathematically defined by Eq. (6). Bi-stability, as well as sudden jumps, occur in ablation efficiency depending on the number of pulses in bursts with the response to changes of the control parameter

peak laser fluence in the pulse F_{pulse}. Further research has been conducted in this work, to compare theoretical modeling using Eq. (6) results with experimental data provided in Fig. 3.

The ablation threshold of $(n+1)$th pulse dependence on the number of pulses n applied before can be expressed as[43,44]:

$$F_{n+1}^{th} = F_{\infty}^{th} + \left(F_1^{th} - F_{\infty}^{th}\right)e^{-kn}, \tag{7}$$

where F^{th}_1 is the single-shot threshold, the F^{th}_∞ multi-shot threshold, k is the empirical parameter in the exponent which characterizes the strength of incubation leading to an early reduction of the threshold. The ablation efficiency dependence on the peak laser fluence F_{pulse} in the pulse for the first pulse in the burst (single pulse irradiation regime) can be evaluated by using classical Eq. (1). The experiment results have good agreement with the numerical calculation results of ablation efficiency for single pulse irradiation (see Fig. 1e). By having calculated the ablation efficiency for the single pulse η^{pulse}_1, it is easy to calculate the ablation efficiency for the second η^{pulse}_2 using Eq. (6). Then, knowing the ablation efficiencies η^{pulse}_2 for the second pulse, the efficiency η^{pulse}_3 for the third pulse in the burst using can be easily calculated in same Eq. (6). Similarly, having η^{pulse}_3 one can easily calculate η^{pulse}_4, and having η^{pulse}_4 easy to calculate η^{pulse}_5, etc. Later, the ablation efficiency of the burst η^{burst}_N can be evaluated as the average value of ablation efficiencies of all pulses in the burst η^{pulse}_n:

$$\eta_N^{burst} = \frac{1}{N}\sum_{n=1}^{N}\eta_n^{pulse}, \tag{8}$$

where N is the number of the pulses in the burst (burst length), n is the number indicating the position of the pulse in the burst. The burst fluence F_{burst} can be computed by multiplying a single pulse fluence by the burst length as $F_{burst} = NF_{pulse}$. The single pulse fluence F_{pulse} was recalculated to the burst fluence in the numerical computation and the experiment.

Simulation versus experiment

The laser ablation efficiency for copper has been tested experimentally and theoretically at burst different fluences and burst lengths. The ultrafast laser with duration $\tau_{FWHM} = 210$ fs, laser wavelength $\lambda = 1030$ nm, burst repetition rate $f_{burst} = 100$ kHz, the temporal distance between pulses in burst $t_{pulse} = 15.5$ ns (intra-burst pulse repetition rate $f_{pulse} = 64.7$ MHz) was used to ablate an array of rectangularly shaped cavities in the copper plate, and ablation efficiency was measured (Fig. 5a,c).

Equations (6), (7), and (8) have been numerically solved by using symbolic and numeric computing software (Maple, Maplesoft). The parameters values used in numerical simulation of toy model equations together, with parameter values obtained in this work as fit of experimental data points together with closest literature values reported for copper using similar laser is provided in Table 2.

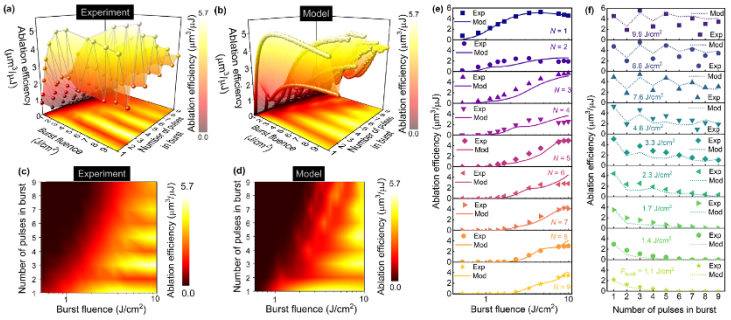

Figure 5. Comparison of the experimental data to the results of theoretical toy modeling. Laser ablation efficiency of copper (color scale) dependence on the burst fluence and the number of pulses in femtosecond burst: (**a**, **b**) 3D views and (**c**, **d**) 2D maps of experimental and modeling results. (**e**) 1D profiles of ablation efficiency dependence on burst fluence at different numbers of pulses in burst ranging from $N = 1$ (top) to $N = 9$ (bottom). (**f**) 1D profiles of ablation efficiency dependence on the number of pulses in a burst at different burst fluences ranging from $F_{burst} = 1.7$ J/cm² (bottom) to 9.9 J/cm² (top). Experimental data points (dots) are quantitatively compared with the predictions of our theoretical model (lines) in (**e**, **f**). Laser parameters: pulse duration $\tau_{FWHM} = 210$ fs, laser wavelength $\lambda = 1030$ nm, burst repetition rate $f_{burst} = 100$ kHz, the temporal distance between pulses in burst $t_{pulse} = 15.5$ ns (intra-burst pulse repetition rate $f_{pulse} = 64.7$ MHz).

Physical parameter	Used in toy model simulation	Achieved in this work as fit of experimental data	Closest literature value	Literature laser parameters	References
F^{th}_1 (J/cm^2)	0.59	0.59 ± 0.02	0.51 ± 0.08	1030 nm, 280 fs, 60 kHz	[45]
δ (nm)	113	113 ± 5	115	1030 nm, 10 ps, 1 kHz	[46]
F^{th}_∞ (J/cm^2)	0.21	–	0.211	800 nm, 250 fs, 1 kHz	[47]
k	0.9	0.84 ± 0.14	F^{th}_2 = 0.4 J/cm^2 F^{th}_3 = 0.25 J/cm^2 F^{th}_{20} = 0.2 J/cm^2	1030 nm, 500 fs, 100 kHz, 25 ns	[21]
ρ (g/cm^3)	8.96	–	8.96	–	[48]
K_{eff} (m^2/g)	2.5	–	μ/ρ_m = 8.8 m^2/g	1050 nm	[37]

Table 2. Physical parameter values used in toy model simulations together with values retrieved in this work as fit parameters of experimental data points and its comparison to closest literature values obtained for copper using similar laser.

The fit parameters $F^{th}_1 = 0.59 \pm 0.02$ J/cm^2, $\delta = 113 \pm 5$ nm were achieved as a fit of experimental data by Eq. (1) in Fig. 1e. This is a standard procedure for obtaining two physical parameter values to define a single pulse ablation threshold and effective penetration depth. The obtained threshold value coincides well with the single pulse threshold literature value $F^{th}_1 = 0.51 \pm 0.08$ J/cm^2 obtained with a similar laser (1030 nm, 280 fs, 60 kHz)[45]. It also corresponds well to literature values of copper oxide removal threshold of $F^{th}_1 = 0.57 \pm 0.03$ J/cm^2 (1064 nm, 10 ps, 100 kHz)[49] and $F^{th}_1 = 0.62$ J/cm^2 (1064 nm, 12 ps, 100 kHz)[50]. However, slightly higher copper ablation threshold values were obtained with femtosecond lasers at shorter wavelength $F^{th}_1 = 0.87$ J/cm^2 (800 nm, 130 fs, 1 kHz)[51] and $F^{th}_1 = 0.86$ J/cm^2 (800 nm, 250 fs, 1 kHz)[47]. A similar single pulse penetration depts of $\delta = 115$ nm has been declared in literature for a similar for laser (1030 nm, 10 ps, 1 kHz)[46]. Those parameters ($F^{th}_1 = 0.59$ J/cm^2, $\delta = 113$ nm) were used in further numerical simulations of toy model equations. The value of multi-shot ablation threshold of $F^{th}_\infty = 0.21$ J/cm^2 was used in toy modeling and was taken from literature as closest multi-pulse threshold value of $F^{th}_{1000} = 0.211$ J/cm^2 experimentally retrieved using similar femtosecond laser (800 nm, 250 fs, 1 kHz)[47]. It coincides well with other literature multi-pulse threshold values of $F^{th}_{1000} = 0.19$ J/cm^2 (1064 nm, 10 ps, 100 kHz)[25] and $F^{th}_\infty = 0.18$ J/cm^2 (800 nm, 130 fs, 1 kHz)[51]. The incubation strength of $k = 0.9$ was used in numerical calculations of toy model. The similar value of $k = 0.84 \pm 0.14$ was retrieved as fit parameter by Eq. (7) utilizing copper ablation threshold values with highest decay ($F^{th}_2 = 0.4$ J/cm^2, $F^{th}_3 = 0.25$ J/cm^2, and $F^{th}_{20} = 0.2$ J/cm^2) experimentally obtained by femtosecond 40 MHz burst laser (1030 nm, 500 fs, 100 kHz, 25 ns) in[21]. Similar values of $k = 0.9 \pm 0.7$ (10 kHz) and $k = 0.6 \pm 0.3$ (1 MHz) were retrieved as fit parameter by Eq. (7) utilizing experimental multi-pulse copper threshold values obtained using green picosecond 82 MHz burst laser (532 nm, 10 ps, 10 kHz–1 MHz, 12.2 ns) in[52]. In all our fits of copper threshold literature values by Eq. (7) the constant single pulse and multi-shot threshold values $F^{th}_1 = 0.59$ J/cm^2 and $F^{th}_\infty = 0.21$ J/cm^2 were used. The density of solid copper of $\rho = 8.96$ g/cm^3 was used in numerical calculations[48].

The only one physical constant used a free parameter in our toy model simulations was the attenuation coefficient of ablation cloud K_{eff}, because its value could not be found in the scientific literature. Nevertheless, we used a value which is comparable to mass attenuation coefficient (also known as the mass absorption coefficient) of solid or liquid copper. The absorption coefficient of solid copper can be evaluated by Eq. (18) utilizing, the extinction coefficient of $\kappa = 6.59$ for copper at $\lambda = 1050$ nm wavelength reported in[53], which gives the absorption coefficient of $\mu = 7.9 \times 10^5$ 1/cm. The mass attenuation coefficient can be evaluated by Eq. (19), having solid copper mass density of $\rho_m = \rho = 8.96$ g/cm^3, one can evaluate the mass absorption coefficient of $\mu/\rho_m = 8.8$ m^2/g. The ablation cloud mostly consists of copper vapor, copper nanoparticles and liquid copper, therefore, evaluation the mass attenuation coefficient for liquid copper would make sense. The density of molten copper of $\rho_m = 7.90$ g/cm^3 and extinctions efficient $\kappa = 2.94$ at $\lambda = 532$ nm wavelength can be taken from[37]. It gives the absorption coefficient of $\mu = 7.0 \times 10^5$ 1/cm and mass attenuation coefficient of $\mu/\rho_m = 8.9$ m^2/g for liquid copper. However, for example the extinction coefficient and absorptivity of nanoparticles might be several times lower than the bulk which also depends on the wavelength[54]. Taking it to account that ablation cloud consists of plasma, vapor, nanoparticles and liquid copper, causing internal reflections and light scattering within the cloud, the reduction of attenuation should be considered. We have chosen approximately three the half times lower attenuation coefficient of $K_{eff} = 2.5$ m^2/g than evaluated for liquid or bulk copper for our toy model simulations of the ablation cloud which gave the best coincidence of numerical to the experimental results. In real experimental conditions, the absorption coefficient of plasma is not constant, because it depends on density and temperature of ablation cloud, and it should drastically differ for odd and even pulses. The similar behavior should also apply to effective penetration depth. However, we wanted to keep our toy model as simple as possible, with all coefficients as constant values.

The calculated ablation efficiency versus burst fluence and burst length is given in Fig. 5b,d, which is in good agreement with experimental data provided in Fig. 5a,c. Furthermore, the data of experimentally measured ablation efficiencies were quantitatively compared to the numerical computation results of the model equations in Fig. 5e,f. The series of cross-sections from the experiment data and modeling results with burst lengths ranging from $N = 1$ to $N = 9$ is shown as a function of burst fluence (Fig. 5e). Our simulation results at each value of the number of pulses in bursts were in good agreement with the ablation efficiency measurements. Also, the series of cross-sections from the experiment data and modeling results with burst fluences ranging from $F_{burst} = 1.7$ J/cm^2 to 9.9 J/cm^2 are shown as a function of burst length (Fig. 5f). The results of numerical computation of our

new toy model equations at each value of the burst fluence were also in good coincidence with experimental values of the ablation efficiency.

3D cavity milling

The burst mode laser micro-machining quality was evaluated by milling a complicated periodical 3D cavity, utilizing a layer-by-layer removal method[16], starting at the sample's top, and ending at the cavity bottom, where the micro-machining was accomplished (Fig. 6).

The 3D computer-aided design model of the cavity with a rectangular array of overlapping hemispheres, similar to compound eyes[55,56] was created (Fig. 6a). The rendered CAD visualization reflected light by an array of overlapping hemispheres with perfect smoothness is depicted in Fig. 6b. The CAD model was sliced into parallel layers with constant thickness by using special software (DMC PRO, Direct Machining Control). After each of the layers was removed, the distance between the focusing lens and the sample surface was modified to keep the beam diameter and its related optimal laser fluence on the ablated surface. The burst fluence was set at 9.9 J/cm^2, and the 3 pulses per burst regime was chosen as processing parameters for the most efficient ablation using burst mode. Complex periodical 3D cavities of overlapping hemispheres were laser machined with a material removal rate of 2.48 mm^3/min (Fig. 6c). The high-quality cavity bottom was smooth with a surface roughness R_q of 0.4 µm. The specimen was further polished with burst of fluence of $F_{burst} = 4.6$ J/cm^2 and the number of pulses in a burst of $N = 6$ and surface roughness R_q of 0.23 µm was reached at plain areas of the copper specimen. The rainbow coloring is seen because of the laser-induced periodical surface structures (LIPSS)[23,57,58] or oxidation and nanostructures[59] created by the laser polishing procedure[60] (Fig. 6c). The sunlight reflected light by laser milled array of overlapping hemispheres is depicted in Fig. 6d.

Conclusions

To conclude, the shielding effect was included in the toy model of laser ablation efficiency using MHz burst irradiation for the first time in this work. The incoming laser radiation attenuation by plasma, vapor, and particle cloud which was created from ablation products of the previous pulse was incorporated by modeling equations of ablation efficiency. The numerical results of model equations showed stable and bi-stable ablation efficiency depending on the burst fluence and burst length which coincided well with the experimental data. The ablation

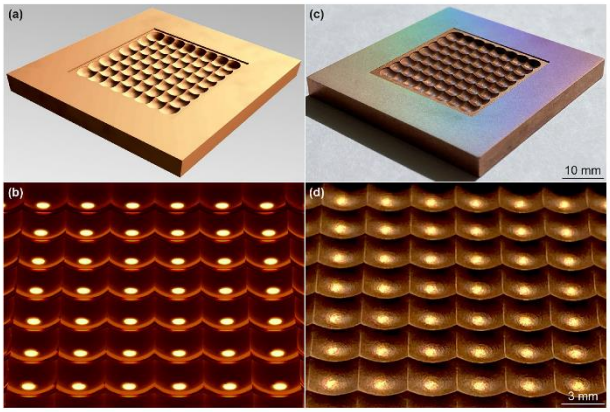

Figure 6. Examples of efficient laser layer-by-layer milling of 3D cavity in copper plate: (**a**) CAD model rectangular array of overlapping hemispheres (compound eye); (**b**) rendered CAD visualization perfectly smooth array of overlapping hemispheres; (**c**) digital camera image of laser milled part with an array of overlapping hemispheres; (**d**) image of the light refraction by laser milled array of overlapping hemispheres. Laser parameters: $N = 3$ pulses per burst, pulse duration $\tau_{FWHM} = 210$ fs, laser wavelength $\lambda = 1030$ nm, burst repetition rate $f_{burst} = 100$ kHz, the temporal distance between pulses in burst $t_{pulse} = 15.5$ ns (intra-burst pulse repetition rate $f_{pulse} = 64.7$ MHz), the lateral distance between bi-directional beam scanning lines of $h = 10$ µm, beam scanning speed of $v_s = 0.33$ m/s, laser power output $P = 7.3$ W, bust fluence $F_{burst} = 9.9$ J/cm^2, ablation efficiency $\eta = 5.66$ µm^3/µJ, material removal rate $dV/dt = 2.48$ mm^3/min, copper plate dimensions $50 \times 50 \times 5$ mm^3, laser milled cavity transverse dimensions 30×30 mm^2, max milled depth 2.0 mm.

was stable for small values of burst fluence and/or large values of burst length because the small amount of ejected material by the previous pulse caused a weak shielding effect for the next pulse and resulted in small or almost no variation in ablation volume per pulse. However, at the high burst fluence values and/or low burst lengths, the high amount of ejected material by the previous pulse caused a strong shielding effect and a drastic decrease in ablated volume per pulse for the next pulse for every even number of femtosecond pulse in the MHz burst. The stability and bi-stability in ablation efficiency were controlled by varying the laser fluence and the number of pulses in the burst. The maximal possible laser milling efficiency with the value of 5.66 $\mu m^3/\mu J$ which exceeds the highest value recorded in scientific literature has been achieved in our work by choosing optimal burst fluence together with burst length. Complex 3D cavities of high quality were laser machined and further polished by using burst processing regimes with the highest ablation rate and lowest roughness.

Methods

Detailed description of the toy model

Here we derive the recurrence relation of ablation efficiency leading to bi-stability. The ablation crater created by Gaussian beam pulse has parabolic shape, with characteristic volume, depending on beam radius, effective penetration depth, peak fluence to threshold ratio, which was mathematically derived and justified in research works[32–34]. Depth of laser ablated parabolic dimple ablated by nth pulse in the burst:

$$H_n = \delta \ln\left(\frac{F_n}{F_n^{\text{th}}}\right), \tag{9}$$

where δ is effective penetration depth, F_n is peak laser fluence in the center of the beam of n pulse, $F^{\text{th}}{}_n$ is the ablation threshold, depending on the number of pulses applied. Diameter of laser ablated parabolic dimple ablated by nth pulse in the burst:

$$D_n^2 = 2w^2 \ln\left(\frac{F_n}{F_n^{\text{th}}}\right), \tag{10}$$

where w is the Gaussian beam spot radius on the sample surface. The volume of the dimple with the shape of a paraboloid of revolution:

$$V_n = \frac{\pi}{8} H_n D_n^2. \tag{11}$$

The volume of laser ablated dimple by nth pulse in the burst expressed using Eqs. (9), (10), and (11):

$$V_n = \frac{\pi}{4} w^2 \delta \ln\left(\frac{F_n}{F_n^{\text{th}}}\right)^2. \tag{12}$$

The peak laser fluence in the Gaussian beam in the pulse:

$$F_{\text{pulse}} = \frac{2E_{\text{pulse}}}{\pi w^2}, \tag{13}$$

where E_{pulse} is the pulse energy of nth pulse in the burst. Ablation efficiency of nth pulse:

$$\eta_n^{\text{pulse}} = \frac{V_n}{E_{\text{pulse}}}. \tag{14}$$

By combining Eqs. (12), (13), and (14) we get the final expression ablation efficiency of nth pulse:

$$\eta_n^{\text{pulse}} = \frac{\delta}{2F_{\text{pulse}}} \ln^2\left(\frac{F_n}{F_n^{\text{th}}}\right). \tag{15}$$

From (15) we can also obtain ablation efficiency for $(n+1)$th pulse:

$$\eta_{n+1}^{\text{pulse}} = \frac{\delta}{2F_{\text{pulse}}} \ln^2\left(\frac{F_{n+1}}{F_{n+1}^{\text{th}}}\right). \tag{16}$$

Shielding of $(n+1)$th pulse by attenuation of ablation cloud created by nth pulse expressed by Beer-Lambert-Bouguer absorption law:

$$F_{n+1} = F_{\text{pulse}} \exp\left(-K_{\text{eff}} C_n L_n\right), \tag{17}$$

where K_{eff}—effective shielding coefficient which takes into account attenuation by particles, vapor, and plasma generated by the previous pulse, C_n is the total concentration of shielding cloud (particles, vapor, and plasma), L_n is the averaged cloud thickness. The absorption coefficient of cloud can be expressed[54,61]:

$$\mu = \frac{4\pi\kappa}{\lambda}, \tag{18}$$

where κ is the extinction coefficient (imaginary part of refractive index) and λ is the wavelength of irradiation. The mass attenuation coefficient (also known as the mass absorption coefficient) can be evaluated as[62,63]:

$$\frac{\mu}{\rho_{\mathrm{m}}}, \tag{19}$$

where ρ_m is the mass density of the cloud. The mass attenuation coefficient μ/ρ_m of liquid or solid copper can be used as effective shielding coefficient K_{eff} with some tolerance in our toy model since attenuation coefficient values of ablation cloud are not available in scientific literature.

From (16) and (17) we get an expression of ablation efficiency for $(n+1)$th pulse:

$$\begin{aligned}\eta_{n+1}^{\mathrm{pulse}} &= \frac{\delta}{2F_{\mathrm{pulse}}}\ln^2\left(\frac{F_{\mathrm{pulse}}\exp\left(-K_{\mathrm{eff}}C_nL_n\right)}{F_{n+1}^{\mathrm{th}}}\right)\\ &= \frac{\delta}{2F_{\mathrm{pulse}}}\left(\ln\left(\frac{F_{\mathrm{pulse}}}{F_{n+1}^{\mathrm{th}}}\right)-K_{\mathrm{eff}}C_nL_n\right)^2.\end{aligned} \tag{20}$$

In the (20) expression the product of concentration and the thickness of the cloud C_nL_n is unknown. It depends on the known material and processing parameters like material density ρ, effective penetration depth δ, peak laser fluence F_{pulse}, and the ablation efficiency of the previous pulse η_n. The unknown parameters will be replaced by the known ones in the final equation.

The mass of ablation debris created by nth pulse, C_n is the total concentration of shielding cloud (particles, vapor, and plasma), L_n is the averaged cloud thickness. The mass m_n of ablation products created by nth pulse can be expressed:

$$m_n = \rho V_n = C_nL_n\frac{\pi D_n^2}{4}, \tag{21}$$

where ρ is the abated material density, V_n is the volume ablated by nth pulse described by Eq. (11), C_n is the total concentration of shielding cloud (particles, vapor, and plasma), L_n is the averaged cloud thickness and D_n cylindrical cloud diameter. Our initial assumption, suggesting that the cloud of ablation products adopts a cylindrical shape, may not be entirely accurate. Instead, it seems that the evolution of the cloud tends to favor a semi-spherical shape within the time scale of 15.5 ns, indicating that this approach might be more appropriate. In real conditions, the ablation cloud is the densest in the center and density decreases to the edges. However, the simplest way of defining plasma in the cylindrical shape with the diameter of the ablated area, certain depth and constant density not depending on the distance from the center. Here, because of simplified cylindrical shape we gain the mathematical advantage in the Beer–Bouguer–Labert exponential absorption equation, and we do not have complex variation within distance from the center, thus the fluence of the next pulse has still Gaussian transverse distribution, only with attenuated peak fluence value, and its lead to parabolic shape cavity ablation with smaller volume. With more realistic, semi-spherical cloud shape we would have mathematically much more complicated equations, and we would not be able to derive simplified recurrence relation equations. Therefore, we have made assumption in our toy model that ablation cloud has a cylindrical shape. The product of ablation cloud concentration and cloud depth can be expressed from Eq. (21):

$$C_nL_n = \frac{4\rho}{\pi}\frac{V_n}{D_n^2}. \tag{22}$$

The ratio between the volume of the dimple and the diameter squared can be expressed from Eqs. (10) and (12):

$$\frac{V_n}{D_n^2} = \frac{\pi}{8}\delta\ln\left(\frac{F_n}{F_n^{\mathrm{th}}}\right). \tag{23}$$

From (22) and (23) we can get:

$$C_nL_n = \frac{\rho\delta}{2}\ln\left(\frac{F_n}{F_n^{\mathrm{th}}}\right). \tag{24}$$

The Eq. (15) can be transformed as follows:

$$\ln\left(\frac{F_n}{F_n^{\mathrm{th}}}\right) = \sqrt{\frac{2F_{\mathrm{pulse}}\eta_n^{\mathrm{pulse}}}{\delta}}. \tag{25}$$

From (24) and (25) we finally achieve an equation describing how the product of concentration and depth of the shielding cloud depends on the ablation efficiency of the previous pulse:

$$C_nL_n = \rho\sqrt{\frac{F_{\mathrm{pulse}}\delta\eta_n^{\mathrm{pulse}}}{2}}. \tag{26}$$

From Eqs. (20) and (26) finally, the new equation can be derived:

$$\eta_{n+1}^{\text{pulse}} = \frac{\delta}{2F_{\text{pulse}}}\left(\ln\left(\frac{F_{\text{pulse}}}{F_{n+1}^{\text{th}}}\right) - K_{\text{eff}}\rho\sqrt{\frac{\delta F_{\text{pulse}}\eta_n^{\text{pulse}}}{2}}\right)^2, \tag{27}$$

this type of equation in mathematics is commonly called recurrence relation because the ablation efficiency η_{n+1} of $(n+1)$th pulse is a function of efficiency η_n of nth pulse as ${\eta^{\text{pulse}}}_{n+1} = f({\eta^{\text{pulse}}}_n)$, mathematically defined by Eq. (27). If the function f is not linear, the bistability may be observed.

The ablation efficiency of the burst η_{burst} can be evaluated as the average value of all ablation efficiencies for all pulses in the burst:

$$\eta_N^{\text{burst}} = \frac{1}{N}\sum_{n=1}^{N}\eta_n^{\text{pulse}}, \tag{28}$$

where N is the number of the pulses in the burst (burst length), n is the number indicating pulse in the burst. The burst fluence F_{burst} can be computed by multiplying a single pulse fluence by the burst length as $F_{\text{burst}} = NF_{\text{pulse}}$. The ablation threshold of $(n+1)$th pulse dependence on the number of pulses nth applied before can be expressed as[44]:

$$F_{n+1}^{\text{th}} = F_{\infty}^{\text{th}} + \left(F_1^{\text{th}} - F_{\infty}^{\text{th}}\right)e^{-kn}, \tag{29}$$

$F^{\text{th}}{}_1$ is the single-shot threshold, the $F^{\text{th}}{}_\infty$ multi-shot threshold, k is the empirical parameter in the exponent which characterizes the strength of incubation leading to an early reduction of the threshold.

Spot diameter evaluation

Here we describe the measurement technique and its errors of spot diameter on the sample. The relationship between the crater diameter D and the peak laser fluence F_0 at the center of the Gaussian beam may be expressed by Eq. (10), assuming that the laser beam has the Gaussian spatial beam profile[25,64]. The ablated craters on copper sample were characterized using optical microscopy. The diameters of the craters were measured using an optical microscope (Eclipse LV100, Nikon) utilizing a high-definition 5-megapixel CCD digital camera (DS-Fi1, Nikon) with a resolution of 2560× 1920. The camera came with (NIS-Elements D, Nikon) image processing program, and (Digital Sight DS-U2, Nikon) controller. In the bright field mode, the objective (LU Plan Fluor 20x, Nikon) was utilized with a magnification factor of 20X and a numerical aperture (NA) = 0.5. A halogen light (LV-HL50PC, Nikon) was used to illuminate the specimen. The digital microscope image's pixel size variance was ≈0.2 µm, far less than the difference in crater size across craters ablated under identical experimental circumstances. As a result, five ablated craters' standard deviation was used to calculate measurement error. The Gaussian beam radiuses w were obtained from the line's slope using a semi-logarithmic plot of the diameter squared of the ablated area ${D_n}^2$ vs pulse energy E_{pulse}. Equations (10) and (13) were utilized to compute the Gaussian beam radiuses based on the linear fit slopes. The average relative error of the beam radius measurements was < 2.7%. To adjust the laser spot radius on the copper sample, the sample's vertical location (z) was moved from 0.0 mm (focal position) to 5.3 mm.

Fluence evaluation

The Eq. (13) was used to evaluate the peak laser fluence in pulse, which is inversely proportional to the square of the spot radius and directly proportional to the laser output power. The average laser power with a relative error of 0.7%, was measured using a power meter (Nova II, Ophir) equipped with a thermal power sensor (30A-BB-18, Ophir). As mentioned before, the beam radius had a relative average error was less than 2.7%. A peak fluence in the pulse was evaluated with an average relative error of < 3.9%. The same error applies to burst fluence evaluations.

Ablation rate and surface roughness evaluation

A stylus profiler (Dektak 150, Veeco) was utilized to measure the depth profiles of laser-ablated cavities. The measurement resolution was set at 0.1 µm in x direction, 1 µm in y direction, and 1 nm in z direction. In Fig. 1c, the example of the profile is displayed. Using information from the profiles, experimental values of the ablation efficiency η_{exp}, which were calculated as the ablated volume per pulse V_{pulse} divided by the pulse energy E_{pulse} were retrieved in the following manner utilizing the volume of the ablated cavities:

$$\eta_{\text{exp}} = \frac{V_{\text{pulse}}}{E_{\text{pulse}}} = \frac{\Delta x\Delta y\Delta z}{E_{\text{burst}}} = \frac{v_x\Delta y h_z}{f_{\text{burst}}E_{\text{burst}}L} = \frac{v_x\Delta y h_z}{PL}, \tag{30}$$

where, $\Delta x = v_x/f_{\text{burst}}$ is the distance between bursts in x direction, v_x is the beam scanning speed in the x direction, f_{burst} is the burst repetition rate, Δy is the distance between scanned lines (hatch) in the y direction, $\Delta z = h_z/L$ is ablated depth per scan, h_z is the ablated depth of the cavity in the z direction, L is the number of layers of beam scanning, E_{burst} is the burst energy defined by $E_{\text{burst}} = NE_{\text{pulse}}$, N is the bust length, and P is the laser output power. The surface roughness R_a values were obtained directly from the laser-milled cavity bottom line profiles. The surface roughness of the cavity bottom was correlated with the ablation depth measurement errors. A cavity's depth measurement had an average relative inaccuracy of 2.5%. With an accuracy of 1.0%, a galvanometer scanner (Intelliscan 14, Scanlab) was used to control the beam scanning speed on sample and the and hatching

distance[65,66]. As mentioned before the average laser power measurements had relative error of 0.7%. As a result, the experimental values of ablation efficiency had an average relative error less than 3.0%.

Data availability

Data underlying the results presented in this paper are not publicly available at this time but may be obtained from the authors upon reasonable request.

Received: 8 November 2023; Accepted: 19 February 2024
Published online: 07 March 2024

References

1. Malinauskas, M. *et al.* Ultrafast laser processing of materials: From science to industry. *Light Sci. Appl.* **5**, e16133–e16133 (2016).
2. Chen, M., He, T. & Zhao, Y. Review of femtosecond laser machining technologies for optical fiber microstructures fabrication. *Opt. Laser Technol.* **147**, 107628 (2022).
3. Bogue, R. Lasers in manufacturing: A review of technologies and applications. *Assembly Autom.* **35**, 161–165 (2015).
4. Khalkhal, E., Rezaei-Tavirani, M., Zali, M. R. & Akbari, Z. The evaluation of laser application in surgery: A review article. *J. Lasers Med. Sci.* **10**, S104–S111 (2019).
5. Kerse, C. *et al.* Ablation-cooled material removal with ultrafast bursts of pulses. *Nature* **537**, 84–88 (2016).
6. Bornschlegel, B. & Finger, J. In-situ analysis of ultrashort pulsed laser ablation with pulse bursts. *J. Laser Micro Nanoen.* **14**, 88–94 (2019).
7. Metzner, D., Lickschat, P., Kreisel, C., Lampke, T. & Weißmantel, S. Study on laser ablation of glass using MHz-to-GHz burst pulses. *Appl. Phys. A* **128**, 637 (2022).
8. Metzner, D., Olbrich, M., Lickschat, P., Horn, A. & Weißmantel, S. X-ray generation by laser ablation using MHz to GHz pulse bursts. *J. Laser Appl.* **33**, 032014 (2021).
9. Metzner, D., Lickschat, P. & Weißmantel, S. Optimization of the ablation process using ultrashort pulsed laser radiation in different burst modes. *J. Laser Appl.* **33**, 012057 (2021).
10. Mishchik, K. *et al.* High-efficiency femtosecond ablation of silicon with GHz repetition rate laser source. *Opt. Lett.* **44**, 2193 (2019).
11. Žemaitis, A., Gaidys, M., Gečys, P., Barkauskas, M. & Gedvilas, M. Femtosecond laser ablation by bibursts in the MHz and GHz pulse repetition rates. *Opt. Express* **29**, 7641 (2021).
12. Audouard, E., Bonamis, G., Hönninger, C. & Mottay, E. GHz femtosecond processing with agile high-power laser. *Adv. Opt. Technol.* **10**, 263–275 (2021).
13. Mur, I. & Petkovšek, R. Near-THz bursts of pulses—Governing surface ablation mechanisms for laser material processing. *Appl. Surf. Sci.* **478**, 355–360 (2019).
14. Gaudiuso, C. *et al.* Laser ablation of silicon with THz bursts of femtosecond pulses. *Sci. Rep.* **11**, 13321 (2021).
15. Gaudiuso, C. *et al.* Experimental and theoretical study of the ablation of silicon with THz bursts of fs laser pulses. *Proc. SPIE* **11989**, 119890H (2022).
16. Žemaitis, A., Gečys, P., Barkauskas, M., Račiukaitis, G. & Gedvilas, M. Highly-efficient laser ablation of copper by bursts of ultrashort tuneable (fs–ps) pulses. *Sci. Rep.* **9**, 12280 (2019).
17. Förster, D. J. *et al.* Shielding effects and re-deposition of material during processing of metals with bursts of ultra-short laser pulses. *Appl. Surf. Sci* **440**, 926–931 (2018).
18. Amouye Foumani, A. *et al.* Atomistic simulation of ultra-short pulsed laser ablation of metals with single and double pulses: An investigation of the re-deposition phenomenon. *Appl. Surf. Sci.* **537**, 147775 (2021).
19. Spellauge, M. *et al.* Influence of stress confinement, particle shielding and re-deposition on the ultrashort pulse laser ablation of metals revealed by ultrafast time-resolved experiments. *Appl. Surf. Sci.* **545**, 148930 (2021).
20. Metzner, D., Lickschat, P. & Weißmantel, S. Influence of heat accumulation during laser micromachining of CoCrMo alloy with ultrashort pulses in burst mode. *Appl. Phys. A* **126**, 84 (2020).
21. Le, H., Karkantonis, T., Nasrollahi, V., Penchev, P. & Dimov, S. MHz burst mode processing as a tool for achieving removal rates scalability in ultrashort laser micro-machining. *Appl. Phys. A* **128**, 711 (2022).
22. Žemaitis, A., Gaidys, M., Gečys, P., Račiukaitis, G. & Gedvilas, M. Rapid high-quality 3D micro-machining by optimised efficient ultrashort laser ablation. *Opt. Lasers Eng.* **114**, 83–89 (2019).
23. Žemaitis, A., Gečys, P., Račiukaitis, G. & Gedvilas, M. Efficient ablation by ultra-short pulse lasers. *Procedia CIRP* **94**, 962–965 (2020).
24. Gaidys, M., Žemaitis, A., Gečys, P. & Gedvilas, M. Efficient picosecond laser ablation of copper cylinders. *Appl. Surf. Sci.* **483**, 962–966 (2019).
25. Žemaitis, A. *et al.* Advanced laser scanning for highly-efficient ablation and ultrafast surface structuring: Experiment and model. *Sci. Rep.* **8**, 17376 (2018).
26. Liu, J. M. Simple technique for measurements of pulsed Gaussian-beam spot sizes. *Opt. Lett.* **7**, 196 (1982).
27. Ni, C. *et al.* Effects of machining surface and laser beam scanning strategy on machinability of selective laser melted Ti6Al4V alloy in milling. *Mater. Des.* **194**, 108880 (2020).
28. Heidrich, S., Willenborg, E. & Richmann, A. Development of a laser based process chain for manufacturing freeform optics. *Phys. Procedia* **12**, 519–528 (2011).
29. van Elteren, J. T., Metarapi, D., Mervič, K. & Šala, M. Exploring the benefits of ablation grid adaptation in 2D/3D laser ablation inductively coupled plasma mass spectrometry mapping through geometrical modeling. *Anal. Chem.* **95**, 9863–9871 (2023).
30. Kažukauskas, E., Butkus, S., Jukna, V., Paipulas, D. & Sirutkaitis, V. Scanning algorithm optimization for achieving low-roughness surfaces using ultrashort laser pulses: A comparative study. *Materials* **16**, 2788 (2023).
31. Li, P. *et al.* Ablation oxidation and surface quality during laser polishing of TA15 aviation titanium alloy. *J. Mater. Res. Technol.* **23**, 6101–6114 (2023).
32. Furmanski, J., Rubenchik, A. M., Shirk, M. D. & Stuart, B. C. Deterministic processing of alumina with ultrashort laser pulses. *J. Appl. Phys.* **102**, 073112 (2007).
33. Račiukaitis, G., Brikas, M. & Gedvilas, M. Efficiency aspects in processing of metals with high-repetition-rate ultra-short-pulse lasers. *Proc. ICALEO M403* https://doi.org/10.2351/1.5061377 (2008).
34. Račiukaitis, G., Gečys, P., Brikas, M., Voisiat, B. & Gedvilas, M. Use of high repetition rate and high power lasers in microfabrication: How to keep the efficiency high?. *J. Laser Micro Nanoeng.* **4**, 186–191 (2009).
35. Förster, D. J., Jäggi, B., Michalowski, A. & Neuenschwander, B. Review on experimental and theoretical investigations of ultra-short pulsed laser ablation of metals with burst pulses. *Materials* **14**, 3331 (2021).
36. Guo, I. *et al.* Lifetime visualization of femtosecond laser-induced plasma on GaP crystal. *Opt Express* **31**, 6877 (2023).
37. Park, M., Gu, Y., Mao, X., Grigoropoulos, C. P. & Zorba, V. Mechanisms of ultrafast GHz burst fs laser ablation. *Sci. Adv.* **9**, eadf639 (2023).

38. Wu, C. & Zhigilei, L. V. Microscopic mechanisms of laser spallation and ablation of metal targets from large-scale molecular dynamics simulations. *Appl. Phys. A* **114**, 11–32 (2014).
39. Park, M., Jeun, J., Han, G. & Grigoropoulos, C. P. Time-resolved emission and scattering imaging of plume dynamics and nanoparticle ejection in femtosecond laser ablation of silver thin films. *Appl. Phys. Lett.* **116**, 234105 (2020).
40. Rouleau, C. M. *et al.* Nanoparticle generation and transport resulting from femtosecond laser ablation of ultrathin metal films: Time-resolved measurements and molecular dynamics simulations. *Appl. Phys. Lett.* **104**, 193106 (2014).
41. Welzel, S., Rousseau, A., Davies, P. B. & Röpcke, J. Kinetic and diagnostic studies of molecular plasmas using laser absorption techniques. *J. Phys. Conf. Ser.* **86**, 012012 (2007).
42. Sinko, J. E., Oh, B. I., Eckel, H.-A. & Scharring, S. The Bouguer–Lambert–Beer absorption law and non-planar geometries. *AIP Conf. Proc.* https://doi.org/10.1063/1.3657031 (2011).
43. de Palo, R. *et al.* Threshold fluence and incubation during multi-pulse ultrafast laser ablation of quartz. *Opt. Express* **30**, 44908 (2022).
44. Ashkenasi, D., Lorenz, M., Stoian, R. & Rosenfeld, A. Surface damage threshold and structuring of dielectrics using femtosecond laser pulses: The role of incubation. *Appl. Surf. Sci.* **150**, 101–106 (1999).
45. Balachninaitė, O., Tamulienė, V., Iččas, L. & Vaičaitis, V. Laser micromachining of steel and copper using femtosecond laser pulses in GHz burst mode. *Results Phys.* **22**, 103847 (2021).
46. Neuenschwander, B., Jaeggi, B., Schmid, M., Rouffiange, V. & Martin, P.-E. Optimization of the volume ablation rate for metals at different laser pulse-durations from ps to fs. *Proc. SPIE 824307* https://doi.org/10.1117/12.908583 (2012).
47. Nathala, C. S. R. *et al.* Ultrashort laser pulse ablation of copper, silicon and gelatin: Effect of the pulse duration on the ablation thresholds and the incubation coefficients. *Appl. Phys. A* **122**, 107 (2016).
48. Lee, I.-M. & Watkins, K. Laser removal of oxides and particles from copper surfaces for microelectronic fabrication. *Opt Express* **7**, 68 (2000).
49. Žemaitis, A., Gaidys, M., Gečys, P. & Gedvilas, M. Influence of nonlinear and saturable absorption on laser lift-off threshold of an oxide/metal structure. *Opt. Lett.* **45**, 6166 (2020).
50. Zhu, H., Zhang, H., Ni, X., Shen, Z. & Lu, J. Picosecond laser lift-off method for fracture and debonding of copper oxide layer grown on copper substrate. *J. Laser Appl.* **31**, 042015 (2019).
51. Zhang, R., McDowell, A., Hegmann, F., Fedosejevs, R. & Tsui, Y. Y. A study of incubation effects in femtosecond laser irradiation of silicon and copper. *Appl. Phys. A* **129**, 131 (2023).
52. Franz, D. *et al.* Picosecond laser microvia drilling of ABF material using MHz burst mode. *Mater. Res. Express* **10**, 096301 (2023).
53. Ordal, M. A., Bell, R. J., Alexander, R. W., Long, L. L. & Querry, M. R. Optical properties of fourteen metals in the infrared and far infrared: Al Co, Cu, Au, Fe, Pb, Mo, Ni, Pd, Pt, Ag, Ti, V, and W. *Appl. Opt.* **24**, 4493 (1985).
54. Zhu, S. *et al.* Split of surface plasmon resonance of gold nanoparticles on silicon substrate: A study of dielectric functions. *Opt. Express* **18**, 21926 (2010).
55. Ou, Z., Huang, M. & Zhao, F. Colorizing pure copper surface by ultrafast laser-induced near-subwavelength ripples. *Opt. Express* **22**, 17254 (2014).
56. Kogos, L. C. *et al.* Plasmonic ommatidia for lensless compound-eye vision. *Nat. Commun.* **11**, 1637 (2020).
57. Gnilitskyi, I. *et al.* High-speed manufacturing of highly regular femtosecond laser-induced periodic surface structures: Physical origin of regularity. *Sci. Rep.* **7**, 8485 (2017).
58. Ackerl, N., Gugger, P., Warhanek, M., Gysel, J. & Wegener, K. Ultra-short pulsed laser marking and coloration of metals with segmented pixel parameter transformation. *J. Laser Micro/Nanoeng.* **15**, 1–6 (2020).
59. Gaidys, M., Selskis, A., Gečys, P. & Gedvilas, M. Stainless steel colouring using burst and biburst mode ultrafast laser irradiation. *Opt. Laser Technol.* **174**, 110561 (2024).
60. Gaidys, M., Žemaitis, A., Gečys, P. & Gedvilas, M. Efficient surface polishing using burst and biburst mode ultrafast laser irradiation. *RSC Adv.* **13**, 3586–3591 (2023).
61. Abdelmalek, A. *et al.* Ablation of copper metal films by femtosecond laser multipulse irradiation. *Appl. Sci.* **8**, 1826 (2018).
62. Smale, L. F., Chantler, C. T., de Jonge, M. D., Barnea, Z. & Tran, C. Q. Analysis of X-ray absorption fine structure using absolute X-ray mass attenuation coefficients: Application to molybdenum. *Radiat. Phys. Chem.* **75**, 1559–1563 (2006).
63. Stolzenberg, U. *et al.* X-ray emission hazards from ultrashort pulsed laser material processing in an industrial setting. *Materials* **14**, 7163 (2021).
64. Liu, J. M. Simple technique for measurements of pulsed Gaussian-beam spot sizes. *Opt. Lett.* **7**, 196 (1982).
65. Bechtold, P., Hohenstein, R. & Schmidt, M. Evaluation of disparate laser beam deflection technologies by means of number and rate of resolvable spots. *Opt. Lett.* **38**, 2934 (2013).
66. Römer, G. R. B. E. & Bechtold, P. Electro-optic and acousto-optic laser beam scanners. *Phys. Procedia* **56**, 29–39 (2014).

Acknowledgements
This project has received funding from the Research Council of Lithuania (LMTLT), Agreement No. S-MIP-22-89.

Author contributions
A.Ž., M.Ga., P.G., and M.Ge. conceived the original idea for the research. M.Ge obtained the funding and supervised the project. P.G. obtained access to the state-of-the-art laser and supervised work in the laboratory. A.Ž. and M.Ga. performed the experiments and analyzed the data. M.Ge. formulated the model, performed the numerical calculations, made a comparison of experimental and numerical data, and wrote the manuscript. All authors discussed the results and commented on the manuscript.

Competing interests
The authors declare no competing interests.

Additional information
Correspondence and requests for materials should be addressed to M.G.

Reprints and permissions information is available at www.nature.com/reprints.

Publisher's note Springer Nature remains neutral with regard to jurisdictional claims in published maps and institutional affiliations.

P3

EFFICIENT SURFACE POLISHING USING BURST AND BIBURST MODE ULTRAFAST LASER IRRADIATION

M. Gaidys, A. Žemaitis, P. Gečys, M. Gedvilas

RSC Adv. **13**, 3586-3591 (2023)
DOI: 10.1039/D2RA05208C

RSC Advances

ROYAL SOCIETY OF CHEMISTRY

PAPER

Cite this: *RSC Adv.*, 2023, **13**, 3586

Efficient surface polishing using burst and biburst mode ultrafast laser irradiation†

Mantas Gaidys, * Andrius Žemaitis, Paulius Gečys and Mindaugas Gedvilas

Received 19th August 2022
Accepted 11th January 2023

DOI: 10.1039/d2ra05208c

rsc.li/rsc-advances

The use of laser irradiation for micromachining is widely applicable and has many benefits. One of the main uses is that it is possible to mill and polish the sample using the same laser system. State-of-the-art laser systems with high average optical power and burst regimes are widely used in technology. The main advantages of burst regimes are the closer fluence values to optimal fluences and residual heat reusage for subsequent pulses. In this study, the influence of MHz burst, GHz burst, and bibursts was investigated for significant surface polishing of copper and stainless-steel samples. Z-scan experiments were performed to determine the optimal number of sub-pulses inside the burst for the lowest surface roughness.

Introduction

Many products used in various industries are significantly influenced by texture and surface quality.[1] Laser micromachining is an appealing method because of the abundance of applications: from cutting[2–5] and drilling[6–8] of various materials to forming two and a half dimensional (2.5D) structures on various surfaces.[9,10] Because sub-micrometer surface roughness is now desired, laser polishing is a prospective polishing method. Laser polishing allows for high precision, good finish quality, a vast range of possible materials, reaching delicate places, polishing complex forms,[11,12] and the ability to micromachine and polish samples using the same laser system.

However, optimal laser processing parameters, such as pulse repetition rate, pulse energy, and pulse overlap, have to be chosen correctly to achieve the best results, which are tedious and time-consuming. Lasers and systems designed for laser micro/nano-fabrication are improved daily. It is now possible to have systems that use MHz and GHz repetition rates with femtosecond laser pulses and high average optical power using burst and biburst modes.[13] These modes allow a significant increase in ablation efficiency[14,15] and significantly improve the ablated surface roughness [15] if the laser processing parameters are optimized correctly. Laser bursts also provide faster processing owing to burst energy division into pulse energies closer to optimal fluences, resulting in the exploitation of more average laser power.[16] Moreover, because of the short time between burst pulses, any residual heat from the previous pulse is reused.[17]

In this study, a state-of-the-art laser working in burst and biburst modes was used for copper and stainless-steel milling and polishing. The number of sub-pulses in MHz and GHz bursts and biburst were controlled. The surface roughness measured by the stylus profiler was investigated as a parameter for defining polishing quality. Different numbers of pulses in burst and biburst regimes resulted in different surface roughness of laser-milled areas in copper and stainless steel. The optimal laser processing parameters were found to achieve the best laser polishing quality with a mirror-like finish.

Materials and methods

Experimental setup

A state-of-the-art solid-state laser (Pharos, Light Conversion) with an average optical power of 7.3 W at a wavelength of

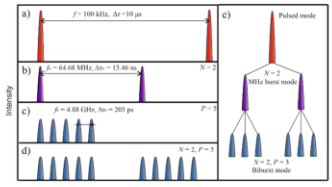

Fig. 1 Schematic representation of different regimes of the laser irradiation. (a) Standard pulsed regime with a pulse repetition rate of $f = 100$ kHz, (b) MHz burst regime with a pulse repetition rate of $f_N = 64.68$ MHz, and the single pulse split into $N = 2$ pulses. The time between burst pulses $\Delta\tau_N = 15.46$ ns, (c) GHz burst regime with burst pulse repetition rate of $f_P = 4.88$ GHz, and the single pulse split into $P = 5$ pulses. The time between burst pulses $\Delta\tau_P = 205$ ps (d) biburst regime, where the single pulse is split into $N = 2$ pulse MHz burst that are subsequently split into $P = 5$ pulse GHz burst, and (e) different visualization of pulsed regimes division into MHz and biburst modes.

Department of Laser Technologies (LTS), Center for Physical Sciences and Technology (FTMC), Savanorių Ave. 231, LT-02300 Vilnius, Lithuania. E-mail: mantas.gaidys@ftmc.lt

† Electronic supplementary information (ESI) available. See DOI: https://doi.org/10.1039/d2ra05208c

1030 nm was used for the experiments. The pulse duration was τ = 210 fs, and the repetition rate was f = 100 kHz (Fig. 1a). The laser system can operate in a pulsed regime and several burst regimes. Three different burst regimes exist: MHz burst, GHz burst, and biburst. While using the MHz regime, a single laser pulse could be divided into multiple pulses with a repetition rate of f_N = 64.68 MHz, corresponding to $\Delta\tau_N$ = 15.46 ns between pulses (Fig. 1b). During the experiment, the burst was divided from $N = 1$ to $N = 9$. While using the GHz burst regime, a single pulse could be divided into numerous pulses with a repetition rate of f_P = 4.88 GHz, corresponding to $\Delta\tau_P$ = 205 ps between pulses (Fig. 1c). During the experiment, the pulse was divided from $P = 2$ to $P = 25$. Finally, using the biburst regime, a single pulse could be divided into several MHz pulses, and each of the MHz pulses could be further divided into several GHz pulses (Fig. 1d). Another visualization of pulse division into subpulses is presented (Fig. 1e).

The laser beam was focused on using a 100 mm focal distance F-theta lens, and the beam was controlled in the x and y directions by applying a galvanometric scanner (Intelliscan 14, Scanlab). The beam radii values were needed in various sample z positions during the experiment and were measured using a well-known D-squared method. The beam radius in the focal plane was equal to 21 μm. The rectangular-shaped cavities with a top dimension of 2 mm × 1 mm were ablated in the copper and stainless-steel samples (Fig. 2). The distance between the scanning lines was kept constant at 10 μm, and the scanning speed was set to 333 mm s^{-1}. The sample position was changed in the z-direction to obtain various fluence values. Each rectangle was scanned numerous times to achieve a depth that could be easily measured using a stylus profiler (Dektak 150+, Veeco). During the MHz and GHz burst experiments, the number of pulses in bursts was changed from $N = 2$ to $N = 9$ and from $P = 2$ to $P = 25$, respectively. During the biburst experiment, every N and P combination was tested.

Beam characteristics

To change the laser fluence, the sample z position was changed. The beam radius increased when the sample was moved in either the positive or negative z-direction. A well-known D-squared method was used to calculate the different beam radii values.[18] During this method, a sample is damaged using laser irradiation at various average laser powers, and the radius of the damage is measured using an optical microscope (BX51, Olympus). A graph of the squared radius of the irradiated damage dependence on fluence is drawn. Using eqn (1) of linear fit on the graph, we obtain the beam radius from the slope at the current sample z position. This experiment was repeated for all z values, which were 0.2, 0.4, 1.0, 1.4, 1.9, 2.4, 2.7, 3.1, 3.8, and 4.9 mm in both directions. We have

$$D^2 = 2w^2 \ln\left(\frac{F}{F_{th}}\right) \quad (1)$$

where D denotes the diameter of the laser irradiation damage of the sample, w denotes the beam radius at a given z position, F denotes the fluence, and F_{th} denotes the ablation threshold.

Measured beam radii values are shown in (Fig. 3). We obtain

$$w(z) = w_0\sqrt{1 + \left(\frac{(z - z_0)\lambda M^2}{\pi w_0^2}\right)^2}, \quad (2)$$

where w_0 denotes the beam waist, z_0 denotes the sample position at the beam's waist, z denotes the sample current position, and λ denotes the laser wavelength, which was 1030 nm, and M^2 denotes the beam quality parameter.

Sample characteristics

For the experiments, 5 mm × 50 mm × 50 mm copper (CW004A, Ekstremalė) and stainless-steel (1.4301, Ekstremalė) samples were used with a surface roughness R_q of 0.1 μm and 0.5 μm, respectively. The copper purity was 99%. The ablated surface roughness R_a was measured using a stylus profiler (Dektak 150, Veeco). A scanning electron microscope (JSM-6490LV, JEOL) was used to visualize the samples.

Results and discussion

Laser polishing is a technique in laser micromachining that entails melting a thin layer of a metal surface that is free of

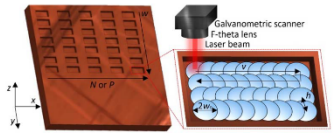

Fig. 2 Design of laser milling and polishing experiment. Rectangle cavities were ablated in a copper and a stainless-steel sample. Beam size was changed in columns by changing the position of the sample. N or P were changed in matrix lines. Here, v is the scanning speed and was kept constant at 333 mm s^{-1}, h is the hatch and was 10 μm, w_0 is the beam radius and was changed from 21 μm to 95 μm. The dashed line represents the mirror jump of galvanometric scanners.

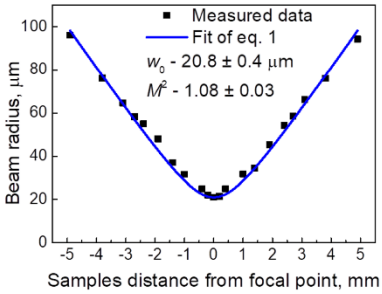

Fig. 3 Laser beam radii at different sample z positions. Black squares represent experimental data, and the blue line represents the fit of equation. The received parameters were beam waist w_0 (20.8 ± 0.4 μm) and beam quality parameter M^2 (1.08 ± 0.03).

fractures and other defects. Using a pulsed laser system, this is done by micro polishing, where the beam is moved along the target's surface to melt the peaks into the valleys and, consequently, gain a more even surface. The molten material is already re-solidified when the subsequent laser pulse hits the surface and creates a new molten pool.[19] Shallow surface melting is the primary cause of this phenomenon. The shallow surface melting zone is created by capillary pressure and liquid curvature caused by the shallow melting of micro asperities, which finally fill the valleys of the metal surface with molten metal.[20] Laser ablation is also very useful for laser polishing. In real-world applications, during the free form ablation process, some ablated debris did not leave the area and instead was deposited back onto the irradiated surface. How big and common those debris are is a probabilistic process that depends on the laser parameters and the geometry of the ablated region. Some larger debris may not be removed with laser surface melting compared to laser ablation. The intensity of the laser beam must be chosen based on the pulse duration and the type of polished material. Consequently, one of the most important parameters for effective laser polishing is laser fluence, which is easily controllable using laser bursts. Even slight changes in fluence can result in a wide range of surface quality finishes. Another major factor is the temperature of the surface of the sample. In the case of stainless-steel, studies have revealed that a surface temperature reaching 600 °C before the next pulse significantly affects surface roughness.[21] However, the accumulated heat can also be used as an advantage when using various burst modes. According to many studies, the use of burst modes with fluences lower than the ablation threshold fluence results in a thin melt layer that enhances surface quality.[22–24]

While using MHz burst mode with fluences lower than 0.5 J cm^{-2}, the surface roughness was quite high, reaching around 1 μm in copper (Fig. 4a). We can also see scanning electron microscope pictures (SEM) in (Fig. 4). A rectangular cavity marked with a blue dot and two pulses in the MHz burst was used, and the depth is equal to 36 μm with a roughness of 1.07 μm. From 0.5 to 1 J cm^{-2} fluence, the surface roughness improved significantly in an interval from 0.2 μm to 0.5 μm. The lowest roughness has 4 or more pulses in the MHz burst. There are a few effects at play here. First, there is the incubation effect, which is that the ablation threshold decreases with an increasing number of pulses in the same spot.[25] The second and most important factor is heat accumulation. Subsequent pulses reach the target material before the heat-affected zone has cooled off, so less energy is needed to remove the material.[26] This is also evident when we compare the beam radii at the same fluences. With $N = 2$ and $N = 3$ pulses in the MHz burst, to achieve a fluence of approximately 0.7 J cm^{-2}, the sample was moved 2.7 mm and 2.4 mm out of focus to increase the beam radii to 57.8 μm and 52.9 μm respectively. The beam radius was increased to only 37.4 μm for $N = 4$ and $N = 5$, to 31.8 μm for $N = 6$ to $N = 8$, and finally, to 24.8 μm for $N = 9$. The smaller beam radius allowed for greater heat accumulation in the area. As illustrated in Fig. 4, we can observe an SEM image with a significantly more even surface with a low roughness of 0.23

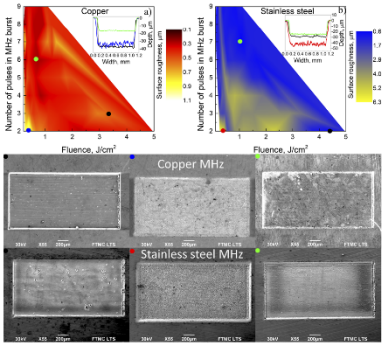

Fig. 4 Surface roughness dependence on fluence and number of pulses in the MHz burst for (a) copper and (b) stainless steel. (a) For copper, black dot and solid line 3 pulses in the MHz burst, 3.3 J cm^{-2} fluence, 0.53 μm surface roughness; blue dot and solid line 2 pulses in the MHz burst, 0.4 J cm^{-2} fluence, 1.07 μm surface roughness; and green dot and solid line 6 pulses in the MHz burst, 0.8 J cm^{-2} fluence, 0.23 μm surface roughness. (b) For stainless steel, black dot and solid line 2 pulses in the MHz burst, 4.4 J cm^{-2} fluence, 0.63 μm surface roughness; red dot and solid line 2 pulses in the MHz burst, 0.6 J cm^{-2} fluence, 5.4 μm surface roughness; and green dot and solid line 7 pulses in the MHz burst, 1.1 J cm^{-2} fluence, 0.67 μm surface roughness. For all color dots, scanning electron microscope pictures are shown.

μm and an ablated depth of 18.1 μm. For fluences higher than 1 J cm^{-2}, the roughness increased again to an interval of 0.5–0.7 μm. At higher fluences, particle shielding also has a stronger negative effect on scattering and absorbing incoming laser irradiation. We can see in Fig. 4 an SEM image marked with a black dot of a milled rectangle with a surface roughness of 0.53 μm. Žemaitis *et al.*[14] showed that the highest ablation efficiency was reached when a MHz burst had 3 pulses. The aforementioned regime resulted in a relatively good quality of surface roughness compared to the other results. However, it could be improved by adding a polishing step using an $N = 6$ regime to decrease the surface roughness even further. Metals exposed to air are covered in an oxide layer with a thickness of up to a few micrometres. Incoming laser irradiation first interacts with the oxide, with a significantly higher ablation threshold[27] and only afterwards with the metal itself. Žemaitis *et al.*[28] demonstrated that a copper sample covered in a Cu_2O oxide has three oxide transmission cases described by different z/z_R values, where $Z_R = \pi w_0^2/(\lambda M^2)$ z_R is the Rayleigh length, z is the sample position, λ is the wavelength of the laser irradiation, and M^2 is the quality parameter of the Gaussian beam. The three transmission cases are as follows: when the sample is very out of focus and z/z_R >>> ⊥1 linear absorption is dominant with a transmission value of $T_0 \approx 60\%$, when the sample is not far from focus and $z/z_R \approx \perp 1$ and is in the saturable absorption region with a transmission value of $T_0 \approx 99\%$, and when the

sample is in focal position with $z/z_R \approx 0$, where nonlinear absorption exceeds absorption saturation in the oxide layer and transmission drops down to $T_0 \approx 44\%$. However, although the difference in the transmission is quite high, its impact decreases significantly when multiple scans are performed on the target's surface.

We observe similar tendencies with stainless steel (Fig. 4b), but because stainless steel has a higher specific heat capacity 0.500 J $(g^{-1}\,K^{-1})$[29] compared to copper 0.385 J $(g^{-1}\,K^{-1})$, it takes more pulses and higher fluences to reach the optimal heat accumulation. For fluences lower than 0.8 J cm^{-2}, the surface quality is quite poor. As depicted in (Fig. 4), visible graining can be observed in the SEM image with a red dot. The ablated depth is equal to 41.7 μm, and the surface roughness is 5.4 μm. For fluences higher than 0.8 J cm^{-2} and with 5 or more pulses in the MHz burst, we observed the optimal window for the highest surface quality on stainless steel. Similar to copper, the higher beam radii at the same 1.1 J cm^{-2} fluences in stainless-steel result in poorer surface quality. The surface roughness only reached a value lower than 1 μm value when the beam radius was decreased below 24.8 μm at $N = 6$ and a higher number of pulses. As demonstrated in (Fig. 4), an SEM image with a green dot showed a surface roughness of only 0.67 μm while using 7 pulses in the MHz burst. However, a similar finish quality can be achieved with fewer pulses in the burst but higher fluence, as can be observed in the SEM image with a black dot (Fig. 4), where 0.63 m surface roughness was achieved with a fluence of 4.4 J cm^{-2} and two burst pulses at MHz. Stainless steel had an overall higher surface roughness because the starting roughness was higher and equal to 0.5 μm compared to 0.1 μm of copper.

Using the GHz laser polishing regime, the surface roughness of copper was in the range of 0.1–0.35 μm for the vast majority of fluence and number of pulses within the burst combinations. SEM images of 0.1 μm roughness are shown for two and three pulses in the GHz burst, as illustrated in Fig. 5, and marked with black and blue dots, respectively, with different fluences in which the first is 0.5 J cm^{-2} and the other 1.1 J cm^{-2}. Even with the worst outcomes for the GHz burst polishing regime, the roughness was only 0.53 μm, as can be observed in the SEM image in Fig. 5, and has a blue dot. This was the worst combination of parameters with 5 pulses at 0.22 J cm^{-2} fluence when the sample was 3.8 mm out of the focal plane. GHz burst mode uses heat accumulation to its fullest effect because of the incredibly small time window between subsequent pulses. However, note that it has been shown that the ablation efficiency drops by about 90%[30] in the GHz burst mode, so it should only be used as a polishing step. As shown in Fig. 5a, the polishing process is very parameter independent.

In the biburst mode polishing, the surface roughness again becomes more parameter dependent. All the results for the biburst combinations are presented in the ESI.† The vast majority of parameter combinations lead to a surface roughness lower than 0.5 μm. However, using 10 or fewer pulses in the GHz burst and fluences for each sub-pulse lower than 0.6 J cm^{-2} result in roughness lower than 0.2 μm. SEM images are shown in (Fig. 5b). High-quality polishing was shown in SEM images

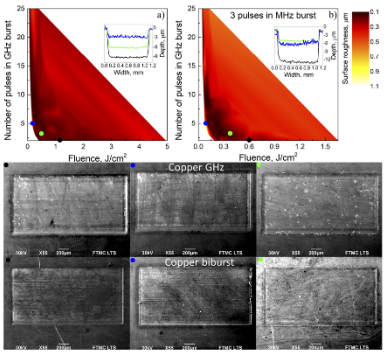

Fig. 5 Surface roughness dependence on fluence and number of pulses in the (a) GHz burst and (b) biburst modes. (a) Black dot and solid line 2 pulses in the GHz burst, 1.1 J cm^{-2} fluence, 0.10 μm surface roughness; green dot and solid line 3 pulses in the GHz burst, 0.5 J cm^{-2} fluence, 0.10 μm surface roughness; and blue dot and solid line 5 pulses in the GHz burst, 0.16 J cm^{-2} fluence, 0.72 μm surface roughness. (b) N is the number of pulses in the MHz burst, and P is the number of pulses in the GHz burst. Black dot and solid line $N = 3$, $P = 2$ pulses in the biburst, 0.6 J cm^{-2} fluence, 0.20 μm surface roughness; blue dot and solid line $N = 3$, $P = 5$ pulses in the biburst, 0.07 J cm^{-2} fluence, 0.74 μm surface roughness; and green dot and solid line $N = 3$, $P = 3$ pulses in the biburst, 0.4 J cm^{-2} fluence, 0.08 μm surface roughness. For all color dots, scanning electron microscope pictures are shown.

with black and green dots, corresponding to $N = 3$, $P = 2$, 0.10 μm roughness and $N = 3$, $P = 3$, 0.08 μm roughness, respectively. Again, the low surface quality is observed only in the very out of focus 3.1 mm and more, milled cavities, and low fluences, such as in SEM image with a blue dot (Fig. 5b). Overall, bibursts result in similar surface roughness at optimal parameters but slightly higher roughness for sub-optimal ones. These tendencies remain unchanged depending on the number of pulses in the MHz burst, as demonstrated in the ESI.†

As with copper, the GHz burst results in the highest quality on stainless steel with vastly different parameters. As illustrated in Fig. 6a, SEM images with red and black dots with a surface roughness of 0.66 μm and 0.55 μm were reached with 2 pulses in the GHz burst, 1.1 J cm^{-2} fluence, and 3 pulses in the GHz burst, 0.5 J cm^{-2} fluence. With copper, poor-quality results are received only when the sample is 3.8 mm or more out of focus when the fluence is 0.1 J cm^{-2}. An example is shown with an SEM image with a green dot, with a corresponding surface roughness of 1.4 μm.

All the biburst results on stainless steel are shown in the ESI.† Surface roughness (Fig. 6b) was similar to the GHz burst mode at optimal parameters with a roughness of 0.57 μm at $N = 3$, $P = 2$ in the SEM image with a black dot and 0.45 μm at $N = 3$, $P = 2$ SEM image with a red dot. High surface roughness is also shown in the SEM image with a green dot, corresponding to a surface roughness of 1.89 μm at $N = 3$, $P = 15$.

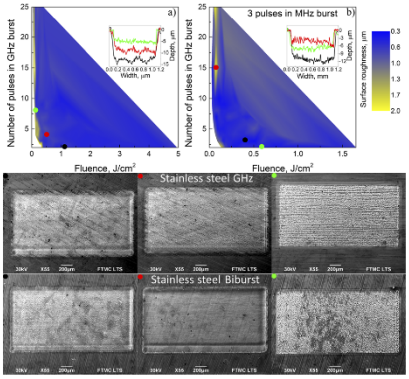

Fig. 6 Surface roughness dependence on fluence and number of pulses in the (a) GHz burst and (b) biburst modes. (a) Black dot and solid line 2 pulses in the GHz burst, 1.1 J cm^{-2} fluence, 0.66 μm surface roughness; red dot and solid line 3 pulses in the GHz burst, 0.5 J cm^{-2} fluence, 0.55 μm surface roughness; and green dot and solid line 8 pulses in the GHz burst, 0.1 J cm^{-2} fluence, 1.4 μm surface roughness. (b) N is the number of pulses in the MHz burst, and P is the number of pulses in the GHz burst. Green dot and solid line $N = 3$, $P = 2$ pulses in the biburst, 0.6 J cm^{-2} fluence, 0.57 μm surface roughness; black dot and solid line $N = 3$, $P = 3$ pulses in the biburst, 0.4 J cm^{-2} fluence, 0.45 μm surface roughness; and red dot and solid line $N = 3$, $P = 15$ pulses in the biburst, 0.05 J cm^{-2} fluence, 1.89 μm surface roughness. For all color dots, scanning electron microscope pictures are shown.

Conclusions

Using 210 fs laser pulses in the burst and biburst regimes, copper and stainless-steel samples were ablated to receive the highest surface quality. It is shown that both MHz and GHz bursts are useful in reducing surface roughness, with MHz burst having the advantage of higher ablation efficiency, while GHz bursts were very parameter independent for the surface quality. The GHz bursts use heat accumulation better because of the shorter time between pulses. R_a surface roughness of 0.23 μm, 0.1 μm and 0.08 μm were achieved for copper in the MHz, GHz and biburst modes, respectively. Additionally, many parameters yielded <0.15 μm R_a for the GHz burst mode. The same tendencies were seen for stainless-steel. The lowest surface roughness for the MHz burst was 0.63 μm, 0.55 μm for the GHz burst, and 0.45 μm for the biburst mode. Using the MHz burst mode, the ablation efficiency is the highest while using 3 pulses in the bursts at the optimal fluence, but the surface roughness is lowest with 6 pulses within the burst. GHz and biburst modes have a significantly lower ablation efficiency but a significantly higher polishing quality that could be used as a finishing step to achieve the desired surface roughness.

Author contributions

M. Gaidys wrote the manuscript, did all the stylus profiler measurements and SEM imaging, performed beam measurement experiments, A. Žemaitis performed polishing experiments, all authors read and corrected the manuscript.

Conflicts of interest

There are no conflicts to declare.

Acknowledgements

This project has received funding from the Research Council of Lithuania (LMTLT), agreement no. S-MIP-22-89.

Notes and references

1 S. Mishra and V. Yadava, *Opt Lasers Eng*, 2015, **73**, 89–122.
2 M. Radovanovic and M. Madic, *Rev. Tehnol. Neconv.*, 2011, **15**, 35.
3 D. Lee, R. Patwa, H. Herfurth and J. Mazumder, *J. Power Sources*, 2012, **210**, 327–338.
4 A. Riveiro, F. Quintero, F. Lusquiños, R. Comesaña and J. Pou, *Appl. Surf. Sci.*, 2011, **257**, 5393–5397.
5 D. Lee, R. Patwa, H. Herfurth and J. Mazumder, *J. Power Sources*, 2013, **240**, 368–380.
6 A. Weck, T. H. R. H. R. Crawford, D. S. S. Wilkinson, H. K. K. Haugen and J. S. S. Preston, *Appl. Phys. A: Mater. Sci. Process.*, 2008, **90**, 537–543.
7 G. Zhou, W. Li, Q. Xiang, W. He, S. Wang, Y. Chen, Y. Hong, W. Yang, M. Lai, S. Chen and H. Xu, *Appl. Surf. Sci.*, 2019, **479**, 512–518.
8 X. Jia, Y. Zhang, Y. Chen, H. Wang, G. Zhu and X. Zhu, *Int. J. Adv. Des. Manuf. Technol.*, 2019, **104**, 1269–1274.
9 A. Žemaitis, M. Gaidys, P. Gečys, G. Račiukaitis and M. Gedvilas, *Opt Lasers Eng*, 2019, **114**, 83–89.
10 M. Gaidys, A. Žemaitis, P. Gečys and M. Gedvilas, *Appl. Surf. Sci.*, 2019, **483**, 962–966.
11 K. C. Phillips, H. H. Gandhi, E. Mazur and S. K. Sundaram, *Adv. Opt. Photonics*, 2015, **7**, 684.
12 A. Žemaitis, M. Gaidys, M. Brikas, P. Gečys, G. Račiukaitis and M. Gedvilas, *Sci. Rep.*, 2018, **8**, 17376.
13 P. Elahi, H. Kalaycioğlu, Ö. Akçaalan, Ç. Şenel and F. Ömer Ilday, *Opt. Lett.*, 2017, **42**, 3808.
14 A. Žemaitis, P. Gečys, M. Barkauskas, G. Račiukaitis and M. Gedvilas, *Sci. Rep.*, 2019, **9**, 12280.
15 A. Žemaitis, M. Gaidys, P. Gečys, M. Barkauskas and M. Gedvilas, *Opt. Express*, 2021, **29**, 7641.
16 B. Jaeggi, S. Remund, R. Streubel, B. Goekce, S. Barcikowski and B. Neuenschwander, *J. Laser Micro/Nanoeng.*, 2017, **12**, 267–273.
17 X. Wolters, G. Bonamis, K. Mishchick, E. Audouard, C. Hönninger and E. Mottay, *Procedia Manuf*, 2019, **36**, 200–207.
18 H. Sun, *Opt. Eng.*, 1998, **37**, 2906.
19 A. Krishnan and F. Fang, *Front. Mech. Eng*, 2019, **14**, 299–319.

20 S. Mohajerani, J. D. Miller, O. R. Tutunea-Fatan and E. V. Bordatchev, *Procedia Manuf*, 2017, **10**, 708–719.
21 F. Bauer, A. Michalowski, T. Kiedrowski and S. Nolte, *Opt. Express*, 2015, **23**, 1035.
22 P. Lickschat, A. Demba and S. Weissmantel, *Appl. Phys. A*, 2017, **123**, 137.
23 A. Michalowski, F. Nyenhuis and G. Kunz, *PhotonicsViews*, 2020, **17**, 42–45.
24 T. Herrmann, F. Harth, B. Henrich, J. L'huillier and M. Hajri, *Laser Tech. J.*, 2016, **13**, 16–19.
25 J. Byskov-Nielsen, J.-M. Savolainen, M. S. Christensen and P. Balling, *Appl. Phys. A*, 2010, **101**, 97–101.
26 B. Neuenschwander, T. Kramer, B. Lauer and B. Jaeggi, *Burst mode with ps- and fs-pulses: Influence on the removal rate, surface quality, and heat accumulation*, ed. S. Roth, Y. Nakata, B. Neuenschwander and X. Xu, 2015, p. 93500U, **https://www.spiedigitallibrary.org/conference-proceedings-of-spie/9350/1/Burst-mode-with-ps-and-fs-pulses-Influence/10.1117/12.2076455.short?SSO=1**.
27 J. Zhang, Y. Wang, P. Cheng and Y. L. Yao, *J. Appl. Phys.*, 2006, **99**, 064902.
28 A. Žemaitis, M. Gaidys, P. Gečys and M. Gedvilas, *Opt. Lett.*, 2020, **45**, 6166.
29 Lamineries Matthey, *Steel 1.4301*, 2013, vol. 41, pp. 1–3.
30 S. M. Remund, M. Gafner, M. V. Chaja, A. Urniezius, S. Butkus and B. Neuenschwander, *Procedia CIRP*, 2020, **94**, 850–855.

P4

INFLUENCE OF NONLINEAR AND SATURABLE ABSORPTION ON LASER LIFT-OFF THRESHOLD OF AN OXIDE/METAL STRUCTURE

A. Žemaitis, **M. Gaidys**, P. Gečys, M. Gedvilas
Opt. Lett. **45**, 6166 (2020)
DOI: 10.1364/OL.404760

6166 Vol. 45, No. 22 / 15 November 2020 / Optics Letters Letter

Optics Letters

Influence of nonlinear and saturable absorption on laser lift-off threshold of an oxide/metal structure

ANDRIUS ŽEMAITIS, MANTAS GAIDYS, PAULIUS GEČYS, AND MINDAUGAS GEDVILAS*

Department of Laser Technologies (LTS), Center for Physical Sciences and Technology (FTMC), Savanorių Ave. 231, LT-02300 Vilnius, Lithuania
**Corresponding author: mgedvilas@ftmc.lt*

Received 7 August 2020; revised 22 September 2020; accepted 5 October 2020; posted 5 October 2020 (Doc. ID 404760); published 9 November 2020

In this work, a new, to the best of our knowledge, model of effective lift-off threshold of an oxide/metal target is presented. The influence of nonlinear processes in the oxide layer on its removal from the metallic samples using a picosecond laser was investigated. Nonlinear and saturable absorption in the layer was incorporated into modeling for prediction of effective laser lift-off threshold fluence change with varying peak intensities in a *z*-scan-type experiment for the first time. The new model coincides well with the experimental results.

https://doi.org/10.1364/OL.404760

The pulsed laser ablation threshold, laser-induced damage threshold (LIDT), and lift-off threshold fluences are used to describe the minimum laser energy per unit area, which is required to remove (ablate) material from the surface. It is well known that the material removal threshold is dependent on many laser processing parameters, such as the number of pulses per spot, irradiation wavelength [1], pulse duration [2], and polarization type [3]. The laser spot size on the sample and its related peak intensity's influence on the ablation threshold are rarely investigated in scientific literature, especially for metals [4]. Contrary, for dielectric coatings, LIDT dependence on the beam spot size is widely known and accepted [5]. A couple of independent scientific groups have developed theoretical models to predict and explain the ablation thresholds of metal dependence on laser beam size [4,6]. Kautek *et al.* proposed the theory called the extended defect model, which explains that the ablation threshold increases when spot size decreases [4]; however, Zhang *et al.* predicts completely different behavior [6]. Thus, there is no complete theoretical model found in the scientific literature that would fully explain the variation of the ablation threshold with varying beam sizes and its related peak intensities.

Metals are covered with oxide layers with thicknesses ranging from tens of nanometers to tens of micrometers [7], which usually are semi-opaque semiconductors and transparent insulators depending on the bandgap. Though, incoming laser irradiation first interacts with the metal oxides and only afterward with the metals themselves. However, the metal oxides are hard to ablate because they possess high laser ablation thresholds [8], which are by the order of magnitude higher than the metal ablation thresholds [9], and the laser ablation is initiated on an oxide/metal interface during the lift-off process [10]. Nonlinear and saturable absorption [11] are commonly observed when metal oxide films are exposed to intense light with intensities ranging from MW/cm^2 to TW/cm^2. Therefore, those oxide layers covering the metal affect the fraction of the incoming laser irradiation dose that reaches the target substrate depending on the intensity applied. The ablation threshold dependencies on pulse duration and its related peak intensities are well known for metal and dielectrics [12], but have never been investigated for an oxide/metal system. The laser lift-off threshold of the metal covered by an oxide is influenced by the nonlinear processes in the oxide layer and has to be taken into account. Thus, the laser lift-off threshold of an oxide/metal depends on the laser intensity applied and can be called the effective lift-off threshold fluence. Moreover, interference-related field enhancement effects influence the oxide layer ablation [13], though it will not be included in our work, since the transfer-matrix method is required for absorbed energy calculations, and nonlinear processes cannot be applied for this method. To the best of our knowledge, the influence of nonlinear and saturable absorption in the metal oxide layer on the effective laser lift-off threshold of an oxide/metal structure has never been investigated in the scientific literature. Therefore, novel experimental and theoretical research on the effective laser lift-off threshold change with varying peak intensities in *z*-scan experiments has been created in this work for the first time.

Here we propose the nonlinear and saturable absorption in the oxide layer on the metal substrate as the two most influencing factors for the effective laser lift-off threshold dependence on the different peak intensities in *z*-scan experiments. The existing analytical normalized transmission equation of the semi-transparent thin layer in open aperture *z*-scan was incorporated into the effective laser lift-off threshold dependence on the sample position in the newly presented model. The *z*-scan-type picosecond laser ablation experiment was conducted, and lift-off thresholds were measured at different sample positions, which caused different beam peak intensities on the processed oxidized copper target material. The numerical calculations

0146-9592/20/226166-04 Journal © 2020 Optical Society of America

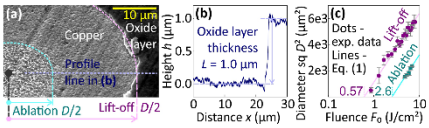

Fig. 1. (a) SEM micrograph, (b) profile, and (c) diameter squared D^2 versus peak laser fluence F_0 of ablated copper and removed oxide layer from copper substrate by lift-off technique. (a) The SEM image was taken at tilt angle of 45°, pulse duration $\tau = 10$ ps, wavelength $\lambda = 1064$ nm, repetition rate $f_p = 100$ kHz, number of pulses $N = 1$, pulse energy $E_p = 51$ μJ, beam radius $w = 33.2 \pm 0.7$ μm, peak laser fluence $F_0 = 3.0$ J/cm^2, peak intensity $I_0 = 0.30$ TW/cm^2, ablated diameter of pristine copper $D = 16.9 \pm 1.8$ μm, and lift-off diameter of oxide layer $D = 60.4 \pm 1.6$ μm. (b) The oxide layer thickness $L = 1.0 \pm 0.1$ μm was evaluated from the height profile. The oxide lift-off threshold fluence 0.57 ± 0.03 J/cm^2 and copper ablation threshold 2.6 ± 0.3 J/cm^2 were retrieved from line fits of experimental data points by Eq. (1) in (c).

using the new proposed model equation coincide well with the experimental results of effective laser lift-off threshold dependence on the z-scan position.

The copper (Cu) sample with a cuprous oxide (Cu_2O) layer was used in the laser ablation experiments. The copper (CW004A, Ekstremalė) target had mirror-like finish with the surface roughness $R_a < 0.1$ μm measured by a stylus profiler (Dektak 150, Veeco). The picosecond laser irradiation source (Atlantic, Ekspla) with a pulse duration $\tau = 10$ ps, wavelength $\lambda = 1064$ nm, pulse energies up to $E_p = 142$ μJ, repetition rate $f_p = 100$ kHz, Gaussian beam with a quality parameter of $M^2 = 1.06$ measured in our previous work [14], and a number of laser pulses per spot $N = 1$ was used in ablation experiments. The laser-treated oxide/metal surface topography was studied by scanning electron microscope (SEM) (JSM-6490LV, JEOL) [Fig. 1(a)] and optical profiler (S neox, Sensofar) [Fig. 1(b)].

The laser-irradiated area consisted of two distinct areas, laser ablation of pristine copper and lift-off of the oxide layer [Fig. 1(a)]. The thickness of the oxide layer measured from the height profile was $L = 1.0 \pm 0.1$ μm [Fig. 1(b)]. The fluence threshold was measured by the ablated crater diameter D dependence on the pulse energy E_p [15]. Taking into account that a laser beam has the Gaussian transverse intensity distribution, the expression for the crater diameter squared D^2 and the laser pulse energy E_p can be written as [15]

$$D^2 = 2w^2 \ln\left(2E_p/(\pi w^2 F_{\text{th}})\right), \tag{1}$$

where w is the Gaussian beam radius on the sample, E_p is the pulse energy, and F_{th} is the threshold fluence. The line extrapolation of $D^2(E_p)$ to the $D^2 = 0$ μm^2 gives the threshold pulse energy $E_{p\,\text{th}}$, the function slope is related to the beam radius w, and the ablation threshold then can be evaluated by $F_{\text{th}} = 2E_{p\,\text{th}}/(\pi w^2)$. The optical microscope (Eclipse LV100, Nikon) was used for the measurements of the ablated diameters of pristine copper and diameters of the removed oxide layer of Cu_2O/Cu samples [Fig. 1(c)]. Threshold values of $F_{\text{th}} = 0.57 \pm 0.03$ J/cm^2 and 2.6 ± 0.3 J/cm^2 were retrieved from line fits by Eq. (1) for oxide lift-off and copper ablation, respectively [Fig. 1(c)]. The literature value of the lift-off threshold for copper oxide removal from the copper sample is $F_{\text{th}} = 0.62$ J/cm^2 ($\tau = 12$ ps, $\lambda = 1064$ nm, $f_p = 100$ kHz, $w = 17$ μm, $N = 1$) [10]. The literature value of ablation threshold of copper by ($\tau = 10$ ps, $\lambda = 1064$ nm, $f_p = 50$ kHz, $w = 41.8$ μm, $N = 1$) laser is $F_{\text{th}} = 2.0$ J/cm^2 [14]. The literature threshold fluence values coincided well with our current work.

The light attenuation propagating through a linearly and nonlinearly absorbing material can be described as [16]

$$dI/dz = -\alpha I - \beta I^2, \tag{2}$$

where $I = I(z)$ is the peak intensity within the sample material, depending on the propagation distance z in the sample; α is the linear absorption coefficient; and β is the nonlinear absorption coefficient. The normalized transmission through the sample can be extracted from the solution of Eq. (2) and expressed as [17]

$$T = e^{-\alpha L}/(\beta I L_{\text{eff}} + 1), \tag{3}$$

where I is the incident intensity, L is the physical sample thickness, and L_{eff} is the effective thickness of the sample [17],

$$L_{\text{eff}} = \left(1 - e^{-\alpha L}\right)/\alpha. \tag{4}$$

Because of the linear absorption saturation behavior, the linear absorption coefficient $\alpha = \alpha(I)$ depends on the peak intensity I, and for homogenous saturation can be expressed as [18]

$$\alpha(I) = \alpha_0/\left(1 + (I/I_s)^2\right), \tag{5}$$

where α_0 is the low-intensity absorption coefficient and I_s is the saturation intensity. The Gaussian beam intensity in the z-scan-type experiment can be expressed as

$$I = I_0/\left(1 + (z/z_R)^2\right), \tag{6}$$

where $I_0 = 2E_p/(\pi w_0^2 \tau)$ is the peak pulse intensity in the center of the Gaussian beam at a focus position, w_0 is the focused beam radius at $1/e^2$ level, τ is the pulse duration, $z_R = \pi w_0^2/(\lambda M^2)$ is the Rayleigh length, λ is the wavelength of irradiation, and M^2 is the quality parameter of the Gaussian beam.

The direct bandgap for Cu_2O is 2.1 eV [19], which is larger than the photon energy 1.17 eV at the wavelength of 1064 nm. The linear absorption coefficient of Cu_2O is $\alpha = 5.2 \times 10^3$ cm^{-1} [20]. Therefore, the transmission of a linearly absorbing oxide layer at low peak intensities in the GW/cm^2 range evaluated by Eq. (3) is $T_0 = \exp(-\alpha_0 L) \approx 60\%$, and the layer can be assumed as semi-opaque. The saturation intensity of the linear absorption coefficient for Cu_2O is $I_s \sim 0.1$ TW/cm^2 [21]; thus, the semi-opaque oxide layer suddenly becomes fully transparent, when peak intensities exceed the saturation intensity. However, by further increasing intensity, the nonlinear absorption becomes dominant, and the oxide layer changes to opaque again. The nonlinear absorption coefficients of Cu_2O are $\beta = 4.3 \times 10^{-9}$ cm/W [20]. Thus, a focused picosecond laser beam with high peak intensities up to 3 TW/cm^2 obtained in our experimental conditions induces nonlinear absorption in the transparent oxide layer on top of the copper target. The nonlinearly absorbing oxide layer transmits only a part of the incoming laser beam to the metal substrate and has to be taken

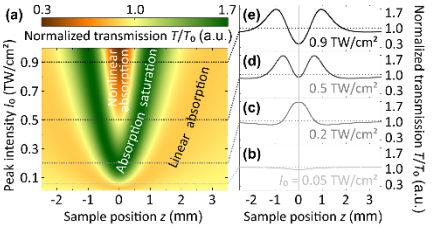

Fig. 2. (a) Calculated normalized transmission T/T_0 (color scale) versus sample position z (bottom axis) and peak pulse intensities I_0 (left axis) for Cu_2O layer. The three different absorption regions are indicated: yellow, linear absorption; green, linear absorption saturation; brown, nonlinear absorption. Profiles of normalized transmission T/T_0 (right axis) dependence on the sample position z (bottom axis) at different peak intensities I_0: (b) 0.05 TW/cm²; (c) 0.2 TW/cm²; (d) 0.5 TW/cm²; (e) 0.9 TW/cm².

into account when predicting effective ablation characteristics of an oxide/metal structure. Equations (3)–(6) have been numerically solved and normalized T/T_0 transmission of the Cu_2O layer was calculated [Fig. 2(a)].

At low peak pulse intensities of $I_0 \approx 0.05$ TW/cm² that are smaller than the saturation intensity $I_s \sim 0.1$ TW/cm², just linear absorption is observed with no saturation and very small nonlinear absorption in the focal position $z \ll \pm z_R$; thus, almost constant normalized transmission $T/T_0 \approx 1$ in all sample z positions is observed [Fig. 2(b)]. With the peak intensity values of ~ 0.2 TW/cm² exceeding the saturation intensity, the oxide layer becomes nearly fully transparent $T/T_0 \approx 1.7$ with a sample position close to the focal point $z \ll \pm z_R$ [Fig. 2(c)]. When peak intensity reaches the value of ~ 0.5 TW/cm², the nonlinear absorption equals the linear intensity saturation; thus, the normalized transmission in the oxide layer reaches a value close to $T/T_0 \approx 1$ in the focal region $z \approx 0$ mm [Fig. 2(d)]. However, the nonlinear absorption is very sensitive to the peak intensity and occurs only in fine focus $z \ll \pm z_R$. Out of the focus in $z \approx \pm 1$ mm, the Cu_2O layer is still transparent with a transmission value of $T/T_0 \approx 1.7$ [Fig. 2(d)]. When peak pulse intensity reaches a high value of ~ 0.9 TW/cm², the nonlinear absorption exceeds the absorption saturation, and normalized transmission drops to the value of $T/T_0 \approx 0.4$ in the focal point. Therefore, the Cu_2O layer becomes opaque in the focal range of the beam. However, the defocused beam in the Rayleigh range $z \approx \pm z_R$ is still transparent because of the saturation of linear absorption with normalized transparency of $T/T_0 \approx 1.7$ [Fig. 2(e)].

The z-scan-type laser lift-off threshold evaluation experiments with controlled laser peak pulse intensities have been conducted in this work. The peak pulse intensities I_0 were ranging from 20 GW/cm² to 3.0 TW/cm². The Rayleigh length of the focused beam was of $z_R \approx 0.83$ mm. The squared lift-off diameters of an oxide layer from copper at different positions z are depicted in [Figs. 3(a) and 3(b)].

Pulse energies of 20 different values have been used at each of the 11 fixed z-scan positions with a fixed laser spot radius on the sample. Every test has been repeated 10 times to get the statistical deviation errors bars. Experimental data points of

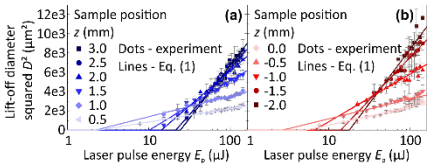

Fig. 3. Lift-off diameter squared D^2 of oxide layer removed from copper dependence on the laser pulse energy E_p at various sample position z values ranging from (a) 0.5 mm to 3.0 mm, step 0.5 mm and from (b) 0.0 mm to −2.0 mm, step −0.5 mm. Solid dots represent the experimental data points, error bars are the statistical deviation from average crater diameter from 10 dimples ablated using the same pulse energy, and solid lines are fits by Eq. (1). Pulse duration $\tau = 10$ ps, laser wavelength $\lambda = 1064$ nm, repetition rate $f_p = 100$ kHz, and number of pulses per spot $N = 1$.

ablated crater diameters were fitted using Eq. (1), and laser spot radiuses at different sample positions z were retrieved as fitting parameters and its errors. The laser spot radius values on the sample ranged from $w_0 = 17.2 \pm 0.3$ μm in the focal region to $w = 48.6 \pm 1.2$ μm out of focus. The fit of experimental data points by Eq. (1) [Figs. 3(a) and 3(b)] also provided information about the effective lift-off threshold fluence of the oxide/copper structure at various positions z of the sample [Fig. 4(a)].

It was found that the effective lift-off threshold is highest near the beam waist $z = 0$ mm, then we saw a sharp drop of effective lift-off threshold to a minimum value at $z = \pm 1$ mm,

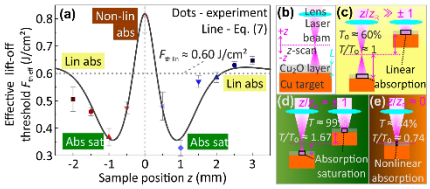

Fig. 4. (a) Effective lift-off threshold $F_{th,eff}$ of oxide/copper dependence on sample z position. Solid dots and error bars represent the effective lift-off threshold values retrieved from the fitting parameters by Eq. (1) [Figs. 3(a) and 3(b)], and the solid gray line is the fit of experimental data points by Eq. (7). Pulse duration $\tau = 10$ ps, wavelength $\lambda = 1064$ nm, repetition rate $f_p = 100$ kHz, and a number of pulses per spot $N = 1$. (b) Principal visual scheme of the proposed model with semi-transparent Cu_2O layer on top of the Cu sample, which partially attenuates the focused picosecond laser beam in z-scan laser ablation experiment with indicated incoming Gaussian beam, focusing lens, and variable sample positions ranging from top $+z$ to bottom $-z$ in respect with the beam focus and its related controlled peak intensities. The copper substrate is indicated with orange color, and the semi-opaque cuprous oxide layer in gray color. The different Cu_2O layer transmission cases are indicated depending on peak pulse intensities: (c) out of focus with sample positions $z/z_R \gg \pm 1$, low intensities of the defocused beam, and linear absorption with transmission value $T_0 \approx 60\%$; (d) sample position $z/z_R \approx \pm 1$ in the saturable absorption intensity region with transmission value $T \approx 99\%$; (e) sample position $z/z_R \approx 0$ in the focus of the beam and high peak intensities, and nonlinear absorption exceeds absorption saturation in the oxide layer and transmission drop to $T \approx 44\%$.

and afterward it increased again [Fig. 4(a)]. A similar drop of the laser-ablated volume per pulse in z-scan ablation at the sample position of $z/z_R \approx 0$ has been observed by Chen *et al.* [22]; however, the drop of ablation rate was not attributed to the increase of threshold fluence in their research. Thus, in this work, we have proposed a new model for the effective lift-off threshold fluence, which considers the attenuation of the incoming laser irradiation by the oxide layer on the metal substrate.

In our proposed ablation model, the laser irradiation is attenuated by the semi-transparent oxide layer, and only a fraction of the incoming laser beam reaches the copper target. The principal visual scheme of our threshold model of a semi-transparent Cu_2O layer with the thickness of $L = 1.0\ \mu m$ on the Cu substrate is depicted in Fig. 4(b). The Gaussian picosecond laser beam is focused by the objective lens, and the peak pulse intensity is varied on the target material by controlling the z-scan position of the sample. The three different absorbing scenarios depending on the peak pulse intensities applied are linear absorption, a saturation of linear absorption, and nonlinear absorption depicted in Figs. 4(c), 4(d), and 4(e), respectively. By having the sample out of the focal position, moderate values of effective lift-off threshold of $F_{th\,lin} \approx 0.60\ J/cm^2$ are observed [Fig. 4(a)]. This is explained by our proposed model that when a highly defocused beam $z/z_R \gg \pm 1$ with low peak intensities is applied on the sample, only linear absorption is observed in the attenuating Cu_2O layer [Fig. 4(c)]; thus, just a fraction $T_0 \approx 60\%$ of the incoming laser beam interacts with the copper in the oxide/metal interface, and moderate energy densities are needed to ablate the copper target material. However, when laser intensities reach the saturable absorption, the oxide layer suddenly becomes transparent, and almost all incoming laser irradiation reaches the pristine copper. Thus, the drop of effective lift-off threshold to $\sim 0.36\ J/cm^2$ is observed [Fig. 4(a)]. It is graphically depicted in our proposed model with moderate intensities above the saturation intensity at sample position $z/z_R \approx \pm 1$ and moderate peak intensities with the normalized transmission of the oxide layer of $T/T_0 \approx 1.67$ [Fig. 4(d)]. Thus, the major part of the incoming laser irradiation $T \approx 99\%$ is transmitted through the oxide layer. When peak pulse intensities in the focal range reach the TW/cm^2 values, the nonlinear absorption becomes dominant and exceeds the absorption saturation; consequently, only a fraction of the incoming laser beam reaches the copper, and the effective lift-off threshold increases to the value of $0.81\ J/cm^2$ [Fig. 4(a)]. It is explained with our model that at the focal position $z/z_R \approx 0$, the beam is focused, and the highest peak intensities are achieved; therefore, the nonlinear absorption is reached, and the oxide layer becomes opaque $T/T_0 \approx 0.74$ [Fig. 4(e)]. Only a small fraction $T \approx 44\%$ of the incoming laser beam goes through the Cu_2O layer and reaches the Cu substrate.

Therefore, taking into account linear absorption, absorption saturation, and nonlinear absorption in the model, it can be assumed that the effective lift-off threshold of oxide/metal is the product of the ablation threshold in linear absorption regime $F_{th\,lin}$ at low peak intensities and the inverse normalized transitivity T_0/T of cuprous oxide layer defined by Eq. (3). The effective lift-off threshold can be expressed as follows:

$$F_{th\,eff} = F_{th\,lin}\,(T_0/T)\,. \tag{7}$$

The effective lift-off threshold $F_{th\,eff} = F_{th\,eff}(z)$ defined by Eq. (7) depends on the sample position z in the z-scan-type laser ablation experiments. The model fit is in good coincidence with the experiment [Fig. 4(a)]. The new model predicts the fall of the effective ablation threshold to minimum values of $F_{th\,eff} \sim 0.36\ J/cm^2$ near the sample position of $z \approx \pm 1$ mm. Also, the model predicts a steep rise of ablation threshold value up to $F_{th\,eff} \sim 0.81\ J/cm^2$ in the focus of the beam. The moderate values of effective ablation threshold $F_{th\,eff}$ close to $F_{th\,lin} \approx 0.60\ J/cm^2$ out of the focus are also predicted.

To conclude, the nonlinear absorption and saturable linear absorption have been incorporated in a theory of effective laser lift-off threshold of oxide/metal structure dependence on z-scan position related peak intensities for the first time. The attenuation of the incoming laser beam by a copper oxide layer on a copper target was included in the ablation model. The new model has a good agreement with the experimental data of the z-scan-type effective lift-off threshold of the cuprous oxide/copper target. Our proposed model opens new insights on the influence of the surface oxide layer on the effective laser lift-off threshold of oxidized metallic samples.

Disclosures. The authors declare no conflicts of interest.

REFERENCES

1. P. Gečys, G. Račiukaitis, M. Ehrhardt, K. Zimmer, and M. Gedvilas, Appl. Phys. A **101**, 373 (2010).
2. D. Giguere, G. Olivie, F. Vidal, S. Toetsch, G. Girard, T. Ozaki, J. C. Kieffer, O. Nada, and I. Brunette, J. Opt. Soc. Am. **24**, 1562 (2007).
3. Z. Sun, M. Lenzner, and W. Rudolph, J. Appl. Phys. **117**, 073102 (2015).
4. O. Armbruster, A. Naghilou, M. Kitzler, and W. Kautek, Appl. Surf. Sci. **396**, 1736 (2017).
5. S. Martin, A. Hertwig, M. Lenzner, J. Kruger, and W. Kautek, Appl. Phys. A **77**, 883 (2003).
6. Y. Zhang, B. Lauer, B. Neuenschwander, and V. Romano, Proc. SPIE **9735**, 97350M (2016).
7. M. Morcillo, B. Chico, D. de la Fuente, and J. Simancas, Int. J. Corros. **2012**, 824365 (2012).
8. J. Zhang, Y. Wang, P. Cheng, and Y. L. Yao, J. Appl. Phys. **99**, 064902 (2006).
9. M. Hashida, A. F. Semerok, O. Gobert, G. Petite, Y. Izawa, and J. F. Wagner, Appl. Surf. Sci. **197-198**, 862 (2002).
10. H. Zhu, H. Zhang, X. Ni, Z. Shen, and J. Lu, J. Laser Appl. **31**, 042015 (2019).
11. A. Gaur, H. Syed, B. Yendeti, and V. R. Soma, J. Opt. Soc. Am. B **35**, 2906 (2018).
12. E. G. Gamaly, A. V. Rode, B. Luther-Davies, and V. T. Tikhonchuk, Phys. Plasmas **9**, 949 (2002).
13. M. Sozet, S. Bouillet, J. Berthelot, J. Neauport, L. Lamaignere, and L. Gallais, Opt. Express **25**, 25767 (2017).
14. A. Žemaitis, M. Gaidys, M. Brikas, P. Gečys, G. Račiukaitis, and M. Gedvilas, Sci. Rep. **8**, 17376 (2018).
15. J. M. Liu, Opt. Lett. **7**, 196 (1982).
16. G. Walters, B. R. Sutherland, S. Hoogland, D. Shi, R. Comin, D. P. Sellan, O. M. Bakr, and E. H. Sargent, ACS Nano **9**, 9340 (2015).
17. W. Liu, J. Xing, J. Zhao, X. Wen, K. Wang, P. Lu, and Q. Xiong, Adv. Opt. Mater. **5**, 1601045 (2017).
18. N. Dong, Y. Li, S. Zhang, N. McEvoy, R. Gatensby, G. S. Duesberg, and J. Wang, ACS Photon. **5**, 1558 (2018).
19. R. Marschall, Adv. Funct. Mater. **24**, 2421 (2014).
20. G. Yang, A. Chen, M. Fu, H. Long, and P. Lu, Appl. Phys. A **104**, 171 (2010).
21. N. A. Saad, M. H. Dar, E. Ramya, S. R. G. Naraharisetty, and D. N. Rao, J. Mater. Sci. **54**, 188 (2018).
22. T. H. Chen, R. Fardel, and C. B. Arnold, Light Sci. Appl. **7**, 17181 (2018).

PP1

HIGH-RATE STAINLESS STEEL LASER COLOURING WITH GHZ FEMTOSECOND BURSTS

M. Gaidys, A. Selskis, P. Gečys, M. Gedvilas
Opt. Laser Technol. 2025 (Submitted, major revision)
DOI:

Manuscript

High-rate Stainless Steel Laser Colouring with GHz Femtosecond Bursts

Mantas Gaidys*[1], Algirdas Selskis[2], Paulius Gečys[1], Mindaugas Gedvilas[1]

[1]Department of Laser Technologies (LTS), Center for Physical Sciences and Technology (FTMC), Savanorių Ave. 231, LT–02300 Vilnius, Lithuania

[2]Department of Characterisation of Materials Structure, Center for Physical Sciences and Technology (FTMC), Saulėtekio Ave. 3, LT-10257 Vilnius, Lithuania

*Corresponding author: mantas.gaidys@ftmc.lt

Abstract

Laser colouring has unique and sought-after advantages but the process has not yet been optimized. Using femtosecond pulses and GHz burst mode we have achieved high colouring rates and various colours. The colours dependence on the number of pulses within the GHz burst and beam scanning speed were tested. Other influencing parameters such as MHz burst, Biburst, hatch, repetition of scans and laser frequency were also tested. The achieved colours were also hydrophobic, which increases their applicability.

Keywords

Laser colouring, femtosecond, burst, stainless steel, wettability, hydrophobic.

Introduction:

The importance of colours in everyday life cannot be understated as it spans across various areas, including safety, communication, aesthetics, culture, marketing and even health as it affects our mood greatly. Various industries have utilized different colouring methods including anodizing [1,2], electroplating [3–5], powder or physical vapor deposition coating [6,7], patination [8], as well as heat, chemical and electrochemical colouring [9–11]. All these methods have various benefits and drawbacks; however, laser colouring has unique and sought-after advantages that resulted in its rise in popularity. Laser colouring offers high precision, permanence, non-contact nature, versatility with materials, environmental friendliness, and suitability for automation and rapid production. A wide range of metals have been coloured using laser irradiation such as, stainless-steel [12–18], titanium [19–23], copper [24–26], aluminium [27,28] and others [29–32].

Laser colouring is used in the medical field to mark surgical instruments, equipment or implants with serial numbers, barcodes and logos, for greater differentiation [33]. Because no coatings or chemicals are used, there is no added risk of harm to the patients. It is also used in the aerospace and automotive industries for marking various parts and components because of laser colourings higher permanence and precision which ensures traceability and compliance with stringent regulations. Moreover, laser colouring can be used as an anti-counterfeiting measure by incorporating hidden or embedded colour-changing elements into documents, banknotes [34] and in the jewellery and branding industries to colour different decorative designs, detailed patterns or logos [23,32].

There are three main ways that laser colouring induces colours on metals. The first one is colour change due to oxidation of the metal when it is irradiated by the laser beam [13,15,21,35–40]. The colour change is two-fold here, the oxide layer itself can have a specific colour or the colour can arise due to the thin film effect. Thin film effect is seen when interference happens between reflected light from the oxide layer and the light reflected from the metal surface itself. If the optical path difference is equal to a certain wavelength or its product with an integer, the specific colour will be seen. The second way to produce colours using laser irradiation is structural colours [41–44]. Like the name suggests, they are achieved by creating laser

induced periodic surface structures (LIPSS). Similar to a one-dimensional grating, LIPSS cause colours due to the diffraction effect [45]. These colours are very angle dependent. The third laser colouring method on metals is structural colours that are not angle dependent and arise from nanostructures and nanoparticles on the metals surface [32,46,47]. These nanoparticles and nanostructures are sporadically distributed after laser irradiation and cause the surface plasmon resonance (SPR) effect. This effect is only seen on plasmonic metals.

While many metals and different colours have been achieved using laser colouring, the process has not yet been fully optimized. Copious amount of laser processing and material parameters have an effect on laser colouring, therefore increasing the time required to perfect the method. In this work, MHz, GHz and biburst burst modes were tested to achieve the highest number of colours and highest possible colouring rate. Laser processing parameters including hatch, repetition of scans and laser frequency were also tested to see whether they increase the colouring rate.

Experimental setup

The experiment was carried out using a solid-state laser (Carbide, Light Conversion) with a wavelength of 1030 nm. Pulse duration was set at 245 fs and pulse repetition rate was set to 100 kHz for the majority of the experiment, but changed to 200 kHz and 300 kHz for the pulse repetition test. The beam waist radius was 20.6 μm and the beam quality factor M^2 was 1.08. The beam was positioned using a galvanometric scanner (Intelliscan 14, ScanLab) and focused using a 100 mm F-theta lens. The laser was capable of different burst regimes: MHz, GHz and biburst. When the laser is working in the normal pulsed mode (Fig. 1a) at 100 kHz the time difference between pulses is equal to 10 μs. These pulses can be divided into smaller subpulses with either MHz or GHz intra-burst repetition rates and the MHz and GHz burst modes work quite similarly. In the MHz burst mode (Fig. 1b), the intra-burst repetition rate is equal to 64.68 MHz with a time difference between subpulses of 15.5 ns, while in the GHz burst mode (Fig. 1c), the intra-burst repetition rate is equal to 2.27 GHz with a time difference between subpulses of 440 ps. The number of pulses within the MHz and GHz bursts are notated by letters N and P, respectively. For the biburst mode (Fig. 1d), when we divide the MHz burst pulses further into the GHz burst pulses, we get the aforementioned biburst mode. It is important to remember, that it does not matter into how many subpulses the pulse is divided into, the overall pulse energy stays the same.

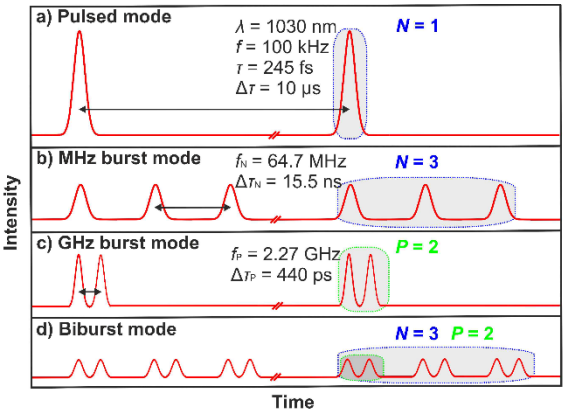

Fig. 1. Schematic illustration of the different laser burst modes. a) pulsed mode b) MHz burst mode; c) GHz burst mode; d) Biburst mode.

Sample characteristics

Stainless steel samples (304, Ekstremalė) 150 mm × 150 mm × 0.4 mm were used for the experiments. Stainless steel 304 is an alloy mainly composed of iron, chromium and nickel. It is used for its advantages such as, high temperature, corrosion resistance, durability, high tensile strength, relatively low price and formability.

Experiment

On the stainless-steel plates, using a galvanometric scanner 5 mm horizontal lines were scanned in a square shape with a 10 µm distance between the lines (hatch) (Fig. 2). The area of the square was set to 5 mm × 5 mm. An array of squares was achieved where laser scanning speed was increased vertically and average laser power was increased horizontally. The scanning speed was increased from 1000 mm/s to 4250 mm/s, while the average laser power was increased from 9.6 W to 40 W.

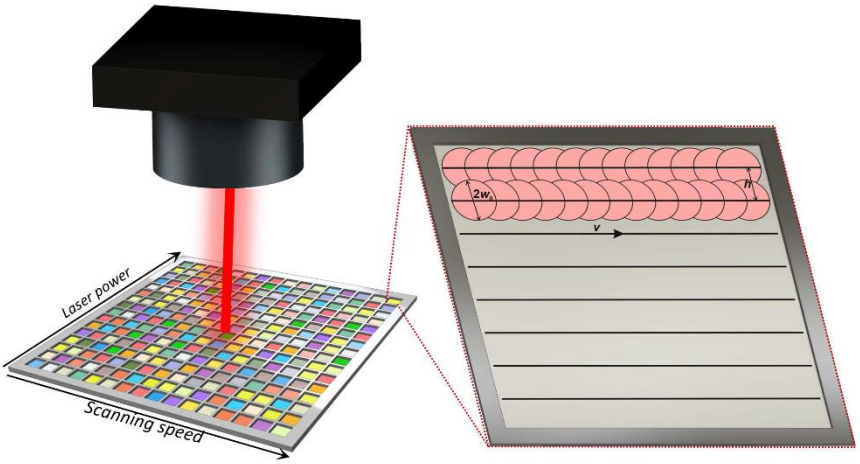

Fig. 2 Schematic representation of the experiment. With the help of a galvanometric scanner, coloured squares are micromachined using laser irradiation on the stainless-steel plates. Scanning speed and laser power are changed during the experiment, which is then repeated with different number of pulses within GHz burst modes or changing other laser processing parameters.

The experiment was repeated at different burst modes with varying number of pulses within the burst. Other laser parameters were also tested. The same experiment was performed but instead of horizontally changing the laser power, other parameters, including hatch, laser frequency and repetition of scans were chosen. Afterwards, the micromachined array of coloured squares on the stainless-steel plates was put inside a white box (LightRoom) with LED lights on top. A picture of the array was taken using a digital camera (Leopard Imaging, LI-IMX563-MIPI-AF) equipped with 7.05 mm lens and 12 MP CMOS image sensor (Sony, IMX563) that was on the roof of the white box to maintain constant conditions for the whole experiment.

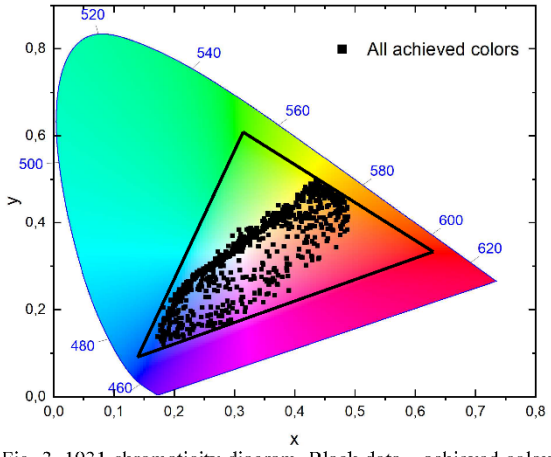

Fig. 3. 1931 chromaticity diagram. Black dots – achieved colours in the experiments. Black triangle – colours that are possible achieve in the model.

The CIE 1931 (Fig. 3) chromaticity diagram represents colour based on human visual perception and is used in many industries, such as printing, photography, television and also scientific literature [19,32,48–53]. The diagram represents all visible colours as seen by the human eye, mapped within a two-dimensional space defined by the x and y chromaticity coordinates. The horseshoe-shaped curve, known as the spectral locus, outlines the limits of human vision in the diagram. Every colour visible to the human eye falls within this curve, however not all colours can be replicated by technology. Therefore, various approximation models are used, and because no model can replicate all colours within the diagram, only the colours in the black triangle can be shown. The diagram includes a point representing white light, located at coordinates $x - 0.333$, $y - 0.333$. Colours closer to this point appear more desaturated, meaning they look closer to white or grey. As it can be seen in (Fig. 3) we have achieved numerous colours filling almost the entire triangle area. Many different blue, purple, orange and yellow colours have been achieved, as well as, a few green and red colours. The later are the fewest and most difficult to obtain in our experiments.

It is important to not only achieve a wide range of colours, but to do it as rapidly as possible. To define the speed of colouring a certain arena we use the colouring rate, denoted as $\mathrm{d}S/\mathrm{d}t$, which is defined as the total coloured area divided by the processing time. For a square area with side length l, the coloured area is equal to l^2. The processing time t can be calculated by considering the number of lines N needed to cover the whole area, each of length l, and the scanning speed v. The number of lines is determined by dividing the side length by the hatch h, so $N = l/h$. Therefore, the processing time becomes $t = Nl/v = l^2/vh$. Substituting this back into the colouring rate equation yields $\mathrm{d}S/\mathrm{d}t = l^2/t = vh$. This demonstrates that the colouring rate simplifies to the product of the scanning speed and the hatch distance. Thus, despite the complexity of various processing parameters, the colouring rate provides a straightforward metric for comparison by focusing on these two key variables.

Different laser processing parameters result in different colours. Our experiment was carried out with $P = 2$, 4, 7, 10, 15 and 25 pulses within the GHz burst. As can be seen from (Fig. 4) we get similar results with $P = 2$, 4, 7, 10 pulses within the GHz burst. Increasing the number of bursts further to $P = 15$ (Fig. 5) results in colours that are far less vibrant but still quite similar to the ones in (Fig. 4). However, increasing the number of pulses within the burst further to $P = 25$ drastically reduces the number of different colours achieved (Fig. 5) as only brown and dark green or dark purple colours can be seen.

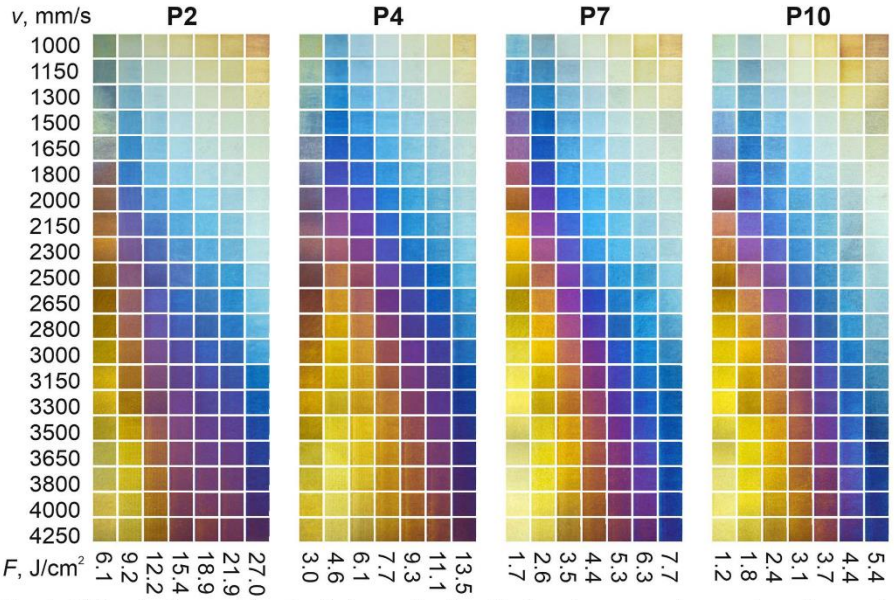

Fig. 4. Different colours achieved with laser colouring. The laser beam scanning speed was increased from 1000 mm/s to 4250 mm/s and average pulse fluence was increased from 12.1 J/cm^2 to 54.1 J/cm^2. The experiment was repeated at $P2$, $P4$, $P7$ and $P10$ pulses within the GHz burst with individual intra-burst pulse fluence listed.

When the accumulated pulse fluence is at F – 12.11 J/cm^2, for P – 2, 4, 7, 10, 15 pulses within the GHz burst a pattern of the colours going from light green, to blue, to purple, to orange and lastly yellow was seen when the laser beam scanning speed was increased from 1000 mm/s to 4250 mm/s. Increasing the accumulated pulse fluence resulted in the existing pattern being kept, however, the colour transitions were more gradient with more transitional colours appearing. When F – 24.31 J/cm^2 and higher accumulated pulse fluences were achieved, the colour pattern changed slightly. The starting colours were light brown, going to light green and turning into light blue that changed to purple, orange and lastly yellow. This allowed to achieve certain colours at a much higher scanning speed. Increasing the laser beam scanning speed further than 4250 mm/s resulted in unstable and not uniform colours that were somewhere between yellow, purple, blue.

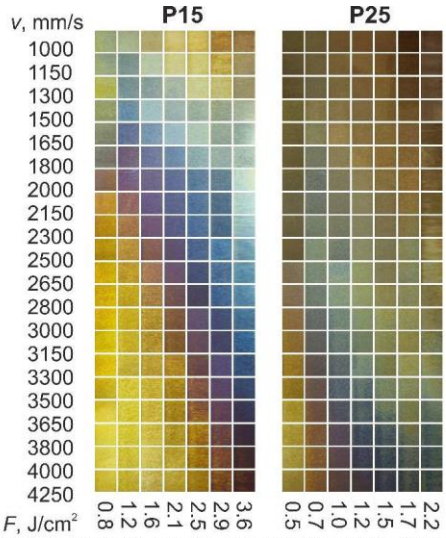

Fig. 5. Different colours achieved with laser colouring. The laser beam scanning speed was increased from 1000 mm/s to 4250 mm/s and average pulse fluence was increased from 12.1 J/cm^2 to 54.1 J/cm^2. The experiment was repeated at *P*15 and *P*25 pulses within the GHz burst with individual intra-burst pulse fluence listed.

Besides the commonly used RBG colour model there are other popular models such as HSL (Hue, Saturation, Lightness). Hue refers to the attribute of a colour that enables us to classify it as red, blue, green, etc. Hue is determined by the dominant wavelength of light that a colour reflects or emits. In colour models like HSL hue is usually represented as a degree on the colour wheel, ranging from 0° to 360°, where each degree corresponds to a specific colour: 0° being red, 60° yellow, 120° green, 180° cyan, 240° blue and 300° magenta. From the CIE diagram (Fig. 3) reveals that only a limited number of vibrant green and red colours are achieved. Vibrant colours correspond to high saturation levels, typically values of 80 or greater. However, the observed saturation is quite low, ranging from 20 to 30, while the lightness is relatively high, between 60 and 85, at different fluences when using 7 or 10 pulses within the GHz burst (Fig. 6, a and b) for the green colours. Increasing the number of pulses within the GHz burst to 15 and 25 (Fig. 6, c and d) causes the green colour saturation to drop further into the 5 to 20 range, and the lightness decreases to between 40 and 70. Similar trends are observed for the red colours, with saturation and lightness values never exceeding 60.

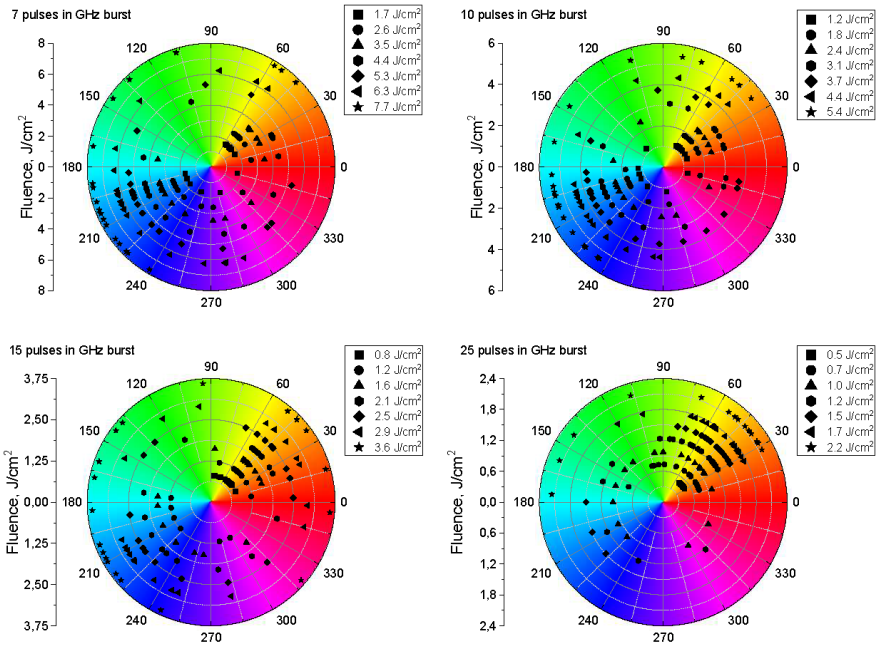

Fig. 6. Hue dependence on fluence polar diagrams with P = 7, 10, 15 and 25 pulses within the GHz burst.

Additional burst modes were tested to determine whether more colours and higher colouring rates could be achieved (Fig. 7a). In the MHz burst mode, regardless of the scanning speed, only brown colours were produced. Notably, similar brown hues could be obtained at scanning speeds exceeding 4250 mm/s. In contrast, in our previous work [14] we primarily achieved various colours using the biburst mode at a much lower scanning speed of 100 mm/s. By increasing the scanning speed to the 1000 – 4250 mm/s range and utilizing $N2P7$ and $N2P10$ biburst modes, it was possible to produce different colours, although these were less vibrant than those in the GHz burst modes. Moreover, increasing the number of pulses in the MHz burst mode to four or more still resulted only in brown colours. This shows, that the GHz burst mode is far superior in achieving vibrant colours and only when increasing the number of N by a minimal amount can any colours be visible at all in the biburst mode. Multiple scans were also tested (Fig. 7b), however no significant changes in colours can be seen. The small visible change can be explained by the fluence change due to the fact that some of the material is ablated with every scan. The last test was performed to see whether more colours or higher scanning rates could be achieved when different burst modes were used on top of one another (Fig. 7c). Since MHz burst yielded no colours at all, it was not tested. In (Fig. 7c) we can see that vibrant colours can be achieved with $P10$ ten pulses in the GHz burst and if we use $N5P10$ biburst mode with 5 pulses in the MHz burst mode and 10 pulses in the GHz burst mode, we will achieve only brown colours. Mixing these two parameter sets yielded some interesting results. If the GHz burst mode is used first, with biburst mode going after, no colours are seen. Contrary, if the biburst mode is used

first with the GHz mode going afterwards, some colours are achieved. The new colours are not as vibrant as in the GHz burst mode but are more vibrant than the ones in the biburst mode even with optimal parameters. While it might be possible to achieve some new duller colours compared to the GHz burst mode, the scanning rate would be significantly lower using this method since multiple scans are needed and using speeds higher than 3000 mm/s yielded different shades of brown only. Therefore, due to these findings, mixing of the burst modes was not studied further.

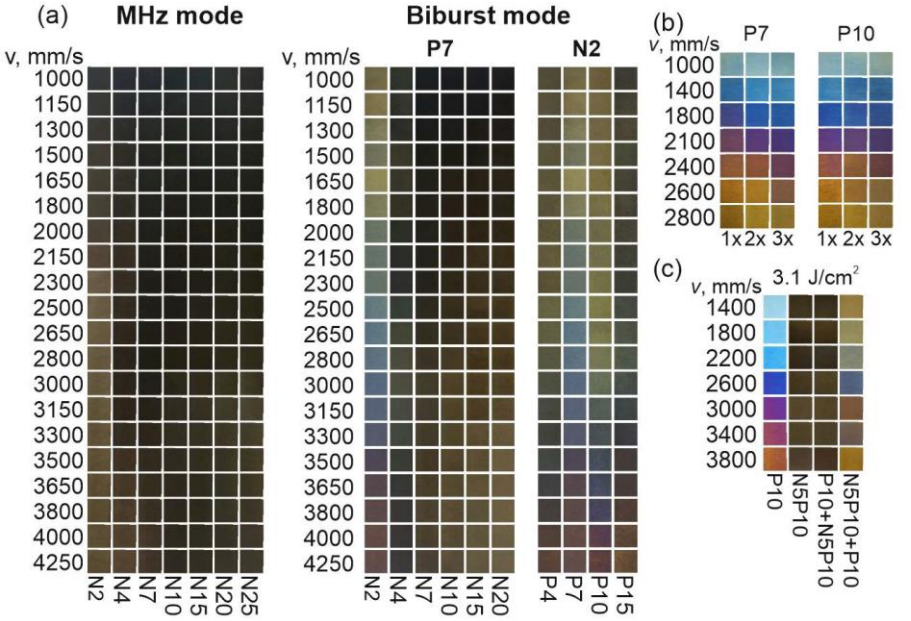

Fig. 7. MHz and Biburst mode colouring test. The laser beam scanning speed was increased from 1000 mm/s to 4250 mm/s and average pulse fluence was constant at 30.8 J/cm^2. N = 2, 4, 7, 10, 15, 20 and 25 pulses within the MHz burst were tested for the MHz burst mode. For the biburst mode $N2P7$, $N4P7$, $N7P7$, $N10P7$, $N15P7$, $N20P7$, $N2P4$, $N2P7$, $N2P10$ and $N2P15$ sets were tested.

Based on the equation $dS/dt = vh$, there are two primary methods to improve the colouring rate: increasing the laser beam scanning speed or the distance between the lines. If identical colours can be achieved with a larger hatch spacing, fewer scanned lines are necessary to colour a given area, potentially improving the colouring rate. As can be seen in (Fig. 8), multiple colours can still be produced even as the hatch spacing increases. However, the colouring rate does not necessarily improve because, to achieve the same colours with a doubled hatch spacing, the scanning speed must be reduced proportionally. Another possibility to increase the colouring rate could be increasing the laser's repetition rate. This could allow for higher scanning speeds to be used if pulse overlap is one of the critical parameters for laser colouring. Pulse overlap would remain the same if both the repetition rate and scanning speed would be increased proportionally. Nevertheless, the results shown in (Fig. 8) indicate that increasing the repetition rate produces the same

colours at the same speed and those colours are significantly less stable as well. This could be explained by the intra-burst repetition rate having the most significant impact on heat accumulation on the target surface.

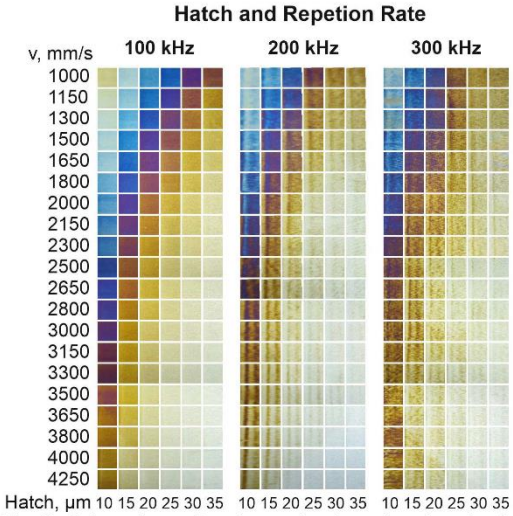

Fig. 8. Colour change from laser colouring when changing hatch, pulse repetition rate and beam scanning speed. $P = 7$ pulses within the GHz burst mode were used with a constant pulse fluence of 30.8 J/cm^2.

Due to the fact that our laser colouring method utilizes hatching, it is possible to fill any custom form or figure with lines with a pre-set spacing. In (Fig. 9) we can see various shapes and colours that can be achieved using laser irradiation. Specifically, (Fig. 9a) displays two half circles with two wavy lines in the middle, all in different colours such as blue, light blue, purple, and orange. In contrast, (Fig. 9 b, c, d) present the same floral circle pattern with a circle in the middle but in different colour schemes: (Fig. 9 b) is entirely blue, while in (Fig. 9 c and d) each leaf and the central circle have different colours ranging from shades of blue to purple and orange. Lastly, (Fig. 9e) shows the logo of the Center for Physical Sciences and Technology (FTMC). These examples demonstrate that even complex shapes are not problematic for this method. However, a significant drawback is the process's extreme sensitivity to minor changes in fluence. Although the laser's irradiation is highly stable, particularly because we can use high powers and divide those pulses into ones with lower individual fluence, we still face challenges in maintaining the sample precisely at the focal position. The primary issue arises from heat accumulation, which increases the sample's temperature and causes slight deformations of the sample surface, thereby altering the focal point. Even though, the deformations can be very small and hard to see with the naked eye, the colour difference is easily noticeable.

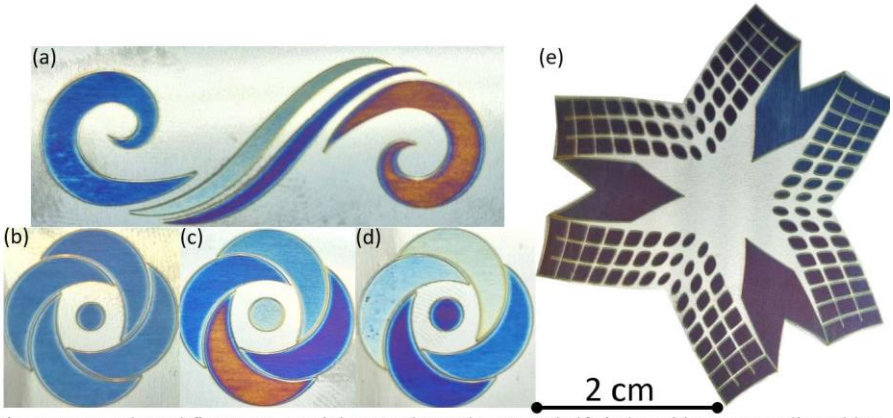

Fig. 9. Laser coloured figures on a stainless-steel sample. a) two half circles with two wavy lines: blue colour's scanning speed 2500 mm/s, grey blue – 1150 mm/s, purple – 3000 mm/s, orange – 4250 mm/s; b) floral pattern: dark blue – 2650 mm/s; c) floral pattern: blue – 2500 mm/s, light blue – 2300 mm/s, purple – 3000 mm/s, orange – 4250 mm/s, grey blue (middle circle) – 1150 mm/s; d) floral pattern: light blue – 1500 mm/s, turquoise – 1000 mm/s, blue – 2300 mm/s, purple – 3000 mm/s. Laser processing parameters: 7 pulses in the GHz burst, pulse fluence 30.8 J/cm^2, intra-burst pulse fluence 4.4 J/cm^2. e) logo of FTMC; dark blue – 3500 mm/s, purple – 4000 mm/s. 7 pulses in the GHz burst, pulse fluence 43.8 J/cm^2, intra-burst pulse fluence 6.3 J/cm^2.

From the three ways that a metal surface could be coloured using laser micromachining, two of them can be easily dismissed. Plasmonic metals are materials that support localised surface plasmon resonances which result in colours that arise from nanostructures and nanoparticles on the metals surface. This effect is the result of the confinement of a surface plasmon in a nanoparticle of size comparable to or smaller than the wavelength of light used to excite the plasmon. However, this happens in noble metals such as gold and silver, with other metals such as copper and aluminium also showing some of these properties. While stainless steel nanoparticles can exhibit localized surface plasmon resonance (LSPR), the resonances are typically broad and weak due to significant damping from high optical losses. The heterogeneous composition of stainless steel introduces multiple scattering centers and impurities, further hindering the efficiency of plasmonic oscillations. Given the weak plasmonic properties of stainless steel, LSPR contributes negligibly to surface coloration. Structural colours arising from LIPSS is also not the reason our stainless-steel samples are coloured. Checking our sample under scanning electron microscope, we did not find any LIPSS on the target's surface, only various different nanoparticles and nanostructures that are ununiformly scattered (Fig. 10d-g). Furthermore, structural colours change from green, to red and blue depending on the viewing angle, whereas our colours do get significantly darker depending on the viewing angle, but do not change colour. Lastly there is the surface oxidation. Because the laser is a significant heat source and various burst modes also assist in heat accumulation [23] it could fasten the oxidation process which results in different colours on the stainless-steel surface. The thin film effect would also explain two observable phenomena. The first one is our small amount of green and red colours achieved (Fig. 3). It could be explained by the fact that no vibrant green or red colours were achieved due to the fact that the oxide layer was too thick for the light to reflect from the sample and interference could not be seen. Also, because the colour is dependent on the optical path difference which in itself depends on the incident angle

of the light, it explains why the colour becomes significantly darker when the angle is changed (Fig. 10a-c).

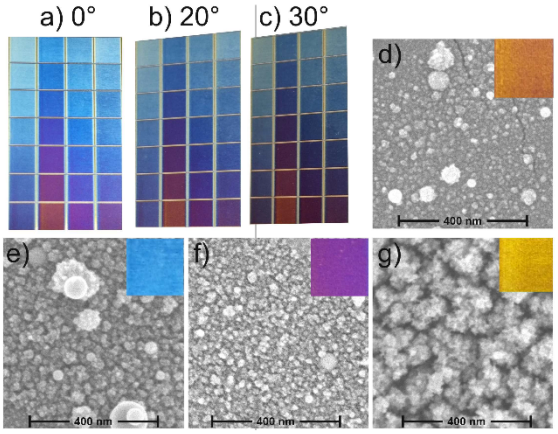

Fig. 10. Laser colouring tilt experiment: a) 0° tilt; b) 20° tilt; c) 30° tilt. d-g) scanning electron microscope images of different colours. Laser processing parameters: 7 pulses within the GHz burst, 18 J/cm^2 pulse fluence.

Table 1. Comparison of laser colouring rates and other parameters in scientific literature. *marks our current work.

Mechanism	Material	Parameters					
		λ	τ	f, kHz	v, mm/s	h, μm	dS/dt, mm^2/s
Oxidation[12]	Stainless–steel	532 nm	20 ns	10 – 200	100 – 600	5 – 15	0.5 – 9
Oxidation[13]	Stainless–steel	1062 nm	100 ns	80 – 100	50 – 225	10 – 20	0.5 – 4.5
Oxidation[14]	Stainless–steel	1030 nm	210 fs	100	100	10	1
Oxidation[15]	Stainless–steel	355 nm	25 ns	40	400 – 500	30	12 – 15
Oxidation[16]	Stainless–steel	532 nm	20 ns	10 – 200	70 – 600	4 – 10	2.8 – 6
Oxidation[17]	Stainless–steel	1064 nm	10 – 350 ns	67 – 1100	2500	10	25
Oxidation[18]	Stainless–steel	1064 nm	4 – 200 ns	1.6 – 1200	50 – 750	10	0.5 – 7.5
Oxidation[53]	Stainless–steel	1061 nm	3 – 2000 ns	1 – 4000	2.5 – 190	20	0.05 – 3.8
Oxidation[22]	Titanium	1064 nm	300 ns	30	25 – 150	200	5 – 30
Oxidation[19]	Titanium	1064 nm	119 ns	225	90 – 600	10	0.9 – 6
Oxidation[20]	Titanium alloy	1030 nm	240 fs	200	20 – 100	5	0.1 – 0.5
Oxidation[26]	Copper	1030 nm	320 fs	10	100	1 – 20	0.1 – 2
Oxidation*	Stainless–steel	1030 nm	245 fs	100	1000 – 4250	10	10 – 42.5
LIPSS[34]	Stainless–steel	800 nm	90 fs	1	1 – 4	50	0.05 – 0.2

LIPSS[54]	Stainless–steel	515 nm	1.5 ns	1000	300 – 2000	1 – 3	0.3 – 6
LIPSS[55]	Copper	800 nm	53 fs	1	0.1 – 3	100	0.01 – 0.3
LIPSS[27]	Aluminium	800 nm	120 fs	1	0.1 – 16	50	0.005 – 0.8
LIPSS[56]	Silicon	800 nm	100 fs	1	1	30	0.03
Nanoparticles[32]	Gold and Silver	1064 nm	10 ps	50	11 – 3000	1 – 13.5	0.011 – 40.5
Nanoparticles[46]	Copper	1064 nm	10 ps	100 – 1000	50 – 5000	10 – 20	0.5 – 100

In this study, a variety of colours were achieved on stainless steel using scanning speeds between 1000 mm/s and 4250 mm/s, with colouring rates ranging from 10 mm²/s to 42.5 mm²/s. If optimal fluence and pulse numbers within GHz bursts are selected, colours such as yellow, orange, blue, purple, and dark green can be achieved at the maximum colouring rate of 42.5 mm²/s. To the best of our knowledge, no other study has reported colouring rates of stainless-steel exceeding 15 mm²/s (Table 1). This is also, to the best of our knowledge, the highest colouring rate achieved through oxidation mechanisms and is only comparable to plasmonic colours obtained from nanoparticles and nanostructures on plasmonic metals. Comparing colouring rates across the literature is challenging, mainly because distance between scanned lines (hatch) is often not listed if the parameter remains constant. However, based on the beam scanning speed alone, our method is at minimum three times faster than reported in comparable studies (Table 2).

Table 2 Comparison of laser beam scanning speeds and other parameters in scientific literature. *marks our current work.

Mechanism	Material	Parameters			
		λ	τ	f, kHz	v, mm/s
Oxidation[39]	Stainless–steel	1064 nm	10 ns	35	10 – 90
Oxidation[36]	Stainless–steel	1064 nm	4 – 260 ns	45 – 500	100 – 1300
Oxidation[57]	Stainless–steel	1064 nm	100 ns	20 – 80	10 – 500
Oxidation[58]	Stainless–steel	1060 nm	100 ns	20 – 99	1 – 250
Oxidation[59]	Stainless–steel/Ti	1060 nm	100 ns	20 – 99	1 – 250
Oxidation*	Stainless–steel	1030 nm	245 fs	100	1000 – 4250
LIPSS[52]	Stainless–steel	1030 nm	50 ps	25	20 – 33.3
LIPSS[44]	Stainless–steel	240 – 2600 nm	104 fs	1	13
LIPSS[60]	Stainless–steel	800 nm	150 fs	5	10 – 130

Changing the colour of a metal is a wanted task, but it could be improved with additional surface functionalities. Changing a metals colour and also making it hydrophobic would be very beneficial because it would make the colours even more long lasting since it would help the metal withstand the environment significantly better. The static water contact angle (SWCA) was measured by depositing a 4 µL volume water drop on a specific laser coloured area using a micropipette (Transferpette, Brand GmbH). The sample was illuminated from one side by a high-parallelism diode backlight and an image of the drop was taken from the other side using a digital camera. The SWCA angle was deduced by using ImageJ software's [61] plugin LBADSA [62]. For a surface to be consider hydrophobic it needs to have SWCA of at least 90° and to be considered superhydrophobic, a SWCA of higher than 150°. The SWCA was measured for uncoloured

stainless steel and also for the first 18 colours for the 7 pulses within the GHz burst with 3.5 J/cm^2 intra-burst pulse fluence regime. Each measurement was done 5 times and the standard deviation was calculated. Uncoloured stainless steel was not hydrophobic and had a contact angle of 50.4 ± 4.4°. In (Fig. 11) it can be seen that all achieved colours are hydrophobic because their SWCA is higher than 90° independent of the hue of the colour. The time frame between the laser colouring and wettability tests was greater than 6 months making not only the colours but also the hydrophobicity long lasting. The samples were kept in ambient air conditions indoors without any noticeable change.

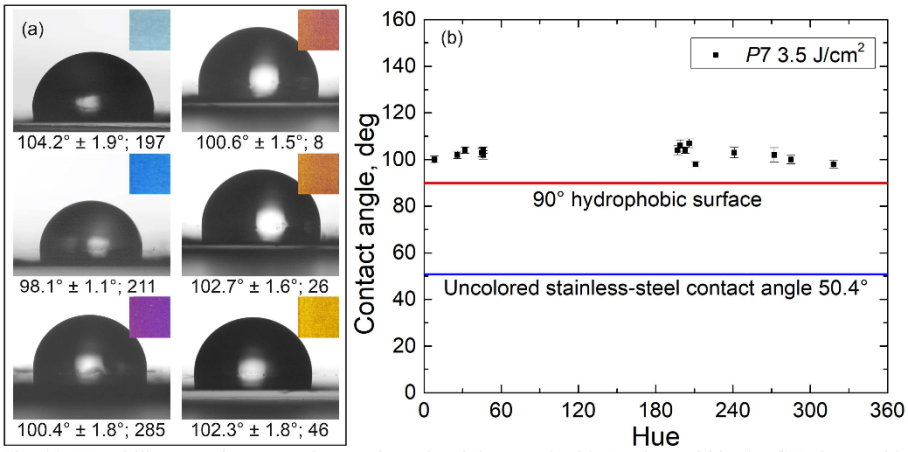

Fig. 11. Wettability experiments on laser coloured stainless steel with 7 pulses within the GHz burst with 3.5 J/cm^2 intra-burst pulse fluence. (a) water droplets on the surface of laser coloured stainless-steel, first number under the picture is the contact angle with standard deviation, second number is the hue of the colour; (b) contact angle dependence hue. Blue line is the contact angle on uncoloured stainless-steel – 50.4 ± 0.7°.

Conclusions

In this work high-rate laser colouring on stainless steel was investigated by optimising different burst modes and scanning speeds. Other laser processing parameters were also tested including: pulse repetition rates, number of scans, hatch and combinations of the burst modes. To the best of our knowledge, fastest stainless-steel colouring rate of 42.5 mm^2/s has been achieved with optimal parameters. The colouring method is due to the oxide formation on the targets surface, because stainless-steel is not a plasmonic metal and no LIPSS were seen from the SEM analysis. Because the laser colouring method is based on hatching, various intricate designs including the logo for the FTMC were coloured. The coloured surfaces were also hydrophobic for all achieved colours which increases the applicability greatly. The colours remained unchanged for a period of time greater than 9 months and the wettability was tested 6 months after the colouring, making both effects long lasting.

Disclosures. The authors declare no conflicts of interest.

Data availability. Data underlying the results presented in this paper are not publicly available at this time but may be obtained from the authors upon reasonable request.

Acknowledgments. This project has received funding from the Research Council of Lithuania (LMTLT), Agreement No. S-MIP-22-89.

Funding. Research Council of Lithuania (LMTLT) (S-MIP-22-89).

Contributions

M.Ga., P.G and M.Ge. conceived the original idea for the project. M. Ga. performed the laser colouring experiments, wrote the manuscripts and visualised the data, A.S performed the scanning electron microscope imaging, P.G. supplied the required equipment for the experiments, M.Ge supervised the work and attained the funding. All authors analysed the findings, discussed the results and commented on the manuscript.

References

[1] G. Napoli, A. Di Schino, M. Paura, and T. Vela, "Colouring titanium alloys by anodic oxidation," *Metalurgija* **57**, 111–113 (2018).

[2] C. J. Donahue and J. A. Exline, "Anodizing and Coloring Aluminum Alloys," *J. Chem. Educ.* **91**, 711–715 (2014).

[3] V. Zalyhina, V. Cheprasova, V. Belyaeva, and V. Romanovski, "Pigments from spent Zn, Ni, Cu, and Cd electrolytes from electroplating industry," *Environ. Sci. Pollut. Res.* **28**, 32660–32668 (2021).

[4] W. Giurlani, F. Gambinossi, E. Salvietti, M. Passaponti, and M. Innocenti, "Color Measurements in Electroplating Industry: Implications for Product Quality Control," *ECS Trans.* **80**, 757–766 (2017).

[5] W. Giurlani, G. Zangari, F. Gambinossi, M. Passaponti, E. Salvietti, F. Di Benedetto, S. Caporali, and M. Innocenti, "Electroplating for Decorative Applications: Recent Trends in Research and Development," *Coatings* **8**, 260 (2018).

[6] F. J. Maile, G. Pfaff, and P. Reynders, "Effect pigments—past, present and future," *Prog. Org. Coatings* **54**, 150–163 (2005).

[7] S. C. Cha and A. Erdemir, *Coating Technology for Vehicle Applications*, in *Coat. Technol. Veh. Appl.*, S. C. Cha and A. Erdemir, Eds. (2015).

[8] B. Gilmour and A. Giumlia-Mair, "What Did Iron Really Look Like? Patination and Coloring Treatments on Iron and Steel," *Mater. Manuf. Process.* **24**, 999–1006 (2009).

[9] T. Letsou, M. ElKabbash, S. Iram, M. Hinczewski, and G. Strangi, "Heat-induced perfect light absorption in thin-film metasurfaces for structural coloring," *Opt. Mater. Express* **9**, 1386 (2019).

[10] G. T. Alliott, R. L. Higginson, and G. D. Wilcox, "Producing a thin coloured film on stainless steels

– a review. Part 1: electrochemical processes," *Trans. IMF* **100**, 128–137 (2022).

[11] S. John, A. Perumal, and B. A. Shenoi, "Chemical colouring of aluminium," *Surf. Technol.* **22**, 15–20 (1984).

[12] X. Ma, X. Nie, J. Zhao, P. Shrotriya, Y. Zhang, Y. Cui, and J. Wang, "Effect of nanosecond pulsed laser parameters on the color making of 304 stainless steel," *Opt. Laser Technol.* **126**, 106104 (2020).

[13] A. J. Antończak, D. Kocoń, M. Nowak, P. Kozioł, and K. M. Abramski, "Laser-induced colour marking—Sensitivity scaling for a stainless steel," *Appl. Surf. Sci.* **264**, 229–236 (2013).

[14] M. Gaidys, A. Selskis, P. Gečys, and M. Gedvilas, "Stainless steel colouring using burst and biburst mode ultrafast laser irradiation," *Opt. Laser Technol.* **174**, 110561 (2024).

[15] Z. L. Li, H. Y. Zheng, K. M. Teh, Y. C. Liu, G. C. Lim, H. L. Seng, and N. L. Yakovlev, "Analysis of oxide formation induced by UV laser coloration of stainless steel," *Appl. Surf. Sci.* **256**, 1582–1588 (2009).

[16] X. Ma, X. Nie, J. Zhao, Y. Han, P. Shrotriya, Y. Wang, and J. Guo, "Coloring stability analysis of nanosecond pulsed laser induced surface coloring on stainless steel," *Opt. Laser Technol.* **123**, 105936 (2020).

[17] Y. F. Xiang, R. L. Mei, F. Azad, L. Z. Zhao, S. C. Su, G. G. Lu, and S. P. Wang, "Investigation by nanosecond fiber laser for hybrid color marking and its potential application," *Opt. Laser Technol.* **147**, 107553 (2022).

[18] H. Roozbahani, M. Alizadeh, H. Handroos, and A. Salminen, "Color Laser Marking: Repeatability, Stability and Resistance against Mechanical, Chemical and Environmental Effects," *IEEE Access* **8**, 214196–214208 (2020).

[19] D. P. Adams, R. D. Murphy, D. J. Saiz, D. A. Hirschfeld, M. A. Rodriguez, P. G. Kotula, and B. H. Jared, "Nanosecond pulsed laser irradiation of titanium: Oxide growth and effects on underlying metal," *Surf. Coatings Technol.* **248**, 38–45 (2014).

[20] X. Sun, W. Wang, X. Mei, A. Pan, Y. Chen, and J. Cui, "High capacity color code prepared on titanium alloy using femtosecond laser," *Opt. Laser Technol.* **145**, 107521 (2022).

[21] A. Pérez del Pino, P. Serra, and J. . Morenza, "Oxidation of titanium through Nd:YAG laser irradiation," *Appl. Surf. Sci.* **197–198**, 887–890 (2002).

[22] A. Pérez del Pino, P. Serra, and J. . Morenza, "Coloring of titanium by pulsed laser processing in air," *Thin Solid Films* **415**, 201–205 (2002).

[23] V. Veiko, G. Odintsova, E. Vlasova, Y. Andreeva, A. Krivonosov, E. Ageev, and E. Gorbunova, "Laser coloration of titanium films: New development for jewelry and decoration," *Opt. Laser Technol.* **93**, 9–13 (2017).

[24] J. Long, P. Fan, M. Zhong, H. Zhang, Y. Xie, and C. Lin, "Superhydrophobic and colorful copper surfaces fabricated by picosecond laser induced periodic nanostructures," *Appl. Surf. Sci.* **311**, 461–467 (2014).

[25] Z. Ou, M. Huang, and F. Zhao, "Colorizing pure copper surface by ultrafast laser-induced near-subwavelength ripples," *Opt. Express* **22**, 17254 (2014).

[26] G. Killaire, J. Walia, S. Rashid, P. Berini, and A. Weck, "Structural and oxide-based colours on laser textured copper," *Appl. Surf. Sci.* **583**, 152440 (2022).

[27] G. Li, J. Li, L. Yang, X. Li, Y. Hu, J. Chu, and W. Huang, "Evolution of aluminum surface irradiated by femtosecond laser pulses with different pulse overlaps," *Appl. Surf. Sci.* **276**, 203–209 (2013).

[28] A. Y. Vorobyev and C. Guo, "Colorizing metals with femtosecond laser pulses," *Appl. Phys. Lett.* **92**, 041914 (2008).

[29] Y. F. Lu and H. Qiu, "Laser coloration and bleaching of amorphous WO3 thin film," *J. Appl. Phys.* **88**, 1082–1087 (2000).

[30] A. Y. Vorobyev and C. Guo, "Spectral and polarization responses of femtosecond laser-induced periodic surface structures on metals," *J. Appl. Phys.* **103**, 16–19 (2008).

[31] A. V. Dostovalov, T. J. Y. Derrien, S. A. Lizunov, F. Přeučil, K. A. Okotrub, T. Mocek, V. P. Korolkov, S. A. Babin, and N. M. Bulgakova, "LIPSS on thin metallic films: New insights from multiplicity of laser-excited electromagnetic modes and efficiency of metal oxidation," *Appl. Surf. Sci.* **491**, 650–658 (Elsevier, 2019).

[32] J.-M. Guay, A. Calà Lesina, G. Côté, M. Charron, D. Poitras, L. Ramunno, P. Berini, and A. Weck, "Laser-induced plasmonic colours on metals," *Nat. Commun.* **8**, 16095 (2017).

[33] N. G. Henriksen, K. Poulios, M. A. J. Somers, and T. L. Christiansen, "Impact of Laser Marking on Microstructure and Fatigue Life of Medical Grade Titanium," *SSRN Electron. J.* **873**, 145020 (2023).

[34] J. Yao, C. Zhang, H. Liu, Q. Dai, L. Wu, S. Lan, A. V. Gopal, V. A. Trofimov, and T. M. Lysak, "Selective appearance of several laser-induced periodic surface structure patterns on a metal surface using structural colors produced by femtosecond laser pulses," *Appl. Surf. Sci.* **258**, 7625–7632 (2012).

[35] B. Jaeggi, B. Neuenschwander, S. Remund, and T. Kramer, "Influence of the pulse duration and the experimental approach onto the specific removal rate for ultra-short pulses," in *Proc. SPIE* **10091**, B. Neuenschwander, C. P. Grigoropoulos, T. Makimura, and G. Račiukaitis, Eds., (2017).

[36] Y. Lu, X. Shi, Z. Huang, T. Li, M. Zhang, J. Czajkowski, T. Fabritius, M. Huttula, and W. Cao, "Nanosecond laser coloration on stainless steel surface," *Sci. Rep.* **7**, 7092 (2017).

[37] L. Lavisse, J. M. Jouvard, L. Imhoff, O. Heintz, J. Korntheuer, C. Langlade, S. Bourgeois, and M. C. M. de Lucas, "Pulsed laser growth and characterization of thin films on titanium substrates," *Appl. Surf. Sci.* **253**, 8226–8230 (2007).

[38] H. Y. Zheng, G. C. Lim, X. C. Wang, J. L. Tan, and J. Hilfiker, "Process study for laser-induced surface coloration," *J. Laser Appl.* **14**, 215–220 (2002).

[39] F. Luo, W. Ong, Y. Guan, F. Li, S. Sun, G. C. Lim, and M. Hong, "Study of micro/nanostructures formed by a nanosecond laser in gaseous environments for stainless steel surface coloring," *Appl. Surf. Sci.* **328**, 405–409 (2015).

[40] K. Tse and J. Robertson, "Work function control at metal high-dielectric-constant gate oxide interfaces," *Microelectron. Eng.* **85**, 9–14 (2008).

[41] K. Ahmmed, C. Grambow, and A.-M. Kietzig, "Fabrication of Micro/Nano Structures on Metals by Femtosecond Laser Micromachining," *Micromachines* **5**, 1219–1253 (2014).

[42] R. Buividas, M. Mikutis, and S. Juodkazis, "Surface and bulk structuring of materials by ripples with long and short laser pulses: Recent advances," *Prog. Quantum Electron.* **38**, 119–156 (2014).

[43] S. Sakabe, M. Hashida, S. Tokita, S. Namba, and K. Okamuro, "Mechanism for self-formation of

periodic grating structures on a metal surface by a femtosecond laser pulse," *Phys. Rev. B* **79**, 033409 (2009).

[44] G. Li, J. Li, Y. Hu, C. Zhang, X. Li, J. Chu, and W. Huang, "Femtosecond laser color marking stainless steel surface with different wavelengths," *Appl. Phys. A* **118**, 1189–1196 (2015).

[45] D. Xu, J. D. Owen, J. C. Papa, J. Reimers, T. J. Suleski, J. R. Troutman, M. A. Davies, K. P. Thompson, and J. P. Rolland, "Design, fabrication, and testing of convex reflective diffraction gratings," *Opt. Express* **25**, 15252 (2017).

[46] P. Fan, M. Zhong, L. Li, P. Schmitz, C. Lin, J. Long, and H. Zhang, "Angle-independent colorization of copper surfaces by simultaneous generation of picosecond-laser-induced nanostructures and redeposited nanoparticles," *J. Appl. Phys.* **115**, 124302 (2014).

[47] A. Y. Vorobyev and C. Guo, "Direct femtosecond laser surface nano/microstructuring and its applications," *Laser Photon. Rev.* **7**, 385–407 (2013).

[48] D. P. Adams, V. C. Hodges, D. A. Hirschfeld, M. A. Rodriguez, J. P. McDonald, and P. G. Kotula, "Nanosecond pulsed laser irradiation of stainless steel 304L: Oxide growth and effects on underlying metal," *Surf. Coatings Technol.* **222**, 1–8 (2013).

[49] J.-M. Guay, G. Killaire, P. G. Gordon, S. T. Barry, P. Berini, and A. Weck, "Passivation of Plasmonic Colors on Bulk Silver by Atomic Layer Deposition of Aluminum Oxide," *Langmuir* **34**, 4998–5010 (2018).

[50] J. Geng, L. Xu, W. Yan, L. Shi, and M. Qiu, "High-speed laser writing of structural colors for full-color inkless printing," *Nat. Commun.* **14**, 565 (2023).

[51] S. N. Chowdhury, P. Nyga, Z. A. Kudyshev, E. Garcia Bravo, A. S. Lagutchev, A. V. Kildishev, V. M. Shalaev, and A. Boltasseva, "Lithography-Free Plasmonic Color Printing with Femtosecond Laser on Semicontinuous Silver Films," *ACS Photonics* **8**, 521–530 (2021).

[52] S. Zhang, Y. Wang, H. Wang, L. Zhong, X. Zhu, G. Zhu, J. Qiu, and X. Zeng, "Laser Writing of Multilayer Structural Colors for Full-Color Marking on Steel," *Adv. Photonics Res.* **5**, 1–9 (2024).

[53] A. Schkutow and T. Frick, "Laser color marking of stainless steel – Investigation of the fluence-dependent and thermal mechanisms in generating laser induced surface modifications," *Procedia CIRP* **124**, 661–664 (2024).

[54] T. Karkantonis, A. Gaddam, X. Tao, T. L. See, and S. Dimov, "The influence of processing environment on laser-induced periodic surface structures generated with green nanosecond laser," *Surfaces and Interfaces* **31**, 102096 (2022).

[55] A. Y. Vorobyev and C. Guo, "Multifunctional surfaces produced by femtosecond laser pulses," *J. Appl. Phys.* **117**, 1033–1040 (2015).

[56] C.-Y. Zhang, J.-W. Yao, H.-Y. Liu, Q.-F. Dai, L.-J. Wu, S. Lan, V. A. Trofimov, and T. M. Lysak, "Colorizing silicon surface with regular nanohole arrays induced by femtosecond laser pulses," *Opt. Lett.* **37**, 1106 (2012).

[57] E. H. Amara, F. Haïd, and A. Noukaz, "Experimental investigations on fiber laser color marking of steels," *Appl. Surf. Sci.* **351**, 1–12 (2015).

[58] V. Veiko, G. Odintsova, E. Gorbunova, E. Ageev, A. Shimko, Y. Karlagina, and Y. Andreeva, "Development of complete color palette based on spectrophotometric measurements of steel oxidation results for enhancement of color laser marking technology," *Mater. Des.* **89**, 684–688

(2016).

[59] V. Veiko, G. Odintsova, E. Ageev, Y. Karlagina, A. Loginov, A. Skuratova, and E. Gorbunova, "Controlled oxide films formation by nanosecond laser pulses for color marking," *Opt. Express* **22**, 24342 (2014).

[60] B. Dusser, Z. Sagan, H. Soder, N. Faure, J. P. Colombier, M. Jourlin, and E. Audouard, "Controlled nanostructrures formation by ultra fast laser pulses for color marking," *Opt. Express* **18**, 2913 (2010).

[61] C. A. Schneider, W. S. Rasband, and K. W. Eliceiri, "NIH Image to ImageJ: 25 years of image analysis," *Nat. Methods* **9**, 671–675 (2012).

[62] A. F. Stalder, T. Melchior, M. Müller, D. Sage, T. Blu, and M. Unser, "Low-bond axisymmetric drop shape analysis for surface tension and contact angle measurements of sessile drops," *Colloids Surfaces A Physicochem. Eng. Asp.* **364**, 72–81 (2010).

PP2

WETTABILITY AND COLOR CHANGE OF COPPER BY CONTROLLING AREA FRACTION OF LASER ABLATED SURFACE

M. Gaidys, S. Maragkaki, A. Mimidis, A. Papadopoulos, A. Lemonis, E. Skoulas, A. Žemaitis, E. Stratakis, M. Gedvilas

Opt. Laser Technol. 2025 (Submitted, under revision)
DOI:

Wettability and Color Change of Copper by Controlling Area Fraction of Laser Ablated Surface

Mantas Gaidys[1], Stella Maragkaki[2], Alexandros Mimidis[2], Antonis Papadopoulos[2], Andreas Lemonis[2], Evangelos Skoulas[2], Andrius Žemaitis[1], Emmanuel Stratakis[2], Mindaugas Gedvilas[1]*

[1]Department of Laser Technologies (LTS), Center for Physical Sciences and Technology (FTMC), Savanoriu Ave. 231, 02300 Vilnius, Lithuania
[2]Institute of Electronic Structure and Laser (IESL), Foundation for Research and Technology (FORTH), N. Plastira 100, Vassilika Vouton, 70013 Heraklion, Crete, Greece

E-mail: mindaugas.gedvilas@ftmc.lt

Abstract

In this research, wettability control by area fraction of laser ablated surface of copper is presented. The functional surfaces with full wettability control from highly hydrophilic to super-hydrophobic were created on copper by nanosecond (ns) and picosecond (ps) laser irradiation. The area fraction and color change were evaluated by digital image processing of microscopic images of the laser-ablated copper surface. The control of the wetting angle from almost 0 degrees to 132 degrees was achieved for both ps and ns pulses by controlling the area fraction of the laser-ablated surface. Cassie, Cassie-Baxter, and Wenzel models were adopted to explain the experimental results. For the first time, the wettability and color of copper were controlled by controlling the area fraction of the laser-ablated surface. It is expected that the current results make an impact on the heat exchanger technology of water heat sinks, cooling units, atmospheric water generators, and fog harvesting and impact numerous applications from power plants to solar thermal water systems devices where highly-hydrophilic to super-hydrophobic copper can be applied.

Keywords

Super-hydrophobic, highly-hydrophilic, area fraction, copper, laser ablation, surface roughness, color change.

1. Introduction

A wide variety of biological breeds found in living nature that have superb functional surface properties include birds [1], plants [2-5], insects [6-10], fish [11], sea mammals [12,13], and reptiles [14]. These unique functionalities like hydrophilicity [15], fog-harvesting [16], structural coloration [17], antibacterial [18], super-hydrophobicity [19], self-cleaning [20], anti-fogging [21], anti-reflective [22], drag-reducing [23], etc. have evolved over millions of years to extremes and provide those species with the ability to live and survive, and

further develop new multi-functions to adapt to the fast-changing environment. The genetic modification of breeds due to natural selection has helped to evolve the specific surface functionalities. In most cases, the unique surface functions come from their morphology in the mesoscale, with the tri-modal dimensions from nano to micro and macro [12,24,25].

The scientific branches such as bionics, nature/bio-inspiration, bio-replication, bio-engineering, and bio-mimetics have evolved during the last two decades to copy excellent surfaces from nature [26-35]. Direct laser writing is a precision micro-fabrication technology with large flexibility options [36-38]. The fabrication of tri-modal structures with the nano-, micro-, and macro-length scales in one surface can be achieved by this technique [39,40]. Moreover, fabrication using ultra-short laser pulses has demonstrated unique features such as efficient ablation [11,41], cold-ablation [42,43], ablation-cooled efficient material removal [44], and bi-stable ablation [45] which enables high precision repeatable texturing for a large versatility of materials. Laser beam interference ablation is a flexible tool for the periodical structuring [46,47]. However, minimal feature size in the sub-micro-scale is restricted by the diffraction limit, which is in the order of irradiation wavelength. On the other hand, the bio-replication of functional surfaces usually requires laser processing beyond the diffraction limit at the nanoscale [27,29]. The diffraction limit can be beaten by reaching a nanoscale resolution with laser-induced periodic surface structures (LIPSS)[48], which can be textured on a large scale with a high rate [49-51].

The super-hydrophobic copper structuring by laser has been reported in numerous scientific works using nanosecond [52-55], picosecond [56,57], and femtosecond [58,59] lasers. However, making the opposite, super-hydrophilic copper, using laser texturing is still an open question. There is no scientific work found in literature, where perfect wetting of copper surface would be achieved by laser irradiation. However, there are other competing techniques capable of producing super-hydrophilic copper, like, electrochemical deposition [60,61], layer-by-layer self-assembly [62], one-step liquidus modification [63], etc.

Highly wetting textured surfaces have shown promise in boiling applications since capillary increases the maximum heat flux that can be dissipated [64-66], which has a huge potential in the heat exchanger technology of water heat sinks [67], fans, and cooling units [67,68]. Also, super-wetting surfaces can be applied as fog-harvesting systems [69-72] that can dramatically improve atmospheric water generator performances [73,74]. The current cutting-edge preparation techniques of super-hydrophilic and super-hydrophobic surfaces require time-consuming processes [61] and complex multiple-steps [60-62], or processes that produce chemically hazardous wastes [75,76]. At the same time, the mechanical durability [77], gradual degradation due to long exposure to outdoor conditions [78], and degradation in time [79] of chemically replicated bio-inspired surfaces in many cases are unsolved problems [80,81]. The laser functionalization of the surface by texturing using ultrashort laser pulses is simple, low-cost, and chemical-free. It can be easily scaled up using commercially available industrial laser-processing

systems [82,83]. The achieved functional properties and surface morphologies of the laser-fabricated textures were found close to the leaf of the cactus [69,84] and the underwater side of the lily leaf [85,86]. The biomimetic fabrication using laser irradiation considering the simplicity of the process and high processing rate together with the robustness of achieved super-wetting surfaces can be applied in power plants [74] and solar thermal water systems [87].

In this work, we demonstrate a novel, single-step, chemical-free fabrication method for producing super-wetting and highly hydrophobic copper surfaces using ns and ps lasers. For the first time, simultaneous control of the wettability and color of copper is achieved by systematically varying the area fraction of the laser-ablated surface, offering a versatile approach for surface modification. Our study adopted the Cassie, Cassie-Baxter, and Wenzel models to explain that as the ablated area fraction increases, the contact angle decreases, enhancing hydrophilicity. Furthermore, significant visual and optical changes such as variations in color distance, gray value, and gray luminance correlate linearly with the ablated area fraction, showcasing the transformative impact of laser parameters. Shorter pulse durations (10 ps) demonstrate a particularly stronger effect than longer (10 ns), underscoring the potential of this technique for advanced material applications.

2. Theoretical background

The characterization of the wetting properties of a surface is defined on the static contact angle measured by a sessile droplet technique [88]. For water droplets, a surface having a contact angle smaller than 90° is hydrophilic, while one larger than 90° is hydrophobic. The Wenzel, Cassie, and Cassie-Baxter models are widely used in the research of wetting behavior and surface interactions, particularly in the context of hydrophobicity and super-hydrophobicity.

On textured rough surfaces with super-hydrophilic properties, the liquid spreads completely and a near-zero contact angle is achieved. Such super-hydrophilic transition of roughened surface is explained by the Wenzel model [89], where the static contact angle in this Wenzel state is smaller than one on a flat hydrophilic surface of the same material.

Contrarily, textured hydrophobic surfaces can provide very different scenarios, depending on which of two distinct wetting states is attained. Super-hydrophobic case, defined by a static contact angle exceeding 150° having a roll-off angle less than 10°, is explained by the Cassie-Baxter model [90] in which air remains trapped inside the texture, causing a liquid to sit on both air and solid. An alternative, super-hydrophobic case is explained in the Wenzel model [89], where the liquid fills the surface structures without air trapped under the water. The static contact angle in this Wenzel state is larger than one on a flat hydrophobic surface of the same material, but typically does not exceed 150°, as it lacks the air trapping characteristic of the Cassie-Baxter state required for superhydrophobicity.

These models are fundamental to understanding how surface textures can influence wetting behavior, therefore the next sub-sections are dedicated to a brief introduction to those classical models.

2.1. Wenzel Model:

This Wenzel model assumes that the liquid completely penetrates the rough surface. The apparent contact angle is a function of the intrinsic contact angle and the surface roughness: [89]

$$\cos\theta^* = r_1 \cos\theta_1, \quad (1)$$

where θ^* is the measured contact angle on the rough surface, r_1 is the ratio of actual surface area to projected surface area, and θ_1 is the intrinsic contact angle on a smooth surface. Wenzel state has a larger surface wettability because the liquid on the surface enters the grooves, increasing the contact area.

2.2. Cassie Model:

This model addresses surfaces with regions of different wettability coexist caused by surface chemical heterogeneity: [91,92]

$$\cos\theta^* = f_1 \cos\theta_1 + f_2 \cos\theta_2, \quad (2)$$

where f_1 and f_2 are the fractions of the surface with different wettability angles θ_1 and θ_2, respectively. The fractional areas of two different surface components fulfill the requirement for the sum of the fractions must be equal as $f_1 + f_2 = 1$, this constraint ensures that no overlapping or missing regions exist.

2.3. Cassie-Baxter Model:

When the composite contact surface is composed of air and solid since the contact angle of liquid and air is 180°, Eq. (2) can be simplified to [93,94]:

$$\cos\theta^* = f_1(1+\cos\theta_1) - 1. \quad (3)$$

where θ^* is the measured contact angle on a composite surface, f_1 is the fraction of the solid-liquid interface area, while the rest fraction $(1 - f_1)$ is air, θ_1 is the intrinsic contact angle. This model assumes that the liquid rests on top of surface roughness features, with air pockets trapped underneath. This creates a composite surface of solid and air, which can drastically increase hydrophobicity.

In scientific literature, the terms Cassie-Baxter and Cassie are commonly used. Cassie-Baxter is used to refer to uneven surfaces incompletely wetted by a liquid when vapor remains under the drop. Cassie is used only for even or rough surfaces of a solid state that is completely wetted by the liquid.

2.4. Wenzel and Cassie-Baxter model:

The wetting angle on rough and heterogeneous surfaces is described using the combined Wenzel and Cassie-Baxter models: [94,95]

$$\cos\theta^* = r_1 f_1 \cos\theta_1 + f_2 \cos\theta_2, \quad (4)$$

which considers surface roughness, where the Wenzel part of Eq. (1) with roughness factor r_1 amplifies the wetting properties (hydrophilic or hydrophobic) and Cassie-Baxter's part of Eq. (2) accounts for surface heterogeneity, using a fractional areas f_1 and f_2 of different surface components to adjust the contact angle.

3. Experimental

3.1. Sample preparation

The samples used for laser texturing and contact angle measurements were square copper substrates (CW004A, Ekstremalė) with dimensions of 50 × 50 mm and a thickness of 5 mm, featuring a purity of 99.9%. These samples had a mirror finish with a surface roughness of approximately Ra ~ 6 nm, measured using a 3D optical profiler (S neox, Sensofar).

3.2. Laser structuring

The principal experimental scheme of laser processing using an irradiation source with optional pulse durations and a galvanometer scanner is depicted in Figure 1.

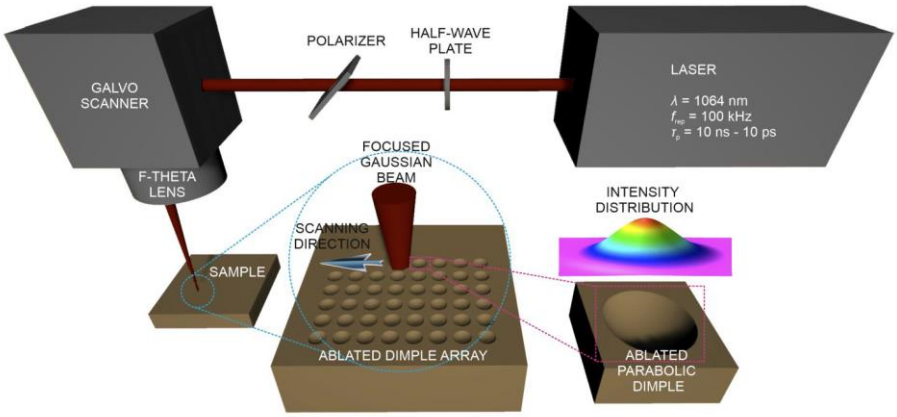

Figure 1. Principal scheme of laser structuring experimental setup: laser irradiation source with optional pulse durations of τ_p = 10 ns and τ_p = 10 ps, the repetition rate of f_{rep} = 100 kHz, irradiation wavelength of λ = 1064 nm, and pulse energy up to E_p = 60 µJ. Beam attenuation for energy control consists of a half-waveplate and the polarizer, a galvanometric scanner equipped with a telecentric f-theta lens for Gaussian beam focus on the surface of the copper sample. The enlarged area in the middle shows a two-dimensional array of dimples ablated by scanning a Gaussian beam on the sample. The enlarged area on the bottom right corner shows a parabolic dimple ablated by a single laser pulse of a Gaussian beam intensity distribution.

Laser structuring experiments were conducted using two laser irradiation sources (Baltic HP, Ekspla, and Atlantic HE, Ekspla) with different pulse durations of τ_p = 10 ns and τ_p = 10 ps, respectively. Both lasers provided light pulses with pulse energy from E_p = 1 μJ up to E_p = 60 μJ at the repetition rate of f_{rep} = 100 kHz, an average power of 6.0 W, and irradiation wavelengths of λ = 1064 nm. The beam position on the metal sample surface was controlled by using a galvanometer scanner (Scangine 14, Scanlab) and scanner application software (SAMLight, SCAPS). Translation of the laser spot on the target material at a controllable speed up to v_{scan} = 1.0 m/s provided the controllable distances between the transverse irradiation spots and distances between bidirectional scanned lines. The telecentric *f*-theta objective lens with a focal length of 80 mm was used to focus the beam on the surface of the target material. The array of rectangular areas with transverse spatial dimensions of 11.5 × 12 mm^2 was laser textured in 29.9 s processing time including all scanner delays. The texturing rate of ~ 5 mm^2/s excluding delays of the scanner was achieved for the area of the whole scanner field of 60 × 60 mm^2. The path of the scanned beam on the copper sample followed a snake-like trajectory consisting of parallel lines of overlapped laser pulses. The beam was scanned along the horizontal axis at a speed of v_{scan} = 1.0 m/s. The distance between consecutive laser pulses was $\Delta x = v_{scan} / f_{rep}$ = 10 μm. A slower translation of the beam, at a speed of 10 mm/s, was applied along the vertical axis. The distance between scanned lines in the vertical direction (hatch) was Δy = 5 μm. The polarization of the beams was oriented along the vertical axis. The laser power was changed during the test from 0.1 W to 0.9 W (step 0.1 W, 9 tests) and from 1.0 W to 6.0 W (step 1.0 W, 6 tests) which provided controllable laser fluence on the sample. The 15 rectangular squares were marked using each laser at different laser powers which provided different laser fluence on the samples. The 15 different values of laser fluences were used, from 0.16 J/cm^2 to 1.44 J/cm^2 (step 0.16 J/cm^2, 9 tests) and from 1.6 J/cm^2 to 9.6 J/cm^2 (step 1.6 J/cm^2, 6 tests). Laser untreated copper is declared in graphs at the laser output power of 0.0 W and corresponding laser fluence of 0.0 J/cm^2.

Figure 2(a) illustrates the fluence-dependant morphological change of copper surface by ablation of a two-dimensional array of parabolic dimples by bidirectional scanning of a Gaussian beam.

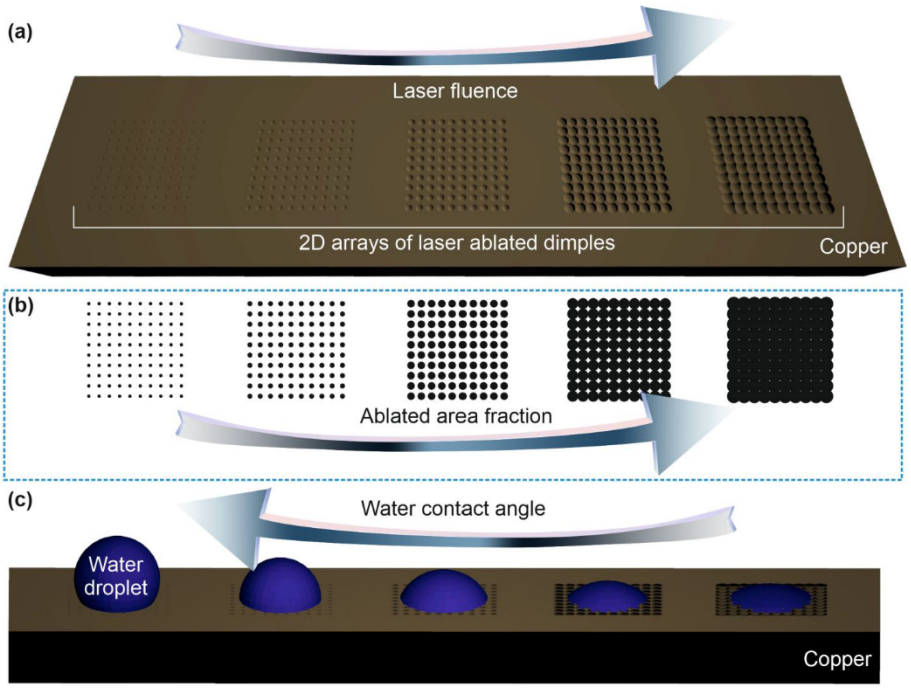

Figure 2. Schematic Illustration of ablated area fraction dependence on laser fluence and its influence on water contact angle: (a) five laser scanned areas consisting of a two-dimensional array of laser ablated dimples and its characteristic surface morphology depending on the laser fluence; (b) schematic representation of laser ablated areas increase with increasing laser fluence; (c) characteristic water contact angle decrease with increasing ablated area fraction and laser fluence.

The schematic representation transverse geometric laser ablated area of the copper is depicted in Figure 2(b). The ablated area fraction increases with the growth of laser fluence. Figure 2(c) illustrates ablated area fraction and fluence-dependant water contact angle. The water contact angle tends to decrease with increasing ablated area fraction and laser fluence.

3.3. Fluence characterization

The radii of the transverse-focused beam spots on the surface of copper were measured by the Liu (D^2) method described in [96]. The dimples were ablated using different pulse energies. Then, the crater size dependence on pulse energy was analyzed and beam spot radii on the sample were retrieved for both irradiation sources. For size characterization of ablated craters (dimples) on copper at different pulse energies an optical microscope (Eclipse LV100, Nikon) was used. The microscope was equipped with

5-megapixel charge-coupled device camera (DS-Fi1, Nikon), camera controller (Digital Sight DS-U2, Nikon), microscope objective (LU Plan Fluor 20x, Nikon), halogen lamp (LV-HL50PC, Nikon), and image processing software (NIS-Elements D, Nikon). The measured laser spot radii on copper were (w_0 = 20 ± 1 μm) equal for both nanosecond and picosecond lasers. The laser spot sizes on the sample were not changed during the tests. The power meter (Nova II, Ophir) equipped with a thermal power sensor (30A-BB-18, Ophir) was employed to measure the average laser power.

3.4. Contact angle measurements

The contact angle characterization was performed using an optical system designed for contact angle and contour analysis (OCA 15EC, Data-Physics Instruments GmbH) equipped with a charge-coupled device camera to capture lateral images of water droplets applied on laser textured and untreated copper. A droplet of deionized water with a volume of 3 μL was deposited by using a pipette (1 - 10 μl Transferpette, Brand). The camera, the water droplet, and the illumination source equipped with a light-emitting diode are perfectly aligned, therefore, the droplet shadow is projected and captured by the digital camera. Average values of contact angle and measurement errors were obtained by software (SCA20, Data-Physics Instruments GmbH). Since it is known that the contact angle of distilled water and laser-irradiated metal surfaces changes approximately 10 days after the irradiation and then reaches a stable value [97,98], all the measurements presented in this work were conducted 15 days after the laser texturing.

3.5. Roughness evaluation

3D optical profiler (S neox, Sensofar) was employed for 3D surface topography imaging of laser ablated copper surface.

3.6. Profile arc length evaluation.

The normalized profile arc length r_1, which is the ratio of actual profile length to projected length was evaluated from height $h = h(x)$ profiles of laser textured copper by the equation:

$$r_1 = \frac{\int_{x_1}^{x_2} \sqrt{1+\left(dh/dx\right)^2}\,dx}{x_2 - x_1}. \qquad (5)$$

The top part of the equation refers to the arc length of the curve, which was calculated using the arc length formula, the bottom part of the equation refers to the straight-line distance between the start x_1 and end points x_2 of the curve, projected onto horizontal axis.

3.7. Optical microscope photographing

Digital images of both laser-processed and untreated copper surfaces were captured using an optical microscope (Nikon Eclipse LV100) equipped with a 5-megapixel high-definition CCD camera (Nikon

DS-Fi1) with a resolution of 2560 × 1920 pixels. The camera was controlled via a Digital Sight DS-U2 controller and NIS-Elements D imaging software, both from Nikon. For imaging, a 10× magnification objective lens (Nikon LU Plan Fluor 10×, NA 0.30) was used in bright field mode, illuminated by a 50 W halogen lamp (Nikon LV-HL50PC). All microscope apertures were fully opened to maximize sample illumination. White balance calibration was performed using a white paper, with RGB component coefficients set to Rw = 1.43, Gw = 1.00, and Bw = 2.13 for color measurement experiments. Exposure time was set to 4 ms with a gain factor of 1.00, initially determined in auto-exposure mode and later applied manually. RGB images were captured at an 8-bit color depth, with a 640 × 480-pixel resolution in BMP format, achieved by averaging a 4 × 4 pixel area from the CCD into one pixel. The actual size of each imaged area was 0.87 × 0.65 mm^2

4. Digital image processing

The digital image processing and area fraction and threshold characterization were performed by using a symbolic and numeric computing environment and software (Maple 18, Maplesoft).

4.1. Area fraction evaluation

The digital image processing procedure used for area fraction calculations of laser-damaged Cu is presented in Figure 3.

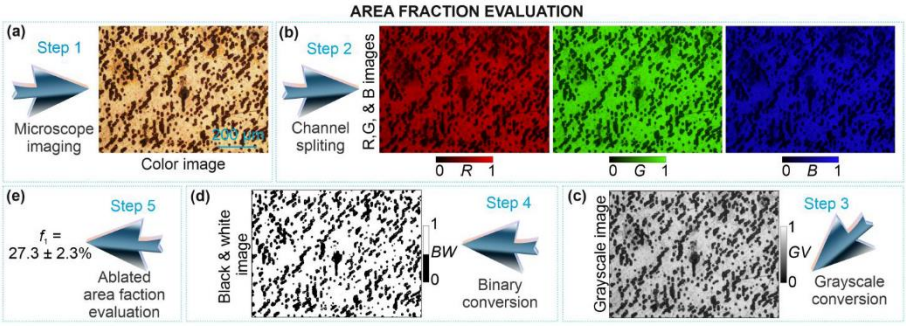

Figure 3. Digital image processing procedure designed for area fraction calculations: (a) step 1 – microscope imaging of laser-treated copper surface; (b) step 2 - color image split to red (R), green (G), and blue (B) channels; (c) step 3 - color-to-grayscale conversion by Eq. (6); (d) step 4 - grayscale image conversion to a black-and-white binary image using Eq. (7); (e) step 5 - calculation of the area fraction of AF = 27.3 ± 2.3 % by Eq. (8).

In step 1 (Figure 3(a)) microscope color image of laser treated copper surface was taken. In step 2 (Figure 3(b)), the color image was split into red (R), green (G), and blue (B) channels. In step 3 (Figure

3(c)) the image was transformed to the grayscale mode by calculating the grayscale value GV using the formula [99]:

$$GV = \max(R, G, B), \tag{6}$$

where R, G, and B are the red, green, and blue components, respectively. The five color-to-grayscale conversion methods have been tested in our work: intensity, luminance, luma, luster, and value [7]. The value method has been chosen because of the highest achieved contrast between grayscale images of the laser-treated and untreated Cu. In step 4 (Figure 3(d)), the grayscale pictures were converted to black-and-white binary mode by using a certain threshold value GV_{th} using formula [100]:

$$BW = \begin{cases} 1, & \text{if} \quad GV \geq GV_{th}; \\ 0, & \text{if} \quad GV < GV_{th}. \end{cases}, \tag{7}$$

In step 5 (Figure 3(e)), the area fraction f_1 of the laser-treated copper Cu in percent was calculated by averaging the equation of binary image intensity [100]:

$$f_1 = \frac{1}{n}\sum_{i=1}^{n} BW_i \times 100\%, \tag{8}$$

where n is the total number of picture pixels, i is the pixel index, BW_i is the binary black-and-white intensity of each pixel in the picture. The computational error in the area fraction f_1 evaluation was taken as the standard deviation of measurements from five sections of the microscope images.

4.2. Threshold evaluation

The digital image processing procedure used for the area threshold determination procedure is depicted in Figure 4.

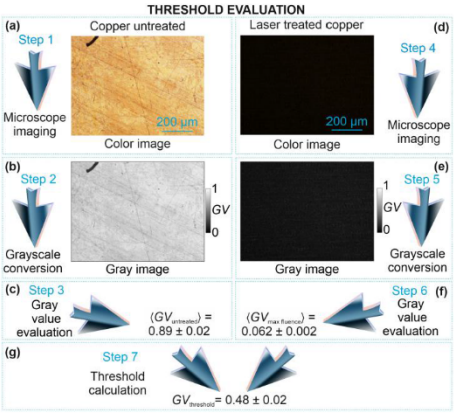

Figure 4. Threshold evaluation procedure: (a) step 1 – microscope imaging of laser-treated copper surface; (b) step 2 - color-to-grayscale conversion by Eq. (6); (c) step 3 - Average grayscale value calculation of untreated copper image of $\langle GV_{\text{untreated}} \rangle = 0.89 \pm 0.02$ by Eq. (9); (d) step 4 - microscope

imaging of laser treated copper surface at a max output power of 6.0 W with a corresponding max fluence of 9.6 J/cm^2; (e) step 5 color-to-grayscale conversion by Eq. (6); (f) step 6 average grayscale value of $\langle GV_{\text{max fluence}} \rangle = 0.062 \pm 0.002$ evaluation by Eq. (9); (g) step 7 - threshold of $GV_{\text{th}} = 0.48 \pm 0.02$ calculation by Eq. (10).

In step 1 (Figure 4(a)) microscope image of untreated copper is taken. In step 2 (Figure 4(b)) the image is converted to the greyscale mode by using Eq. (6). In step 3 (Figure 4(c)) the averaged gray value of the image is evaluated by formula [100]:

$$\langle GV \rangle = \frac{1}{n} \sum_{i=1}^{n} GV_i \,, \tag{9}$$

where the average is denoted by angle brackets, n is the total number of picture pixels, i is the pixel index, GV_i is the grayscale value of each pixel in the picture. The standard deviation as a computational error in the grayscale value $\langle GV \rangle$ evaluation was taken from five sections of the microscope images. The pictures were divided into 5 sections with a size of 128 × 480 pixels. The area fraction color was calculated for each section. The $\langle GV_{\text{untreated}} \rangle = 0.89 \pm 0.02$ of untreated copper (laser output power 0.0 W corresponding fluence 0.0 J/cm^2) is calculated. In step 4 (Figure 4(d)) the microscope image of laser-treated copper at the maximum available laser output power of 6.0 W is taken. In step 5 (Figure 4(e)) the image is converted to the greyscale mode. In step 6 (Figure 4(f)) the averaged gray value of the image is evaluated by using Eq. (9). The $\langle GV_{\text{max fluence}} \rangle = 0.062 \pm 0.02$ of laser-treated copper (maximum laser output power 6.0 W and corresponding max fluence 9.6 J/cm^2) is calculated. The threshold was selected as a mean of average values of untreated Cu (0.0 W) and laser-treated coper at maximum available laser power (6.0 W) [100]:

$$GV_{\text{threshold}} = \frac{GV_{\text{untreated}} + GV_{\text{max fluence}}}{2} \,. \tag{10}$$

In step 7 (Figure 4(g)) the threshold value calculated by Eq. (10) was $GV_{\text{threshold}} = 0.48 \pm 0.02$.

4.3. Luminance evaluation

The luminance GL of grayscale was computed from RGB optical microscope images by using a formula based on the NTSC standard [99,101]:

$$GL = 0.3R + 0.59R + 0.11B \,. \tag{11}$$

where R, G, and B are red, green, and blue components of the sample images after laser treatment.

4.4. Color distance evaluation.

The color distance CD was calculated between digital optical microscope images of the copper surface before and after laser treatment was calculated by using equation [102]:

$$CD^2 = \left(R_{\text{untreated}} - R_{\text{fluence}}\right)^2 + \left(G_{\text{untreated}} - G_{\text{fluence}}\right)^2 + \left(B_{\text{untreated}} - B_{\text{fluence}}\right)^2 . \tag{12}$$

where $R_{untreated}$, $G_{untreated}$, $B_{untreated}$, $R_{fluence}$, $G_{fluence}$, and $B_{fluence}$ are red, green, and blue components of the sample images before (untreated) and after laser treatment (at a certain value of laser fluence). The averaging procedure is performed by using equation (9). The average color difference $\langle CD \rangle$ and the standard deviation of it were calculated from the data achieved from five sections of images.

5. Results and discussion

5.1. Contact angle, color, and area fraction evaluation

The experimental results of the wettability and color change of copper depending on the laser fluence are depicted in Figure 5 (all experimental data is provided in supplementary material Figure S1).

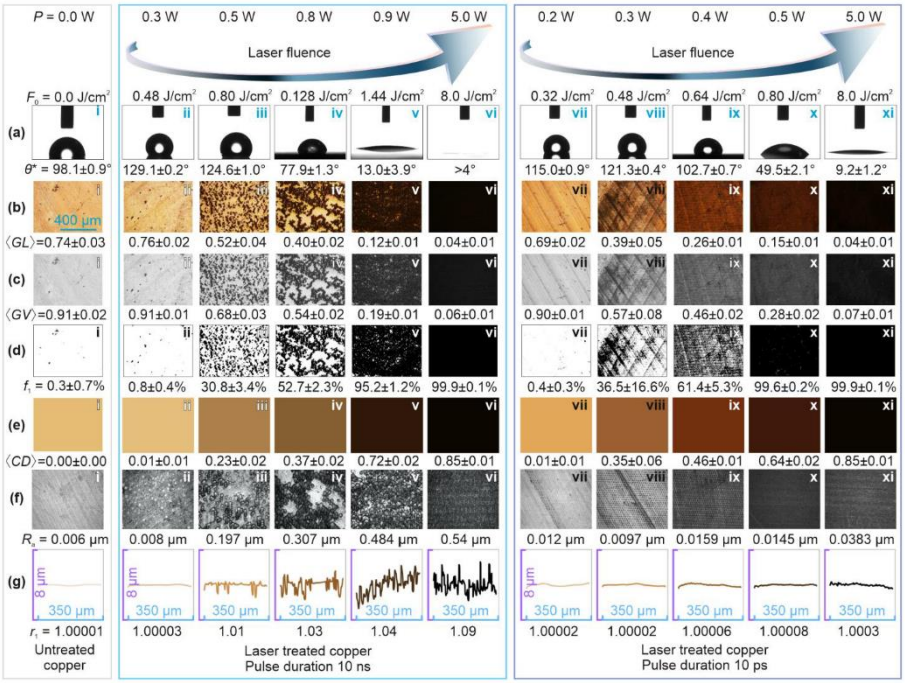

Figure 5. (a) Water droplet images on copper surface treated by laser at different laser fluences. (b) RGB color digital optical microscope images of the Cu surface. (c) Color optical microscope images converted to grayscale mode. (d) Grayscale images were converted to black-and-white binary images with the threshold *value* of $GV_{th} = 0.48 \pm 0.02$. (e) The reconstructed average color of color images of copper. (f) 3D optical profiler images of the copper surface. (g) Line profiles of laser-treated copper surface. The laser fluence used for treatment: (i) $F_0 = 0.0$ J/cm² (untreated); (ii) 0.48 J/cm²; (iii) 0.80 J/cm²; (iv) 0.128 J/cm²; (v) 1.44 J/cm²; (vi) 8.0 J/cm²; (vii) 0.32 J/cm² (viii) 0.48 J/cm² (ix)

0.64 J/cm^2 (x) 0.80 J/cm^2, and (xi) 8.0 J/cm^2. Pulse durations used (ii-vi) τ_p = 10 ns and (vii-xi) τ_p = 10 ps. The scale bar provided in (b)(i) is valid for all images in (b-d) rows.

Water droplet images on copper surfaces treated by laser at different laser fluences are provided in Figure 5(a). The measured contact angle θ^* values are given below each image. The contact angle decreased with increasing laser fluence for both nanosecond and picosecond laser irradiation regimes. The microscope RGB color images are provided in Figure 5(b). The average grayscale *luminance* $\langle GL \rangle$ calculated by Eq. (11) is given below each image. The size of each RGB microscope image is 0.87 × 0.65 mm^2. The RGB color image conversion to the grayscale mode is provided in Figure 5(c). The average grayscale *value* $\langle GV \rangle$ calculated by Eq. (9) is given below each image. The grayscale image conversion and black-and-white images are provided in Figure 5(d). The area fraction is calculated from black-and-white images by using Eq. (8) given below each image. The area fraction of the laser-ablated surface increases with increasing peak laser fluence for both nanosecond and picosecond laser irradiation regimes. The reconstructed color of microscope RGB images of the surface of copper is provided in Figure 5(e). The average color distance $\langle CD \rangle$ calculated by Eq. (12) is provided below each image. The grayscale luminance $\langle GL \rangle$, grayscale value $\langle GV \rangle$ and color distance $\langle GV \rangle$ of each image increased linearly with increasing peak laser fluence for both nanosecond and picosecond laser irradiation regimes. The 3D optical profiler images are provided in Figure 5(f). The surface roughness values R_a is provided below each image. The surface roughness R_a for both nanosecond and picosecond pulse duration increases with increasing laser fluence. However, the R_a values for picosecond pulses are more than 10 times smaller than for nanosecond pulses. The line profiles of the laser-treated copper surface are provided in Figure 5(g) (all experimental data of line profiles is provided in the supplementary material Figure S2). The normalized profile arc length r_1 values calculated by Eq. (5) are provided below the profiles. The normalized profile arc length values increase for both nanosecond and picosecond pulse durations. However, the r_1 values for picosecond pulses are more than 100 times smaller than for the nanosecond pulses. It can be considered that laser-induced surface roughness and increased profile length for nanosecond pulses reduced the contact angles to values close to zero degrees [103]. However, for picosecond pulses the roughness is more than 10 times and the profile arc length is more than 100 times lower than for the nanosecond pulses. The contact angle also decreases to zero degrees, the Wenzel model can not be directly applied for the interpretation of the experimental results.

5.2. Contact angle and color vs area fraction

The plots depicting how different surface characteristics (contact angle, color distance, gray value, and gray luminance) vary with the ablated area fraction for two different laser pulse durations: τ_p = 10 ns

and τ_p = 10 ps is depicted in Figure 6 (all experimental data is provided in the supplementary material Figure S3, Figure S4, and Figure S5).

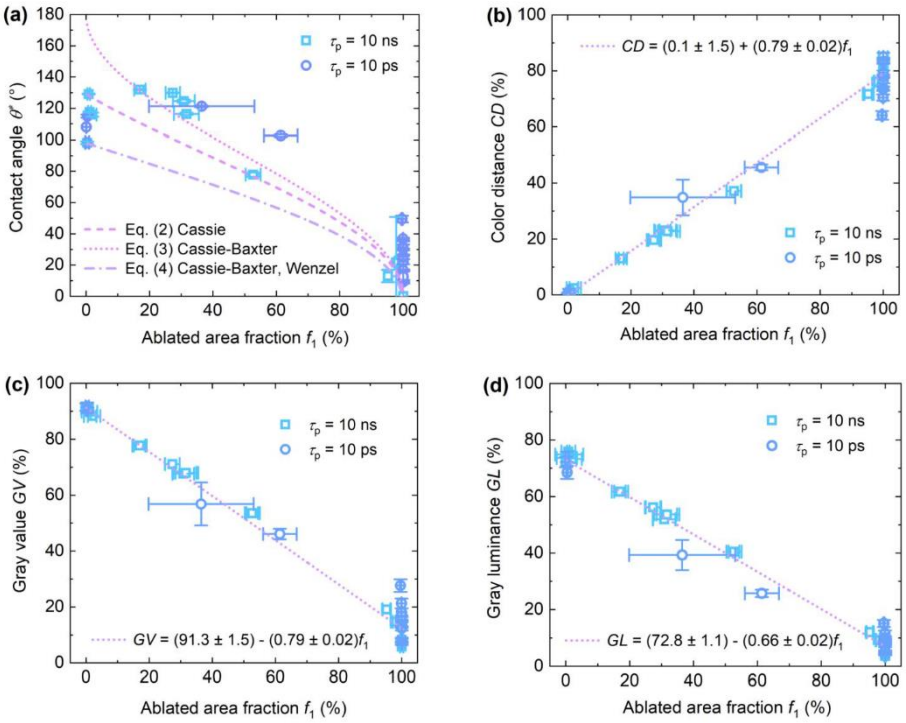

Figure 6. Water static contact angle θ^* (a), color distance *CD* (b), gray value *GV* (c), and gray luminance *GL* (d) depend on the area fraction f_1 of laser-ablated copper. The open squares and open circles correspond to laser processing using irradiation at different pulse durations of τ_p = 10 ns and τ_p = 10 ps, respectively. The dot, dash, and dot-dash lines in (a) are fits of the experimental data point by Eq. (2), Eq. (3), and Eq. (4), respectively. The horizontal error bars in (a-d) indicate the standard deviation in the area fraction measurements taken from five sections of the microscope images. Vertical error bars in (a) correspond to the difference in contact angle measured on the left and right sides of the droplet. Vertical error bars in (b-d) indicate the standard deviation in the color distance, gray value, and gray luminance evaluation from five sections of the microscope images. Common processing conditions: irradiation wavelength λ = 1064 nm, spot size on the sample w_0 = 20 µm; pulse repetition rate f_{rep} = 100 kHz, beam scanning speed on the sample v_{scan} = 1.0 m/s, the lateral distance between laser pulses Δx = 10 µm, the lateral distance between bidirectional scanned lines in snake-like beam

trajectory Δy = 5 µm. The water contact angle on laser-textured surfaces was measured 15 days after laser processing.

The contact angle decreases as the ablated area fraction increases, meaning the surface becomes more hydrophilic (Figure 6(a)). The theoretical models provide predictions for how the contact angle should change based on different surface states (e.g., Cassie or Cassie-Baxter, representing different wettability regimes). Fitting parameters for Eq. (2), Eq. (3), and Eq. (4) for curves given in Figure 6(a) are depicted Table 1.

Table 1 Fitting parameters used Figure 6(a).

Contact angle θ_1	**Contact angle θ_2**	**Profile arc length r_1**	**Equation**	**Model**	**Reference**
0°	129°	-	(2)	Cassie	[91,92]
0°	-	-	(3)	Cassie-Baxter	[93,94]
4°	98°	1.01	(4)	Cassie-Baxter, Wenzel	[94,95]

For Cassie model Eq. (2) the contact angles of θ_1 = 0° which correspond well to the experimental value minimal contacted angle of <4° of laser structured copper at high fluence (8 J/cm^2) (Figure 5(a)(vi)), and θ_2= 129° correspond well to the experimental value maximal measures angle of laser structured copper at low fluence (0.48 J/cm^2) (Figure 5(a)(ii)).

For Cassie-Baxter model Eq. (3) the contact angles of θ_1 = 0.0° which correspond well to the experimental value minimal contacted angle of <4° of laser structured copper at high fluence (8 J/cm^2)

For the combined Cassie-Baxter and Wenzel model Eq. (4) the contact angles of θ_1 = 4° which correspond well to the experimental value minimal contacted angle of <4° of laser structured copper at high fluence (8 J/cm^2) (Figure 5(a)(vi)), and θ_2= 98° correspond well to the experimental value maximal measures angle of laser unstructured copper (0.0 J/cm^2) (Figure 5(a)(i)).

There is good agreement between experimental data and theoretical fits, especially for the τ_p = 10 ps pulses (Figure 6(a)). The color change increases linearly with the ablated area fraction. A linear fit is provided: $CD = (0.1\pm1.5) + (0.79\pm0.02)f_1$ (Figure 6(a)). The τ_p = 10 ps pulses appear to cause a more rapid color change compared to τ_p = 10 ns pulses at low ablation fractions. (Figure 6(b)). The gray value decreases as the ablated area fraction increases, suggesting that the surface becomes darker as more material is ablated. The linear fit equation is: $GV = (91.3\pm1.5) - (0.79\pm0.02)f_1$ Similar trends are observed for both τ_p = 10 ns and τ_p = 10 ps, though there may be subtle differences in behavior at low ablation fractions (Figure 6(c)). Gray luminance decreases as the ablation fraction increases, consistent with the gray value trends. The linear fit is $GL = (72.8\pm1.1) - (0.66\pm0.02)f_1$. Both τ_p = 10 ns and

τ_p = 10 ps pulses show similar trends, with a gradual reduction in luminance as ablation increases (Figure 6 (e)).

6. Conclusions

To conclude, here we reported on a novel single-step and chemical-free fabrication method for the creation of super-wetting and highly hydrophobic copper surfaces using nanosecond and picosecond lasers. The wettability and color of copper were controlled by controlling the area fraction of the laser-ablated surface. Our adopted Cassie, Cassie-Baxter, and Wenzel models indicate that as the ablated area fraction increases, the contact angle decreases, indicating that the surface becomes more hydrophilic. Both color distance, gray value, and gray luminance increase or decrease linearly with the ablated area fraction of the copper surface, indicating significant visual and optical changes due to surface modification. The pulse duration (ps or ns) plays a role in the degree of these changes, with shorter pulse durations (10 ps) typically having a stronger effect. Thanks to the laser-texturing process, super-wetting surfaces can be efficiently scaled up to cover large areas, even on complex shapes. This scalability makes them ideal for enhancing fog harvesting in atmospheric water generators and improving the performance of heat exchanger technologies used in water heat sinks, fans, and cooling units.

Disclosures. The authors declare no conflicts of interest.

Data availability. Data underlying the results presented in this paper are not publicly available at this time but may be obtained from the authors upon reasonable request.

Acknowledgments. M.Ga., A.Ž., and M.Ge. received funding from the Research Council of Lithuania (LMTLT), agreement no. S-MIP-22-89. This work was also supported by the EU-Horizon 2020 Nanoscience Foundries and Fine Analysis (NEP) Project (Grant agreement ID 101007417) having benefited from the access provided by the Foundation for Research and Technology Hellas (FORTH) (Access project ID 177).

Funding. Research Council of Lithuania (LMTLT) (S-MIP-22-89). This project has received funding from the European Union's Horizon 2020 research and innovation programme, under grant agreement No 101007417 NFFA-Europe Pilot.

Contributions

M.Ga., A.Ž., and M.Ge. conceived the original idea for the project. E.St. supervised for collaboration work and internship of M.Ge. and A.Ž. at IESL-FORTH. E.Sk. hosted the stay of M.Ge. and A.Ž. at IESL-FORTH.

A.L. helped with software development and A.P. helped with technical support at IESL-FORTH. S.M. and A.M. performed the water contact angle measurements at IESL-FORTH. M.Ge. performed the structuring using nanosecond and picosecond lasers at LTS-FTMC. M.Ga. conducted the surface topography measurements and surface roughness measurements using a 3D optical profiler at LTS-FTMC. M.Ge. supervised all the findings of this work, adopted the Casei-Baxter and Wenzel models, performed the digital image analysis, and numerical calculations, analyzed the data, and wrote the manuscript. All authors analyzed the findings, discussed the results, and commented on the manuscript.

References

1 Gaidys, M., Selskis, A., Gečys, P. & Gedvilas, M. Stainless steel colouring using burst and biburst mode ultrafast laser irradiation. *Optics & Laser Technology* **174**, 110561, doi:10.1016/j.optlastec.2024.110561 (2024).

2 Zorba, V. *et al.* Biomimetic Artificial Surfaces Quantitatively Reproduce the Water Repellency of a Lotus Leaf. *Advanced Materials* **20**, 4049-4054, doi:10.1002/adma.200800651 (2008).

3 Neinhuis, C. Characterization and Distribution of Water-repellent, Self-cleaning Plant Surfaces. *Annals of Botany* **79**, 667-677, doi:10.1006/anbo.1997.0400 (1997).

4 Barthlott, W. & Neinhuis, C. Purity of the sacred lotus, or escape from contamination in biological surfaces. *Planta* **202**, 1-8, doi:DOI 10.1007/s004250050096 (1997).

5 Stratakis, E., Ranella, A. & Fotakis, C. Biomimetic micro/nanostructured functional surfaces for microfluidic and tissue engineering applications. *Biomicrofluidics* **5**, 13411, doi:10.1063/1.3553235 (2011).

6 Clapham, P. B. & Hutley, M. C. Reduction of Lens Reflexion by the "Moth Eye" Principle. *Nature* **244**, 281-282, doi:10.1038/244281a0 (1973).

7 Gao, X. & Jiang, L. Biophysics: water-repellent legs of water striders. *Nature* **432**, 36, doi:10.1038/432036a (2004).

8 Zheng, Y., Gao, X. & Jiang, L. Directional adhesion of superhydrophobic butterfly wings. *Soft Matter* **3**, 178-182, doi:10.1039/b612667g (2007).

9 Parker, A. R. & Lawrence, C. R. Water capture by a desert beetle. *Nature* **414**, 33-34, doi:10.1038/35102108 (2001).

10 Hamilton, W. J. & Seely, M. K. Fog basking by the Namib Desert beetle, Onymacris unguicularis. *Nature* **262**, 284-285, doi:10.1038/262284a0 (1976).

11 Raciukaitis, G. B., Marijus; Gecys, Paulius; Voisiat, Bogdan; Gedvilas, Mindaugas. Use of High Repetition Rate and High Power Lasers in Microfabrication: How to Keep the Efficiency High? *Journal of Laser Micro/Nanoengineering* **4**, 186-191, doi:10.2961/jlmn.2009.03.0008 (2009).

12 Bixler, G. D. & Bhushan, B. Bioinspired rice leaf and butterfly wing surface structures combining shark skin and lotus effects. *Soft Matter* **8**, 11271, doi:10.1039/c2sm26655e (2012).

13 Skoulas, E., Manousaki, A., Fotakis, C. & Stratakis, E. Biomimetic surface structuring using cylindrical vector femtosecond laser beams. *Sci Rep* **7**, 45114, doi:10.1038/srep45114 (2017).

14 Comanns, P. *et al.* Directional, passive liquid transport: the Texas horned lizard as a model for a biomimetic 'liquid diode'. *J. Royal Soc. Interface* **12**, 20150415, doi:10.1098/rsif.2015.0415 (2015).

15 Zhao, J., Liu, Z., Low, S. C., Xu, Z. & Tan, S. H. Biomimetic hydrophilic CuO-nanocluster/nanofibrous thin-film skeleton/hydrophilic CuO-nanocluster architecture membrane for efficient and stable solar water evaporation. *Journal of Alloys and Compounds* **969**, 172377, doi:10.1016/j.jallcom.2023.172377 (2023).

16 Breuer, C., Cordt, C., Hiller, B., Geissler, A. & Biesalski, M. Using Paper as a Biomimetic Fog Harvesting Material. *Advanced Materials Interfaces* **11**, doi:10.1002/admi.202301048 (2024).

17 Dumanli, A. G. & Savin, T. Recent advances in the biomimicry of structural colours. *Chem Soc Rev* **45**, 6698-6724, doi:10.1039/c6cs00129g (2016).

18 Ivanova, E. P. *et al.* Bactericidal activity of black silicon. *Nat Commun* **4**, 2838, doi:10.1038/ncomms3838 (2013).

19 Bhushan, B. & Jung, Y. C. Natural and biomimetic artificial surfaces for superhydrophobicity, self-cleaning, low adhesion, and drag reduction. *Progress in Materials Science* **56**, 1-108, doi:10.1016/j.pmatsci.2010.04.003 (2011).

20 Xu, Q., Zhang, W., Dong, C., Sreeprasad, T. S. & Xia, Z. Biomimetic self-cleaning surfaces: synthesis, mechanism and applications. *J R Soc Interface* **13**, doi:10.1098/rsif.2016.0300 (2016).

21 Domke, M., Sonderegger, G., Kostal, E., Matylitsky, V. & Stroj, S. Transparent laser-structured glasses with superhydrophilic properties for anti-fogging applications. *Applied Physics A* **125**, doi:10.1007/s00339-019-2953-6 (2019).

22 Papadopoulos, A. *et al.* Biomimetic Omnidirectional Antireflective Glass via Direct Ultrafast Laser Nanostructuring. *Adv Mater* **31**, e1901123, doi:10.1002/adma.201901123 (2019).

23 Žemaitis, A., Mikšys, J., Gaidys, M., Gečys, P. & Gedvilas, M. High-efficiency laser fabrication of drag reducing riblet surfaces on pre-heated Teflon. *Materials Research Express* **6**, 065309, doi:10.1088/2053-1591/ab0b12 (2019).

24 Feng, L. *et al.* Super-Hydrophobic Surfaces: From Natural to Artificial. *Adv. Mater.* **14**, 1857-1860, doi:10.1002/adma.200290020 (2002).

25 Tseng, P. *et al.* Directed assembly of bio-inspired hierarchical materials with controlled nanofibrillar architectures. *Nat. Nanotechnol.* **12**, 474-480, doi:10.1038/nnano.2017.4 (2017).

26 Si, Y., Dong, Z. & Jiang, L. Bioinspired Designs of Superhydrophobic and Superhydrophilic Materials. *ACS Cent. Sci.* **4**, 1102-1112, doi:10.1021/acscentsci.8b00504 (2018).

27 Zhang, C., McAdams, D. A., 2nd & Grunlan, J. C. Nano/Micro-Manufacturing of Bioinspired Materials: a Review of Methods to Mimic Natural Structures. *Adv. Mater.* **28**, 6292-6321, doi:10.1002/adma.201505555 (2016).

28 Das, S., Kumar, S., Samal, S. K., Mohanty, S. & Nayak, S. K. A Review on Superhydrophobic Polymer Nanocoatings: Recent Development and Applications. *Ind. Eng. Chem. Res.* **57**, 2727-2745, doi:10.1021/acs.iecr.7b04887 (2018).

29 Sanchez, C., Arribart, H. & Giraud Guille, M. M. Biomimetism and bioinspiration as tools for the design of innovative materials and systems. *Nat. Mater.* **4**, 277-288, doi:10.1038/nmat1339 (2005).

30 Whitesides, G. M. Bioinspiration: something for everyone. *Interface Focus* **5**, 20150031, doi:10.1098/rsfs.2015.0031 (2015).

31 Wood, J. Bioinspiration in Fashion-A Review. *Biomimetics* **4**, 16, doi:10.3390/biomimetics4010016 (2019).

32 Bormashenko, E. Wetting transitions on biomimetic surfaces. *Philos. Trans. Royal Soc. A* **368**, 4695-4711, doi:10.1098/rsta.2010.0121 (2010).

33 Huang, C. & Guo, Z. The wettability of gas bubbles: from macro behavior to nano structures to applications. *Nanoscale* **10**, 19659-19672, doi:10.1039/c8nr07315e (2018).

34 Zemaitis, A. *et al.* Controlling the wettability of stainless steel from highly-hydrophilic to super-hydrophobic by femtosecond laser-induced ripples and nanospikes. *RSC Adv* **10**, 37956-37961, doi:10.1039/d0ra05665k (2020).

35 Stratakis, E. *et al.* Laser engineering of biomimetic surfaces. *Materials Science and Engineering: R: Reports* **141**, 100562, doi:10.1016/j.mser.2020.100562 (2020).

36 Anscombe, N. Direct laser writing. *Nat. Photonics* **4**, 22-23, doi:10.1038/nphoton.2009.250 (2010).

37 Selimis, A., Mironov, V. & Farsari, M. Direct laser writing: Principles and materials for scaffold 3D printing. *Microelectron. Eng.* **132**, 83-89, doi:10.1016/j.mee.2014.10.001 (2015).

38 Žemaitis, A., Gudauskytė, U., Steponavičiūtė, S., Gečys, P. & Gedvilas, M. The ultrafast burst laser ablation of metals: Speed and quality come together. *Optics & Laser Technology* **180**, 111458, doi:10.1016/j.optlastec.2024.111458 (2025).

39 Jonusauskas, L. *et al.* Mesoscale laser 3D printing. *Opt. Express* **27**, 15205-15221, doi:10.1364/OE.27.015205 (2019).

40 Žemaitis, A., Gečys, P. & Gedvilas, M. High throughput and low surface roughness laser layer-by-layer milling using nanosecond (ns), picosecond (ps), and hybrid ns-ps pulses: A comparative study. *Optics and Lasers in Engineering* **176**, 108046, doi:10.1016/j.optlaseng.2024.108046 (2024).

41 Raciukaitis, G., Brikas, M. & Gedvilas, M. Efficiency aspects in processing of metals with high-repetition-rate ultra-short-pulse lasers. *Proc. ICALEO*, M403, doi:10.2351/1.5061377 (2008).

42 Hada, M. *et al.* Cold ablation driven by localized forces in alkali halides. *Nat. Commun.* **5**, 3863, doi:10.1038/ncomms4863 (2014).

43 Chichkov, B. N., Momma, C., Nolte, S., Alvensleben, F. & Tünnermann, A. Femtosecond, picosecond and nanosecond laser ablation of solids. *Appl. Phys. A* **63**, 109-115, doi:10.1007/bf01567637 (1996).

44 Kerse, C. *et al.* Ablation-cooled material removal with ultrafast bursts of pulses. *Nature* **537**, 84-88, doi:10.1038/nature18619 (2016).

45 Zemaitis, A., Gaidys, M., Gecys, P. & Gedvilas, M. Bi-stability in femtosecond laser ablation by MHz bursts. *Sci Rep* **14**, 5614, doi:10.1038/s41598-024-54928-7 (2024).

46 Molotokaite, E. G., Mindaugas; Raciukaitis, Gediminas; Girdauskas, Valdas. Picosecond Laser Beam Interference Ablation of Thin Metal Films on Glass Substrate. *Journal of Laser Micro/Nanoengineering* **5**, 74-79, doi:10.2961/jlmn.2010.01.0016 (2010).

47 Gedvilas, M. *et al.* Thermo-chemical microstructuring of thin metal films using multi-beam interference by short (nano- & picosecond) laser pulses. *Thin Solid Films* **634**, 134-140, doi:10.1016/j.tsf.2017.05.010 (2017).

48 Drogowska-Horna, K. A. *et al.* Periodic surface functional group density on graphene via laser-induced substrate patterning at Si/SiO2 interface. *Nano Research* **13**, 2332-2339, doi:10.1007/s12274-020-2852-3 (2020).

49 Öktem, B. *et al.* Nonlinear laser lithography for indefinitely large-area nanostructuring with femtosecond pulses. *Nat. Photonics* **7**, 897-901, doi:10.1038/nphoton.2013.272 (2013).

50 Indrisiunas, S., Svirplys, E. & Gedvilas, M. Large-Area Fabrication of LIPSS for Wetting Control Using Multi-Parallel Femtosecond Laser Processing. *Materials (Basel)* **15**, doi:10.3390/ma15165534 (2022).

51 Indrišiūnas, S. & Gedvilas, M. Control of the wetting properties of stainless steel by ultrashort laser texturing using multi-parallel beam processing. *Optics & Laser Technology* **153**, 108187, doi:10.1016/j.optlastec.2022.108187 (2022).

52 Ma, L. *et al.* Hybrid Nanosecond Laser Processing and Heat Treatment for Rapid Preparation of Super-Hydrophobic Copper Surface. *Metals* **9**, 668, doi:10.3390/met9060668 (2019).

53 He, A., Liu, W., Xue, W., Yang, H. & Cao, Y. Nanosecond laser ablated copper superhydrophobic surface with tunable ultrahigh adhesion and its renewability with low temperature annealing. *Appl. Surf. Sci.* **434**, 120-125, doi:10.1016/j.apsusc.2017.10.143 (2018).

54 Chun, D.-M., Ngo, C.-V. & Lee, K.-M. CIRP Annals. *CIRP Ann.* **65**, 519-522, doi:10.1016/j.cirp.2016.04.019 (2016).

55 Long, J. *et al.* Formation mechanism of hierarchical Micro- and nanostructures on copper induced by low-cost nanosecond lasers. *Appl. Surf. Sci.* **464**, 412-421, doi:10.1016/j.apsusc.2018.09.055 (2019).

56 Long, J. *et al.* Superhydrophobic and colorful copper surfaces fabricated by picosecond laser induced periodic nanostructures. *Appl. Surf. Sci.* **311**, 461-467, doi:10.1016/j.apsusc.2014.05.090 (2014).

57 Long, J., Zhong, M., Fan, P., Gong, D. & Zhang, H. Wettability conversion of ultrafast laser structured copper surface. *J. Laser Appl.* **27**, S29107, doi:10.2351/1.4906477 (2015).

58 Fu, P., Shi, X., Jiang, F. & Xu, X. Superhydrophobic nanostructured copper substrate as sensitive SERS platform prepared by femtosecond laser pulses. *Appl. Surf. Sci.* **501**, 144269, doi:10.1016/j.apsusc.2019.144269 (2019).

59 Long, J. *et al.* Superhydrophobic surfaces fabricated by femtosecond laser with tunable water adhesion: from lotus leaf to rose petal. *ACS Appl. Mater. Interfaces* **7**, 9858-9865, doi:10.1021/acsami.5b01870 (2015).

60 Liu, Q., Tang, Y., Luo, W., Fu, T. & Yuan, W. Fabrication of superhydrophilic surface on copper substrate by electrochemical deposition and sintering process. *Chin. J. Chem. Phys.* **23**, 1200-1205, doi:10.1016/j.cjche.2014.11.034 (2015).

61 Youngsuk, N., Sharratt, S., Byon, C., Sung Jin, K. & Ju, Y. S. Fabrication and Characterization of the Capillary Performance of Superhydrophilic Cu Micropost Arrays. *J. Microelectromech. Syst.* **19**, 581-588, doi:10.1109/jmems.2010.2043922 (2010).

62 McDonald, B. T. & Cui, T. Superhydrophilic surface modification of copper surfaces by Layer-by-Layer self-assembly and Liquid Phase Deposition of TiO(2) thin film. *J. Colloid Interface Sci.* **354**, 1-6, doi:10.1016/j.jcis.2010.09.036 (2011).

63 Zhong, L., Feng, J. & Guo, Z. An alternating nanoscale (hydrophilic–hydrophobic)/hydrophilic Janus cooperative copper mesh fabricated by a simple liquidus modification for efficient fog harvesting. *J. Mater. Chem. A* **7**, 8405-8413, doi:10.1039/c9ta01906e (2019).

64 Rahman, M. M., Olceroglu, E. & McCarthy, M. Role of wickability on the critical heat flux of structured superhydrophilic surfaces. *Langmuir* **30**, 11225-11234, doi:10.1021/la5030923 (2014).

65 Takata, Y., Hidaka, S., Masuda, M. & Ito, T. Pool boiling on a superhydrophilic surface. *Int. J. Energy Res.* **27**, 111-119, doi:10.1002/er.861 (2003).

66 Kim, B. S., Lee, H., Shin, S., Choi, G. & Cho, H. H. Interfacial wicking dynamics and its impact on critical heat flux of boiling heat transfer. *Appl. Phys. Lett.* **105**, 191601, doi:10.1063/1.4901569 (2014).

67 Huang, Z., Hwang, Y. & Radermacher, R. Review of nature-inspired heat exchanger technology. *Int. J. Refrig.* **78**, 1-17, doi:10.1016/j.ijrefrig.2017.03.006 (2017).

68 Zuazua-Ros, A., Martín-Gómez, C., Ramos, J. C. & Gómez-Acebo, T. Bio-inspired Heat Dissipation System Integrated in Buildings: Development and Applications. *Energy Procedia* **111**, 51-60, doi:10.1016/j.egypro.2017.03.007 (2017).

69 Ju, J. *et al.* A multi-structural and multi-functional integrated fog collection system in cactus. *Nat. Commun.* **3**, 1247, doi:10.1038/ncomms2253 (2012).

70 Chen, D. *et al.* Bioinspired superhydrophilic-hydrophobic integrated surface with conical pattern-shape for self-driven fog collection. *J. Colloid Interface Sci.* **530**, 274-281, doi:10.1016/j.jcis.2018.06.081 (2018).

71 Kostal, E., Stroj, S., Kasemann, S., Matylitsky, V. & Domke, M. Fabrication of Biomimetic Fog-Collecting Superhydrophilic-Superhydrophobic Surface Micropatterns Using Femtosecond Lasers. *Langmuir* **34**, 2933-2941, doi:10.1021/acs.langmuir.7b03699 (2018).

72 Bai, F., Wu, J., Gong, G. & Guo, L. Biomimetic "Cactus Spine" with Hierarchical Groove Structure for Efficient Fog Collection. *Adv. Sci.* **2**, 1500047, doi:10.1002/advs.201500047 (2015).

73 Tu, Y., Wang, R., Zhang, Y. & Wang, J. Progress and Expectation of Atmospheric Water Harvesting. *Joule* **2**, 1452-1475, doi:10.1016/j.joule.2018.07.015 (2018).

74 Davidson, K. B., Asiabanpour, B. & Almusaied, Z. Applying Biomimetic Principles to Thermoelectric Cooling Devices for Water Collection. *Environ. Nat. Resour. Res.* **7**, 27, doi:10.5539/enrr.v7n3p27 (2017).

75 Nakajima, D. *et al.* A Superhydrophilic Aluminum Surface with Fast Water Evaporation Based on Anodic Alumina Bundle Structures via Anodizing in Pyrophosphoric Acid. *Materials* **12**, 3497, doi:10.3390/ma12213497 (2019).

76 Ruiz, M. M., Schroeder, W. F. & Hoppe, C. E. The use of a fatty acid/β-Hydroxyester blend to enhance the surface hydrophilicity of crosslinked poly(ethylene glycol) coatings. *Prog. Org. Coat.* **135**, 313-320, doi:10.1016/j.porgcoat.2019.06.021 (2019).

77 Verho, T. *et al.* Mechanically durable superhydrophobic surfaces. *Adv. Mater.* **23**, 673-678, doi:10.1002/adma.201003129 (2011).

78 Manca, M. *et al.* Durable Superhydrophobic and Antireflective Surfaces by Trimethylsilanized Silica Nanoparticles-Based Sol−Gel Processing. *Langmuir* **25**, 6357-6362, doi:10.1021/la804166t (2009).

79 Sun, Y. & Guo, Z. Recent advances of bioinspired functional materials with specific wettability: from nature and beyond nature. *Nanoscale Horiz.* **4**, 52-76, doi:10.1039/c8nh00223a (2019).

80 Han, Z., Jiao, Z., Niu, S. & Ren, L. Ascendant bioinspired antireflective materials: Opportunities and challenges coexist. *Prog. Mater. Sci.* **103**, 1-68, doi:10.1016/j.pmatsci.2019.01.004 (2019).

81 Han, Z., Feng, X., Guo, Z., Niu, S. & Ren, L. Flourishing Bioinspired Antifogging Materials with Superwettability: Progresses and Challenges. *Adv. Mater.* **30**, e1704652, doi:10.1002/adma.201704652 (2018).

82 Fraggelakis, F., Mincuzzi, G., Lopez, J., Manek-Honninger, I. & Kling, R. Texturing metal surface with MHz ultra-short laser pulses. *Opt. Express* **25**, 18131-18139, doi:10.1364/OE.25.018131 (2017).

83 Gaidys, M., Žemaitis, A., Gečys, P. & Gedvilas, M. Efficient picosecond laser ablation of copper cylinders. *Appl. Surf. Sci.* **483**, 962-966, doi:10.1016/j.apsusc.2019.04.002 (2019).

84 Zhang, S., Huang, J., Chen, Z. & Lai, Y. Bioinspired Special Wettability Surfaces: From Fundamental Research to Water Harvesting Applications. *Small* **13**, doi:10.1002/smll.201602992 (2017).

85 Liu, M., Wang, S. & Jiang, L. Nature-inspired superwettability systems. *Nat. Rev. Mater.* **2**, doi:10.1038/natrevmats.2017.36 (2017).

86 Marmur, A. The Lotus effect: superhydrophobicity and metastability. *Langmuir* **20**, 3517-3519, doi:10.1021/la036369u (2004).

87 Liu, X., Liu, H., Yu, X., Zhou, L. & Zhu, J. Solar thermal utilizations revived by advanced solar evaporation. *Curr. Opin. Chem. Eng.* **25**, 26-34, doi:10.1016/j.coche.2019.07.004 (2019).

88 Bigelow, W. C., Pickett, D. L. & Zisman, W. A. Oleophobic monolayers. *J. Colloid Sci.* **1**, 513-538, doi:10.1016/0095-8522(46)90059-1 (1946).

89 Wenzel, R. N. Resistance of Solid Surfaces to Wetting by Water. *Industrial & Engineering Chemistry* **28**, 988-994, doi:10.1021/ie50320a024 (1936).

90 Cassie, A. B. D. & Baxter, S. Wettability of porous surfaces. *Transactions of the Faraday Society* **40**, 546, doi:10.1039/tf9444000546 (1944).

91 Baxter, S. & Cassie, A. B. D. 8—the Water Repellency of Fabrics and a New Water Repellency Test. *Journal of the Textile Institute Transactions* **36**, T67-T90, doi:10.1080/19447024508659707 (1945).

92 Cassie, A. B. D. & Baxter, S. Large Contact Angles of Plant and Animal Surfaces. *Nature* **155**, 21-22, doi:10.1038/155021a0 (1945).

93 Li, C., Zhang, J., Han, J. & Yao, B. A numerical solution to the effects of surface roughness on water-coal contact angle. *Sci Rep* **11**, 459, doi:10.1038/s41598-020-80729-9 (2021).

94 Milne, A. J. & Amirfazli, A. The Cassie equation: how it is meant to be used. *Adv Colloid Interface Sci* **170**, 48-55, doi:10.1016/j.cis.2011.12.001 (2012).

95 Shim, M. H., Kim, J. & Park, C. H. The effects of surface energy and roughness on the hydrophobicity of woven fabrics. *Textile Research Journal* **84**, 1268-1278, doi:10.1177/0040517513495945 (2014).

96 Liu, J. M. Simple technique for measurements of pulsed Gaussian-beam spot sizes. *Opt. Lett.* **7**, 196-198, doi:10.1364/ol.7.000196 (1982).

97 Kietzig, A. M., Hatzikiriakos, S. G. & Englezos, P. Patterned superhydrophobic metallic surfaces. *Langmuir* **25**, 4821-4827, doi:10.1021/la8037582 (2009).

98 Gregorčič, P., Šetina-Batič, B. & Hočevar, M. Controlling the stainless steel surface wettability by nanosecond direct laser texturing at high fluences. *Appl. Phys. A* **123**, doi:10.1007/s00339-017-1392-5 (2017).

99 Kanan, C. & Cottrell, G. W. Color-to-grayscale: does the method matter in image recognition? *PLoS One* **7**, e29740, doi:10.1371/journal.pone.0029740 (2012).

100 Gedvilas, M. *et al.* Percolation effect of a Cu layer on a MWCNT/PP nanocomposite substrate after laser direct structuring and autocatalytic plating. *RSC Adv* **8**, 30305-30309, doi:10.1039/c8ra04813d (2018).

101 Gedvilas, M. V., Bogdan; Raciukaitis, Gediminas. Grayscale Marking of Anodized Aluminium Plate by Using Picosecond Laser and Galvanometer Scanner. *Journal of Laser Micro/Nanoengineering* **9**, 267-270, doi:10.2961/jlmn.2014.03.0017 (2014).

102 Gedvilas, M. *et al.* Colour-Difference Measurement Method for Evaluation of Quality of Electrolessly Deposited Copper on Polymer after Laser-Induced Selective Activation. *Sci Rep* **6**, 22963, doi:10.1038/srep22963 (2016).

103 Drelich, J. & Chibowski, E. Superhydrophilic and superwetting surfaces: definition and mechanisms of control. *Langmuir* **26**, 18621-18623, doi:10.1021/la1039893 (2010).

Supplementary material

Wettability and Color Change of Copper by Controlling Area Fraction of Laser Ablated Surface

Mantas Gaidys[1], Stella Maragkaki[2], Alexandros Mimidis[2], Antonis Papadopoulos[2], Andreas Lemonis[2], Evangelos Skoulas[2], Andrius Žemaitis[1], Emmanuel Stratakis[2], Mindaugas Gedvilas[1]*

[1]Department of Laser Technologies (LTS), Center for Physical Sciences and Technology (FTMC), Savanoriu Ave. 231, 02300 Vilnius, Lithuania
[2]Institute of Electronic Structure and Laser (IESL), Foundation for Research and Technology (FORTH), N. Plastira 100, Vassilika Vouton, 70013 Heraklion, Crete, Greece

E-mail: mindaugas.gedvilas@ftmc.lt

The full set of experimental data of the wettability and color change of copper surface depending on the laser power is depicted in Figure S1.

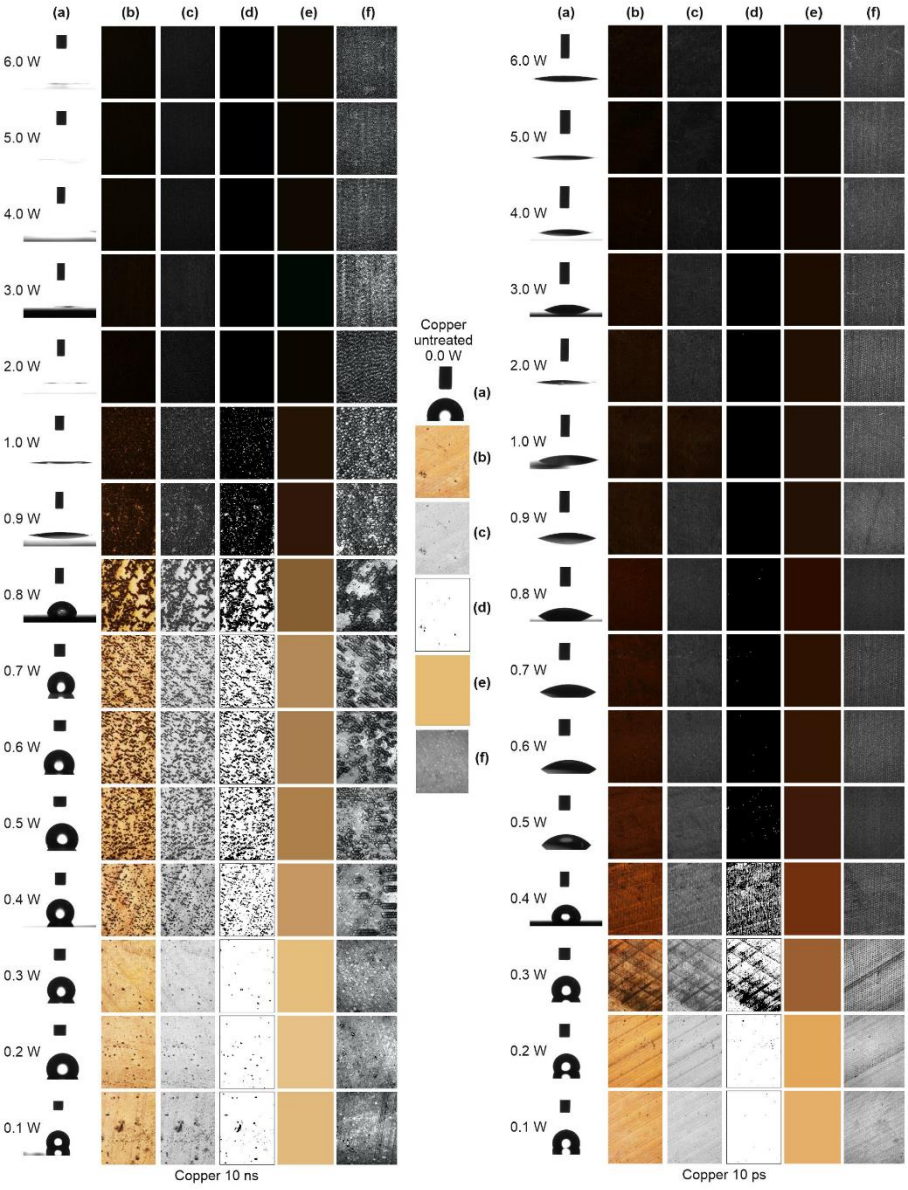

Figure S1. (a) Water droplet images on copper surface treated by laser at different laser powers from 6.0 W (top) to 0.1 W (left), untreated copper 0.0 W (middle). (b) RGB color digital optical microscope images of the Cu surface. The size of each microscope image is 0.65 × 0.87 mm^2. (c) The color optical microscope images are converted to grayscale mode. (d) The grayscale images were converted to black-

and-white binary images. (e) The reconstructed average color of color images of laser-treated copper. (f) 3D optical profiler images of the copper surface. Pulse durations 10 ns (left) and 10 ps (right). Untreated copper (0.0 W) (middle).

The height line profiles of the copper surface structured by laser at different laser powers are given in Figure S2.

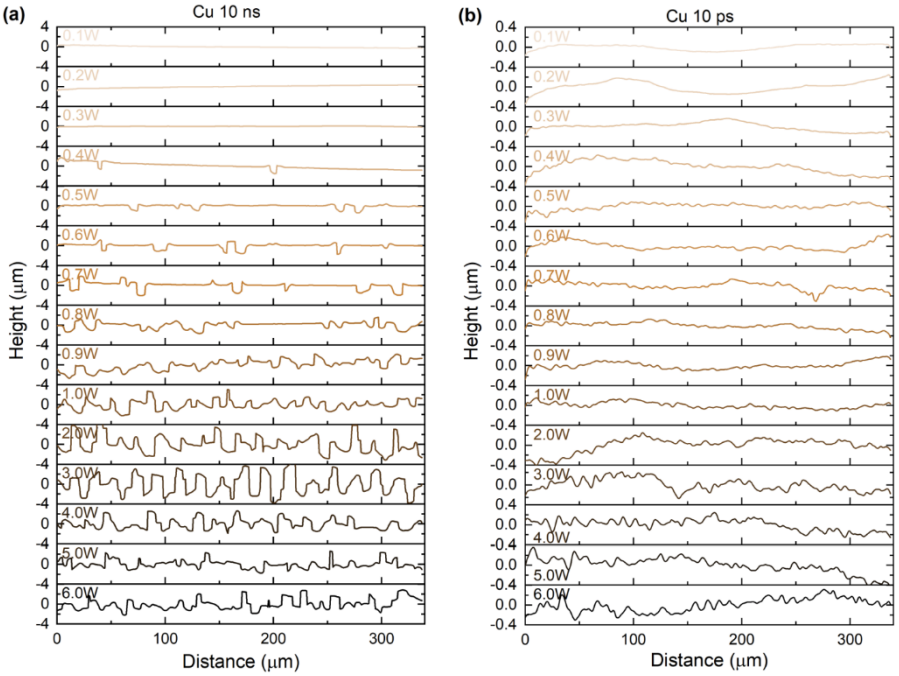

Figure S2. Height of line profiles dependence on transverse distance for copper structured by nanosecond (pulse duration τ_p = 10 ns) (a) and picosecond (pulse duration τ_p = 10 ps) (b) pulses at different laser irradiation powers from 0.1 W (top) to 6.0 W (bottom). Processing conditions: irradiation wavelength λ = 1064 nm, spot size on the sample w_0 = 20 μm; pulse repetition rate f_{rep} = 100 kHz, beam scanning speed on the sample v_{scan} = 1.0 m/s, the lateral distance between laser pulses Δx = 10 μm, the lateral distance between bidirectional scanned lines in snake-like beam trajectory Δy = 5 μm.

Figure S2 (a) shows the surface profiles of copper after being exposed to 10 ns pulse duration laser at increasing power (from 0.1 W to 6.0 W). At low power (0.1–0.6 W) there are minimal height variations, with very small surface undulations close to the baseline of 0 μm. At moderate power (0.7–1.0 W) there

are more pronounced height variations, with noticeable surface features such as shallow peaks and valleys. Ablation effects begin to appear at higher powers. At high power (2.0–6.0 W) the surface roughness increases dramatically. The profiles show deep valleys and sharp peaks, suggesting significant material removal and possible melting or vaporization. The surface appears to be much rougher, with height fluctuations approaching ± 4 µm.

Figure S2(a) shows the surface profiles of copper after exposure to 10 ps pulse duration laser at increasing power (from 0.1 W to 6.0 W). At low powers (0.1–0.6 W) surface height remains close to 0 µm, with only very minor undulations, similar to the 10 ns pulse case. At moderate powers (0.7–1.0 W) the height variations are still relatively small, but they are smoother compared to the 10 ns case. The surface remains largely intact, with some minor ablation features appearing at higher powers. At high powers (2.0–6.0 W) the surface starts showing more pronounced features as the power increases, but the ablation appears smoother and more controlled compared to the 10 ns pulses. The height variations remain within the range of - 0.4 µm to + 0.4 µm, indicating much less material removal or surface disruption compared to the nanosecond pulses.

The 10 ns pulse duration (Figure S2(a)) leads to much more aggressive surface modifications, with deeper and more chaotic ablation features, especially at higher powers. The surface roughness increases significantly as power rises. The 10 ps pulse duration (Figure S2(b)) results in more controlled and subtle changes to the surface, with smaller ablation depths and smoother profiles even at higher powers. This indicates that shorter pulses (picosecond) tend to produce more precise ablation, while longer pulses (nanosecond) result in more widespread surface damage.

Water contact angle and ablated area fraction dependence on the laser irradiation power for copper structured by nanosecond and picosecond pulses is depicted in Figure S3.

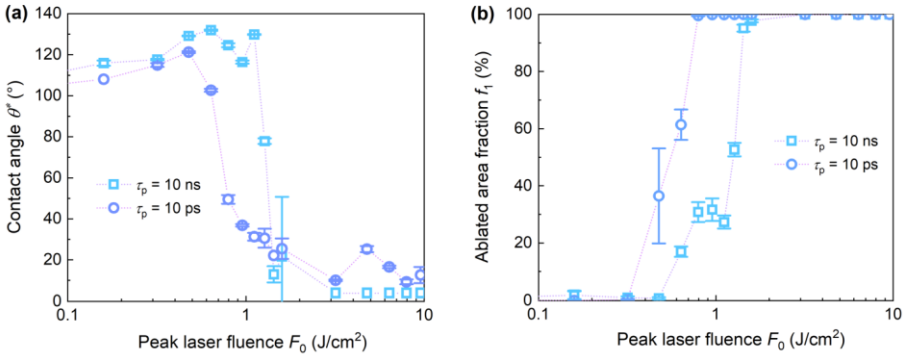

Figure S3. (a) Contact angle θ^* dependence on peak laser fluence F_0. (b) Ablated area fraction f_1 dependence on peak laser fluence F_0. Common processing conditions: irradiation wavelength λ = 1064 nm, spot size on the sample w_0 = 20 µm; pulse repetition rate f_{rep} = 100 kHz, beam scanning

speed on the sample v_{scan} = 1.0 m/s, the lateral distance between laser pulses Δx = 10 µm, the lateral distance between bidirectional scanned lines in snake-like beam trajectory Δy = 5 µm. Laser pulse duration: τ_p = 10 ns - open squares; τ_p = 10 ps - open circles. The water contact angle on laser-textured surfaces was measured 15 days after laser processing.

At low fluences (~0.1–0.5 J/cm^2), the contact angle remains high, indicating minimal changes in surface hydrophobicity. At fluences between 0.5 J/cm^2 and 1 J/cm^2, there is a sharp drop in contact angle, particularly for the τ_p = 10 ns. For both pulse durations, the contact angle stabilizes at lower values (~10°–20°) as fluence increases beyond 1 J/cm^2, indicating a transition to a more hydrophilic surface (Figure S3(a)). Contact angle (hydrophobicity) decreases as laser fluence increases, likely due to surface modification, which makes the surface more hydrophilic.

At fluences below 1 J/cm^2, the ablated area fraction is minimal for both pulse durations. There is a steep increase in ablated area fraction near 1 J/cm^2. For τ_p = 10 ps, the ablation onset occurs slightly earlier and results in a higher ablated fraction compared to τ_p = 10 ns (Figure S3(b)). Ablation begins around 1 J/cm^2, and the ps pulses (10 ps) lead to a higher ablation fraction than ns pulses (10 ns), suggesting that the shorter pulse duration is more effective at removing material.

Normalized profile arc length and surface roughness R_a of copper structured by laser depending on peak laser fluence are depicted in Figure S4.

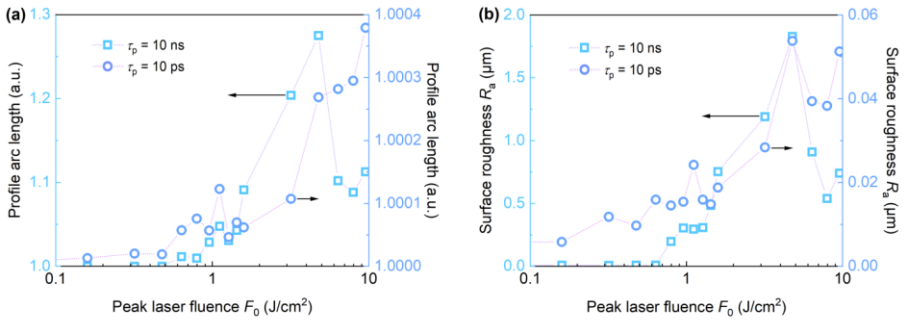

Figure S4. Normalized arc length of height profile line (a) and surface roughness R_a (b) dependence on the peak laser fluence of copper surface structured by nanosecond (τ_p = 10 ns - open squares) and picosecond (τ_p = 10 ps - open circles) pulses.

Figure S4 illustrates the relationship between peak laser fluence profile arc length and surface roughness**.** The profile arc length increases as the peak laser fluence increases for both pulse durations, but the behavior is more pronounced at higher fluences (Figure S4(a)). The curve for τ_p = 10 ps shows a more gradual increase compared to the τ_p = 10 ns case, especially as the fluence exceeds 1 J/cm^2. At

low fluence <1 J/cm² both curves are relatively flat, showing minimal change in arc length (Figure S4(a)).

Surface roughness increases as the laser fluence increases for both pulse durations, but the behavior is more significant for τ_p = 10 ns (Figure S4(b)). The roughness is relatively low (less than 0.5 µm) at low fluences (<1 J/cm²), but it spikes significantly for τ_p = 10 ns around 10 J/cm², reaching values as high as 2 µm. The τ_p = 10 ps, curve also shows an increase but at a much slower rate compared to the τ_p = 10 ns curve.

Normalized profile arc length and surface roughness R_a of copper structured by laser depending on static water contact angle are depicted in Figure S5.

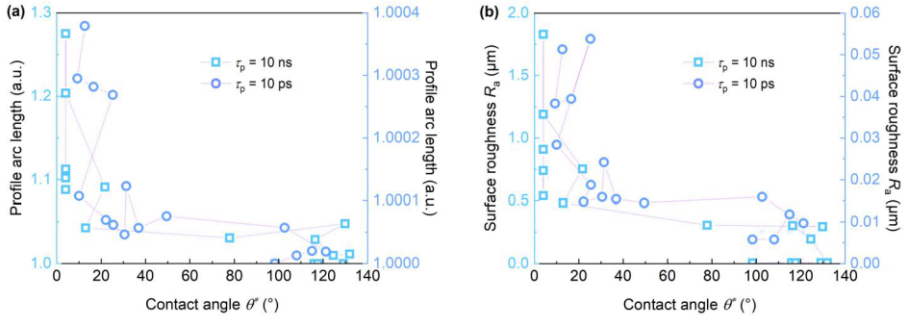

Figure S5. Normalized arc length of height profile line (a) and surface roughness R_a (b) dependence on the static water contact angle of copper surface structured by nanosecond (τ_p = 10 ns - open squares) and picosecond (τ_p = 10 ps - open circles) pulses.

Figure S5 shows how profile arc length and surface roughness relate to the contact angle θ^*, for two laser pulse durations. The graphs present how these surface characteristics change with varying contact angles, which reflects material wettability and texture, in response to laser processing.

The profile arc length decreases sharply as the contact angle increases from 0° to around 40° for both pulse durations Figure S5(a). For ns pulses, the profile arc length starts around 1.2 and decreases more drastically than for ps pulses. After the initial drop, both curves flatten, and the profile arc length stabilizes in the value range of 1.0 - 1.1 for contact angles greater than 60°. The curve for ps pulses is smoother compared to the ns pulses, showing a more gradual transition between contact angles.

For ns pulses, roughness starts near 2 µm at low contact angles (0°–10°) and decreases sharply to below 1 µm as the contact angle approaches 40° Figure S5(b). For ps pulses, the decrease is less dramatic but follows a similar trend, starting at around 1.5 µm and flattening after 40°. At higher contact angles (60° to 140°), surface roughness stabilizes at low values (below 0.5 µm), with slight fluctuations but no significant changes for either pulse duration.

NOTES

NOTES

NOTES

Vilniaus universiteto leidykla
Saulėtekio al. 9, III rūmai, LT-10222 Vilnius
El. p. info@leidykla.vu.lt, www.leidykla.vu.lt
bookshop.vu.lt, journals.vu.lt
Tiražas 25 egz.